CONTROL OF DIFFUSIVE TIME SCALES IN ZEOLITIC IMIDAZOLATE FRAMEWORKS FOR THE KINETIC SEPARATION OF LIGHT HYDROCARBONS

A Dissertation
Presented to
The Academic Faculty

by

Brian R. Pimentel

In Partial Fulfillment
Of the Requirements for the Degree
Doctor of Philosophy in the School of
Chemical & Biomolecular Engineering

Georgia Institute of Technology
May 2018

CONTROL OF DIFFUSIVE TIME SCALES IN ZEOLITIC IMIDAZOLATE FRAMEWORKS FOR THE KINETIC SEPARATION OF LIGHT HYDROCARBONS

Approved by:

Dr. Ryan P. Lively, Advisor
School of Chemical &
Biomolecular Engineering
Georgia Institute of Technology

Dr. Christopher W. Jones
School of Chemical &
Biomolecular Engineering
Georgia Institute of Technology

Dr. Krista S. Walton
School of Chemical &
Biomolecular Engineering
Georgia Institute of Technology

Dr. Angus P. Wilkinson
School of Chemistry and
Biochemistry
Georgia Institute of Technology

Dr. David S. Sholl
School of Chemical &
Biomolecular Engineering
Georgia Institute of Technology

Date Approved: March 21st, 2018

ACKNOWLEDGEMENTS

I'd like to many people to whom I owe a significant debt of gratitude for supporting me through this graduate program. To my advisor, Dr. Lively, for giving me the oportunity to join and build this new lab. You said from day one that our work would be a partnership, and I thank you for your dedication to a relationship where your door was always open, where we spent far too many hours trying to work things out together on the white board and just "drawing it bigger" when it didn't make any sense. The Ph.D. experience would have been a far more unpleasant one without your commitment to my success.

To my parents, for their numerous sacrifices to get me to where I am today, and for only asking me when I'm going to graduate a couple dozen times. To my lab mates, Melinda Jue and Simon Pang, whose friendship, intellectual contributions, and numerous distractions made banging my head against a scientific wall bearable, and whose efforts in building the Lively Lab have been invaluable. To my friends in the department, Taylor Sulmonneti, Nils Persson, Brandon Plaisance, Ross Verploegh; thank you for keeping me sane outside outside of work hours and sharing in the terrible experience of studying for quals.

Finally, to my girlfriend Bonnie. For your love and support since the day we've met, your continuous sacrifices, for teaching me the importance of making lists, and for being the most reliable constant in my life. I'm lucky to have met you, and I'm ready for our next adventure together.

TABLE OF CONTENTS

LIST OF TABLES

LIST OF FIGURES

LIST OF SYMBOLS AND ABBREVIATIONS

Letters, and letter-like symbols

H_{ads}	Heat of adsorption	[kJ mmol^{-1}]
W_p	Pressure work	[J mol^{-1}]
$\dot{n}$	Molar flow rate	[mmol s^{-1}]
u_0	Superficial velocity	[cm/s]
Đ	Darken Corrected Diffusivity	[cm^2 s^{-1}]
B	Boilup ratio	[-]
C	Adsorbed concentration	[mmol g^{-1}]
D	Diffusivity	[cm^2 s^{-1}]
E	Activation energy	[kJ mol^{-1}]
J	Molar flux	[mmol s^{-1} cm^{-2}]
K	Mass transfer coefficient	[cm s^{-1}]
L	Length, mobility coefficient	[cm], [J cm^2 mol^{-1} K^{-1} s^{-1}]
M	Sample uptake	[g g^{-1}]
P	Pressure	[bar]
R	Ideal gas constant, radius, reflux ratio	[J mol^{-1} K^{-1}], [cm], [-]
T	Temperature	[K]
a	Crystal radius	[cm]
b	Langmuir affinity constant	[mmol g^{-1}bar^{-1}]
c	BET constant	[-]
d	Particle diameter	[cm]
q	Adsorbed quantity	[mmol g^{-1}]

r	Radial length	[cm]
t	Time	[s]
v, V	Adsorbed gas quantity, Volume	[ccSTP]
x	Liquid phase mole fraction	[-]
y	Gas phase mole fraction	[-]
z	Reduced spreading pressure, length	[-], [m]
$\mathcal{P}$	Permeability	[Barrers]
$\mathcal{S}$	Sorption coefficient	[mmol g^{-1} bar^{-1}]

Greek symbols

α, α'	Fractional uptake, selectivity, heat transfer ratio	[-]
β'	Heat capacity ratio	[-]
η	Efficiency	[-]
θ	Reduced saturation pressure	[-]
μ	Chemical potential, viscosity	[J mol^{-1}], [Pa s]
π	Spreading pressure, pi	[Pa], [-]
σ	Standard error	[unit]
τ	Time constant	[s]
ϵ	Void fraction	[-]
ϕ	Ratio of time constants	[-]

Super and subscripts

0	Saturation, initial
∞	Equilibrium value
i, j	Species i, j

m	Molar
s	Saturation
t	At time t

SUMMARY

As worry about the sustainability of current economies continues to grow, significant technological efforts are still necessary to reduce CO_2 emissions and avoid catastrophic climate consequences. Energy demands worldwide are far outpacing the added renewable capacity, and recent sources of cheap fossil fuels seem to only delay the necessary implementation of renewable energy programs. However, the continued processing of hydrocarbon resources, whether for fuels, plastics, or chemicals will likely be a reality for the foreseeable future. Given that the energy expended in the industrial separation of chemicals represent a significant portion of the global power consumption, the chemicals industry finds itself in a uniquely influential position to ensure the environmental health of the planet.

Most chemicals today are separated by distillation, an extremely robust and effective process, but one that by nature is quite energy intensive. However, advanced separation methods, such as membranes and adsorption, have the potential to replace distillation as a lower energy alternative, but are currently material limited. The goal of this thesis is to investigate new sorbent materials for the kinetic separation of light hydrocarbons and incorporate them into a viable mass transfer contactor for use in a pressure swing adsorption unit. Three objectives are set to achieve this goal. **i)** The fundamental measurement of adsorption and diffusion phenomena within zeolitic imidazolate frameworks, and the investigation of how the structural flexibility of these affect guest transport. **ii)** Determining the role of diffusive time scales in the kinetically-selective uptake of a multicomponent mixture and the manipulation of those time scales

for the separation of such a mixture. **iii)** The operation and evaluation of a kinetic pressure swing adsorption system for the separation of light hydrocarbons using structured Metal-Organic Framework fiber sorbent beds.

The first objective demonstrated that adsorbent material flexibility is inherently linked with guest transport phenomena. Moreover, different structures are found to not be equally flexible; topological configurations can affect the flexibility of a pore based on its number of ring members. Furthermore, the flexibility of the structures is found to impart a unique temperature dependence on diffusion, where the changing pore rigidity leads to non-Arrhenius behavior.

Exploring the second objective, idealized batch separations of multicomponent mixtures allowed for the tuning of the diffusive time constants in a kinetically-controlled adsorptive separation. It was demonstrated that differences in mass transfer may only be exploited at the relevant time scale of the process, which may be manipulated by changing the sorbent size or diffusion rates of the guest species via temperature changes. The transition from equilibrium-control to kinetic-control in a ethane/propane breakthrough system was demonstrated by only changing the crystal size, reversing the selectivity of the sorbent.

The third objective culminated in the synthesis of ZIF-8/cellulose acetate fiber sorbent composites up to 60%, which were assembled into modules and employed in the kinetic separation of propane/propylene. Equimolar mixtures were separated up to an 81 mol% propane product, demonstrating the viability of the materials as kinetic sorbents for hydrocarbon separations.

CHAPTER 1. INTRODUCTION

1.1 Energy and Sustainability in the Global Chemicals Industry

Mankind's capability to manipulate the natural world is intrinsically tied to its ability to harness energy from different sources and direct them towards a purpose. Early examples outside of human labor were largely mechanical and can be said to include beasts of burden, windmills, or water wheels. Chemical energy in the form of wood or charcoal provided heat when burned that allowed for the manipulation of metals and metal ores. It was during the industrial revolution where the way we directed energy began to increase in complexity.

The development of steam power and the later growing availability of petroleum products developed alongside new methods of mass production, and as a result mechanization of both industry and lifestyle became more prevalent. Coal and other forms of fossil fuels became the dominant energy source and global energy consumption per capita began to increase dramatically. [1] It was this increase in carbon-based energy usage that began the meteoric rise of atmospheric CO_2 levels, which now threatens to destabilize the global climate (**Figure 1.1**).[1]

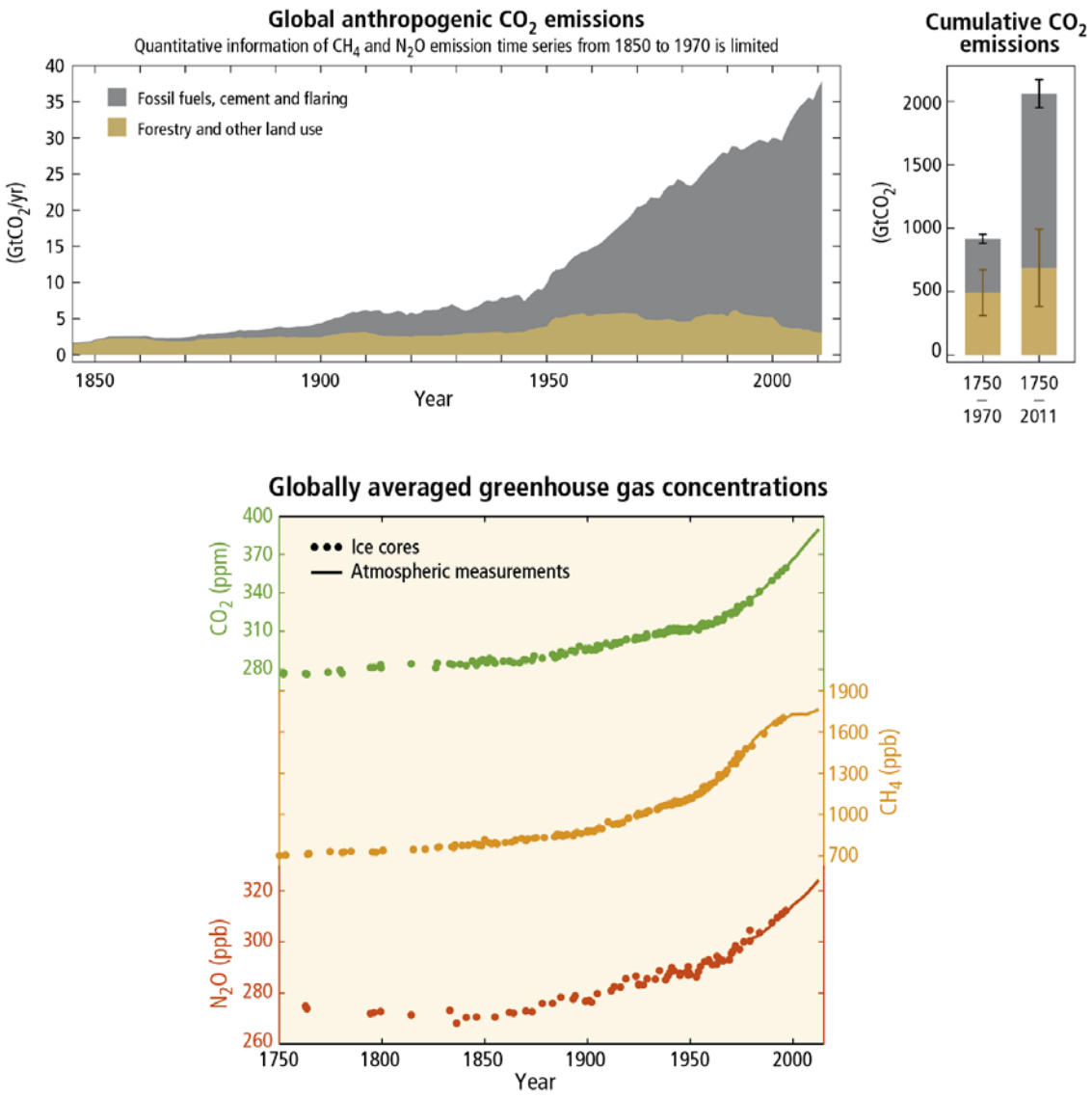

Figure 1.1 (*Top*) Global anthropogenic CO_2 emissions from forestry and other land use as well as from burning of fossil fuel, cement production and flaring. Cumulative emissions of CO2 from these sources and their uncertainties are shown as bars and whiskers, respectively, on the right hand side. (*Bottom*) Atmospheric concentrations of the greenhouse gases carbon dioxide (CO2, green), methane (CH4, orange) and nitrous oxide (N2O, red) determined from ice core data (dots) and from direct atmospheric measurements (lines).[1]

Current global energy consumption stands at approximately 575 Quad (quadrillion BTU), and is a steadily increasing value over the last few decades, with most of that growth attributable to Asia and Oceania (**Figure 1.2**). [2] The United States alone represents

approximately 98 Quad, and about 32% of that energy is consumed by industrial processes (**Figure 1.3**).[3] A large number of industrial systems, and certainly almost all chemical processes, incorporate some form of a separation process. This is so much so, that approximately half of industrial energy consumption is consumed in a separation process, ultimately accounting for 10-15% of national energy usage.

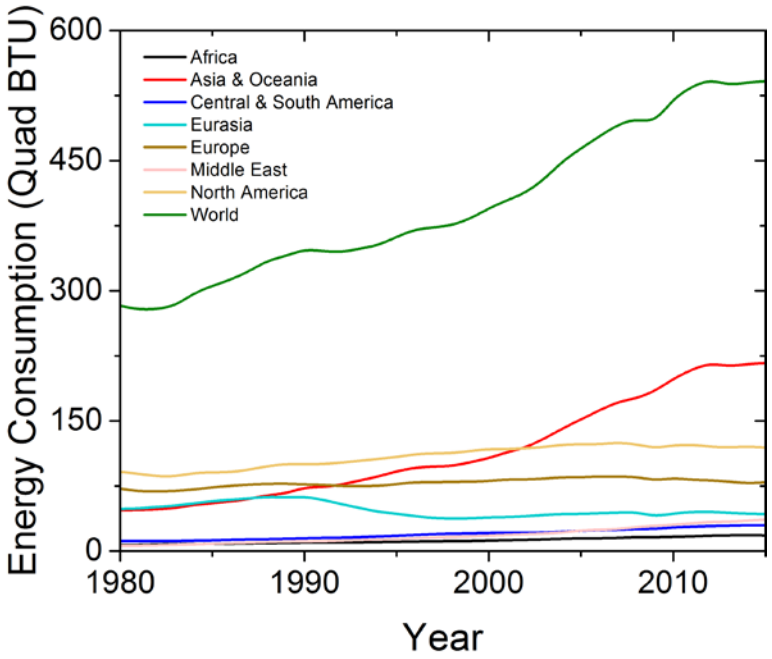

Figure 1.2 World primary energy consumption by region. [2]

Almost 80% of industrial separation energy consumption comes in the form of some thermal separation, that is to say, distillation, evaporation, etc. Despite the high degree of heat integration present in most modern processes, the need to vaporize the feed in these thermal separations typically results in an unrecoverable energy penalty and high energy costs. Although still technologically infeasible for many common separations, the substitution of distillation processes with more thermodynamically efficient options, like membranes or adsorption, could significantly reduce global energy consumption and aid in the reduction of greenhouse gas emissions.

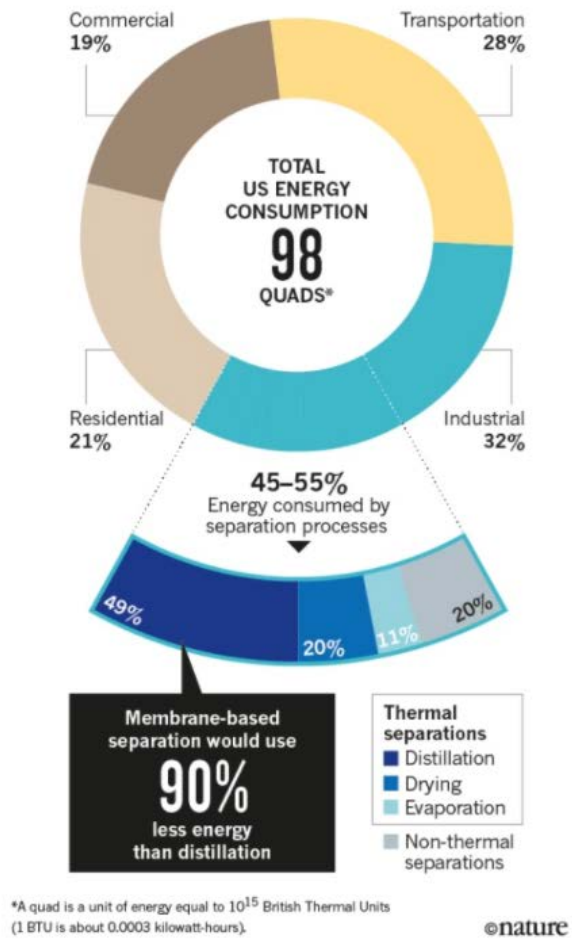

Figure 1.3 Breakdown of U.S. energy consumption by sector, highlighting the potential gains in energy savings by targeting thermal-based chemical separations. Reprinted with permission, Copyright Springer Nature 2016[3]

The chemical and petroleum industry, as the main operators of distillation equipment and consumers of raw materials, are in a unique position to enact lasting change and ensure the sustainability of the Earth's climate and resources. By investing in new separation technologies and embracing renewable chemistry principles, significant amounts of energy and resources can be saved annually. Realistically, this change will not come to fruition until these technologies are economically viable, which is to say, either the economic landscape must change, or the technological capabilities need to approach profitability.

1.2 Changing Energy Sources and Chemical Feedstocks

Within the United States, large increases in domestic natural gas production as a result of hydraulic and horizontal fracturing activities have shifted the energy and chemical feedstock landscape (Figure 1.4). Natural gas production continues to set record highs as coal usage in electricity steadily declines.[4] Petroleum remains a dominant energy source, largely due to the difficulties in replacing it as a high-density transport fuel. This increase in natural gas production brings a concurrent increase in natural gas liquids (NGLs) production, for which several domestic world-scale light crackers have already been commissioned. [5]

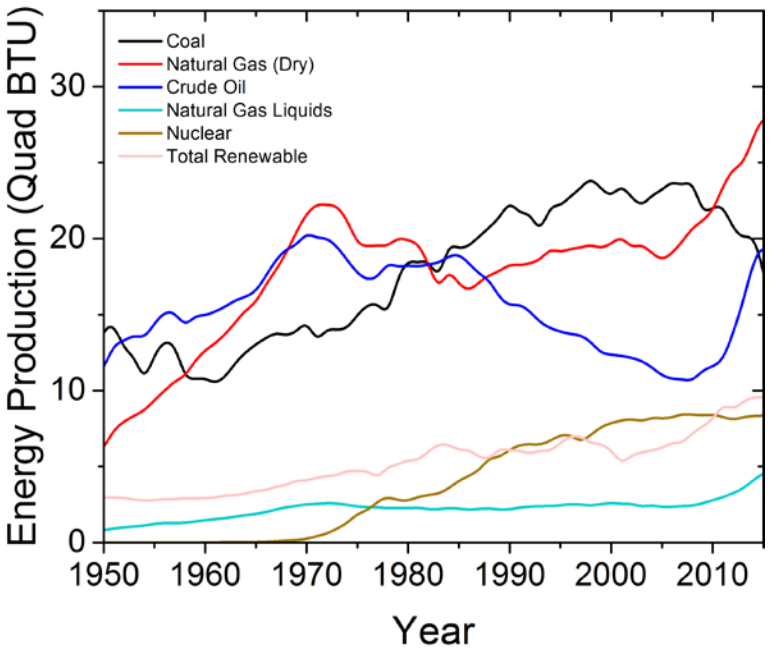

Figure 1.4 Yearly primary energy production in the United States by source. [4]

The increase in light cracking feedstock results in greater production of C_2 and C_3 hydrocarbons, which feeds the growing demand for polypropylene and polyethylene production. The polymer production from olefin monomer of PE and PP generally requires high purity (>99.5%) products on the order of millions of tonnes per year. These market

factors combine to make olefin/paraffin separations extremely important target for energy reduction efforts.

1.3 Modern Gas Separations

Many modern gas separation techniques are based on the Linde process of cryogenic distillation, where gases are cooled via pressure expansion into their two-phase envelope and distilled as a vapor-liquid mixture (**Figure 1.5**). The use of turbo-expanders for these columns is a large source of energy consumption and noise.[6] These distillation columns are generally capital intensive and take good advantage of economies of scale, but similarly prohibit the addition of incremental capacity. Other schemes generally involve adsorption of a gas component into a reactive liquid, most useful for extraction of acid gases from non-polar carriers. These schemes also have a large energetic penalty in the reversal of the gas-solvent interaction.

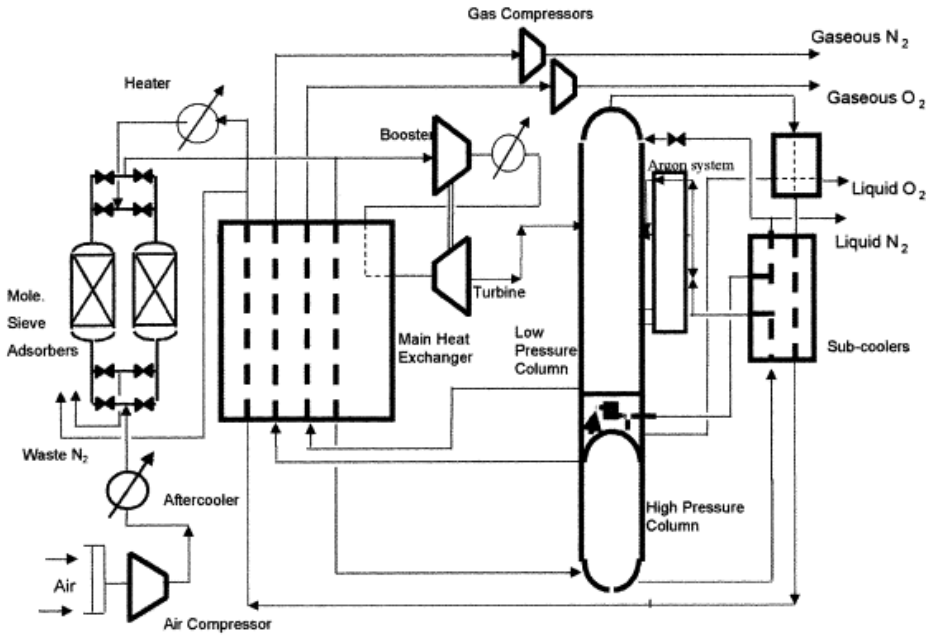

Figure 1.5 Simplified process flow diagram for a low-pressure air separation plant. Reprinted with permission, Copyright Elsevier 2002 [7]

Olefin/paraffin separations are generally quite difficult due to the similar boiling points of the hydrocarbon species; they require distillation towers with many stages and often employ cryogenic refrigeration cycles, making them extremely energy intensive. However, this can be an opportunity for the field to make significant improvements to state-of-the-art separations technology to introduce timely energy and cost reduction strategies that ease the difficulty of light hydrocarbon processing (**Figure 1.6**).

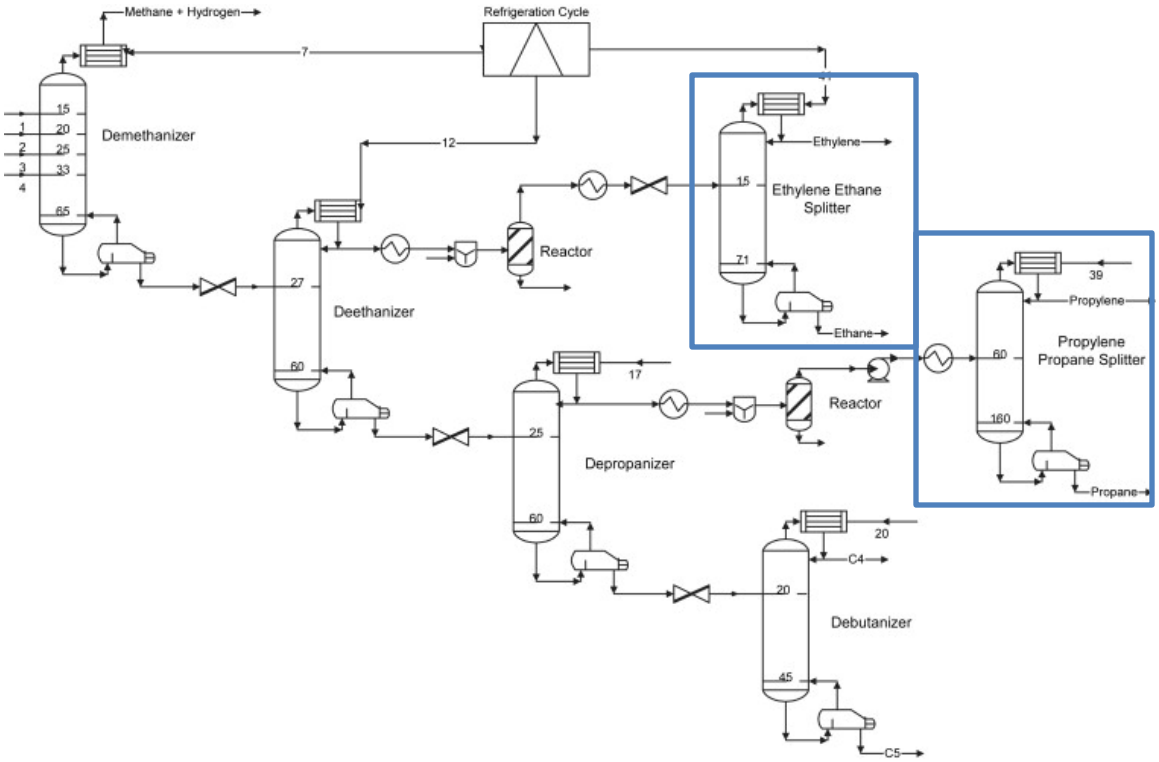

Figure 1.6 Flowchart of a Quattor Petrochemical Co. olefins production plant using cracked naphtha as a process feed. Reactors are used to hydrogenate acetylene and diene minor products into olefins. Typical feed into the splitters are 70-80% olefin. Reprinted with permission, Copyright Elsevier 2010 [8]

1.4 Advanced Separations Techniques

Although distillation is by far the most common and robust method of chemical separation, emerging separation technologies aim to achieve the same levels of purities and recoveries through the use of more thermodynamically efficient techniques. Membranes

offer a selective barrier through which molecules may pass, although may be difficult to manufacture in a defect-free manner in the case of inorganic membranes.

Pressure and temperature swing adsorption typically relies on the difference in surface interactions between two gas molecules, and adsorption systems are significantly easier to scale and manufacture than membranes. The most common sorbent materials are often carbons, silicas, and zeolites, but these separations are inherently material limited and are only as good as the sorbent employed. A great number of metal-organic frameworks are constantly being developed for the purposes of creating new, more selective, sorbents. A sub-class of the sorptive separation is the kinetic separation, which leverages differences in diffusion rates through a microporous sorbent rather than differences in thermodynamic adsorption coefficients. Typical materials for this separation are small-pore zeolites, or carbon molecular sieves. However, the variety of MOF structures available and the ability to more easily control crystal dimensions creates an opportunity for new kinetically-selective materials to be employed in industrial gas separations

Current olefin/paraffin separations techniques—outside of distillation—largely rely on facilitated transport mechanisms or other forms of preferential charged interactions with the olefinic π-bond. Facilitated transport membranes suffer from depletion of the carrier and a resultant decrease in flux, while polymeric membranes are prone to plasticization by heavy hydrocarbons.[9-10] Recent developments in carbon molecular sieve membranes exploit the differences in kinetic diameter to separate the C_2 and C_3 pairs based on differences in diffusivities, although they exhibit low permeabilities.[11-13] Sorption-based strategies tend to result in lower recovery despite being able to achieve high purities[11, 14] The use of kinetically selective sorbents, much like what is often used to separate CO_2 from

CH_4 or O_2 from N_2, could provide an easily scalable alternative to olefin/paraffin distillation enhancements. Indeed, examples of kinetic propane/propylene separation exist using Zeolite 4A and achieving polymer-grade purities with recovery in excess of 80% in the presence of N_2.[15] Metal-Organic Frameworks, being of varied topology, chemistry, and physical dimension, are promising candidates for this exploration of new materials to further enhance this approach.

1.5 Thesis Objectives

The overall objective of this thesis is to enable the use of diffusionally-selective metal-organic frameworks in the kinetic pressure swing adsorption of light hydrocarbons. To achieve this goal, this thesis will span the fundamental measurement and understanding of host and guest-host interactions, demonstrate the potential for kinetic adsorption control via proof-of-concept experiments, and finally produce scalable structured mass transfer contactors for use in pilot separation configurations.

1.5.1 Objective 1

The fundamental measurement of adsorption and diffusion phenomena within zeolitic imidazolate frameworks, and the investigation of how the structural flexibility of these affect guest transport.

To appropriately design a novel pressure swing adsorption cycle, the fundamental sorbate-sorbent interactions must be understood. In typical systems, this generally means characterization of the adsorption parameters as a function of temperature and pressure. However, in the design of a kinetic separation system, understanding the rate of diffusion

within the sorbent as a function of guest molecule is equally important. Exploring and understanding how the sorbent structure and composition affects this mass transfer informs the selection of appropriate materials for a given separation. This knowledge will be created through the measurement of single component isotherms and diffusivities across two different structures, comparing their molecular sieving capabilities, and using those data to draw conclusions between material structure and flexibility.

1.5.2 Objective 2

Determining the role of diffusive time scales in the kinetically-selective uptake of a multicomponent mixture and the manipulation of those time scales for the separation of such a mixture.

Metal-Organic Frameworks have some advantages over traditional sieving materials, namely that control of the crystal size is possible across several orders of magnitude. By controlling the diffusive time scale of the adsorption system, we can demonstrate a transition between kinetically and thermodynamically dominated processes utilizing the same sorbent. This could result in either an enhancement of material selectivity or a wholesale reversal, where a single sorbent could be operated in distinct selectivity regimes. Understanding the dependence of material selectivity on the relative time scales of the transient mass-transfer processes will produce the necessary knowledge to appropriately scale cycle parameters.

1.5.3 Objective 3

The operation and evaluation of a kinetic pressure swing adsorption system for the separation of light hydrocarbons using structured Metal-Organic Framework fiber sorbent beds.

The final goal of this work is to explore the realistic operation of a kinetic pressure swing adsorption cycle using diffusionally selective metal-organic frameworks. This will be completed by the incorporation of the previously characterized sorbent within a porous polymer fiber, forming a structured tube bundle for high surface area contact and low operational pressure drop. As with all cycle development work, the effect of feed rate and cycle time on purity and recovery will be assessed to evaluate the performance potential of this new separation unit.

1.6 References

1. Pachauri, R. K.; Allen, M. R.; Barros, V. R.; Broome, J.; Cramer, W.; Christ, R.; Church, J. A.; Clarke, L.; Dahe, Q.; Dasgupta, P., *Climate change 2014: synthesis report. Contribution of Working Groups I, II and III to the fifth assessment report of the Intergovernmental Panel on Climate Change*. IPCC: 2014.

2. International Energy Statistics - Total Primary Energy Consumption. Energy Information Administration: eia.gov, 2018.

3. Sholl, D. S.; Lively, R. P., Seven chemical separations: to change the world: purifying mixtures without using heat would lower global energy use, emissions and pollution--and open up new routes to resources. *Nature* **2016,** *532* (7600), 435-438.

4. U.S. Primary Energy Production by Source. www.eia.gov ed.; Energy Information Administration: 2018.

5. Chang, J., Visibility clears on the 2nd wave of US petrochemical projects. *ICIS Chemical Business* 12 April, 2017, 2017.

6. Bloch, H. P.; Soares, C., *Turboexpanders and process applications*. Gulf Professional Publishing: 2001.

7. Castle, W. F., Air separation and liquefaction: recent developments and prospects for the beginning of the new millennium. *International Journal of Refrigeration* **2002,** *25* (1), 158-172.

8. Fábrega, F. M.; Rossi, J. S.; d'Angelo, J. V. H., Exergetic analysis of the refrigeration system in ethylene and propylene production process. *Energy* **2010,** *35* (3), 1224-1231.

9. Staudt-Bickel, C.; Koros, W. J., Olefin/paraffin gas separations with 6FDA-based polyimide membranes. *J. Membr. Sci.* **2000,** *170* (2), 205-214.

10. Das, M.; Koros, W. J., Performance of 6FDA–6FpDA polyimide for propylene/propane separations. *J. Membr. Sci.* **2010,** *365* (1), 399-408.

11. Xu, L.; Rungta, M.; Koros, W. J., Matrimid® derived carbon molecular sieve hollow fiber membranes for ethylene/ethane separation. *J. Membr. Sci.* **2011,** *380* (1), 138-147.

12. Koros, W. J.; Zhang, C., Materials for next-generation molecularly selective synthetic membranes. *Nat. Mat.* **2017,** *16*, 289.

13. Xu, L.; Rungta, M.; Brayden, M. K.; Martinez, M. V.; Stears, B. A.; Barbay, G. A.; Koros, W. J., Olefins-selective asymmetric carbon molecular sieve hollow fiber membranes for hybrid membrane-distillation processes for olefin/paraffin separations. *J. Membr. Sci.* **2012,** *423-424*, 314-323.

14. Han, S.-S.; Park, J.-H.; Kim, J.-N.; Cho, S.-H., Propylene Recovery from Propylene/Propane/Nitrogen Mixture by PSA Process. *Adsorption* **2005,** *11* (1), 621-624.

15. Grande, C. A.; Rodrigues, A. E., Propane/propylene separation by pressure swing adsorption using zeolite 4A. *Ind. Eng. Chem. Res.* **2005,** *44* (23), 8815-8829.

CHAPTER 2. BACKGROUND AND THEORY

This chapter discusses the background knowledge related to the adsorption and diffusion of gases and vapors in microporous materials. The chapter first addresses a brief review of the state-of-the-art in zeolitic imidazolate framework sorbents and membranes, including their fundamental adsorption and transport properties. This is followed by fundamental thermodynamic descriptions of adsorption and diffusion in microporous materials, along with details of the experimental techniques for measuring both. Finally, the application of these materials towards a Pressure Swing Adsorption Cycle and the typical modifications appropriate for the improvement of performance metrics and the enabling of kinetically-selective cycle designs are described.

2.1 Zeolitic Imidazolate Frameworks

Zeolitic imidazolate framework (ZIF) materials are an emerging subclass of metal–organic frameworks (MOFs) containing imidazolate building units. While stable and porous MOF materials containing imidazole linkers were originally synthesized by the Chen group in 2003,[1] these materials rose to distinction with discovery of the incredible thermal and chemical stability of ZIFs,[2] meriting a distinct naming convention from other MOFs. Over 150 ZIF structures have been synthesized, incorporating numerous different

types of functional groups and enabling a diverse variety of topologies and chemical functionalities within their structures.

The robustness of these MOF structures has made them attractive for numerous applications, including catalysis,[3] electronic devices,[4] drug delivery,[5] and more. Two of the most promising applications are utilization as the selective component of membranes and as sorbents. For these applications, the key performance metrics are stability and selectivity in all applications, as well as permeance and sorption capacity for membranes and sorbents, respectively. Current ZIF materials have demonstrated considerable potential for these separation applications, hopefully making industrial implementation attainable in the near future. The primary motivating advantage of ZIFs relative to traditional materials such as zeolites or polymers is the potential for fine control over the pore aperture, framework chemistry, surface area, and pore volume. Furthermore, the combination of reasonable chemical, mechanical, and thermal stability allows ZIFs to be easily processed into realistic separation devices. This ability to process—combined with pore aperture dimensions similar to many gas pair molecular dimensions—u uniquely position ZIFs within the MOF family as primary candidates for gas separations. Although certain exceptions to this general observation may be found within MOF materials,[6-9] ZIFs as a class possess the appropriate combination of properties that are more readily amenable to gas separations. Other MOFs often exhibit pore windows too large for sieving behavior and may suffer from irreversible adsorption to open metal centers and structural stability in the presence of acid gases or moisture.

2.1.1 Physical and Chemical Properties of ZIFs

The industrial importance of zeolites made synthesis of MOFs with zeolite topologies an alluring goal. Most initial MOF structures contained the linear benzenedicarboxylate (BDC) or benzenetricarboxylate (BTC; providing 120° bonding angles) ligands.[10] Changing the organic linkers to the 5-membered ring imidazole altered the accessible bonding angle as shown in **Figure 2.1**. The importance of these imidazolate-based materials gained significance when the You group[11] correctly reasoned that the bonding angles using an imidazolate linker created a 145° angle between adjacent metal centers. This angle is similar to the bond angles found between Si—O—Si connections in zeolites. Indeed, the bonding angle design concept proved powerful. Utilizing the imidazole analogue benzimidazole, the Chen group reported the synthesis of a structure with the SOD topology, the ZIF that would later become known as ZIF-7.[2]

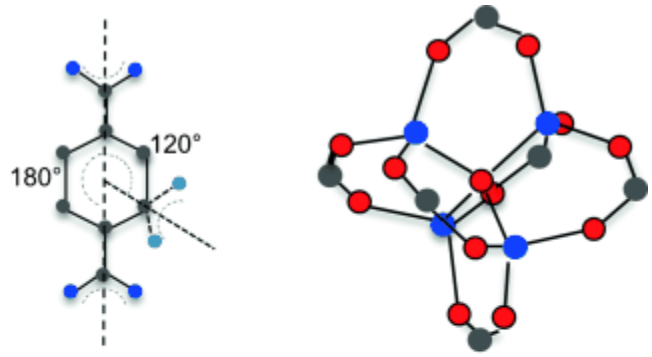

(a) Bonding Angle and SBU for Carboxylate linkers

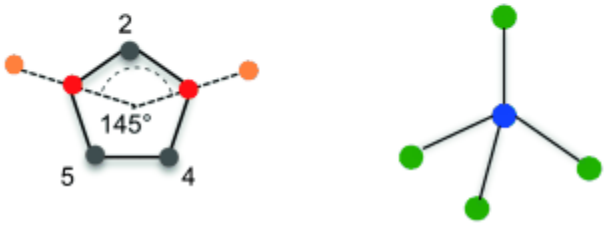

(b) Bonding Angle and SBU for Imidazolate linkers

Figure 2.1 Metal–ligand coordination for (a) carboxylate linker where the M–BDC–M angle is around 120° resulting in an octahedral structural building unit (SBU), and (b) imidazolate linkers where the M–Im–M angle is 145° resulting in a tetrahedral SBU. C: grey, O: blue, N: red, metal: orange. This figure has been adapted from a previous reference.[10, 12]

The imidazolate building unit has enabled several other zeolite topologies to be synthesized based on the similarity in bond angles. However, the true distinction that earned these materials a unique naming convention was the incredible thermal and chemical stabilities observed by Yaghi's group for ZIF-8, ZIF-7 and ZIF-11.[12] Thermal stability was evaluated for ZIF-8 and ZIF-11 from TGA, finding that the material did not show appreciable mass loss between 200 °C and 400 °C when heating at 10 K min^{-1} in an air environment. The chemical stability was evaluated by boiling the material in water, toluene, methanol, and aqueous sodium hydroxide. Material properties did not change appreciably over seven days for the chemical treatments. With these findings, the first 12 ZIFs were named, consisting of imidazole, benzimidazole, and methyl-imidazole (mIm) ligands with primarily zinc and cobalt metal ions, although indium was also used.

Interaction between framework species in microporous materials and different adsorbates can induce molecular rearrangements that are observed as steps in the adsorption isotherm. In zeolites such as silicalite-1, the process corresponds to adsorbate rearrangement.[13] Early experiments observing stepped isotherms for ZIFs in N_2 and Ar adsorption[12] were interpreted as a rearrangement of the adsorbed molecules since the XRD measurements before and after the adsorption measurements were identical. Subsequent in situ measurements revealed that the stepped isotherms originated from structural deformation of the ZIF material at high pressures[14] or high adsorbate activities.[15] This leads to a crystallographic transition that increases the accessible pore size and volume and correspondingly the adsorbate uptake. The transition enables the uptake of large molecules beyond the original pore aperture via rotation of the imidazolate linkers.

Later work focusing on modeling N_2 adsorption in ZIF-8 via Grand Canonical Monte Carlo (GCMC) calculations evaluated the importance of framework flexibility on adsorption isotherms.[15] The use of the evacuated crystal structure parameters reproduced experimental uptake values at low pressures but could not capture the increase in pore volume associated with linker rotation. The authors found that the structure shown in **Figure 2.2**, which was formed under mechanical strain of 1.47 GPa in a diamond anvil cell, could reproduce the experimental data. These mechanical pressures are substantially higher than the adsorbate pressures observed to cause the structure deformation, and was corroborated via in situ XRD measurements at loadings beyond the observed isotherm step.[15] Recent neutron powder diffraction experiments have tracked the structural transition in ZIF-7, where the loading of CO_2 deforms the benzimidazole linkers in the six-

membered cages to the point of opening the structure and increasing the adsorption capacity.[16]

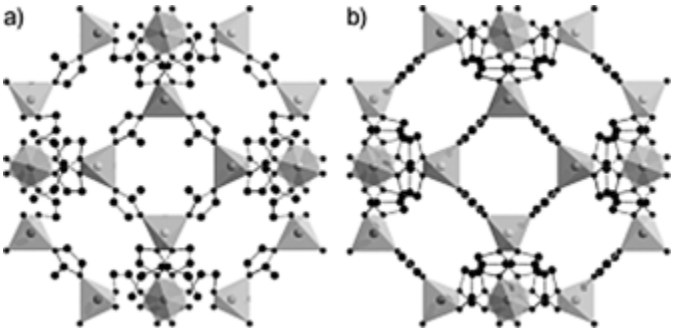

Figure 2.2 Visualization of the structural transformation of ZIF-8 (a) under 1.47 GPa of hydrostatic pressure (b). Reprinted with permission, Copyright Wiley-VCH 2014[14]

The flexible nature of ZIF frameworks is evident from works measuring adsorption of molecules larger than the ZIF's crystallographic pore size.[17-23] While under static conditions ligands may appear rigid,[24] slight modifications in adsorbate activity can induce dynamic behavior in ligand positioning that is more important when considering realistic adsorption and membrane applications.[25-26] The resultant molecular sieving abilities of ZIF materials is less effective relative to rigid materials such as Zeolite 5A.[19-20] Instead, researchers have observed a somewhat sharp decrease in measured diffusivities of species larger than the ZIF's crystallographic pore size to a nonzero value, exhibited in **Figure 2.3a**.[27] Indeed, ZIFs exhibit much weaker "diffusion cutoffs" than their topologically identical zeolite counterparts, where diffusivities approach zero sharply after a critical adsorbate kinetic diameter. This flexibility is further highlighted in **Figure 2.3b**. The activation energy of diffusion for ZIF-8 increases almost linearly with kinetic diameter,[28] in contrast to 4A and 5A zeolites, which see a sharp increase at kinetic diameters nearing their pore size.

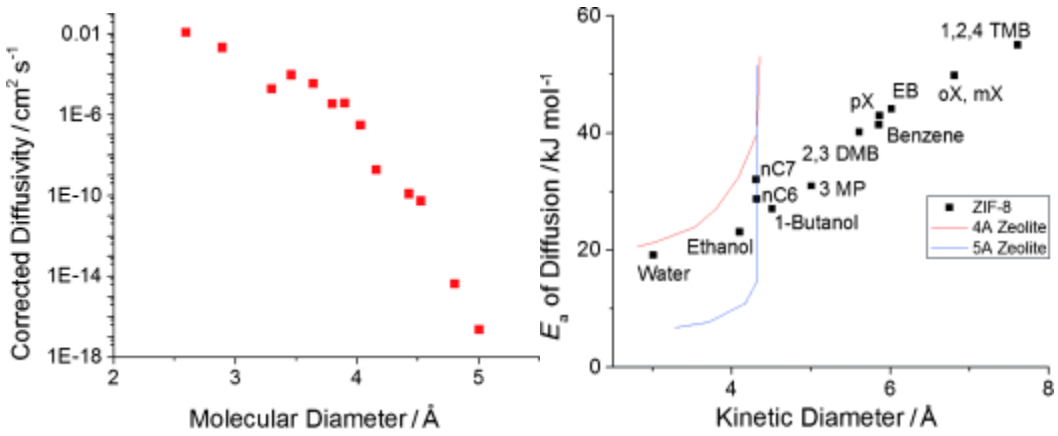

Figure 2.3 (a) Corrected intracrystalline diffusivity of gases in ZIF-8 as a function of molecular diameter (measured by mixed-matrix permeation and ZIF crystal volumetric uptake). ZIF-8 has a nominal pore size of 3.4 Å. Reprinted with permission, Copyright American Chemical Society 2012[27] (b) Activation energy of diffusion in ZIF-8 with increasing kinetic diameter. 4A and 5A zeolites display a drastic increase in diffusion activation energy past their respective pore aperture diameter because of their structural rigidity. Data obtained by gravimetric uptake techniques. Reprinted with permission, Copyright American Chemical Society 2013[28]

The framework flexibility of ZIFs is crucial to the diffusivity of mobile species within the material. Including flexibility has been key to accurately modeling gas diffusivities in ZIFs, especially for species similar in size to the nominal pore size.[26, 29-30] Sholl and co-workers[29, 31] reported pore limiting diameter histograms of ZIF-8, showing variations in the structure beyond its rigid pore diameter, though these still fall short of the kinetic diameter of some of the larger molecules with experimentally-reported uptakes. In the calculation of CH_4 and Xe diffusivity through ZIF-8, the use of the full window size distribution resulted in diffusivities 5 and 13 orders of magnitude greater, respectively, than using a time-averaged rigid approximation.[29] These modifications to rigid structure approximations result in a drastic improvement in calculated diffusivity of larger gases. These modifications also highlight situations where flexibility is unimportant, such as

adsorbates below the pore limiting diameter (H_2) that cause little change in calculated diffusivities with the addition of flexibility effects.

More recent modeling work has elucidated further the role of linker flexibility in diffusion. Verploegh et al. computationally studied the diffusion of a variety of molecules through the ZIF-8 pore aperture, suggesting that in addition to the inherent rotational flexibility of the pore linkers, the sorbate species themselves deform the aperture to a larger and broader window size distribution.[32] This helps to explain how molecules far beyond the kinetic diameter of predicted flexible pore apertures are still able to move through the restricted ZIF structure. Other work has similarly demonstrated the effect of sorbate-induced deformations in zeolites for the separation of ethane and ethylene, which suggests that even materials traditionally thought of as rigid have appreciable flexibility when adsorption of pore-size molecules is concerned.[33]

2.1.2 Synthesis Strategies

Figure 2.4 is a compilation of the different ZIFs classified based on their framework topology reported since the original synthesis. Both the ZIF and MAF naming conventions are noted. Analyzing the division of structures, several observations can be made for synthetic conditions using a single ligand, two ligands, different solvents, and different metal counterions. The typical synthesis conditions utilize zinc nitrate salts and the organic ligand under solvothermal conditions, utilizing dimethylformamide (DMF) as the solvent, as has been recently reviewed.[34-35] DMF is known to degrade under solvothermal conditions to dimethylamine, a base capable of deprotonating the imidazole ligand and initiating the crystallization process. Many modifications to these conditions

have been demonstrated to affect the structure and morphology, including changing the solvent and metal source and using ambient synthesis temperatures.

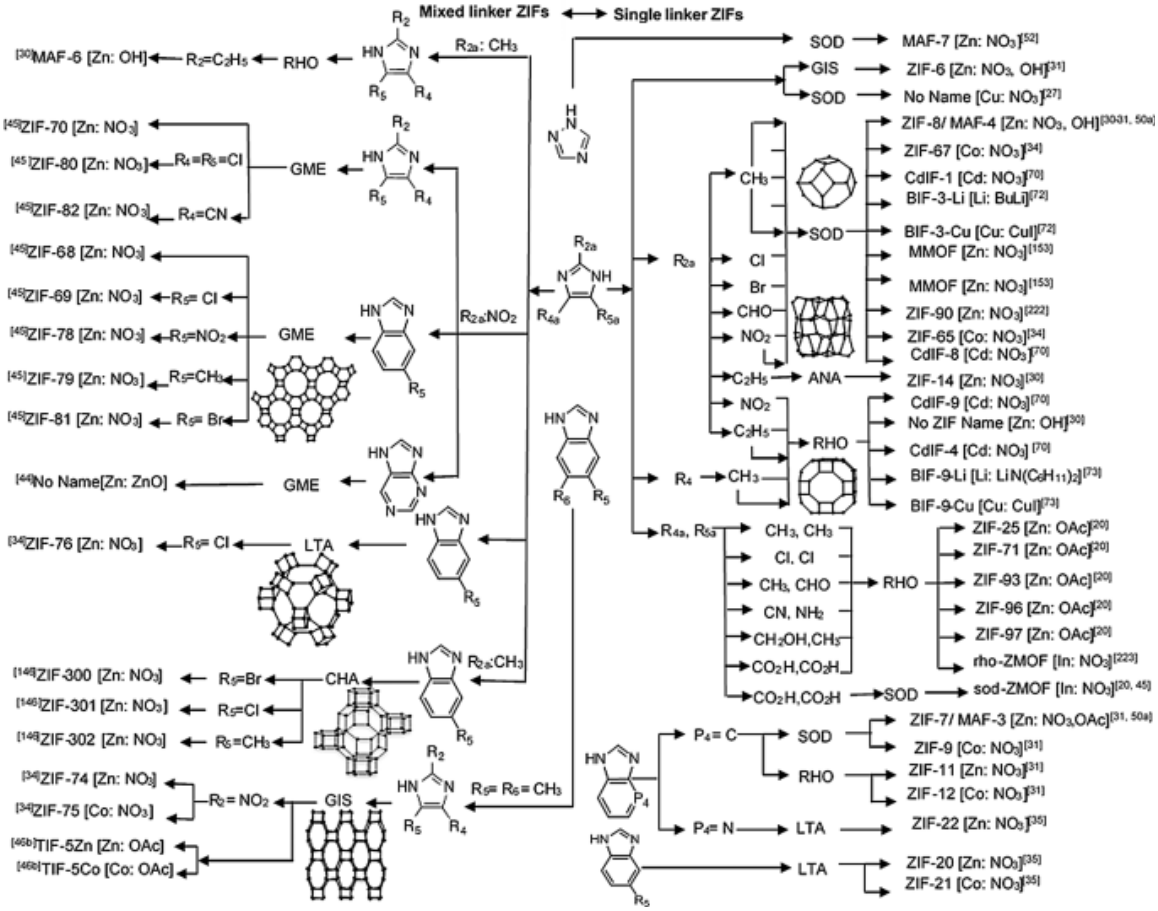

Figure 2.4 A summary of common single-linker and mixed-linker ZIFs classified based on the topology they form for a specific ligand or combination of ligands. Information about the ZIF name and metal source that was used to synthesize the respective materials is provided. The structures of different topologies are also illustrated schematically. Substituents not mentioned correspond to hydrogen substitution. References in the scheme correspond to numbering in the original publication.[36]

While the solvent can provide a structure-directing effect through occupying open space, it was also observed that the solvent could control the structure through altering ligand–ligand interactions. Using ethanol as the solvent, the benzimidazole linker formed the SOD topology. Adding toluene to the synthesis mixture formed the RHO topology.[37] The authors suggested that the toluene interacted with the aromatic ring of the benzimidazole linker, preventing the more dense SOD from forming.

The broad functional group tolerance of ZIF materials provides the ability to tune the ligand polarity, which has been shown to affect adsorption properties.[38-39] Many of these functional groups can be incorporated into the SOD and RHO topologies as a single ligand, creating a fixed pore aperture. The substituents on the organic linker affect not only the resulting ZIF topology, but also alter the pore volume, surface area, and aperture size available for gas diffusion. For the SOD topology, the bulky phenyl substituent on the benzimidazole (ZIF-7) decreases the pore aperture relative to the methyl group of 2-methylimidazole (ZIF-8) and the nitro group of 2-nitroimidazole (ZIF-65).

Only certain imidazolate linkers have been used to synthesize porous structures that are appropriate for membrane and adsorption applications. Bulkier ligands eliminate meaningful porosity while unfunctionalized imidazole linkers tend to produce nonporous structures. One route to decouple the ligand properties and porosity effects is through synthesizing materials containing two ligands. Creating combinations of two organic linkers has been treated in two different matters; these have been distinctly named hybrid and mixed linker systems. Mixed linker systems contain two linkers, but will only assemble into porous structures over a limited relative concentration range. The limited composition range that the combination of the two organic linkers produce porous structures effectively limits the ability to tune the structure-function properties.

Hybrid materials overcome the limited tunability of mixed linker systems, consisting of two linkers that can be incorporated over a wide range of relative compositions in a single topology. The technique was inspired from previous hybrid MOF synthesis reports. The first reported ZIF hybrid systems were ZIF-7-8 and ZIF-8-90.[40] The similarity in size between 2-imidazolecarboxyaldehyde (Imca) and 2-methylimidazole

(mIm) allowed synthesis of the ZIF-8-90 hybrids across the full range of compositions without altering the structure. The composition of the final structure was enriched in Imca across the composition space relative to the initial ligand composition, the reason for which is not completely understood. For the ZIF-7-8 hybrid, the steric bulk of the benzimidazole (bzIm) affected the crystal structure, resulting in a transition in structure around 35 mol % bzIm from an X-ray diffraction (XRD) spectrum characteristic of ZIF-8 to a ZIF-7 structure at a high mole fraction of bzIm. As with the ZIF-8-90 hybrid, the ratio of bzIm/mIm incorporated into the framework was greater than the ratio of bIm/mIm in the initial synthesis mixture. Moreover, the substitution of the Imca linker into the ZIF-8-90 hybrid system did not exhibit a major transition from the ZIF-8 structure to the ZIF-90 structure (as opposed to the ZIF-7-8 system), thus permitting a nearly continuous spectrum of Imca substitution.

Solvent Assisted Linker Exchange (SALE)[41] is an approach to synthesize isostructural MOFs by exchanging the linker in a parent MOF with another desired linker. The underlying mechanism driving the linker exchange is not completely known, but it is has been achieved through two different methods. One mechanism involves ligand exchange between free ligand and those in the framework of a particle[42-43] while the other mechanism entails exchange of the ligand between two already formed particles[43] While both mechanisms are possible for MOFs, the solution-to-particle mechanism has only been demonstrated for ZIFs, reflecting the chemical stability of ZIFs. Recent work by Jayachandrababu et al. investigated the spatial distribution of hybrid ZIF linkers formed by both non-solvent crystallization and SALE processes using fluorescence microscopy. It conclusively demonstrates that hybrid materials synthesized in solution have a uniform

radial composition, while SALE exchanged materials exhibit a definitive core-shell morphology due to the diffusion-limited nature of the process.[44] Related work using computational modeling of ^{1}H CRAMPS NMR further suggests that ordering of the different linkers within the unit cell is entirely random in solution-synthesized hybrids.[45]

The particle size is a function of the nucleation and growth processes. The nuclei grow to larger sizes through monomer addition, or particle addition. Ideally, nucleation and growth are temporally or spatially isolated so narrow particle size distributions are obtained. Small particles can be obtained utilizing conditions that favor nucleation over growth. The crystallization mechanism for ZIFs depends on many factors including the solvent, additives, metal source, and overall conditions. Modulating the ratio and nature of the nutrients present in the synthesis mixtures alters the distribution of species and affect both nucleation and growth rates simultaneously.

Another important growth modulator is the counterion of the zinc source. Many sources of zinc can be utilized, including nitrate, chloride, carbonate, and acetate salts and zinc oxide and these have been shown to affect particle size. The counterion serves as a coordination modulator, where the difference in acidity of conjugate acids can affect the population of the species present in the growth solution.

2.1.3 Zeolitic Imidazolate Frameworks in Gas Separations

ZIFs were identified as promising candidates for both adsorptive gas storage and separations in the early stages of their discovery. Indeed, their chemical and thermal stability combined with tunable pore apertures and high surface areas provide a perfect combination for materials capable of adsorptive separations of industrial gas pairs. With

the initial focus on post-combustion CO_2 capture, ZIFs are now being studied for other gas separations perhaps better suited for ZIF's molecular sieving characteristics including hydrocarbons, light gases, and biofuel separations.

The underlying separation mechanism for membranes is the difference in flux between different species. The gas separation performance is usually described in terms permeability, P, and selectivity, α with higher values being desired for increased productivity and gas purity, respectively. One method to achieve high selectivity is increasing the difference between gas diffusivity between two species in the membrane. Small differences in gas diffusivity that are proportional to the kinetic diameter can be amplified by creating a material with pore dimensions between the kinetic diameters, creating an effective "cut-off" diameter for diffusion. The small pore apertures of ZIFs position them as ideal candidates for this type of molecular sieving permselective gas separation membranes.

2.1.3.1 As Adsorbents

Knowledge of the interaction mechanism between a molecule and adsorbent is critical to understanding both adsorption capacities and diffusional behavior. The potential adsorption sites within ZIFs are associated with the ligand and the metal center. The actual sites are the product of the material topology, chemical nature of the organic linker, and adsorbate partial pressure of the system.[46-48] In contrast to other MOF materials, gas adsorption in ZIFs has shown a remarkably low dependence on metal-adsorbate interaction.[49-52] This low dependence arises from insufficient free space near the zinc metal centers, as demonstrated by DFT calculations of H_2 adsorption in ZIF-8.[53]

The steric hindrance encountered by gases adsorbing near the ZIF metal cluster means that the most effective way of modifying CO_2 adsorption selectivity and capacity are variations in the material topology and organic linker substituents. Several groups have explored the relationship between imidazolate functionalities and CO_2 adsorption capacities within a single topology.[47, 54-57]20, 45, 134b, 139 The quadrupole moment of CO_2 results in higher adsorption interactions for materials that have more polar ligands. Frameworks exhibiting an asymmetry in their linker functionalities show a significant advantage in CO_2 adsorption over symmetric ligands counterparts. .[54] A later publication[58] highlighted how the effect of ligand polarizability and topology are interrelated phenomena.

While many adsorbents rely on the use of polar ligands, other materials increase CO_2 adsorption by incorporation of amine functionalities known to bind to CO_2 as an acid–base pair. Thompson et al.[59] demonstrated mixed linker substitutions and post-synthetic modifications of sodalite topologies, incorporating amine functionalities into ZIF-8 and ZIF-8-90 hybrid frameworks. ZIF-8 was modified by the incorporation of 2-amino-benzimidazole, a linker containing a primary amine functionality, with up to 47 mol % linker substitution. ZIF-8-90 (50/50) was modified by post-synthetic reaction of ethylenediamine to produce a primary amine. Both modifications resulted in decreasing pore volume and surface area with substitution while increasing the CO_2 heat of adsorption. The inclusion of amines and other reactive functionalities via similar techniques in ZIFs could represent an alternative way to increase adsorbent affinity towards CO_2.

The use of ZIFs as selective adsorbents has been applied to the thermodynamic separation of olefin/paraffin hydrocarbon pairs.[19, 60-63] ZIFs have been shown to exhibit

marginally selective adsorption of the saturated hydrocarbon in unary isotherms and IAST calculations. The lack of open metal centers and charged surface groups cause electrostatic interactions to be outweighed by the more prominent vdW forces within the framework. This does not favor the π-bonded olefin species, and instead leads to the marginally selective adsorption of the more polarizable paraffin through nonspecific interactions. This trend is in stark contrast to commonly used hydrocarbon adsorbents, such as other MOFs and traditional zeolite materials, which through open metal centers or charged surface groups exhibit strong electrostatic interactions and show significant selectivity to the olefin.[62, 64-65]

Kinetic separations of gas pairs exploit differences in diffusivities to create a transient adsorptive selectivity different from its equilibrium selectivity. Generally, adsorptive materials with microporosity near the kinetic diameter of both species are able to take advantage of slight differences in molecular size to enable these kinetic separations. Li et al.[66] demonstrated the applicability of kinetic separation of propene/propane using ZIF-8 and a 2-chloroimidazole analog (MMOF) to achieve significant diffusive selectivity towards the olefin. A ratio of diffusivities of 125 and 60 for the two materials were recorded, respectively, exemplifying the effect that a small (~0.1 Å) difference in crystal pore size can have on diffusion selectivities.

The inherent hydrophobicity of ZIFs makes them attractive for recovery of C_1–C_4 alcohols from dilute aqueous solutions.[17, 22, 67-70] Alcohol adsorption is characterized by an S-shaped isotherm with low affinities at lower alcohol activities followed by a sudden increase in adsorption.. The sharp increase in uptake occurs at lower pressures for longer carbon chain lengths. This shape is attributed to initial alcohol cluster formation near the

organic linker followed by pore filling at higher activities. [69] The heat of adsorption increases with larger carbon chains; therefore, ZIFs show promising adsorptive selectivity for *n*-butanol/water separations, but seem much less useful in MeOH/water.[17, 22] The overall alcohol selectivity is quite high as the water adsorption is largely negligible in many ZIFs. The exception is ZIF-90 whose carboxaldehyde functionality is quite hydrophilic and exhibits a 18 mmol g^{-1} water uptake at saturation and 308 K.[22]

2.1.3.2 As Membranes

Ideally, ZIF membranes would be thin films of continuous self-supporting material. However, real ZIFs are not sufficiently mechanically stable to be self-supporting and have been synthesized on different supports, including common inorganic and organic supports that are porous to provide mechanical stability and minimize resistance to mass transport. Moreover, real ZIF thin films also have grain boundaries that serve as defects and provide non-selective gas transport. Defects can be limited through increasing the membrane layer thickness, but this simultaneously decreases the productivity of the membrane unit.

Synthesizing these dense membranes is achieved through a variety of techniques adapted from homogeneous synthesis. The techniques applied for ZIF membrane fabrication can be generally classified as: (i) primary synthesis, (ii) seeded growth, and (iii) electrospray deposition. These methods involve contacting the porous support with a precursor synthesis solution. After membrane formation, ZIF membranes generally need to be "activated" through solvent removal before characterization and testing. Techniques like substrate functionalization and membrane activation can be combined with membrane synthesis techniques to make high quality membranes.

Mixed matrix membranes (MMMs) consisting of a non-polymeric separating agent (discrete phase) and an easily processable polymer (continuous phase) have been proposed to overcome material limitations associated with both. ZIF MMMs are normally grouped into composite dense films and asymmetric composite membranes based on the membrane morphology. It is widely agreed that the incorporation of ZIF particles enhances the permeability of the hybrid membrane by reducing chain packing and introducing more free space into the system (i.e., the ZIF porosity), although the goal is to usually increase both selectivity and permeability. As a result, higher ZIF loadings are typically required for improved membranes performance; however, there is likely an upper bound of achievable ZIF particle loadings. Nanometer-sized ZIF particles are preferred to micron-sized particles to fabricate asymmetric membranes with thin selective layer; however, small particles are difficult to disperse.

Given their strong diffusive selectivity towards the olefin, ZIF-8 inorganic membranes show selectivity toward the olefin greater than 30 with permeabilities beyond 100 Barrer. These values vary even within a single study greatly. Indeed, membrane propylene permeabilities may range from 82 to 250 Barrer.[71] While some variation is associated with measurement conditions, this data make it clear that inorganic membranes suffer from a high degree of variability in performance arising from an extreme sensitivity to synthesis and preparation conditions.

Recently, a scalable method was disclosed that utilized hollow fibers to fabricate highly selective membranes, called interfacial microfluidic membrane processing.[72] The method spatially isolated the growth precursors, but utilized two different solvents (octanol and water) to ensure membrane formation on only the inside of the hollow fiber. Internal

functionalization ensured that the fibers could be densely packed without intergrowth between adjacent fibers. The method could produce multiple fibers simultaneously with similar properties as the single fiber, demonstrating the potential for scale-up of the process.

ZIF-8 appears uniquely suited for several potential gas separation applications that include CO_2 removal from CH_4 streams (acid gas removal) or N_2 (post-combustion CO_2 capture) and separating N_2 from O_2. The promise stems from the similarity between the crystallographic pore diameter of ZIF-8 (3.4 Å) that falls between these pairs (kinetic diameters of O_2 (3.467 Å) and N_2 (3.64 Å), CO_2 (3.3 Å) and CH_4 3.76 Å). Unfortunately, ZIF-8 performance falls short of expectations since the material framework is quite flexible.

2.2 Fundamentals of Adsorption

2.2.1 Theory of Adsorption in Microporous Materials

At its most basic level, physisorption (i.e., physical adsorption) is the intermolecular interaction of a gas molecule with a solid surface, resulting in an adsorbed phase on the surface of the solid. This phase is now closer to a liquid than a gas, and although adsorbed molecules don't exert pressure themselves, they are at equilibrium with a gas of certain chemical potential that surrounds the solid. This equilibrium relation depends only on temperature, and the curve describing adsorbed quantities as a function of driving force is called an isotherm. At low pressures, system pressure can be substituted for fugacity with little loss of fidelity.

Several things determine the shape of the isotherm, most generally they are the properties of the sorbate (gas) and the sorbent (solid), and how those interact with each other. Increasingly favourable molecular interactions lead to “sharper” isotherms, i.e., greater uptakes at lower pressures. Molecular polarizability strongly contributes to interactions with the surface, and therefore molecules with dipole or quadrupole moments tend to adsorb strongly to surfaces. Similarly, higher hydrocarbons adsorb more strongly than smaller ones due to increased electron density. Specific functional groups on a surface may result in additional interactions, such as nitrogen or oxygen containing functionalities that interact strongly and specifically with certain molecules. This is particularly common in CO_2 capture and the use of amine groups for their acid-base properties.

The microstructure of the sorbent is also quite important, and is most evident when using condensable gases, or gases near their saturation pressure (i.e. 77 K N_2). IUPAC has official classifications for isotherm shape types, each generally being indicative of a particular microstructure (**Figure 2.5**).

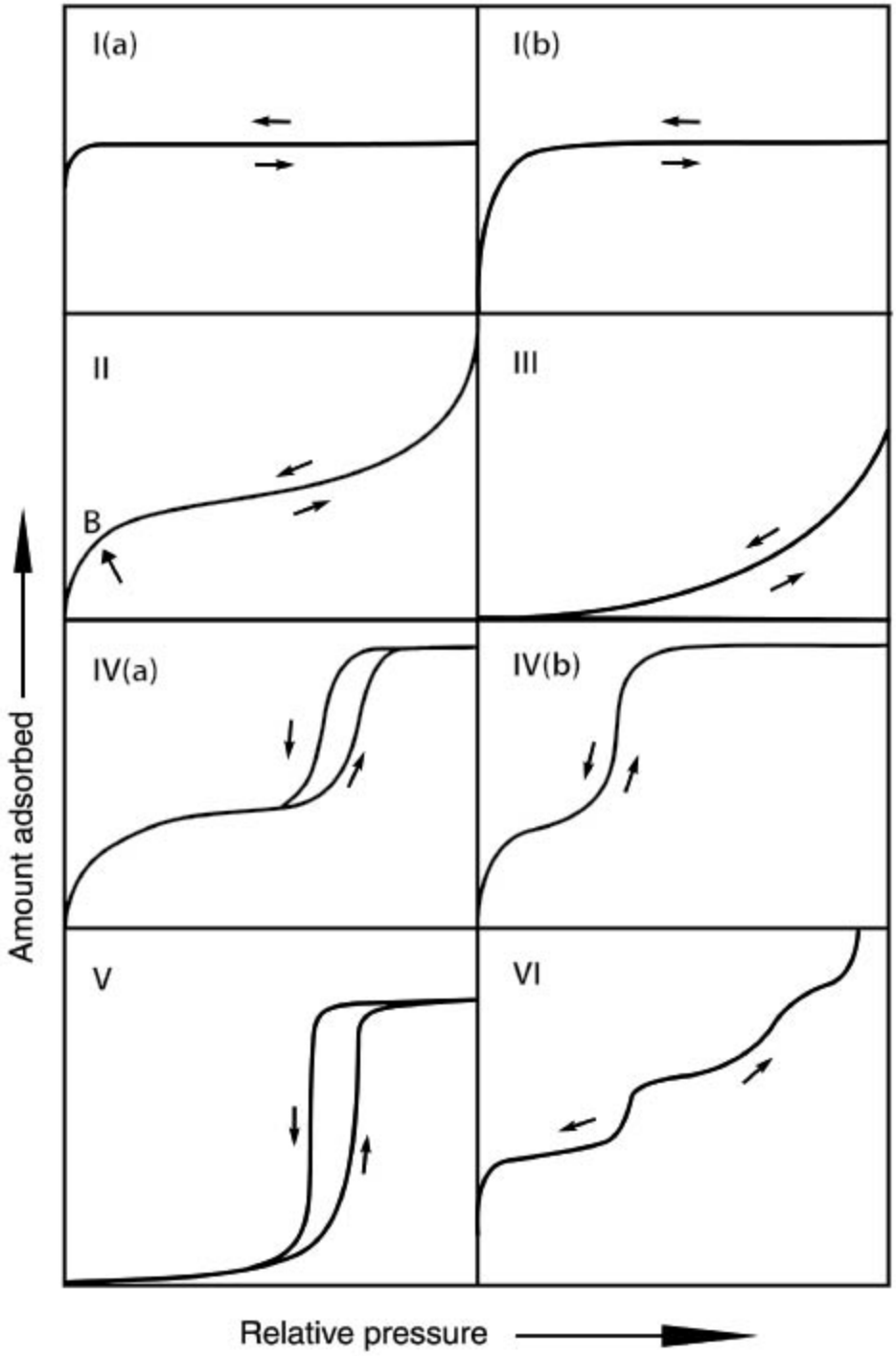

Figure 2.5 IUPAC classification of physisorption isotherm shapes and hysteresis loops. Reprinted with permission, Copyright IUPAC ® 2015[73]

Type I(a) isotherms represent the majority of MOF adsorption isotherms, where uniform micropore distributions result in extremely sharp uptakes since smaller pores

generally lead to stronger interactions. Type I(b) represents a variation on the isotherm where a broader distribution of pores is present. Type IV isotherms are micro and mesoporous sorbents, where capillary condensation occurs in the mesopores and the hysteresis on the desorption branch depends on pore size and adsorption temperature. Type V isotherm represents unfavorable sorbate-sorbent interactions followed by clustering and pore filling, as is typically the case in adsorption of water on hydrophobic materials. Types II, II and VI are not relevant to this discussion.

Two isotherm models must be explicitly addressed here, the Langmuir isotherm and the Extended Langmuir Isotherm. The Langmuir isotherm describes isotherm Type I(a) isotherms, and takes the form of

$$C_i = \frac{C_{s,i} b_i P_i}{1 + b_i P_i} \tag{2.1}$$

The Extended Langmuir formulation uses single-component values and is the simplest form of a multicomponent competitive isotherm. It is commonly used for similar gases with reasonable accuracy

$$C_i = \frac{C_{s,i} b_i P_i}{1 + \sum_{j=1}^{n} b_j P_j} \tag{2.2}$$

2.2.2 Thermodynamic Analysis of Isotherm Data

The two major single component analyses associated with gas-phase adsorption isotherms in microporous materials are the Brunauer–Emmett–Teller (BET) analysis for

surface area determination, and the determination of isosteric heats of adsorption as a measure of adsorption strength.

A third analysis concerns the determination of competitive adsorption isotherms from single-component isotherms, referred to Ideal Adsorbed Solution Theory (IAST)

2.2.2.1 Brunauer–Emmett–Teller Analysis

Because adsorption is a surface-mediated phenomenon, high specific surface area is generally seen as an indicator of high material performance in gas adsorption. A larger surface area indicates a greater number of gas sorption sites, and by extension, greater adsorption capacity, although this also depends on specific pore volume at higher pressures. The BET method of surface area determination is the largely agreed upon technique by which surface area of porous materials is determined. It is an extension of the Langmuir surface area analysis, in which gas is assumed to adsorb onto the surface of the material in a monolayer. The BET method allows for the adsorption of multilayers on the surface considering interaction between the sorbate layers to allow for a theoretically infinite layer thickness (**2.3)**; the linearization of the equation generally only holds between the ranges of $0.05 < P/P_0 < 0.30$ and defines the typically applied BET analysis range.[74] Nitrogen vapor at 77 K is the most common adsorbate for this analysis.

$$\frac{1}{v\left[\frac{P_0}{P}-1\right]} = \frac{c-1}{v_m c}\left(\frac{P}{P_0}\right) + \frac{1}{v_m c} \tag{2.3}$$

However, the strict applicability of this formulation to microporous materials has been questioned, due to BET analysis being unable to account for the adsorptive interaction

of other nearby walls, high radius of curvature of some MOF pores, or the sharp pore-filling events that occur at low saturation pressures in such tight pore spaces. Work by Walton and Snurr addressed this issue and established a set of consistency criteria for the application of BET analysis towards MOF materials.[75] These criteria are used as inclusion/exclusion rules for the relative pressure range to be used in BET analysis.

(1) The selected range must have increasing values of $v(P_0 - P)$ vs P/P_0

(2) The interaction parameter c, must be greater than zero

(3) The selected range should correspond to the linear region of the BET plot

In general, the applicable BET range for MOF materials is significantly lower than the standard BET range, often below $P/P_0 = 0.05$.

2.2.2.2 Isoteric Heats of Adsorption

The adsorption of a molecule onto a surface is an exothermic event and the heat released upon adsorption corresponds to the difference in free energy between the gas phase molecule and the adsorbed state. The magnitude of this release is known as the heat of adsorption, ΔH_{ads}, and is generally expressed in units of kJ/mol and often as $-\Delta H_{ads}$ to report a positive value. Molecules that adsorb into a deeper energy well, i.e. a more favorable adsorption site, exhibit greater releases of energy. Adsorption energies below 30 kJ/mol are considered physisorption and largely reversible via pressure swing; higher energies are considered to be chemisorption and not rapidly desorbed via pressure change.

ΔH_{ads} can be directly measured via calorimetric adsorption experiments, in which the quantity of heat released is matched to the moles of gas adsorbed in a volumetric

experiment (see Section 2.2.3.1). These experiments are somewhat rare, as ΔH_{ads} can also be calculated from thermodynamic principles without the need for sensitive calorimetric equipment. If we describe the adsorption onto a surface as a phase transition, the Clausius-Clapeyron equation can be applied to determine the coexistence curve of a system at a constant number of moles.

$$\frac{dP}{dT} = \frac{L}{T\Delta v} \tag{2.4}$$

Where in this case, the specific latent heat is the difference between the liquid-like adsorbed phase and the gas phase, and is taken to be ΔH_{ads}. Furthermore, the change in specific molar volume can simply be approximated as the molar volume of the gas, as it generally greatly exceeds the liquid volume and can be described by the ideal gas law **(2.5)**.

$$\frac{dP}{P} = -\frac{\Delta H_{ads}}{R}\frac{dT}{T^2} \tag{2.5}$$

The integration of the modified equation leads to the linearized form of the Clausius-Clayperon **(2.6)**. Measuring the isotherms of the same sorbate-sorbent system at various temperatures, the equation can be used to fit isostere points, i.e, points with the same adsorbed quantity, to determine ΔH_{ads}. Variations on this analysis exist where points are taken instead to be at constant surface coverage θ, though these necessarily assume a Langmuir-type isotherm which may or may not be applicable.

$$\ln\left(\frac{P_1}{P_2}\right) = -\frac{\Delta H_{ads}}{R}\left(\frac{1}{T_2} - \frac{1}{T_1}\right) \tag{2.6}$$

Care must be taken when analysing isotherms with small temperature differences or with very sharp isotherms that shift little with adsorbate pressure. In these cases, small uncertainty in measurement translate to exceedingly large uncertainties in the fitted parameter value. Furthermore, it is recommended that a sufficient number of points be taken across temperature values that have similar adsorbed loadings, or a well-fitted continuous equation (isotherm model or polynomial) be used to accurately interpolate between measured points. A linear interpolation in a region of high isotherm curvature is a common source of unaccounted error in the determination of ΔH_{ads}.

A true Langmuir isotherm exhibits a constant ΔH_{ads} with loading, as only one type of adsorption site exists and therefore only one ΔH_{ads}, though in practice most microporous materials exhibit an initially high value that gradually approaches the heat of vaporization of the adsorbate. Exceptions to this rule exist, and an analysis of ΔH_{ads}often serves to determine the number of distinct adsorption sites present within the material or the presence of a phase transition within the system.

2.2.2.3 Ideal Adsorbed Solution Theory

IAST models the adsorption of multiple components upon a surface by making use of separate single-component isotherms at a given temperature. The major assumption is that the components on the surface form an *ideal* solution, and therefore may be somewhat limited in describing non-ideal adsorption phenomena, such as clustering or cooperative effects.[76]

For a given partial pressure of adsorbates, an adsorbed phase exists in which the fugacity of each component equals the gas phase fugacity for 3D materials and where the

spreading pressure of both components are equal. A detailed derivation of the component equations can be found in most thermodynamic textbooks. Specifically, Do[77] sets out the following algorithm for the determination of IAST equilibrium calculations **(2.7)-(2.15)**.

(1) The initial reduced spreading pressure can be estimated by

$$z = \frac{\pi A}{RT} = \sum_{\mathrm{j=1}}^{\mathrm{n}} y_j \int_0^P \frac{C_{\mu j}}{P_j} dP_j \tag{2.7}$$

(2) The hypothetical pressure of each component equivalent to the spreading pressure is iterated by Newton-Raphson until convergence, using the actual partial pressures as initial guesses.

$$P_j^{0(k+1)} = P_j^{0(k)} - \frac{G\left(P_j^{0(k)}\right)}{G'\left(P_j^{0(k)}\right)} \tag{2.8}$$

Where

$$G = \int_0^{P_j^0} \frac{C_{\mu j}}{P_j} dP_j - z \tag{2.9}$$

$$G' = \frac{C_{\mu j}^0}{P_j^0} \tag{2.10}$$

(3) Recalculate the new spreading pressure using the new hypothetical pressures by Newton-Raphson until convergence

$$z^{k+1} = z^k - \frac{F}{F'} \tag{2.11}$$

Where

$$F(z^k) = \sum_{j=1}^{n} \frac{Py_j}{P_j^0} - 1 \tag{2.12}$$

$$F'(z^k) = -\sum_{j=1}^{n} \frac{Py_j}{P_j^0 C_{\mu j}^0} \tag{2.13}$$

(4) Return to step (2) until the spreading pressure z converges to a value

The total adsorbed quantity is given by

$$\frac{1}{C_{\mu T}} = \sum \frac{x}{C_\mu^0} \tag{2.14}$$

$$x_i = \frac{Py_i}{P_i^0} \tag{2.15}$$

When performing these calculations it is important to make use of isotherms that include high fugacities of the weaker component, as the algorithm may at times attempt to extrapolate to higher spreading pressures to satisfy the equilibrium conditions. Similarly, this makes the form of the isotherm or polynomial extrapolation applied to the isotherm of particular importance.

2.2.3 Experimental Techniques for the Measurement of Isotherms

2.2.3.1 Volumetric Techniques

The volumetric determination of isotherms is the most common technique used to measure adsorption of gases onto porous materials. They consist of two volumes: a larger manifold volume of known volume, which is filled with the sorbate of interest before each measured point, and a smaller sample volume that contains a measured quantity of the sorbent and is evacuated prior to measurement. The determination of the unoccupied volume in the sample cell is referred to as the "free space", and is measured by helium under a non-adsorbing assumption.

Each volume contains various pressure transducers and are separated by a dosing valve. The machine works on a mass balance, dosing some amount of gas from the manifold volume to the sample volume, and then closing the valve. The total dosed volume is calculated by the difference in initial versus final pressure in the manifold volume, while the adsorbed volume is calculated by the difference in expected pressure and measured pressure at equilibrium, where the difference is assumed to be adsorbed onto the surface of the material. In both cases, the appropriate equations of state for the gas must be used, especially when sorbates exhibit non-ideal (i.e, compressible) behavior. The associated error of physisorption measurements was described by De Lange in a recent publication.[78]

Although this is an equilibrium technique, kinetic effects may severely affect the accuracy of the measurement. When dealing with diffusionally restrictive materials, the approach to equilibrium may result in excessively long measurement times or artificially low adsorbed quantities. In the extreme, a sample may appear completely non-porous to

N_2 physisorption analysis. These limitations may take the form of restrictive pore sizes at low temperatures such as 3A zeolite or carbon molecular sieves during 77 K N_2 experiments, or of less restrictive pores with larger sorbates, such as propane adsorption in ZIF-8. When dealing with these systems, it is important to ensure that pressure equilibrium criteria is sufficiently strict for the specific sorbate-sorbent pair. "Typical" equilibration criteria for N_2 adsorption in microporous materials at 77 K is $\Delta P/P = 0.01\%$ over 35 s.

There exist several solutions to the problem of excessively long equilibration times. The most general and simplest solution to this problem is to reduce the diffusion length, i.e. utilize smaller crystals. This can be achieved by either crushing the sample or modifying synthesis conditions. Instead of 77 K N_2, the analysis could be run at 87 K using Ar, which still has a saturation pressure of 1 bar. Indeed, this is the common solution for 3A zeolites where the use of a smaller molecule and higher temperature allows for faster diffusion into the framework. Sorbate parameters in subsequent analyses must be altered accordingly to account for differences in molecular properties.

In a similar vein, the use of CO_2 as a sorbate at 273 K is often used to probe ultramicropores, although atmospheric pressure only represents $P/P_0 = 0.03$ and generally cannot be exceeded with glass sample tubes. The downside of this analysis is that CO_2 tends to produce broader pore size distributions due to strong quadrupole interactions and potential adsorption to surface functional groups.

2.2.3.2 Gravimetric Techniques

Gravimetric adsorption refers to the measurement of adsorbed sorbate quantities by detecting a change in sample mass as a function of changing external partial pressure. As

sample adsorbs onto the surface of the sample, its mass increases. The set-up generally consists of a sample hung from a microbalance and control over the external partial pressures, either by a sealed dosing pressure system or an open flow system where the inlet gas composition is changed. The traditional quartz spring set-up is a gravimetric apparatus. A correction for buoyancy effects is generally required.

This technique is often used in high-pressure measurements such as the adsorption of CO_2 in shale samples or the evaluation of hydrogen storage materials. On the other hand, flow systems can measure multicomponent adsorption by changing the inlet stream from a pure component to a mixed stream; however, this assumes negligible adsorption of the initial gas, the validity of which depends on the system. When combined with compositional sampling of the equilibrium headspace via gas chromatography, direct measurement of multicomponent equilibrium is possible, but uncommon.

The most common application of gravimetric sorption is towards the adsorption of vapor species in a non-adsorbing carrier gas. A humidified carrier stream is combined with a dry carrier stream to produce a partially saturated stream which is made to contact the sample. After each change in flow conditions, equilibrium sample mass above the baseline is taken as adsorption. Care must be taken at high humidities, as the use of small powders may lead to interparticle condensation and artificially high adsorption values. When using samples which strongly adsorb water from the air such as zeolites, these machines may have trouble reaching sufficiently high temperatures to completely remove the adsorbed species.

2.3 Fundamentals of Diffusion

2.3.1 Fickian Diffusion in Microporous Materials

The classical description of diffusion through porous media is that of Fickian diffusion, which relates the flux of a species to its concentration gradient using a mobility term referred to as the diffusion coefficient. In heterogeneous systems, this coefficient is often an "effective diffusivity" which considers the different forms of molecular diffusion that may compete within a particle, such as surface and Knudsen diffusion. The commonly used equation in the absence of bulk diffusion and flow takes the form of

$$J_i = -D_i \frac{\partial C_i}{\partial x} \tag{2.16}$$

This conveniently lends itself to explicit analytical solutions under various geometries, many of which have been solved and detailed in *The Mathematics of Diffusion* by Crank.[79] Traditional Fickian diffusion models give good results when single component diffusion is being evaluated in "well-behaved" materials, but is unable to describe certain behaviors and non-idealities that arise in multicomponent systems.

Various adjustments to the Fickian equation are often made, namely corrections to the diffusion coefficient. The most common correction is known as the "Darken correction", or the thermodynamic correction factor, where the driving force is taken to be the gradient of the chemical potential of the species on a surface, rather than the concentration gradient.[80] This yields an apparent concentration-dependent diffusivity that depends on the shape of the isotherm. More accurately, it describes an ideally

concentration-independent “thermodynamically-corrected” diffusivity that is the modified by the thermodynamic correction factor, as described by

$$D_{T,i} = Đ_i \frac{\partial \ln P}{\partial \ln C_i} \tag{2.17}$$

In all commonly used isotherms, the correction factor approaches unity as fractional loading approaches zero, and is exactly equal to one in Henry isotherms. The Langmuir relation is analytically given as

$$\frac{\partial \ln P}{\partial \ln \theta} = \frac{1}{1-\theta} \tag{2.18}$$

Many analytical isotherms have similar expressions for the correction factor. In the case of large adsorption steps, the average corrected diffusivity for a Langmuir isotherm is given by

$$\begin{aligned} \frac{D_T}{Đ} = \frac{5}{U_\infty^5 - U_0^5}\Big[\frac{1}{6}\ln\left[\frac{1+U_\infty+U_\infty^2}{(1-U_\infty)^2}\frac{(1-U_0)^2}{1+U_0+U_0^2}\right] \\ -\frac{1}{\sqrt{3}}tan^{-1}\left(1+\frac{2U_\infty}{\sqrt{3}}\right)+\frac{1}{\sqrt{3}}tan^{-1}\left(\frac{1+2U_0}{\sqrt{3}}\right)+\frac{U_0^2-U_\infty^2}{2}\Big] \end{aligned} \tag{2.19}$$

where $U_0 = \theta_0^{1/3}$; $U_\infty = \theta_\infty^{1/3}$, and θ_0 and θ_∞ are the initial and final surface coverage, respectively.[27]

The incorporation of the chemical potential as a driving force is extremely important in multi-component diffusion, and leads to interesting behavior that is not predicted under Fickian diffusion approaches. Under this formulation, the flux is given by

$$J_i = -L_i C_i \frac{\partial \mu_i}{\partial z} \tag{2.20}$$

Where the chemical potential of an ideal gas is described as

$$\mu_i = \mu_i^0 + RT \ln P_i \tag{2.21}$$

We assume that there exists a set of adsorbed concentrations that are in equilibrium with the gas phase, and that these can be related by a function whose inverse in vector form is

$$P_i = f(C_i) \tag{2.22}$$

Substituting equations, we achieve a flux expression in the form of a hypothetical pressure

$$J_i = -(L_i RT) C_i \frac{\partial \ln P_i}{\partial z} \tag{2.23}$$

It is more useful to express the flux as a function of concentration, however, and therefore make the following differentiation via chain rule

$$\frac{\partial \ln P_i}{\partial z} = \frac{1}{P_i} \frac{\partial P_i}{\partial z} = \frac{1}{p_i} \sum_{\mathrm{j}=1}^{\mathrm{n}} \frac{\partial P_i}{\partial C_j} \frac{\partial C_j}{\partial z} \tag{2.24}$$

And resubstitute into the flux equation while grouping terms into D_i^0, the corrected diffusivity term. Here we see the previously developed thermodynamic correction factor modified by the surface concentration

$$J_i = -D_i^0 \sum_{j=1}^{n} C_i \frac{\partial \ln P_i}{\partial C_j} \frac{\partial C_j}{\partial z} \tag{2.25}$$

The equation may then be further grouped as

$$\underline{J} = -\underline{\underline{D}} \frac{\partial \underline{C}}{\partial z} \tag{2.26}$$

Where now the diffusivity of each species depends not only on its own concentration and gradient, but on the gradient of the other species in the mixture. The use of the extended Langmuir isotherm allows us an explicit expression for $\underline{\underline{D}}$

$$\underline{\underline{D}} = \begin{cases} D_i^0 \dfrac{C_i}{C_{s,j}\left[1 - \sum_{k=1}^{n} \dfrac{C_k}{C_{s,k}}\right]} & for\ i \neq j \\ D_i^0 \left[1 + \dfrac{C_i / C_{s,i}}{1 - \sum_{k=1}^{n} \dfrac{C_k}{C_{s,k}}}\right] & for\ i = j \end{cases} \tag{2.27}$$

This diffusivity matrix can describe a behavior referred to as “uphill diffusion”, where a species diffuses into a material against its adsorbed concentration gradient (“uphill” rather than “downhill”). However, when the concentration gradient is reformulated as a chemical potential, diffusion is still seen to occur as a “downhill” process.

In cases with significant differences in diffusivities this results in a transient adsorbed concentration overshoot within a particle, as seen in **Figure 2.6**.

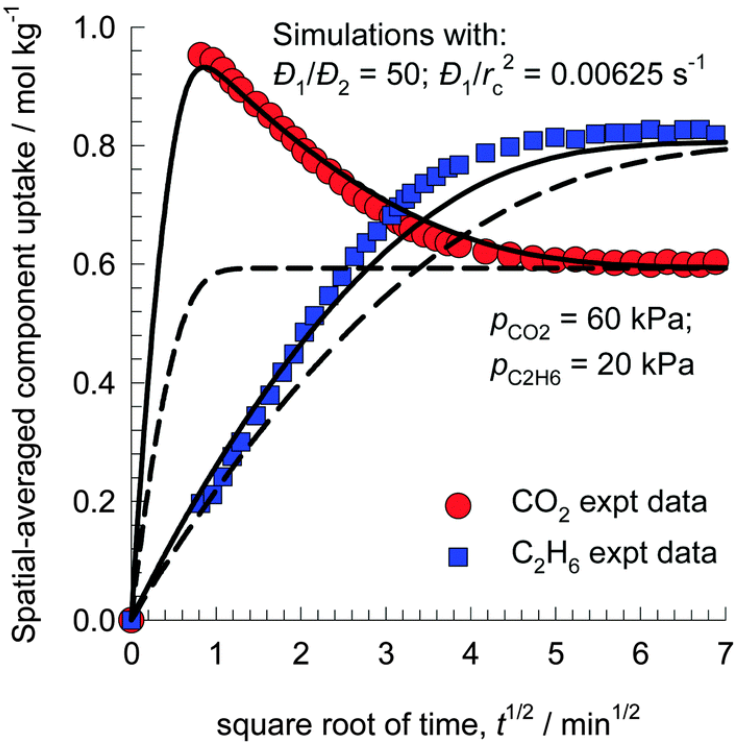

Figure 2.6 Experimental data of Binder and Lauerer[81-82] for the spatial-averaged transient uptake $CO_2(1)/C_2H_6(2)$ gas mixtures DDR zeolite. Dashed lines represent the use of traditional Fickian diffusion while solid lines represent the coupled chemical potential formulation. Reprinted with permission, Copyright Royal Society of Chemistry 2016 [83]

Given the potential for such non-ideal behaviors to occur in separation processes, it is vital to employ the correct mathematical framework when describing diffusion-based phenomena to ensure process modeling and design accuracy.

2.3.2 Maxwell-Stefan Diffusion in Microporous Materials

The Maxwell-Stefan formulation of diffusion arises from a force balance on diffusing molecules that considers frictional forces between molecules as they pass each other, represented as cross terms in the diffusivity matrix, which are multiplied by the various chemical gradients of the species. Maxwell-Stefan relations simplify to the Fickian

solution under dilute conditions, where intermolecular friction coefficients become less important. This is the case in material topologies that possess large cages separated by small windows. In these scenarios, the diffusive jump of one molecule is very weakly coordinated with another due to the one-at-a-time nature of the movement.[84] For this reason, use of the full Maxwell-Stefan formulation to describe diffusion in ZIFs was not pursued. A full derivation and explanation of the Maxwell-Stefan formulation is beyond the scope of this chapter and can be found in textbooks such as *Adsorption Analysis: Equilibrium and Kinetics* by Do.[77]

2.3.3 Measuring Diffusion

Accurate determination of microporous diffusivity is a critical step in sorbent characterization, as species diffusivity controls mass transfer in sorbent applications and contributes significantly to productivity in membrane applications. Furthermore, the ratio of sorption and diffusion values between two species dictate the overall selectivity in any given application, and large errors in measurement may lead to erroneous designs. In several processes, mass transport at the micropore level is the determining factor of unit throughput. For example, a packed bed reactor may be utilizing only a fraction of its total catalyst load due to slow diffusion relative to reaction rates. Inaccurate values of membrane diffusivities and their change with temperature may lead to significant errors in process design when building a new separation train. In adsorption, mass transfer into the sorbent particle can dictate the sharpness of the breakthrough, or even selectivity, and may complicate the bed or column operation.

The determination of equilibrium isotherms for both gas and vapor systems is well established and readily available via commercial instruments and software packages using either gravimetric or volumetric techniques. However, the analysis of transient uptake data is much more nuanced and not routine, and therefore is generally not included in the analysis software of most sorption equipment.

Typically, the measured transient uptake is normalized and fit to the analytical solution of the diffusion problem using appropriate geometric coordinates and boundary conditions. In all cases, the value of the diffusivity parameter is fit, and other parameters may be estimated with varying degrees of certainty, or be fit themselves. The most commonly applied boundary condition to the diffusion problem is the instantaneous step-change in surface concentration from $C=C_0$ to $C=C_1$ at t=0, where the entire sorbent is assumed to be at C_0 at t<0. In a sphere of radius *a* this yields

$$\frac{M_t}{M_\infty} = 1 - \frac{6}{\pi^2}\sum_{n=1}^{\infty}\frac{1}{n^2}\exp(-\frac{Dn^2\pi^2 t}{a^2}) \tag{2.28}$$

Entire books have been written about measuring and interpreting diffusion data; the following gives a small overview of the experimental macroscopic techniques used to measure diffusion and some original commentary on their appropriate application.

2.3.3.1 Volumetric Techniques

The volumetric technique of diffusion measurement, more often referred to as the pressure decay method, uses the volumetric isotherm measuring apparatus described previously. Here, the pressure in the sample cell that is generally monitored to assess

approach to equilibrium is recorded in its entirety. In a similar way that final change in pressure is equated with mass uptake in isotherm experiments, the normalized pressure as a function of time within the sample cell serves to indicate the transient adsorbed quantity within the sample.

Volumetric adsorption systems generally lend themselves to the implementation of the step-change boundary condition in **(2.28)**. However, in the case of strongly adsorbing sorbents or small dosing volumes relative to the experimental sample mass, depletion of the gas phase concentration by incorporation into the adsorbed phase may occur. This tends to increase the apparent rate of diffusion, and can be modeled appropriately for a sphere as adsorption from a depleting volume via the following equation given by Crank as "Adsorption from a Stirred Solution of Limited Volume" **(2.29)**[79]

$$\frac{M_t}{M_\infty} = 1 - \sum_{n=1}^{\infty} \frac{6\alpha(\alpha+1)\exp\left(-\frac{Dq_n^2 t}{R^2}\right)}{9 + 9\alpha + q_n^2\alpha^2} \tag{2.29}$$

where q_n are the non-zero roots of

$$\tan(q_n) = \frac{3q_n}{3 + \alpha q_n^2} \tag{2.30}$$

and α relates the total dosed sorbate to the total sorbate uptake at equilibrium, defined as

$$\frac{M_\infty}{VC_0} = \frac{1}{1+\alpha} \tag{2.31}$$

In experimental scenarios, it may be more accurate to describe the crystal as a population of varied radii, as samples are rarely monodisperse. It is easy to modify the previous equation to incorporate a distribution of particles by using

$$\frac{M_t}{M_\infty} = 1 - \sum_i \chi_i \sum_{n=1}^{\infty} \frac{6\alpha(\alpha+1)\exp\left(-\frac{Dq_n^2 t}{a_i^2}\right)}{9 + 9\alpha + q_n^2\alpha^2} \tag{2.32}$$

where χ_i is the fraction of the crystal population exhibiting a radius R_i.

In instances of rapidly diffusing species and strong adsorption, it is possible for the rate of uptake to be affected by the rate of gas dosing into the sample cell, i.e. valve control. Brandani published a mathematical analysis of the limits of the piezometric method as it relates to valve limitation.[85] In short, the sorbate may diffuse into the sample faster than it is able to enter into the cell, meaning that the transient change in system pressure is controlled by the rate of mass flow into the system rather than by the diffusive behavior. The design of an adsorption system with pressure transducers on both sides of the valve is the best way to conclusively identify this behavior. Alternatively, an analysis of characteristic time scales in the paper results in operational regimes of bounded error fit depending on system parameters.

2.3.3.2 Gravimetric Techniques

In gravimetric experiments, the transient sample mass is monitored after sorbate dosing or changes in the relative humidity of the inlet stream. In the case of flow systems, the surface concentration at equilibrium can be expected to be constant within experimental error, and therefore one could reasonably employ the step-change condition in **(2.28)**.

However, the chamber in which the sample is held is generally quite large relative to the volumetric inlet flowrate and gas residence times may often exceed 1-2 minutes. Importantly, the flow of gas into the sample chamber is not perfect plug flow, which would result in an instantaneous surface concentration change if we ignore external transport barriers. It is more accurately modeled as a continuously stirred tank (CST), where the change in concentration within the chamber (and therefore we assume the surface) is approximated by an exponential approach to the inlet concentration,

$$C(t) = C_0\left[1 - \exp\left(-\frac{t}{\tau}\right)\right] \tag{2.33}$$

where $\tau = V/\dot{V}$, the ratio of the chamber volume to the feed volumetric flowrate (note, in *The Mathematics of Diffusion,*[79] Crank uses $\beta = 1/\tau$). This is very significant, because ignoring the limit of exceedingly short residence times, this boundary condition yields a very different analytical solution to the diffusion equation,

$$\begin{aligned}\frac{M_t}{M_\infty} = 1 - \frac{3D\tau}{a^2}\exp\left(-\frac{t}{\tau}\right)\left\{1 - \left(\frac{a^2}{D\tau}\right)^{\frac{1}{2}}\cot\left(\left(\frac{a^2}{D\tau}\right)^{\frac{1}{2}}\right)\right\} \\ + \frac{6a^2}{\pi^2 D\tau}\sum_{n=1}^{\infty}\frac{\exp(-(Dn^2\,\pi^2\,t)/a^2\,)}{n^2(n^2\,\pi^2 - a^2/D\tau)}\end{aligned} \tag{2.34}$$

This boundary condition leads to an uptake curve that looks sigmoidal in short times when plotted against $t^{\frac{1}{2}}$, rather than linear, which is generally indicative of surface barriers to diffusion or other external transport limitations. Furthermore, it necessitates independent measurements of the time constant or a multivariate fit to the data. To demonstrate the

existence of a non-step profile within the sample chamber, the vapor composition at the outlet of the VTI-SA+ unit was monitored via mass spectroscopy over a complete isotherm run of several steps. Isotherms were performed in triplicate using empty sample pans with all runs programmed in sequence. Both ethanol and hexane were investigated to determine any dependence of τ on the organic vapor. The initial stream equilibration bypass in this experiment was switched off, but reading of the raw data indicated that the mass flow controllers in the system settled within a few seconds at most.

Characteristic plots of the normalized outlet concentration are presented in **Figure 2.7**, where it is clear the concentration change within the sample chamber follows more closely an exponential function than a step-change. In general, the first isotherm step of the sequence (not of each run) was found to have a noticeably longer time constant independent of vapor, and ethanol in general had shorter time constants than hexane, though both display a good deal of variation. There seems to be no chemical-specific explanation for this behavior, and there is furthermore no obvious trend of τ with relative saturation, which would relate to the mass flow controller set point. In experiments described in later chapters, the average time constant collected from both vapors (107 s) and the associated standard error (36 s) will be used in the analysis.

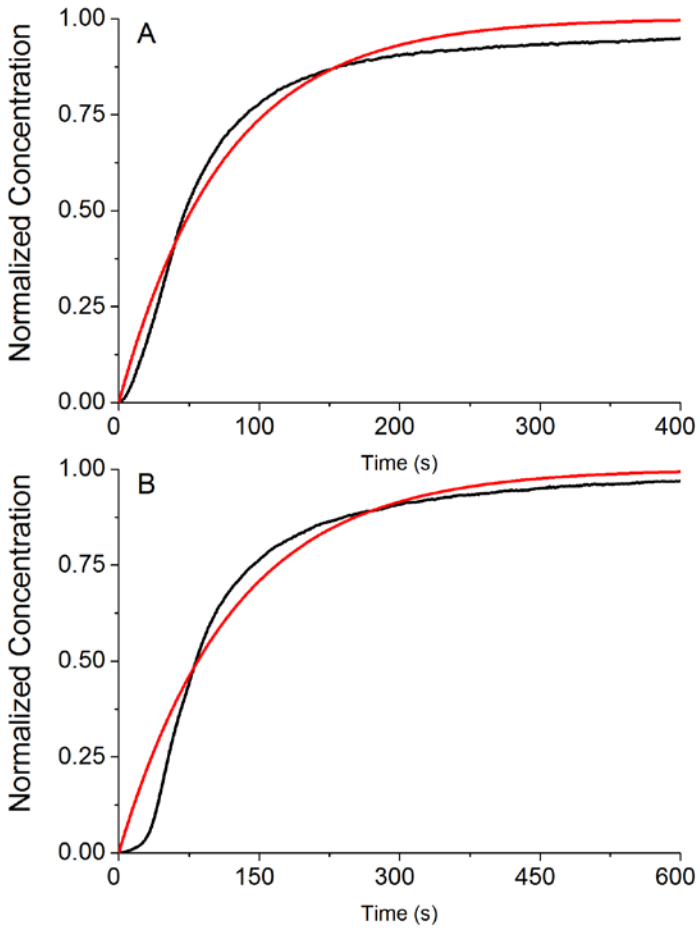

Figure 2.7 Normalized VTI-SA+ outlet concentration of (A) ethanol and (B) hexane after a set-point change. Black indicates the mass spectrometer output while red is the exponential curve fit.

In a similar manner to which volumetric adsorption kinetics may be affected by the speed of the valve opening, the time constant of the concentration change may severely limit the ability to estimate diffusivity if the diffusion phenomena is sufficiently fast. The ratio of the diffusive and the external time constants can be described as $\phi = a^2/D\tau$, and a plot of the analytical solutions with varying values of ϕ is shown in **Figure 2.8**. As ϕ decreases, the uptake is increasingly dominated by the boundary condition rather than by microporous diffusion.

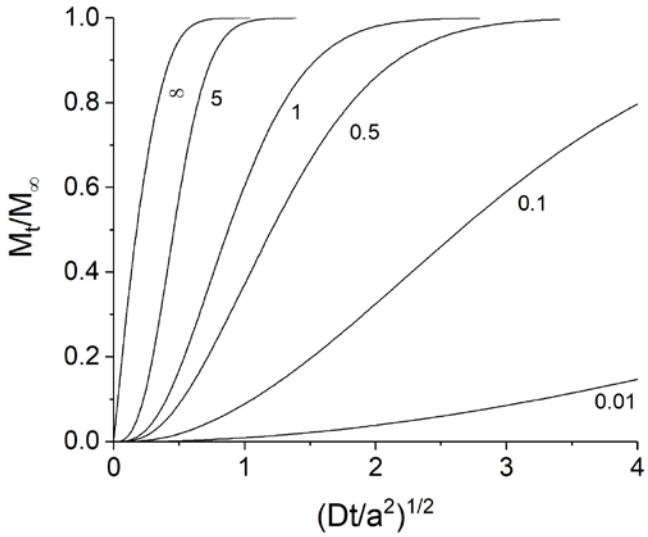

Figure 2.8 Analytical solutions to exponential boundary condition diffusion as a function of $\boldsymbol{\phi}$

With decreasing ϕ, the analytical solution becomes less sensitive to the value of the diffusivity constant, and introduces increasing margins of error in the data fitting. To demonstrate this principle, we estimate the associated error in diffusivity assuming a standard deviation in the reproducibility of the data of 2.5% of total uptake at 50% uptake. This measure of the reproducibility error is an estimate of our own data. The error in diffusivity can be estimated by combination of variances assuming uncorrelated variables **(2.35),** where

$$\sigma_D^2 = \sigma_M^2 \left(\frac{\partial D}{\partial M}\right)^2 + \sigma_\tau^2 \left(\frac{\partial D}{\partial \tau}\right)^2 \tag{2.35}$$

Given the complex nature of the equation, $\partial D/\partial x_i$ were estimated by applying the Derivative function to the analytical solution of the uptake in Wolfram Mathematica rather than solved analytically. **Figure 2.9** demonstrates the increasing error associated with the estimation of the diffusion parameter as ϕ decreases.

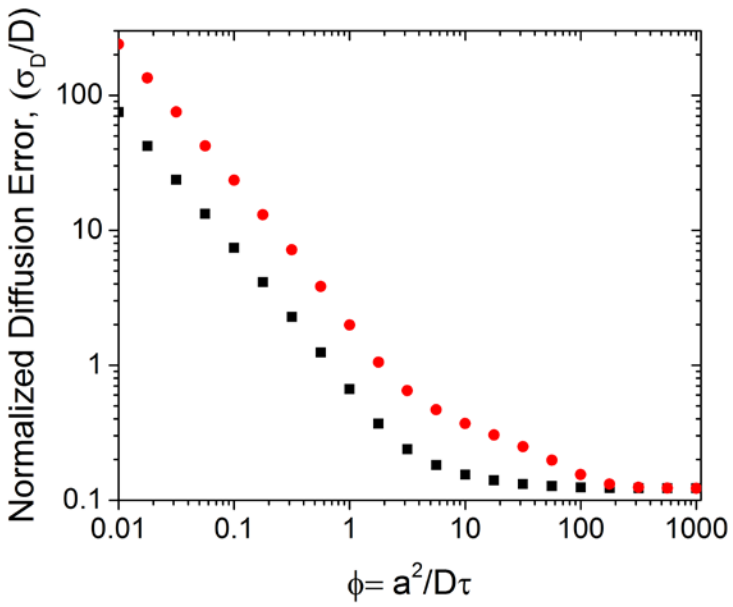

Figure 2.9 Estimated error in fitted diffusivity as a function of ϕ in the case of an exponential boundary condition with $CV_M = 2.5\%$. ■ represents the error of the diffusion fit using a known time constant while ● includes the error associated with $\sigma_\tau = 36\ s$.

In the case with a known τ, the relative error in the fit begins to rise noticeably at values $\phi < 10$ and becomes significant at $\phi < 1$, although literature often considers "in agreement" diffusivity values on the same order of magnitude. Including our measured deviations in τ increases the estimated error by a noticeable factor at $\phi < 100$. This analysis should serve as an "upper limit" for the measurable diffusivity values in each experiment, where ϕ should likely be kept above 10 to minimize the role of external control on fit sensitivity. Other significant sources of error in data collection, such as sampling rate, and in fitting, such as goodness of fit, are omitted from this analysis for simplicity. Overall diffusion values between single variable and multi-variate fit are generally within

an order of magnitude, although we discovered that some uptakes demonstrated τ values well above our measured average and were necessary for a reasonable fit, although they did not necessarily affect the fitted diffusivity value significantly. There may then exist significant unexplained variation in the time constant across solvents and concentration steps, in which case the relative error of fitting the time constant could be reduced. **Table 3.2** contains the numerical values of the various fit conditions.

2.3.3.3 Confounding Factors in Diffusion

The experimental techniques described in this chapter can be classified as "macroscopic techniques", meaning that they measure the overall mass transfer occurring in the system. This contrasts with microscopic techniques such as pulsed field gradient NMR, which can differentiate motion of the sorbate within the crystal versus that outside of it. Importantly, this means that macroscopic measurements are prone to confounding factors and mass transfer resistances in addition to the experimental limitations described previously. The three most commonly encountered confounding factors in macroscopic diffusion are external resistances, thermal effects, and material defects, including surface barriers. These phenomena affect the observed rate of mass transfer in some way, and invalidate the common assumption of adsorption controlled by isothermal diffusion leading to erroneous values.

External resistances in purely microscopic materials generally refers to interparticle sorbate diffusion and describes the hindered motion of the sorbate in the confined space between crystals. This is functionally similar to meso- and macropore diffusion within a pellet when utilizing hierarchical materials. Two factors are responsible for the magnitude

of the interparticle diffusion resistance: The size of the crystals being used in the experiment and the depth of the sample bed in the apparatus configuration. As crystals shrink in diameter, the spaces between them become smaller, resulting in slower diffusion from the bulk phase into some of the occluded crystals. This problem is exacerbated when the depth of the sample bed in the cell is large. Now, not only is there slow diffusion between the crystals, but the overall length of that diffusion path is extended. Essentially, there is now significant asymmetry in the gas phase concentration throughout the length of the bed, leading to a violation of the step-change boundary condition and artificially lower diffusion coefficients. Avoiding this effect is generally achieved using large crystals and the dispersion of the sample across the sample cell, ideally to the point of using a monolayer of crystals (i.e., use less sample).[86]

The simplest modeling of diffusion events is isothermal, however, thermal effects in diffusion arise from the exothermic adsorption of a sorbate onto the material surface. Only when the heat removal in the system via conduction, convection, and radiation is high relative to the generation rate from adsorption and diffusion can the system be considered isothermal. The non-isothermal effects of adsorption affect both the temperature dependence of the isotherm and the diffusivity; although small pressure steps reduce the effect of changing diffusivity, previous work has demonstrated that invariance to step size does not preclude non-isothermal behavior.[87]

Adsorption becomes dominated by thermal effects in the cases where diffusion occurs very quickly and exhibits a high heat of adsorption, upon which further uptake of the sorbate is dictated by the cooling of the particle rather than by mass transfer. Because heat effects are more pronounced at the long-time region of the uptake curve, reasonable

estimates can sometimes be obtained from the short-time fitting of non-isothermal behavior. Intrusion of thermal effects can be diagnosed by measuring the diffusion response to a decreased sample mass or increasing external surface area/volume ratio in the sample cell, much like in the case of interparticle resistance. The solution to non-isothermal diffusion can be found in literature, although using it appropriately requires the measurement of several other system parameters, such as heat capacities and several component isotherms. Briefly, comparison of the dimensionless parameters that arise in the non-isothermal solution gives a check for thermal effects.[88]

$$\alpha' = \frac{ha}{C_s}\frac{r^2}{D}\,, \beta' = \frac{\Delta H}{C_s}\left(\frac{\partial q}{\partial T}\right)_p \tag{2.36}$$

Where $\alpha'/\beta' > 60$ yields less than 15% error over 0-85% fractional uptake when fit using the isothermal solution.

A third confounding mass resistance in macroscopic techniques is the existence of material defects in microporous materials; this includes crystalline defects like grain boundaries as well as surface barriers. Other defects, such as point defects in MOFs are sometimes deliberately incorporated into the structure to tune adsorption properties and have a measurable effect on component diffusion.[89] Significant evidence exists for the existence of grain boundary defects in zeolites, where PFG NMR diffusion data is significantly faster than macroscopic techniques, indicating a pathway hindrance within the microstructure.[90] At times, these can be inferred from the overall morphology of the crystals, several MOFs displaying twinned or intergrown shapes.

Surface barriers are harder to identify and some amount of debate exists within the MOF literature as to their existence. Single crystal microimaging experiments on SAPO-34 conclusively demonstrated that different crystals often have varied surface permeabilities while maintaining constant intracrystalline diffusion values.[91] This provides a rational explanation for the discrepancies often seen between microscopic and macroscopic measurements. This type of behavior has yet to be conclusively demonstrated in MOFs. In macroscopic measurements, it generally presents itself as a sigmoidal curve in the early times when plotted against $\sqrt{t}$. It is qualitatively similar, but mathematically distinct from the exponential boundary condition described previously. Further details can be found in diffusion texts.[86]

One article reports decreasing overall n-butanol diffusivity with decreasing crystal size and rationalizes these results by introducing a surface resistance parameter to their diffusion results, which becomes more important with greater surface area to volume ratios.[92] However, this work also postulates that the permeability of the barrier changes over several orders of magnitude, does not consider the exponential boundary condition described in Chapter 2.3.3.2, and uses exceedingly small crystal sizes in their measurements, likely introducing other external resistances. The effect of various exposed facets has been studied by Pang et al., suggesting that surface permeability may be a strong function of outer morphology, a variable not often controlled for in material syntheses.[93] However, some of the crystals used in that work may have been too small to be reliably under microporous control.

There have been various reports of ZIF-8 diffusivities which agree quite well with PFG NMR measurements, which typically indicate intracrystalline control of macroscopic

diffusion. Further work is needed to settle the issue, but it may be that the presence of surface barriers may be dependent on crystal morphology, material activation, and synthesis conditions employed.

2.4 Pressure Swing Adsorption

The commercial application of solid adsorbents for gas separations comes in the form of pressure swing adsorption (PSA) technology. In its simplest form, it requires a material that can selectively adsorb one gas species over another at a high pressure, then regenerate the sorbent by releasing the adsorbed species at a lower pressure, preparing it for use in the next cycle. Pressure swing adsorption is inherently a transient operation differentiating it from typical separation techniques that have continuous steady state operation.[94]

In general, PSA systems produce a high purity light component (either weaker adsorbing or slower diffusion) product, and a less pure heavy product (stronger adsorbing or faster diffusing), with generally lower fractional recoveries that would be achievable through distillation. This means that PSA is the preferred method of separation when the light component is desired and the feed is cheap. The heavy component is recoverable, but requires additional capital modifications to the unit. Furthermore, much like membranes, feeds available at high pressures are attractive to allow for the reduction of mechanical energy costs. Although adsorption may not require the severe thermodynamic costs of boiling and condensing vapors present in distillation, mechanical energy is generally more expensive than heat.

Industrial PSA applications focus on the separation of industrial gases, such as air separation or hydrogen purification from fuel gas. Newer technologies include the recovery

of methane from landfill gas and the isomeric separation of linear and branched hydrocarbons. The following provides a short discussion of preliminary adsorbent testing for PSA, basic cycle configurations, and modifications to the technology for kinetic separations.

2.4.1 Packed Bed Breakthrough Experiments

The initial evaluation of a sorbent involves the use of packed bed breakthrough experiments, in which the feed stream is fed to a clean bed of sorbent, typically along with an inert tracer component, and the system outlet concentration is monitored by mass spectrometry (MS) or flame-ionization detector (FID). The value of the outlet concentration curves relative to the non-adsorbing tracer along with known system flowrates are used to determine the adsorbed capacity of the bed via mass balance. It may be initially charged with a weakly adsorbing component, and the experiment continues until the outlet concentrations equal the feed conditions. Generally, “breakthrough capacity” is reported as the adsorbed quantity at the time when the outlet concentration of the heavy component is equal to 5% of its feed, and indicates the point at which the bed should be regenerated. These breakthrough experiments may be carried out as a single component adsorption experiment or with an adsorbing mixture to demonstrate selective behavior of one component over another.

2.4.2 The Skarstrom Cycle

The Skarstrom cycle refers to one of the first applications of PSA technology, and is considered the simplest form of the process, consisting of four steps in two beds: 1) Pressurization of the bed with feed to the operating pressure 2) Adsorption of the incoming

feed and concurrent production of high-purity light product 3) Countercurrent pressure blowdown to a lower pressure (typically atmosphere) partially regenerating the sorbent 4) Countercurrent low-pressure purge with product to further clean the sorbent and push the adsorbed concentration front towards the feed inlet. Two beds are operated simultaneously, one adsorbing while the other desorbs, resulting in continuous production of gas from the unit.

2.4.2.1 Modifications to the Skarstrom Cycle

Several simple modifications to the Skarstrom cycle are common improvements used to increase product recovery, throughput, and sorbent capacity.

The first improvement to the cycle, the pressure equilibration step, uses the blowdown of one bed to partially pressurize the other via their respective product ends. The bed is then further reduced in pressure by blowdown to atmosphere. This helps conserve energy by reducing the compression requirements of the unit, and conserves the separation work as the gas is somewhat product-rich. The overall result of this modification is a significant increase in product recovery. More complex blowdown and equilibration schemes exist with units of 4 or more beds, where several pressure equilibration steps may take place as well as the use of blowdown as purge gas. Greater energy conservation, throughputs, and efficiencies are possible in these set-ups at the expense of more complex process operation and increase capital expenditures. A representation of a typical cycle is illustrated in **Figure 2.10.**

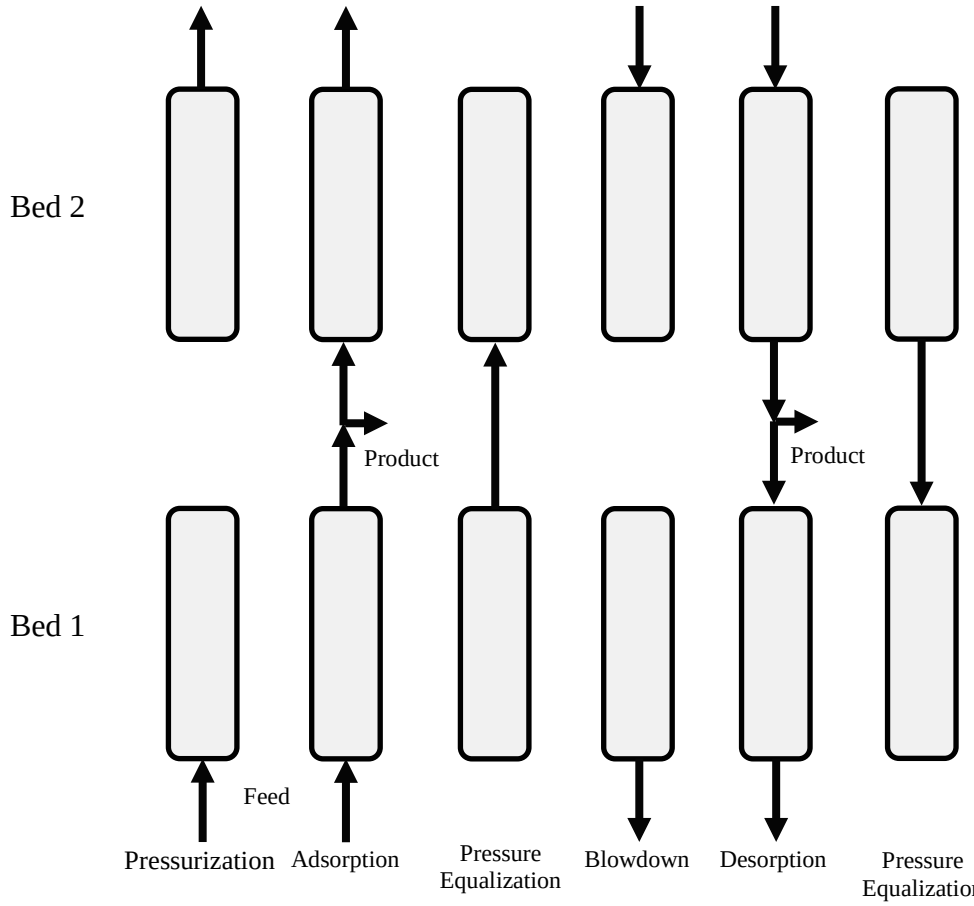

Figure 2.10 Typical steps in a modified 2-bed Skarstrom cycle. Adapted from previous work with permission, Copyright Wiley 2004[94]

The simplest modification to a Skarstrom cycle lies in the modification of the product purge step, generally referred to as a Vacuum Pressure Swing Adsorption (VPSA). Rather than purging with gas from the product tank, the bed is regenerated by a countercurrent vacuum step. Here, an increase in product recovery comes at the expense of greater mechanical energy costs. Some of the compression costs may be avoided by operating at an adsorption pressure only slightly above atmosphere and relying on the vacuum desorption to generate a working capacity. This tends to produce a low-pressure product, and must be accounted for is process design and economics.

2.4.3 Kinetic Pressure Swing Adsorption

Kinetic separations rely on the difference of uptake rates from the gas phase into the sorbent; this mass transfer is generally controlled by intracrystalline diffusion of the target species within the sorbent, and therefore also by the surface-area-to-volume ratio of the sorbent particles. In these cases, diffusionally restrictive sorbents discriminate between molecules based on molecular size (or configuration, in the case of branched isomers), and therefore generally exhibit pore apertures on the order of the kinetic diameters of the molecules. In the limit of infinite selectivity, the separation becomes one of true molecular sieving where the larger molecule cannot enter the sorbent. The most common kinetic sorbents are carbon molecular sieves (CMS) for the separation of CO_2 from CH_4 or O_2 from N_2.[95-99] Examples of small-pore and tuneable pore size zeolites also exist in literature.[100]

As a first approximation of the analytical solutions to Fickian diffusion, kinetic selectivity between two components is

$$\alpha_{1,2} = \frac{\mathcal{S}_1}{\mathcal{S}_2}\sqrt{\frac{D_1}{D_2}} \tag{2.37}$$

In this case, it is important to notice that the sorption coefficient of the two adsorbents is relevant to the selectivity, and that molecules with higher sorption coefficients tend to be larger and therefore have lower diffusivities. This leads to the competition of the two components for control of the selectivity and may mask the presence of a kinetic selectivity given that diffusivities are found under a square root. Generally, a ratio of diffusivities of 100 or more is necessary to yield reasonable product purities under kinetic control.

With appropriate choice of operational time scales, kinetic separations are achievable, however, the choice of that time scale is not trivial. In **Figure 2.11**, the concentration profiles associated with various cycle times in kinetic diffusion are presented. This demonstrates the risk of operating at too fast a cycle time (inefficient use of sorbent) or too slow (equilibration of the particle), therefore, the characteristic R^2/D of the system becomes an important design parameter.

Kinetic separations can produce at higher purities what would generally be the more strongly adsorbed component in PSA systems, essentially "reversing" the selectivity of the unit. This is uniquely applicable to air separations, where the production of purified N_2 takes place by kinetic separation using CMS, while high purity O_2 is recovered via the use of ion-exchanged zeolites operating in the equilibrium regime. A unique case is the CO_2 from CH_4 separation mentioned earlier, where the stronger adsorbing component is also the faster one, and leads to a sorption-enhanced kinetic separation.

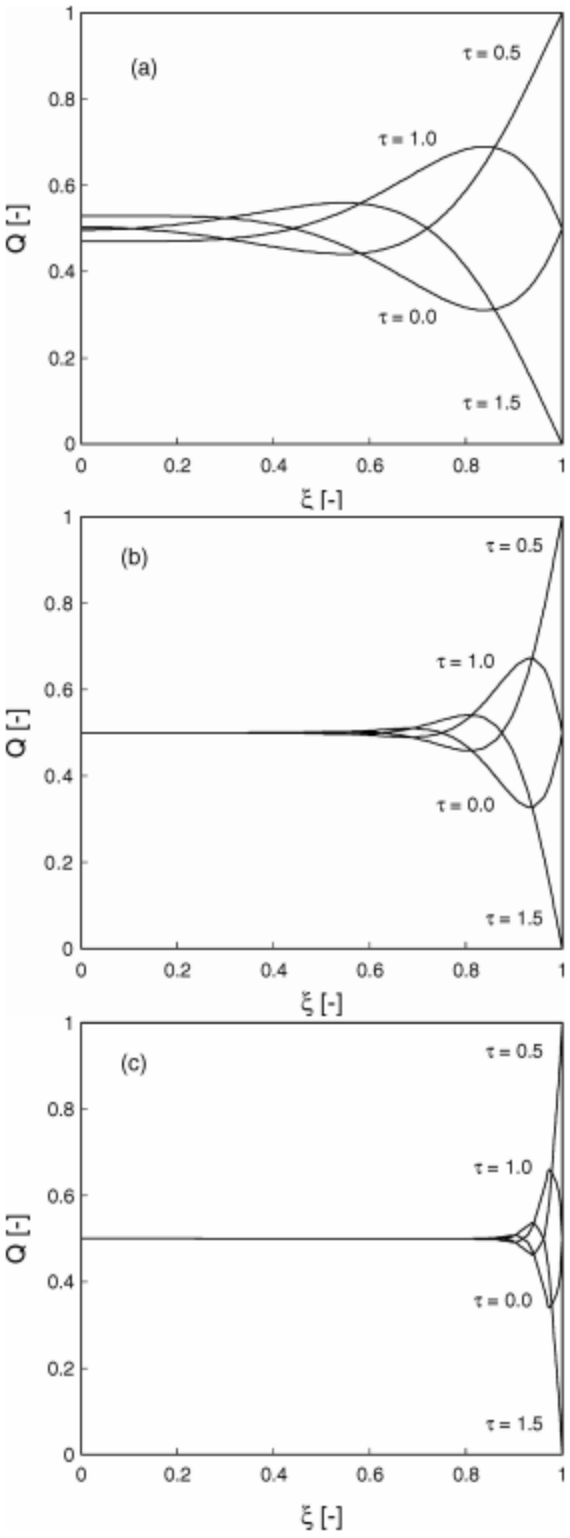

Figure 2.11 Interparticle concentration profiles for varying half cycle times, $\boldsymbol{t_c}$, under sinusoidal concentration forcing at the surface. (a) $\boldsymbol{a = 0.05}$, (b) $\boldsymbol{a = 0.01}$, and (c) $\boldsymbol{a = 0.001}$. $\boldsymbol{a = Dt_c/R_p^2}$, $\boldsymbol{\tau = t/t_c}$. Reprinted with permission, Copyright Springer Nature 2005.[101]

2.4.3.1 Competing Time Scales in Kinetic Separations

Given the added degree of time-dependence inherent to kinetic separations, it is important to understand the various time scales within the adsorption process that compete against diffusionally selective behavior. In a broad sense, there are two types of time scales that need to be managed: 1) The boundary conditions, such as cycle time and gas velocity, which must be long enough to allow for meaningful adsorption of the fast component, but short enough to keep the adsorption and desorption of the slow component to a minimum (i.e., keep sorbate particles far away from equilibrium). This time scale is dictated by the respective diffusive time scales of each species, R^2/D_i. 2) Non-selective forms of mass transfer, which slow down uptake into the sorbent and reduce the kinetic selectivity of the system. Namely, these are the film resistance from the gas phase into the solid phase and the mesoporous diffusion through the sorbent binder. In fiber sorbents, these can be significantly reduced relative to pelletized materials. These rates can be roughly evaluated as a sum of resistances in series[77]

$$\begin{aligned}\frac{1}{K_{overall}} &= Film + Mesopore + Micropore \\ &= \frac{R_f \varepsilon^2}{3 \cdot k_f} + \frac{R_p^2 \varepsilon}{15 \cdot D_p} + \frac{R_c^2}{15K \cdot D_c}\end{aligned} \tag{2.38}$$

Because film resistance is essentially non-selective and mesoporous resistance is at best Knudsen selective, their inclusion to any significant degree reduces the kinetic selectivity of the system. These are a function of sorbent geometry and system engineering, in which small binder dimensions with large pores combined with fast gas velocities yield the best results. It is then obvious why the use of fiber sorbents are beneficial in these

operations; tuneable polymer porosity reduces mesoporous resistance, while small fiber size and parallel bundle arrangements allow for faster gas velocities which result in lower film resistance at equal pressure drop.

The time scale of intracrystalline diffusion, R^2/D_i, can be manipulated by either the changing of particle size or by controlling the structure-property relations that dictate component diffusion. The formation of small crystals is generally feasible in many systems, either synthetically or by mechanical means, although the growth of large crystals is highly dependent on the specific material and is not easily achievable in many systems. Component diffusivities are nearly impossible to control without altering the structure or moving to an entirely different one, although manipulating the operating temperature will affect both components as activated processes. In this case, the result will be similar to that in membranes, where competition between activated sorption and diffusion of both components determines the change in selectivity, which may be insensitive to temperature.

If we assume that kinetic adsorption into a sorbent is governed by sorption−diffusion-type permeation, we can describe it as

$$\mathcal{P} = \mathcal{S}\mathcal{D} \tag{2.39}$$

the temperature dependence of which can be described via van't Hoff and Arrhenius relationships, respectively, as

$$\mathcal{S} = \mathcal{S}_0 \exp\left(-\frac{H_s}{RT}\right) \tag{2.40}$$

$$\mathcal{D} = \mathcal{D}_0 \exp\left(-\frac{E_d}{RT}\right) \tag{2.41}$$

$$\mathcal{P} = \mathcal{P}_0 \exp\left(-\frac{E_p}{RT}\right) \tag{2.42}$$

Whereby substitution results in

$$E_p = E_d + H_s \tag{2.43}$$

Comparing the energies of permeation for species in a mixture then determines whether kinetic selectivity for a given molecule will increase or decrease with temperature, or in the case of equal energies, stay the same. An interesting demonstration of this principle of activation energy of permeation in membranes was conducted by Kapteijn et al. for single component feeds.[102]

2.5 References

1. Tian, Y.-Q.; Chen, Z.-X.; Weng, L.-H.; Guo, H.-B.; Gao, S.; Zhao, D.-Y., Two polymorphs of cobalt(II) imidazolate polymers synthesized solvothermally by using one organic template N,N-dimethylacetamide. *Inorg. Chem.* **2004,** *43*, 4631-5.

2. Xiaochun, H.; Jiepeng, Z.; Chen, X.-M., [Zn(bim)2]•(H2O)1.67: A metal-organic open-framework with sodalite topology. *Chin. Sci. Bull.* **2003,** *48*, 1531-1534.

3. Lee, J.; Farha, O. K.; Roberts, J.; Scheidt, K. a.; Nguyen, S. T.; Hupp, J. T., Metal-organic framework materials as catalysts. *Chem. Soc. Rev.* **2009,** *38*, 1450-9.

4. Allendorf, M. D.; Schwartzberg, A.; Stavila, V.; Talin, a. A., A roadmap to implementing metal-organic frameworks in electronic devices: challenges and critical directions. *Chemistry (Weinheim an der Bergstrasse, Germany)* **2011,** *17*, 11372-88.

5. Horcajada, P.; Serre, C.; Maurin, G.; Ramsahye, N. A.; Balas, F.; Vallet-Regí, M.; Sebban, M.; Taulelle, F.; Férey, G., Flexible porous metal-organic frameworks for a controlled drug delivery. *J. Am. Chem. Soc.* **2008,** *130* (21), 6774-6780.

6. Cavka, J. H.; Jakobsen, S.; Olsbye, U.; Guillou, N.; Lamberti, C.; Bordiga, S.; Lillerud, K. P., A New Zirconium Inorganic Building Brick Forming Metal Organic Frameworks with Exceptional Stability. *J. Am. Chem. Soc.* **2008,** *130* (42), 13850-13851.

7. Loiseau, T.; Serre, C.; Huguenard, C.; Fink, G.; Taulelle, F.; Henry, M.; Bataille, T.; Férey, G., A Rationale for the Large Breathing of the Porous Aluminum Terephthalate (MIL-53) Upon Hydration. *Chemistry – A European Journal* **2004,** *10* (6), 1373-1382.

8. Ferey, G.; Latroche, M.; Serre, C.; Millange, F.; Loiseau, T.; Percheron-Guegan, A., Hydrogen adsorption in the nanoporous metal-benzenedicarboxylate M(OH)(O2C-C6H4-CO2) (M = Al3+, Cr3+), MIL-53. *Chem. Commun.* **2003,** (24), 2976-2977.

9. Horcajada, P.; Surble, S.; Serre, C.; Hong, D.-Y.; Seo, Y.-K.; Chang, J.-S.; Greneche, J.-M.; Margiolaki, I.; Ferey, G., Synthesis and catalytic properties of MIL-100(Fe), an iron(iii) carboxylate with large pores. *Chem. Commun.* **2007,** (27), 2820-2822.

10. Li, H.; Eddaoudi, M.; O'Keeffe, M.; Yaghi, O. M., Design and synthesis of an exceptionally stable and highly porous metal-organic framework. *Nature* **1999,** *402* (6759), 276-279.

11. Tian, Y.-Q.; Cai, C.-X.; Ji, Y.; You, X.-Z.; Peng, S.-M.; Lee, G.-H., [Co5(im)10·2 MB]∞: A Metal-Organic Open-Framework with Zeolite-Like Topology. *Angew. Chem. Int. Ed.* **2002,** *41* (8), 1384-1386.

12. Park, K. S.; Ni, Z.; Côté, A. P.; Choi, J. Y.; Huang, R.; Uribe-Romo, F. J.; Chae, H. K.; O'Keeffe, M.; Yaghi, O. M., Exceptional chemical and thermal stability of zeolitic imidazolate frameworks. *Proc Natl Acad Sci U S A* **2006,** *103* (27), 10186-10191.

13. Llewellyn, P. L.; Coulomb, J. P.; Grillet, Y.; Patarin, J.; Lauter, H.; Reichert, H.; Rouquerol, J., Adsorption by MFI-type zeolites examined by isothermal microcalorimetry and neutron diffraction. 1. Argon, krypton, and methane. *Langmuir* **1993,** *9* (7), 1846-1851.

14. Moggach, S. A.; Bennett, T. D.; Cheetham, A. K., The Effect of Pressure on ZIF-8: Increasing Pore Size with Pressure and the Formation of a High-Pressure Phase at 1.47 GPa. *Angew. Chem. Int. Ed.* **2009,** *48* (38), 7087-7089.

15. Fairen-Jimenez, D.; Moggach, S. A.; Wharmby, M. T.; Wright, P. A.; Parsons, S.; Dueren, T., Opening the Gate: Framework Flexibility in ZIF-8 Explored by Experiments and Simulations. *J. Am. Chem. Soc.* **2011,** *133* (23), 8900-8902.

16. Zhao, P.; Lampronti, G. I.; Lloyd, G. O.; Suard, E.; Redfern, S. A. T., Direct visualisation of carbon dioxide adsorption in gate-opening zeolitic imidazolate framework ZIF-7. *Journal of Materials Chemistry A* **2014,** *2* (3), 620-623.

17. Zhang, K.; Lively, R. P.; Zhang, C.; Koros, W. J.; Chance, R. R., Investigating the Intrinsic Ethanol/Water Separation Capability of ZIF-8: An Adsorption and Diffusion Study. *J. Phys. Chem. C* **2013,** *117* (14), 7214-7225.

18. Diestel, L.; Bux, H.; Wachsmuth, D.; Caro, J., Pervaporation studies of n-hexane, benzene, mesitylene and their mixtures on zeolitic imidazolate framework-8 membranes. *Microporous Mesoporous Mater.* **2012,** *164*, 288-293.

19. Peralta, D.; Chaplais, G.; Simon-Masseron, A.; Barthelet, K.; Chizallet, C.; Quoineaud, A.-A.; Pirngruber, G. D., Comparison of the Behavior of Metal-Organic Frameworks and Zeolites for Hydrocarbon Separations. *J. Am. Chem. Soc.* **2012,** *134* (19), 8115-8126.

20. Peralta, D.; Chaplais, G.; Simon-Masseron, A.; Barthelet, K.; Pirngruber, G. D., Separation of C-6 Paraffins Using Zeolitic Imidazolate Frameworks: Comparison with Zeolite 5A. *Ind. Eng. Chem. Res.* **2012,** *51* (12), 4692-4702.

21. Chang, N.; Gu, Z.-Y.; Yan, X.-P., Zeolitic Imidazolate Framework-8 Nanocrystal Coated Capillary for Molecular Sieving of Branched Alkanes from Linear Alkanes along with High-Resolution Chromatographic Separation of Linear Alkanes. *J. Am. Chem. Soc.* **2010,** *132* (39), 13645-13647.

22. Zhang, K.; Lively, R. P.; Dose, M. E.; Brown, A. J.; Zhang, C.; Chung, J.; Nair, S.; Koros, W. J.; Chance, R. R., Alcohol and water adsorption in zeolitic imidazolate frameworks. *Chem. Commun.* **2013,** *49* (31), 3245-3247.

23. Peralta, D.; Chaplais, G.; Paillaud, J.-L.; Simon-Masseron, A.; Barthelet, K.; Pirngruberb, G. D., The separation of xylene isomers by ZIF-8: A demonstration of the extraordinary flexibility of the ZIF-8 framework. *Microporous Mesoporous Mater.* **2013,** *173*, 1-5.

24. Morris, W.; Stevens, C. J.; Taylor, R. E.; Dybowski, C.; Yaghi, O. M.; Garcia-Garibay, M. A., NMR and X-ray Study Revealing the Rigidity of Zeolitic Imidazolate Frameworks. *J. Phys. Chem. C* **2012,** *116* (24), 13307-13312.

25. Zhou, W.; Wu, H.; Udovic, T. J.; Rush, J. J.; Yildirim, T., Quasi-Free Methyl Rotation in Zeolitic Imidazolate Framework-8. *J. Phys. Chem. A* **2008,** *112* (49), 12602-12606.

26. Hertaeg, L.; Bux, H.; Caro, J.; Chmelik, C.; Remsungnen, T.; Knauth, M.; Fritzsche, S., Diffusion of CH4 and H-2 in ZIF-8. *J. Membr. Sci.* **2011,** *377* (1-2), 36-41.

27. Zhang, C.; Lively, R. P.; Zhang, K.; Johnson, J. R.; Karvan, O.; Koros, W. J., Unexpected Molecular Sieving Properties of Zeolitic Imidazolate Framework-8. *J. Phys. Chem. Lett.* **2012,** *3* (16), 2130-2134.

28. Zhang, K.; Lively, R. P.; Zhang, C.; Chance, R. R.; Koros, W. J.; Sholl, D. S.; Nair, S., Exploring the Framework Hydrophobicity and Flexibility of ZIF-8: From Biofuel Recovery to Hydrocarbon Separations. *J. Phys. Chem. Lett.* **2013,** *4* (21), 3618-3622.

29. Haldoupis, E.; Watanabe, T.; Nair, S.; Sholl, D. S., Quantifying Large Effects of Framework Flexibility on Diffusion in MOFs: CH4 and CO2 in ZIF-8. *Chemphyschem* **2012,** *13* (15), 3449-3452.

30. Chokbunpiam, T.; Chanajaree, R.; Saengsawang, O.; Reimann, S.; Chmelik, C.; Fritzsche, S.; Caro, J.; Remsungnen, T.; Hannongbua, S., The importance of lattice flexibility for the migration of ethane in ZIF-8: Molecular dynamics simulations. *Microporous Mesoporous Mater.* **2013,** *174*, 126-134.

31. Watanabe, T.; Sholl, D. S., Accelerating Applications of Metal–Organic Frameworks for Gas Adsorption and Separation by Computational Screening of Materials. *Langmuir* **2012,** *28* (40), 14114-14128.

32. Verploegh, R. J.; Nair, S.; Sholl, D. S., Temperature and Loading-Dependent Diffusion of Light Hydrocarbons in ZIF-8 as Predicted Through Fully Flexible Molecular Simulations. *J. Am. Chem. Soc.* **2015,** *137* (50), 15760-15771.

33. Bereciartua, P. J.; Cantín, Á.; Corma, A.; Jordá, J. L.; Palomino, M.; Rey, F.; Valencia, S.; Corcoran, E. W.; Kortunov, P.; Ravikovitch, P. I., Control of zeolite framework flexibility and pore topology for separation of ethane and ethylene. *Science* **2017,** *358* (6366), 1068-1071.

34. Stock, N.; Biswas, S., Synthesis of Metal-Organic Frameworks (MOFs): Routes to Various MOF Topologies, Morphologies, and Composites. *Chem. Rev.* **2012,** *112*, 933-969.

35. Férey, G., Hybrid porous solids: past, present, future. *Chem. Soc. Rev.* **2008,** *37*, 191-214.

36. Pimentel, B. R.; Parulkar, A.; Zhou, E.-k.; Brunelli, N. A.; Lively, R. P., Zeolitic Imidazolate Frameworks: Next-Generation Materials for Energy-Efficient Gas Separations. *ChemSusChem* **2014,** *7* (12), 3202-3240.

37. He, M.; Yao, J.; Liu, Q.; Zhong, Z.; Wang, H., Toluene-assisted synthesis of RHO-type zeolitic imidazolate frameworks: synthesis and formation mechanism of ZIF-11 and ZIF-12. *Dalton Transactions* **2013,** *42* (47), 16608-16613.

38. Houndonougbo, Y.; Signer, C.; He, N.; Morris, W.; Furukawa, H.; Ray, K. G.; Olmsted, D. L.; Asta, M.; Laird, B. B.; Yaghi, O. M., A Combined Experimental-Computational Investigation of Methane Adsorption and Selectivity in a Series of Isoreticular Zeolitic Imidazolate Frameworks. *J. Phys. Chem. C* **2013,** *117* (20), 10326-10335.

39. Chen, E. Y.; Liu, Y. C.; Sun, T. Y.; Wang, Q.; Liang, L. J., Effects of substituent groups and central metal ion on hydrogen adsorption in zeolitic imidazolate frameworks. *Chem. Eng. Sci.* **2013,** *97*, 60-66.

40. Thompson, J. A.; Blad, C. R.; Brunelli, N. A.; Lydon, M. E.; Lively, R. P.; Jones, C. W.; Nair, S., Hybrid Zeolitic Imidazolate Frameworks: Controlling Framework Porosity and Functionality by Mixed-Linker Synthesis. *Chem. Mater.* **2012,** *24* (10), 1930-1936.

41. Karagiaridi, O.; Bury, W.; Mondloch, J. E.; Hupp, J. T.; Farha, O. K., Solvent-Assisted Linker Exchange: An Alternative to the De Novo Synthesis of Unattainable Metal-Organic Frameworks. *Angew. Chem. Int. Ed.* **2014,** *52*, 2-13.

42. Gross, A. F.; Sherman, E.; Mahoney, S. L.; Vajo, J. J., Reversible ligand exchange in a metal-organic framework (MOF): toward MOF-based dynamic combinatorial chemical systems. *J. Phys. Chem. A* **2013,** *117* (18), 3771-6.

43. Kim, M.; Cahill, J. F.; Fei, H.; Prather, K. a.; Cohen, S. M., Postsynthetic ligand and cation exchange in robust metal-organic frameworks. *J. Am. Chem. Soc.* **2012,** *134*, 18082-8.

44. Jayachandrababu, K. C.; Sholl, D. S.; Nair, S., Structural and Mechanistic Differences in Mixed-Linker Zeolitic Imidazolate Framework Synthesis by Solvent Assisted Linker Exchange and de Novo Routes. *J. Am. Chem. Soc.* **2017,** *139* (16), 5906-5915.

45. Jayachandrababu, K. C.; Verploegh, R. J.; Leisen, J.; Nieuwendaal, R. C.; Sholl, D. S.; Nair, S., Structure Elucidation of Mixed-Linker Zeolitic Imidazolate Frameworks by Solid-State 1H CRAMPS NMR Spectroscopy and Computational Modeling. *J. Am. Chem. Soc.* **2016,** *138* (23), 7325-7336.

46. Liu, D.; Zheng, C.; Yang, Q.; Zhong, C., Understanding the Adsorption and Diffusion of Carbon Dioxide in Zeolitic Imidazolate Frameworks: A Molecular Simulation Study. *J. Phys. Chem. C* **2009,** *113* (12), 5004-5009.

47. Hou, X.-J.; Li, H., Unraveling the High Uptake and Selectivity of CO2 in the Zeolitic Imidazolate Frameworks ZIF-68 and ZIF-69. *J. Phys. Chem. C* **2010,** *114* (32), 13501-13508.

48. Sirjoosingh, A.; Alavi, S.; Woo, T. K., Grand-Canonical Monte Carlo and Molecular-Dynamics Simulations of Carbon-Dioxide and Carbon-Monoxide Adsorption in Zeolitic Imidazolate Framework Materials. *J. Phys. Chem. C* **2010,** *114* (5), 2171-2178.

49. Peralta, D.; Chaplais, G.; Simon-Masseron, A.; Barthelet, K.; Pirngruber, G. D., Synthesis and adsorption properties of ZIF-76 isomorphs. *Microporous Mesoporous Mater.* **2012,** *153*, 1-7.

50. Perez-Pellitero, J.; Amrouche, H.; Siperstein, F. R.; Pirngruber, G.; Nieto-Draghi, C.; Chaplais, G.; Simon-Masseron, A.; Bazer-Bachi, D.; Peralta, D.; Bats, N., Adsorption of CO2, CH4, and N-2 on Zeolitic Imidazolate Frameworks: Experiments and Simulations. *Chemistry-a European Journal* **2010,** *16* (5), 1560-1571.

51. Guo, H.-c.; Shi, F.; Ma, Z.-f.; Liu, X.-q., Molecular Simulation for Adsorption and Separation of CH4/H-2 in Zeolitic Imidazolate Frameworks. *J. Phys. Chem. C* **2010,** *114* (28), 12158-12165.

52. Battisti, A.; Taioli, S.; Garberoglio, G., Zeolitic imidazolate frameworks for separation of binary mixtures of CO2, CH4, N-2 and H-2: A computer simulation investigation. *Microporous Mesoporous Mater.* **2011,** *143* (1), 46-53.

53. Zhou, M.; Wang, Q.; Zhang, L.; Liu, Y.-C.; Kang, Y., Adsorption Sites of Hydrogen in Zeolitic Imidazolate Frameworks. *J. Phys. Chem. B* **2009,** *113* (32), 11049-11053.

54. Morris, W.; Leung, B.; Furukawa, H.; Yaghi, O. K.; He, N.; Hayashi, H.; Houndonougbo, Y.; Asta, M.; Laird, B. B.; Yaghi, O. M., A Combined Experimental-Computational Investigation of Carbon Dioxide Capture in a Series of Isoreticular Zeolitic Imidazolate Frameworks. *J. Am. Chem. Soc.* **2010,** *132* (32), 11006-11008.

55. Banerjee, R.; Furukawa, H.; Britt, D.; Knobler, C.; O'Keeffe, M.; Yaghi, O. M., Control of Pore Size and Functionality in Isoreticular Zeolitic Imidazolate Frameworks and their Carbon Dioxide Selective Capture Properties. *J. Am. Chem. Soc.* **2009,** *131* (11), 3875–3877.

56. Amrouche, H.; Aguado, S.; Perez-Pellitero, J.; Chizallet, C.; Siperstein, F.; Farrusseng, D.; Bats, N.; Nieto-Draghi, C., Experimental and Computational Study of Functionality Impact on Sodalite-Zeolitic Imidazolate Frameworks for CO2 Separation. *J. Phys. Chem. C* **2011,** *115* (33), 16425-16432.

57. Liu, Y.; Liu, J.; Chang, M.; Zheng, C., Effect of Functionalized Linker on CO2 Binding in Zeolitic Imidazolate Frameworks: Density Functional Theory Study. *J. Phys. Chem. C* **2012,** *116* (32), 16985-16991.

58. Morris, W.; He, N.; Ray, K. G.; Klonowski, P.; Furukawa, H.; Daniels, I. N.; Houndonougbo, Y. A.; Asta, M.; Yaghi, O. M.; Laird, B. B., A Combined Experimental-Computational Study on the Effect of Topology on Carbon Dioxide Adsorption in Zeolitic Imidazolate Frameworks. *J. Phys. Chem. C* **2012,** *116* (45), 24084-24090.

59. Thompson, J. A.; Brunelli, N. A.; Lively, R. P.; Johnson, J. R.; Jones, C. W.; Nair, S., Tunable CO2 Adsorbents by Mixed-Linker Synthesis and Postsynthetic Modification of Zeolitic Imidazolate Frameworks. *J. Phys. Chem. C* **2013,** *117* (16), 8198-8207.

60. van den Bergh, J.; Gucuyener, C.; Pidko, E. A.; Hensen, E. J. M.; Gascon, J.; Kapteijn, F., Understanding the Anomalous Alkane Selectivity of ZIF-7 in the Separation of Light Alkane/Alkene Mixtures. *Chem. Eur. J.* **2011,** *17* (32), 8832-8840.

61. Gucuyener, C.; van den Bergh, J.; Gascon, J.; Kapteijn, F., Ethane/Ethene Separation Turned on Its Head: Selective Ethane Adsorption on the Metal-Organic Framework ZIF-7 through a Gate-Opening Mechanism. *J. Am. Chem. Soc.* **2010,** *132* (50), 17704-17706.

62. Boehme, U.; Barth, B.; Paula, C.; Kuhnt, A.; Schwieger, W.; Mundstock, A.; Caro, J.; Hartmann, M., Ethene/Ethane and Propene/Propane Separation via the Olefin and Paraffin Selective Metal-Organic Framework Adsorbents CPO-27 and ZIF-8. *Langmuir* **2013,** *29* (27), 8592-8600.

63. Bux, H.; Chmelik, C.; Krishna, R.; Caro, J., Ethene/ethane separation by the MOF membrane ZIF-8: Molecular correlation of permeation, adsorption, diffusion. *J. Membr. Sci.* **2011,** *369* (1-2), 284-289.

64. Bloch, E. D.; Queen, W. L.; Krishna, R.; Zadrozny, J. M.; Brown, C. M.; Long, J. R., Hydrocarbon Separations in a Metal-Organic Framework with Open Iron(II) Coordination Sites. *Science* **2012,** *335* (6076), 1606-1610.

65. Ruthven, D. M.; Reyes, S. C., Adsorptive separation of light olefins from paraffins. *Microporous Mesoporous Mater.* **2007,** *104* (1–3), 59-66.

66. Li, K.; Olson, D. H.; Seidel, J.; Emge, T. J.; Gong, H.; Zeng, H.; Li, J., Zeolitic Imidazolate Frameworks for Kinetic Separation of Propane and Propene. *J. Am. Chem. Soc.* **2009,** *131* (30), 10368-10369.

67. Nalaparaju, A.; Zhao, X. S.; Jiang, J. W., Molecular Understanding for the Adsorption of Water and Alcohols in Hydrophilic and Hydrophobic Zeolitic Metal-Organic Frameworks. *J. Phys. Chem. C* **2010,** *114* (26), 11542-11550.

68. Saint Remi, J. C.; Remy, T.; Van Hunskerken, V.; van de Perre, S.; Duerinck, T.; Maes, M.; De Vos, D.; Gobechiya, E.; Kirschhock, C. E. A.; Baron, G. V.; Denayer, J. F. M., Biobutanol Separation with the Metal-Organic Framework ZIF-8. *Chemsuschem* **2011,** *4* (8), 1074-1077.

69. Zhang, K.; Zhang, L.; Jiang, J., Adsorption of C-1-C-4 Alcohols in Zeolitic Imidazolate Framework-8: Effects of Force Fields, Atomic Charges, and Framework Flexibility. *J. Phys. Chem. C* **2013,** *117* (48), 25628-25635.

70. Gee, J. A.; Chung, J.; Nair, S.; Sholl, D. S., Adsorption and Diffusion of Small Alcohols in Zeolitic Imidazolate Frameworks ZIF-8 and ZIF-90. *J. Phys. Chem. C* **2013,** *117* (6), 3169-3176.

71. Pan, Y.; Li, T.; Lestari, G.; Lai, Z., Effective separation of propylene/propane binary mixtures by ZIF-8 membranes. *J. Membr. Sci.* **2012,** *390*, 93-98.

72. Brown, A. J.; Brunelli, N. A.; Eum, K.; Rashidi, F.; Johnson, J.; Koros, W. J.; Jones, C. W.; Nair, S., Interfacial microfluidic processing of metal-organic framework hollow fiber membranes. *Science* **2014,** *345* (6192), 72-75.

73. Thommes, M.; Kaneko, K.; Neimark, A. V.; Olivier, J. P.; Rodriguez-Reinoso, F.; Rouquerol, J.; Sing, K. S. W., Physisorption of gases, with special reference to the evaluation of surface area and pore size distribution (IUPAC Technical Report). *Pure Appl. Chem.* **2015,** *87* (9-10), 1051-1069.

74. Brunauer, S.; Emmett, P. H.; Teller, E., Adsorption of gases in multimolecular layers. *J. Am. Chem. Soc.* **1938,** *60* (2), 309-319.

75. Walton, K. S.; Snurr, R. Q., Applicability of the BET method for determining surface areas of microporous metal-organic frameworks. *J. Am. Chem. Soc.* **2007,** *129*, 8552-6.

76. Myers, A. L.; Prausnitz, J. M., Thermodynamics of mixed-gas adsorption. *AlChE J.* **1965,** *11* (1), 121-127.

77. Do, D. D., *Adsorption Analysis : Equilibria and Kinetics*. Imperial College Press: London, 1998; p xxi, 892 p.

78. De Lange, M. F.; Vlugt, T. J. H.; Gascon, J.; Kapteijn, F., Adsorptive characterization of porous solids: Error analysis guides the way. *Microporous Mesoporous Mater.* **2014,** *200* (0), 199-215.

79. Crank, J., *The Mathematics of Diffusion*. 2nd ed.; Oxford University Press: Oxford, 1975.

80. Darken, L. S., Diffusion, mobility and their interrelation through free energy in binary metallic systems. *Trans. Aime* **1948,** *175*, 184-201.

81. Binder, T.; Lauerer, A.; Chmelik, C.; Haase, J. r.; Kärger, J. r.; Ruthven, D. M., Microimaging of Transient Intracrystalline Concentration Profiles during Two-Component Uptake of Light Hydrocarbon–Carbon Dioxide Mixtures by DDR-Type Zeolites. *Ind. Eng. Chem. Res.* **2015,** *54* (36), 8997-9004.

82. Lauerer, A.; Binder, T.; Chmelik, C.; Miersemann, E.; Haase, J.; Ruthven, D. M.; Kärger, J., Uphill diffusion and overshooting in the adsorption of binary mixtures in nanoporous solids. *Nature communications* **2015,** *6*, 7697.

83. Krishna, R., Tracing the origins of transient overshoots for binary mixture diffusion in microporous crystalline materials. *PCCP* **2016,** *18* (23), 15482-15495.

84. Krishna, R., Diffusion in porous crystalline materials. *Chem. Soc. Rev.* **2012,** *41* (8), 3099-3118.

85. Brandani, S., Analysis of the piezometric method for the study of diffusion in microporous solids: Isothermal case. *Adsorption* **1998,** *4* (1), 17-24.

86. Kärger, J. R., Douglas M; Theodorou, Doros N, *Diffusion in Nanoporous Materials*. Wiley-VCH: Weinheim, Germany, 2012; Vol. 1, p 513.

87. Chihara, K.; Suzuki, M.; Kawazoe, K., Effect of heat generation on measurement of adsorption rate by gravimetric method. *Chem. Eng. Sci.* **1976,** *31* (6), 505-507.

88. Ruthven, D. M.; Lee, L. K.; Yucel, H., Kinetics of non-isothermal sorption in molecular sieve crystals. *AlChE J.* **1980,** *26* (1), 16-23.

89. Wu, H.; Chua, Y. S.; Krungleviciute, V.; Tyagi, M.; Chen, P.; Yildirim, T.; Zhou, W., Unusual and highly tunable missing-linker defects in zirconium metal–organic framework UiO-66 and their important effects on gas adsorption. *J. Am. Chem. Soc.* **2013,** *135* (28), 10525-10532.

90. Vasenkov, S.; Böhlmann, W.; Galvosas, P.; Geier, O.; Liu, H.; Kärger, J., PFG NMR study of diffusion in MFI-type zeolites: evidence of the existence of intracrystalline transport barriers. *The Journal of Physical Chemistry B* **2001,** *105* (25), 5922-5927.

91. Saint Remi, J. C.; Lauerer, A.; Chmelik, C.; Vandendael, I.; Terryn, H.; Baron, G. V.; Denayer, J. F.; Kärger, J., The role of crystal diversity in understanding mass transfer in nanoporous materials. *Nat. Mat.* **2016,** *15* (4), 401.

92. Tanaka, S.; Fujita, K.; Miyake, Y.; Miyamoto, M.; Hasegawa, Y.; Makino, T.; Van der Perre, S.; Cousin Saint Remi, J.; Van Assche, T.; Baron, G. V., Adsorption and diffusion phenomena in crystal size engineered ZIF-8 MOF. *The Journal of Physical Chemistry C* **2015,** *119* (51), 28430-28439.

93. Pang, S. H.; Han, C.; Sholl, D. S.; Jones, C. W.; Lively, R. P., Facet-specific stability of ZIF-8 in the presence of acid gases dissolved in aqueous solutions. *Chem. Mater.* **2016,** *28* (19), 6960-6967.

94. Ruthven, D.; Farooq, S.; Knaebel, K., *Pressure Swing Adsorption*. VCH: New York.

95. Rocha, L. A.; Andreassen, K. A.; Grande, C. A., Separation of CO 2/CH 4 using carbon molecular sieve (CMS) at low and high pressure. *Chem. Eng. Sci.* **2017,** *164*, 148-157.

96. Grande, C.; Rodrigues, A., Adsorption kinetics of propane and propylene in zeolite 4A. *Chem. Eng. Res. Des.* **2004,** *82* (12), 1604-1612.

97. Kapoor, A.; Yang, R. T., Kinetic separation of methane—carbon dioxide mixture by adsorption on molecular sieve carbon. *Chem. Eng. Sci.* **1989,** *44* (8), 1723-1733.

98. Grande, C. A.; Silva, V. M. T. M.; Gigola, C.; Rodrigues, A. r. E., Adsorption of propane and propylene onto carbon molecular sieve. *Carbon* **2003,** *41* (13), 2533-2545.

99. Seemann, A.; Richter, E.; Jüntgen, H., Modelling of a pressure swing adsorption process for oxygen enrichment with carbon molecular sieve. *Chemical Engineering & Technology* **1988,** *11* (1), 341-351.

100. Kuznicki, S. M.; Bell, V. A.; Nair, S.; Hillhouse, H. W.; Jacubinas, R. M.; Braunbarth, C. M.; Toby, B. H.; Tsapatsis, M., A titanosilicate molecular sieve with adjustable pores for size-selective adsorption of molecules. *Nature* **2001,** *412* (6848), 720.

101. Ahn, H.; Brandani, S., A new numerical method for accurate simulation of fast cyclic adsorption processes. *Adsorption* **2005,** *11* (2), 113-122.

102. Kapteijn, F.; van de Graaf, J. M.; Moulijn, J. A., One-component permeation maximum: Diagnostic tool for silicalite-1 membranes? *AlChE J.* **2000,** *46* (5), 1096-1100.

CHAPTER 3. SORPTION AND DIFFUSION OF GASES AND VAPORS IN ZEOLITIC IMIDAZOLATE FRAMEWORKS

The understanding of the fundamental properties of adsorption and diffusion of a material are critical for their effective implementation in separation schemes. This chapter focuses on the characterization of ZIF-8 and ZIF-11 via various sorption and diffusion measurement techniques to determine their inherent host-guest properties with respect to various gas and vapor molecules of interest. Qualitative structure-property relations are also developed with regards to the inherent flexibility of ZIF materials and how these affect the transport properties of structure.

ZIF-11 is shown to be a framework that permits more rapid diffusion of guest molecules relative to ZIF-8, despite having a smaller average pore aperture. This is attributed to enhanced window flexibility of the 8-MR over the 6-MR, which is further manifested as a distinctively lower diffusive selectivity for guest molecules presented here. This flexibility is demonstrated via analysis of solid state NMR techniques and supplemented by molecular dynamics simulations.

The temperature dependence of guest diffusion in ZIF-11 is shown to be extremely high (and perhaps non-Arrhenius) using kinetic uptake measurements of CH_4 over a range of cryogenic temperatures. This is hypothesized to be related to the temperature dependence of the linker flexibility, wherein the structure experiences significant flexibility changes with temperature that increase the diffusive energy barrier beyond expected rigid-pore diffusion.

The work in this chapter could not have been possible without the contributions of Dr. Melinda Jue (vapor uptake measurements), Dr. Ross Verploegh (MD simulations), and Erkang Zhou (^{2}H NMR solid echo analysis).

Portions of this chapter have been reprinted with permission from Pimentel, B. R.; Lively, R. P., Enabling kinetic light hydrocarbon separation via crystal size engineering of ZIF-8. *Ind. Eng. Chem. Res.* **2016,** *55* (48), 12467-12476. Copyright American Chemical Society 2016.

3.1 Materials and Methods

3.1.1 Materials

This work made use of the following chemicals: 1-methylimidazole (99%, Alfa Aesar), 2-methylimidazole (97%, Alfa Aesar), benzimidazole (99%, Alfa Aesar), sodium formate (98%, Alfa Aesar), methanol (ACS grade, VWR), NH_4OH (Sigma Aldrich, 28-30% NH_3 in water), toluene (99.7%, Alfa Aesar), n-propanol (Sigma Aldrich, 99.9%), n-butanol (Alfa Aesar 99%), n-hexane (Acros, 99%), 1-hexene (Acros, 97%), n-heptane (Alfa Aesar, 99%), zinc nitrate hexahydrate (99%, Alfa Aesar), zinc acetate (Alfa Aesar 97%). The following gases were used in this work: nitrogen (UHP, Airgas), helium (UHP, Airgas), methane (99.99%, Airgas), ethane (99.99%, Airgas), propane (99.5%, Tech Air), propylene (99.5%, TechAir), and n-butane (99.5%, TechAir). All materials were used as received without any further purification

3.1.2 Synthesis of ZIF Materials

3.1.2.1 ZIF-11 Synthesis

18 μm ZIF-11. 0.6 g of benzimidazole was dissolved in 16.8 g of methanol and 3.8 g of NH_4OH in a 50 mL round-bottom flask. To this, a solution of 0.55 g of Zn Acetate in 16.4 g of methanol and 13 g of toluene was added. The sample was stirred until mixed then allowed to stand for 4 h. White crystals were filtered through a 2.5 μm filter paper followed by 22 μm filter paper and washed with methanol then dried under vacuum at 353 K overnight.

11 μm ZIF-11. 0.3 g of benzimidazole linker was dissolved in 8.4g of methanol and 1.9g of NH_4OH in a 25ml round bottom flask. To this, a solution of 0.28 g of ZnAc in 8.4 g of methanol and 6.5 g of toluene was added. Solution was stirred at 500 rpm for 2 h, after which crystals were collected by centrifuge and washed with methanol three times. Samples were dried under vacuum at 373 K overnight.

3.1.2.2 ZIF-8 Synthesis

145 μm ZIF-8. ZIF-8 samples exhibiting 145 μm diffusive lengths were synthesized in a glass vial in methanol as per previous work.[1] Briefly, 2.205 g of zinc nitrate hexahydrate was dissolved in 25 mL of methanol. A total of 1.215 g of 2-methylimidazole and 0.504 g of sodium formate were dissolved in a separate 25 mL solution of methanol. The zinc solution was poured into the imidazole solution and stirring was stopped after mixing. The vial was kept capped at 90 °C for 24 h, then washed, and sieved through 120 μm mesh. Samples were dried at 80 °C under vacuum overnight to remove adsorbed methanol. Under scanning electron microscopy, these crystals were shown to often be either cracked or broken, likely as a result of growing from a flat surface such as the vial

wall. Because of these irregularities in their geometry, these crystals were not used in diffusion measurements.

1.5 µm ZIF-8. ZIF-8 samples of 1.5 µm were synthesized in a glass vial in methanol as per previous work.[2] Briefly, 0.734 g of zinc nitrate hexahydrate was dissolved in 50 mL of methanol. A total of 0.810 g of 2-methylimidazole and 0.810 g of 1-methylimidazole were dissolved in a separate 50 mL solution of methanol. The second solution was poured into the first, and stirring was stopped after mixing. The vial was kept capped at room temperature for 24 h, then washed, and filtered. Samples were dried at 80 °C under vacuum overnight to remove adsorbed methanol.

3.1.3 Material Characterization

Crystals were characterized using powder X-ray diffraction (XRD; PANalytical X'pert PRO multipurpose diffractometer and PANalytical Empyrean with a rotating sample stage), scanning electron microscopy (SEM; Hitachi SU8230 cold-field-emission scanning electron microscope), and cryogenic N2 physisorption (Microtrac BELSORP-max). All XRD patterns matched simulated structural reflections, while SEM provided a means to measure the crystal size distribution (**Table 3.1**, **Figure 3.1 & 3.2**). XRD patterns for both ZIF-11 and ZIF-8 samples **Figure 3.3 & Figure 3.4** suggest samples of high crystallinity and appropriate phase composition by matching of the major crystallographic reflections. There is no significant pattern difference between samples of varying crystal dimensions.

Table 3.1 Crystal distribution statistics of the ZIF samples in this studies

Sample Name	Volumetric Mean Crystal Radius (μm)	Standard Error (μm)
ZIF-8 1.5 μm	1.5	0.1
ZIF-11 18 μm	18	3
ZIF-11 11 μm	11	1

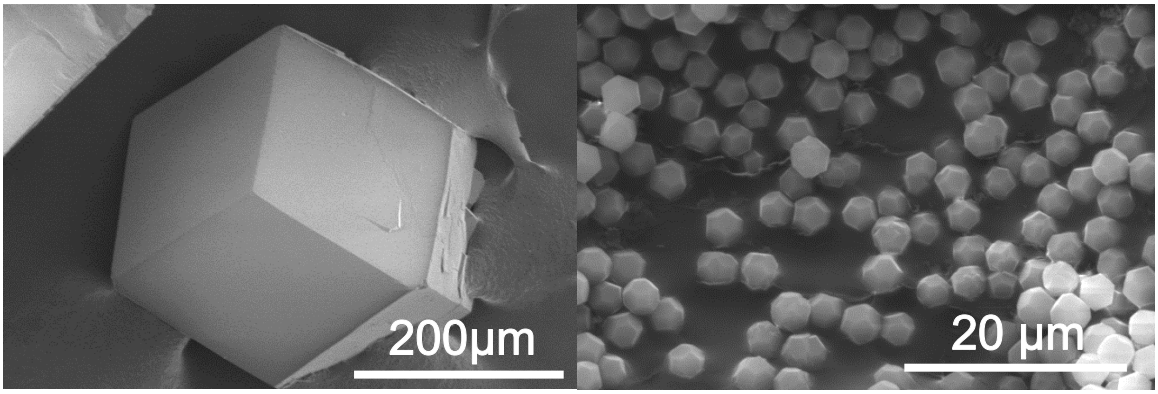

Figure 3.1 145 μm diffusive length ZIF-8 crystal (left) and 1.5 μm radius ZIF-8 crystals showing sharp rhombic dodecahedral facets

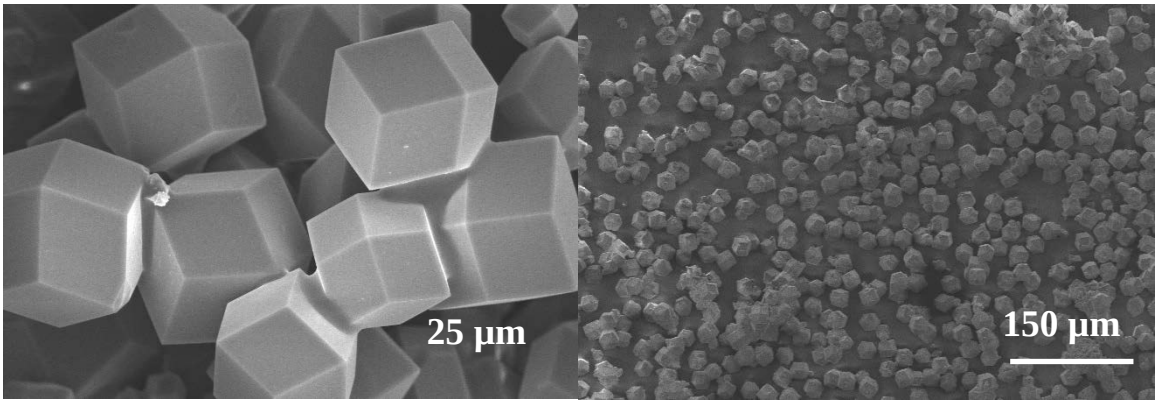

Figure 3.2 18 μm ZIF-11 (left) and 11 μm sample (right) demonstrating sharp crystal features and single crystal morphologies.

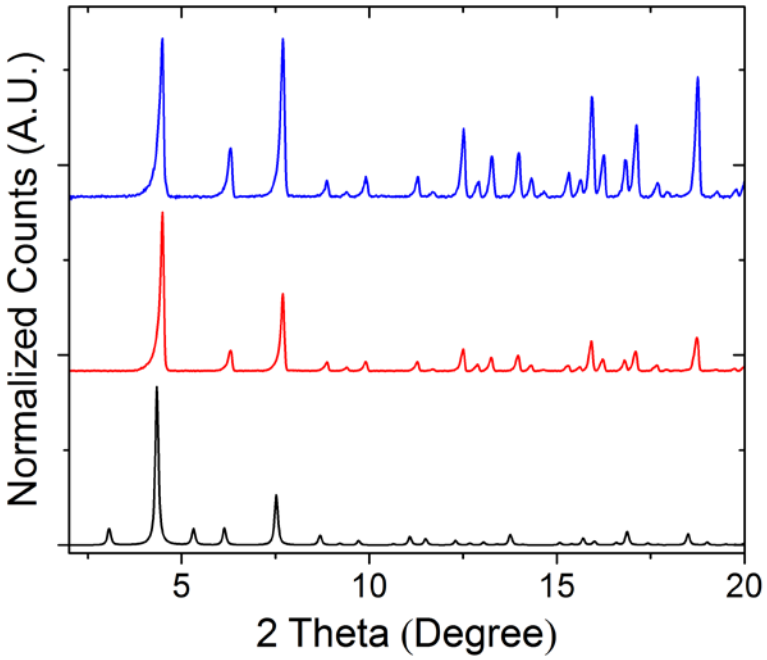

Figure 3.3 Powder XRD pattern of ZIF-11 samples. 11 μm (blue), 18 μm (red), predicted (black)

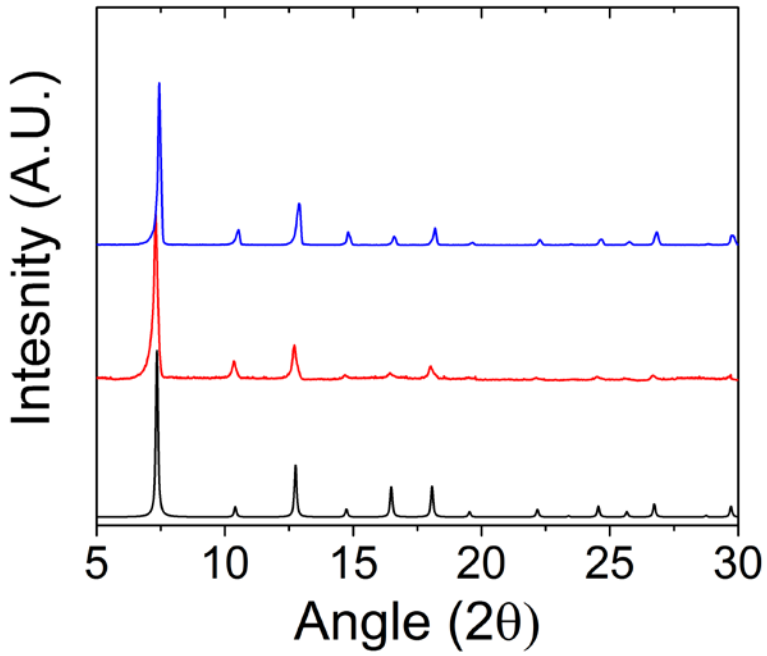

Figure 3.4 Powder XRD pattern of ZIF-8 samples. 145 μm (blue), 1.5 μm (red), predicted (black)

N_2 physisorption at 77 K experiments revealed a high degree of microporosity within all ZIF-8 samples, with the characteristic "gate-opening" step from 5 to 9 × 10^{-3} P/P_0 (**Figure 3.5**) and Brunauer−Emmett−Teller surface areas of 1350 m^2/g (145 μm) and

1400 m^2/g (1.5 μm) and pore volumes of 0.64 and 0.66 cm^3/g, respectively.[3] From these values, we believe that the samples are of similar quality and differences in the internal microporosity should have a minimal effect on their separation performance. The ZIF-11 structure is commonly reported as non-porous by N_2 physisorption at 77 K, [4-5] though some authors report porosity when synthesized in low water content DEF.[6] Indeed, our attempts at characterizing ZIF-11 in this manner resulted not in an isotherm of zero adsorption, but rather the inability to equilibrate a single adsorption step after 24 hours. This indicates an extremely slow rate of diffusion, but not complete exclusion of the molecule from the framework. Clearly, ZIF-11 is porous at 77 K, as numerous works have demonstrated uptake of H_2,[7-8] possibly as an alternative to N_2 porosity characterization. Moreover the framework accepts molecules as large as toluene at near ambient temperatures, as reported later in this chapter.

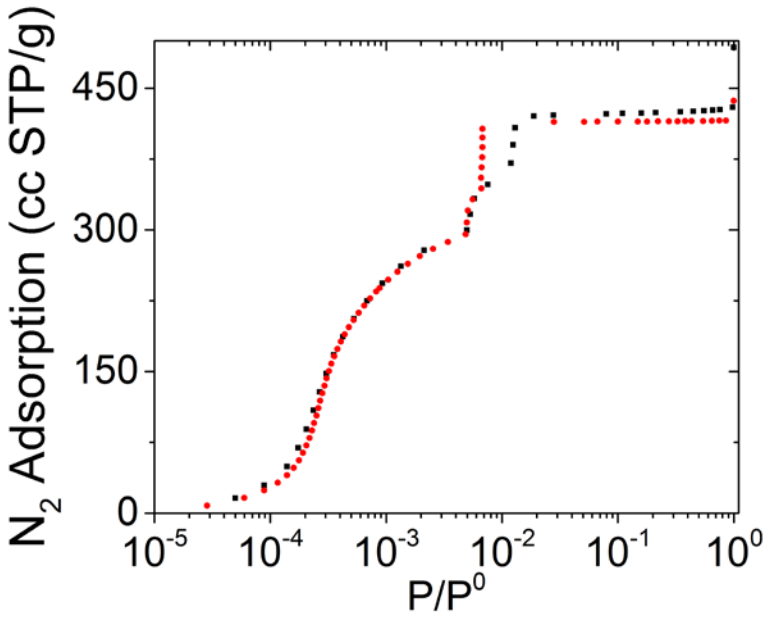

Figure 3.5 N_2 physisorption at 77 K of ZIF-8 samples. Red- 145 μm ZIF-8, Black – 1.5 μm ZIF-8.

3.1.4 Adsorption and Diffusion Measurements

Vapor sorption experiments were carried out in a TA Instruments VTI-SI+, which employs a microgram balance to determine the gravimetric uptake of the sorbent sample during an experiment. A nitrogen stream is humidified in the system vapor saturator and combined with a dry nitrogen stream at appropriate ratios to create the necessary partially humidified stream, which is then flowed over the sample and reference chamber. Relative saturation points are set by vapor pressure calculations using the Wagner vapor pressure equations; water streams are additionally tuned by the use of a dew-point mirrors. The stream is initially routed through a sample bypass for 3 minutes to ensure full stream equilibration before opening valves to the sample. Samples were activated in a stream of dry nitrogen at 90 °C until equilibrated or up to 4 hours.

Single-component excess isotherms of ethane, propane, propylene, and n-butane were measured via volumetric adsorption techniques in a Micromeritics HPVA-II from 253 to 333 K, depending on the gas. Samples were activated at 110 °C for 8 h prior to each adsorption experiment. Subambient temperatures were accessed with the use of a cold head and an associated helium compressor from ColdEdge Technologies. Near-zero occupancy diffusion of propane and n-butane was also measured by pressure decay techniques. We assume that no difference in the adsorption isotherms exists between crystals of different sizes. Diffusion measurements were carried out with an approximately 10 mg of sample; the sample was dispersed on the walls of the sample cell with methanol to minimize interparticle resistance, and the adsorption was calculated to be isothermal (over the time scales of diffusion) per the Ruthven−Lee isothermal criterion.[9-10] Uptake curves were matched to the full analytical solution of sorbate diffusion from a finite volume into a

sphere of known particle-size distribution.[11] We also confirmed that the uptake experiments were free of confounding valve resistances by following the procedure established by Brandani.[12]

3.1.5 Computational Methods

The experimental crystal structures of ZIF-11 (*VEJZOA*) and ZIF-8 (*VELVOY*) as reported by Park et al.[13] were obtained from the Cambridge Structural Database[14] (CSD). The intraZIF force field (FF)[15] was used to model the intra-framework flexibility of both ZIF-8 and ZIF-11. Molecular dynamics (MD) were performed in the NPT ensemble with fixed cell angles using LAMMPS[16] at 308 K and 1.0 bar. The MD simulations used a pairwise cutoff of 15.5 Å, a timestep of 1 fs, and temperature and stress damping parameters of 100 and 1000 fs respectively. Both the cell parameters and atomic coordinates were energy minimized before each MD simulation with the conjugate gradient and Hessian-free truncated Newton minimization routines. An equilibration period of 200 ps was performed before each MD production period of 1 ns. Snapshots were recorded every 0.5 ps for calculation of the window diameter distributions. Window diameter distributions were measured for singular windows using a grid based method described in previous studies.[17-18] The 6-MR of ZIF-11 opens upon energy-minimization whereas the experimental structure reports that this window is “closed.”

3.2 Results and Discussion

3.2.1 Alcohol and Water Vapor in ZIF-11

Due to their hydrophobic nature and demonstrated long-term stability in water, ZIFs have often been incorporated in mixed-matric pervaporation membranes and other schemes for the recovery of dilute bio-alcohols from water.[19-27] Much work has targeted ZIF-8 as the sorbent phase, but ZIF-11 has remained largely unexplored, despite its more hydrophobic benzimidazole linkers.[28]

3.2.1.1 Single Component Sorption Isotherms and IAST Selectivity

Adsorption isotherms for alcohols and water vapor in ZIF-11 shown in **Figure 3.6** exhibit type V isotherms often seen in other hydrophobic materials with cage structures. The behavior is attributable to initial clustering on the surface followed by pore filling at higher activities, typically indicative of weak adsorbate-adsorbent interactions.[29] Pore filling occurs at lower activity with increasing carbon number, although it occurs in butanol at too low an activity to be observed at 35 °C, but has been demonstrated in ZIF-8[30-31] and likely exhibits similar behavior in ZIF-11. Water uptake in ZIF-11 is minimal until high relative humidities, where it is greater than that measured in ZIF-8, likely due to the larger cage size of ZIF-11 providing more available volume for liquid-like water.

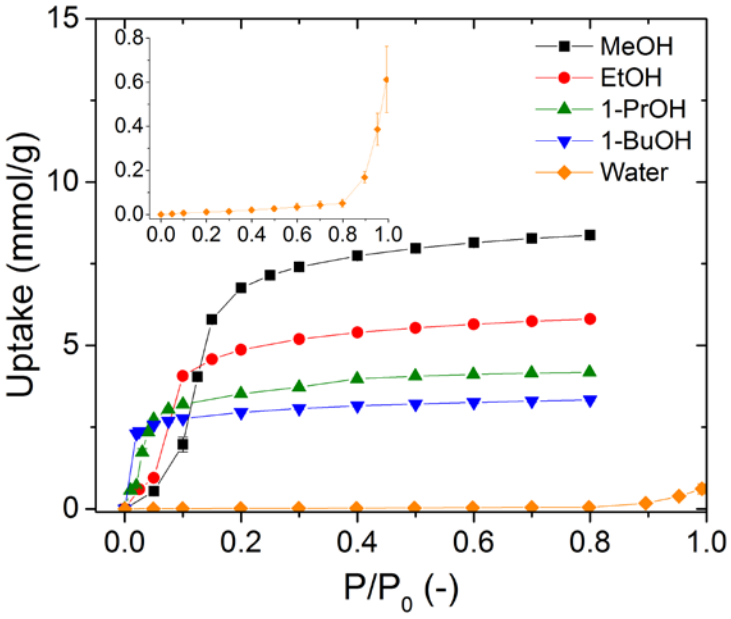

Figure 3.6 Alcohol and water vapor sorption isotherms in ZIF-11 at 35 °C. Error bars represent the standard error of triplicates.

Since water has a smaller kinetic diameter than any bio-alcohol, pervaporation membranes must rely on sorption selectivity to not only drive the separation, but also overcome the disadvantageous diffusive selectivity. Adsorptive selectivity in ZIF-11 from vapors of water/alcohol mixtures was estimated using the Ideal Adsorbed Solution Theory (IAST) (**Figure 3.7**), which uses single-phase adsorption isotherms to estimate multi-component adsorption selectivity.[32-33]

IAST predicts increasing selectivity with carbon number given the earlier pore-filling activities of the higher alcohols. While n-butanol and propanol selectivities are high due to sharp isotherms, ethanol shows poorer performance given the more noticeable S-shape of adsorption. Ethanol/water selectivity of ZIF-11 is less than that of ZIF-8 or F^- MFI, due to the significantly higher water uptake in ZIF-11 that occurs near saturation, where dilute alcohol recovery via pervaporation generally operates.[34-35] Methanol vapor

pressure in dilute aqueous mixtures is still largely within the initial low-uptake region of the isotherm and therefore is not able to capitalize on the large pore filling event exhibited at higher activities, which results in lower selectivity.

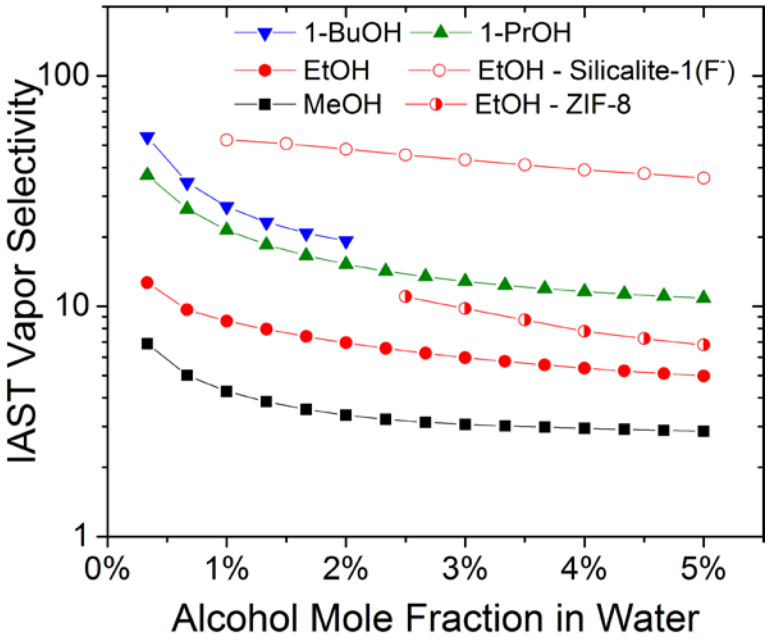

Figure 3.7 Alcohol/Water selectivities in ZIF-11 as predicted by IAST at 35 °C. Silicalite[34] and ZIF-8[35] data reproduced from published literature.

3.2.1.2 Single Component Diffusivity

As has been widely reported in ZIFs, the flexibility of the imidazole linkers allows for the adsorption of molecules well beyond the crystallographically determined aperture size.[1, 36-38] The pore aperture of the eight-member ring in ZIF-11 is reported as 3.2 Å,[39] although the uptake of much larger molecules has been clearly demonstrated here.

Alcohol diffusivities in ZIF-11 at 35 °C plotted in **Figure 3.8** show relatively small variations with increasing carbon number; methanol and butanol separated by only two orders of magnitude despite both being larger than the nominal pore aperture. This contrasts sharply with ZIF-8, where differences between methanol and ethanol or ethanol and butanol are two and four orders of magnitude, at 25 and 50 °C, respectively.[31, 40] The loading-dependent corrected diffusivity of alcohols in ZIF-11 show a relatively flat profile during the initial plateaus and pore filling portions of the isotherms, but turn upward at near full occupancy. This is likely the result of molecular clustering that retards diffusion but becomes less pronounced near saturation, similar to reported behavior in ZIF-8.[40]

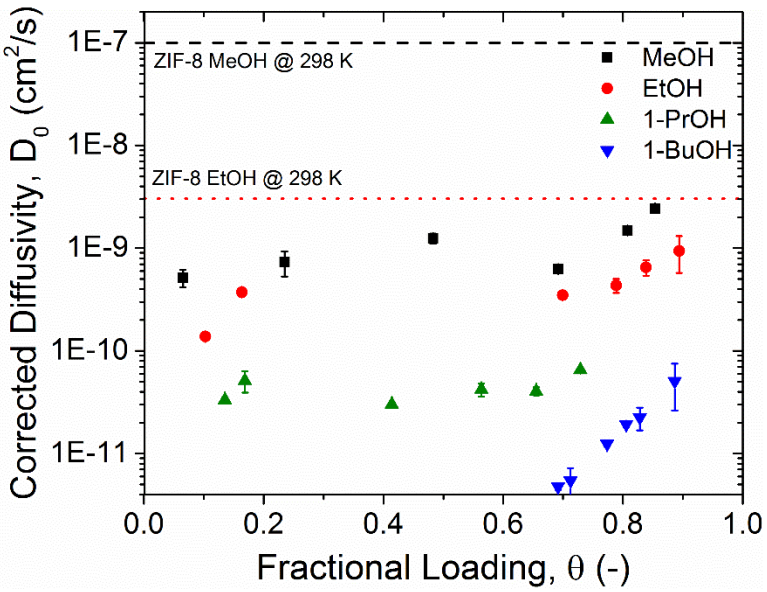

Figure 3.8 Diffusion of alcohols in ZIF-11 at 35 °C as a function of loading. Error bars represent the standard error of triplicates. Dashed line data represents a nominal average over a range of loadings.[40]

To ensure the accuracy of measured diffusivities and data fitting techniques, the diffusivity of various uptake points was calculated with both a one and a two-parameter fit **Table 3.2** as well as comparing the diffusivity values obtained from using different size crystals for the same diffusing species **Table 3.3**. Details of these fits are provided in **Chapter 2**.

Table 3.2 Calculated transport diffusivities in 1-parameter vs 2-parameter fits for ethanol at 35 °C in ZIF-11. $\boldsymbol{\tau_1}$has a value of 107 s

P/P^*	**0.025**	**0.05**	**0.1**	**0.15**	**0.2**	**0.3**
D_2/D_1	0.62	1.13	0.69	1.07	0.91	0.38
τ_2	180	79	374	99	119	122

Table 3.3 N-propanol diffusivity comparison of the samples used in this study

Sample	Diffusivity, cm^2/s (τ, sec)[a]	
18 μm crystals	7.6×10^{-11} (107)	2.3×10^{-10} (1245)
11 μm crystals	1.7×10^{-10} (107)	3.2×10^{-10} (325)

The relative magnitudes of the diffusivities under different fitting conditions point to a multivariate fit as an important but not necessarily crucial aspect of diffusion measurements, while the similar values in diffusivity in differing crystal sizes signal the similarity in samples and lack of surface phenomena affecting diffusion in smaller crystals.

3.2.2 Hydrocarbon Adsorption and Diffusion in ZIF-8, -11

3.2.2.1 Single Component Isotherms

In ZIF-8 Single-component gas isotherms show a typical Langmuir response in their uptake (**Figure 3.9**) with n-butane as the highest carbon number molecule having the steepest response. No evidence of flexible "gate-opening" transitions was observed. Isosteric heats of adsorption (**Figure 3.10**) show an upward trend uncorrelated to sorbate latent heats of vaporization. This upward trend has been previously attributed to both nonpolar interactions and changing adsorbate molar volumes with the system temperature.[41]

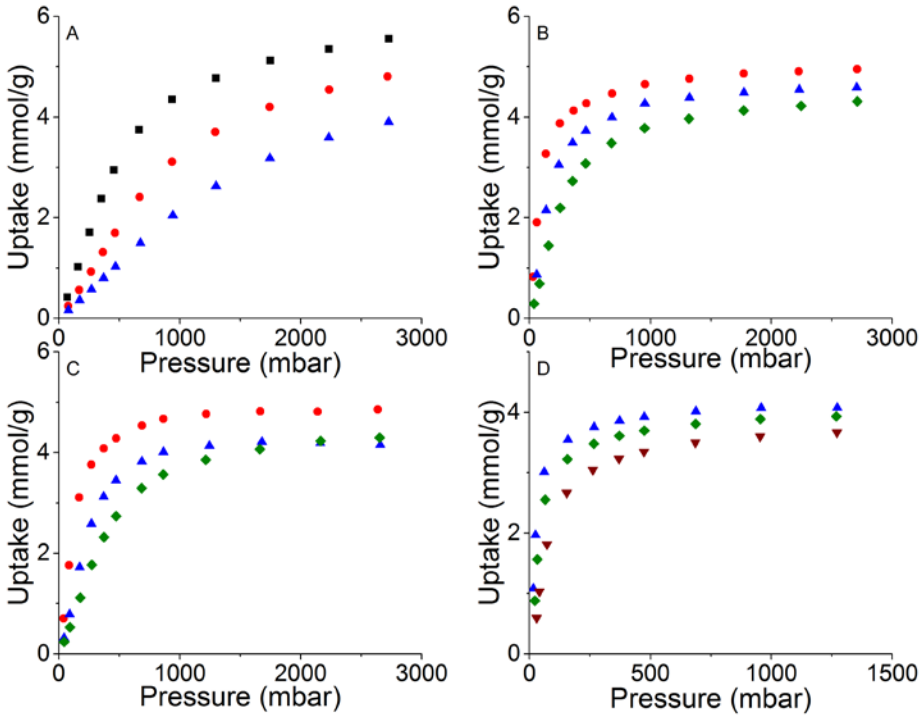

Figure 3.9 Adsorption isotherms of (A) ethane, (B) propane, (C) propylene, and (D) butane in ZIF-8: ■ 253 K; ● 273 K; ▲ 293 K; ◆ 313 K; ▼ 333 K.

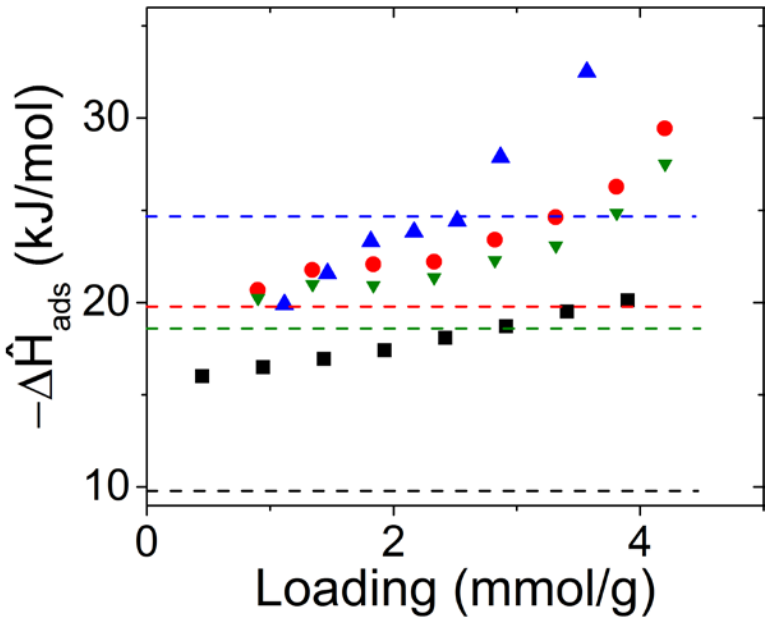

Figure 3.10 Isosteric heats of adsorption in ZIF-8 for ■ ethane, ● propane, ▼ propylene, and ▲ butane. Dotted lines represent the heats of vaporization of the pure components

Surprisingly, adsorption behavior in ZIF-11 is very similar to that of ZIF-8, and molecules are largely able to enter the structure despite the smaller pore aperture. All hydrocarbon species studied display a Langmuir isotherm with almost complete saturation at the lowest experimentally accessible saturations. **Figure 3.11** summarizes the uptake of measured hydrocarbons at 35 °C, where all gas species display an observable Langmuir isotherm, while all vapor species are almost immediately saturated at the lowest accessible humidities. Out of the measured components, no significant sorption selectivity arises within the olefin/paraffin pair or with increasing carbon number in the vapors, although toluene demonstrated the greatest uptake, likely from both packing and favorable aromatic-aromatic interactions with the benzimidazole linkers. Some small entropic packing contribution to sorption has been previously reported in ZIF-8,[31] where branched alkanes demonstrated greater saturation capacity than linear alkanes.

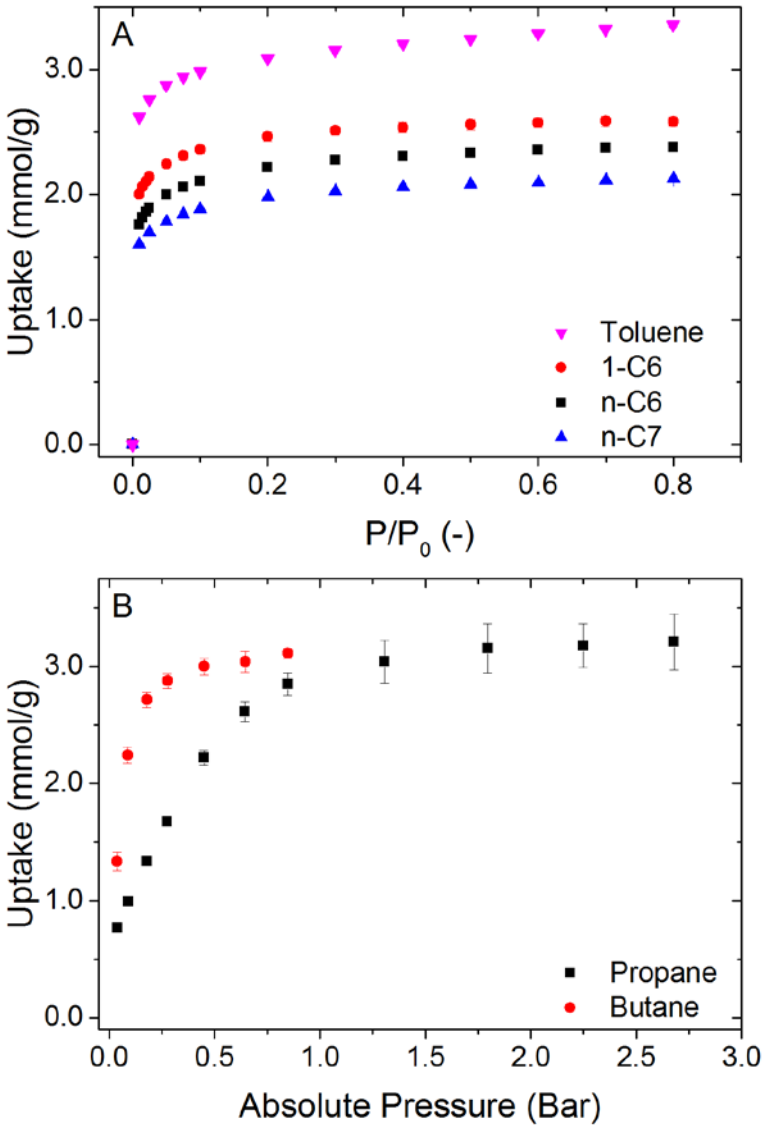

Figure 3.11 Vapor (A) and gas (B) hydrocarbon isotherms in ZIF-11 at 35 °C. Error bars represent the standard error of triplicates.

During isotherm measurements, rising equilibration times with increasing carbon number vapors indicate slower diffusivities, and this necessitated smaller crystal sizes to maintain experimental measurements within reasonable time scales. Molecules larger than toluene were deemed too slow diffusing to be of any practical application at this temperature and therefore not measured.

3.2.2.2 Single Component Diffusivity

The diffusivities of propane and butane in ZIF-8 were measured using 1.5 μm crystals that exhibited good morphological properties and measurable diffusive time scales. The ZIF-8 samples denoted with 145 μm exhibited excellent Fickian-type uptake behavior of the NGL molecules but were not used in these experiments because of significant irregularities in their crystal geometries, which would confound reliable estimation of the diffusion coefficients. Kinetic uptake curves of propane and butane at 293 K (**Figure 3.12**) exhibit linear behavior against $t^{1/2}$ in the short time, indicating no significant external mass-transfer resistances. Thermodynamically corrected diffusivity decreases with increasing carbon number (**Table 3.4**), but both propane and butane remain permeable despite kinetic diameters beyond the crystallographic 3.4 Å pore aperture, as is widely reported in the literature. Uptake of ethane and propylene was measured using the volumetric technique, but the uptake rates were deemed too rapid for the accurate estimation of the diffusion coefficients of these light gases in ZIF-8. The diffusion coefficients of propane and butane match reasonably well with previously published data,[1] while the activation energies differ slightly from the expected values based on other work.[31]

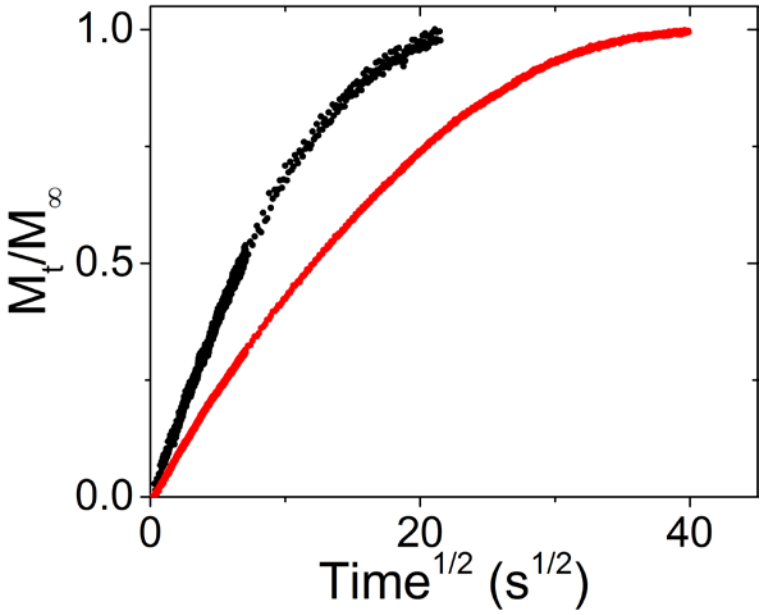

Figure 3.12 Normalized pressure decay curves for the diffusion of propane (black) and butane (red) in R = 1.5 μm ZIF-8 crystals at 293 K indicating no external mass-transfer resistances

Table 3.4. Thermodynamically Corrected Diffusivities and Activation Energies of Diffusion at Near-Zero Occupancy in ZIF-8 at 293 K

	Đ (cm^2/s)	E_D (kJ/mol)
Ethane[a]	1.6 x 10^{-8}	16
Propylene[a]	1.4 x 10^{-9}	22
Propane[b]	1.5 x 10^{-11}	34
Butane[b]	2.4 x 10^{-12}	33

[a] From Verploegh et al.[18] [b] Measured in this work via pressure decay experiments.

Linear hydrocarbons at 35 °C (**Figure 3.13)** show decreasing diffusivity with increasing carbon number, spanning approximately four orders of magnitude in diffusion coefficients from propane to n-heptane. Only the first few points in our gas isotherms (propane and butane) demonstrated enough uptake to confidently fit to an analytical solution, and exhibit little loading-dependence on diffusivity over the range observed. However, larger hydrocarbon vapor systems saturated at very low activities, and therefore

most points aggregate at $\theta > 0.7$. Their diffusivities increase substantially approaching saturation, a trend also seen in light hydrocarbon diffusion in ZIF-8.[40] Overall, these results are qualitatively in agreement with loading-dependent diffusion trends in ZIF-8. However, the diffusivities of propane and butane in ZIF-11 are faster than that of ZIF-8,[1, 42] which is surprising, given ZIF-11's smaller pore aperture and the bulkiness of benzimidazole ligands relative to 2-methylimidazole.

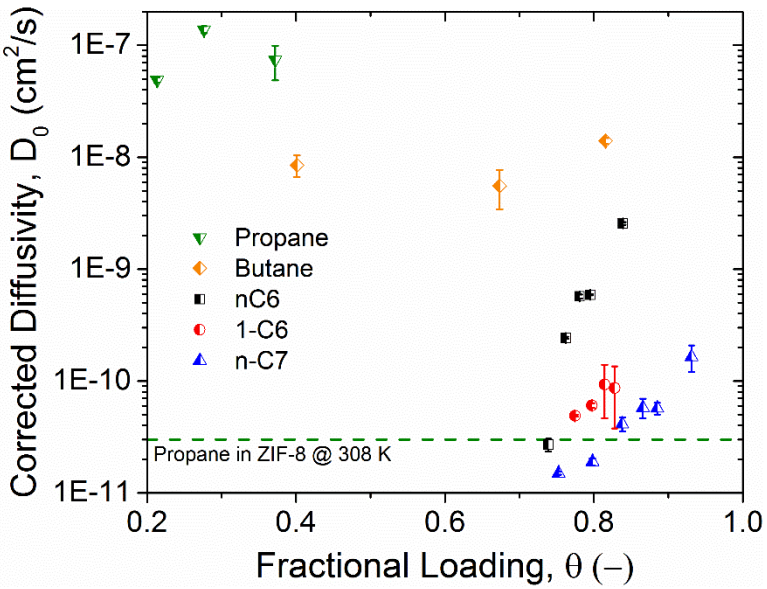

Figure 3.13 Diffusion of hydrocarbons in ZIF-11 at 35 °C as a function of loading. Error bars represent the standard error of triplicates. Dashed line data represents data measured at infinite dilution.[42]

Interestingly, the alcohols in this study, despite having kinetic diameters larger than equivalent hydrocarbons, show significantly slower diffusion through the ZIF-11 crystal. This is similarly reported in ZIF-8, where methanol diffusion is slower than ethane, despite being 0.8 Å smaller in kinetic diameter.[40] This has been attributed to clustering within the framework caused by hydrogen bonding, which introduces sorbate-sorbate interactions within the micropores and retards diffusive jumps form one cage into another.[40, 43] However, the comparison that needs to be made here is that in alcohols, diffusion through

ZIF-8 is faster than it is in ZIF-11, while hydrocarbons demonstrate the opposite behavior by a significant margin. It is possible that the flexibility of the ZIF-11 system is somehow greater than that of ZIF-8, resulting in faster hydrocarbon diffusion, but the increased surface hydrophobicity leads to increased hindering and clustering effects which more significantly retard the diffusion of alcohols, hence the reversal in behavior.

3.2.3 The Role of Linker Flexibility in Microporous Diffusion

The need to account for structural flexibility in prediction of diffusive measurement is now well documented in literature and was discussed previously in Chapter 2. However, there still exists the question of how different structures may exhibit that flexibility, and what the combined effects of topology, linker size, and temperature are on overall diffusion rates.

3.2.3.1 Flexibility as a Function of Structure

It is reasonable to assume that not all MOF structures experience ligand flexibility in the same way or to the same degree. Indeed, we hypothesize that the differences in structural flexibility between ZIF-8 and ZIF-11 can largely explain the non-obvious diffusion comparisons reported in this chapter. Although reports exist in which the linker position is measured as a function of sorbate loading,[44] and computational work has been able to predict a time-dependent distribution of window sizes,[17-18] no work has been able to directly measure the dynamic flexibility of ZIF linkers until recently.[45]

With the use of deuterium-enriched imidazolate linkers and ^{2}H solid echo NMR techniques, Zhou et al. could measure the amplitude of linker motion along the zinc-

nitrogen axis via analysis of the Pake doublet splitting.[46] This motion was quantified as a function of temperature for ZIF-7, -8, and -11.

Containing the same benzimidazole linker, both ZIF-7 and ZIF-11 exhibit somewhat similar ligand jump angles at 300 K in **Figure 3.14**, although ZIF-11 is measured to be a more flexible ligand. The amplitude of the linker motion is likely dominated by a thermal energy term, related to the moment of inertia of the ligand, and somewhat affected by the electrostatic environment of the topology.

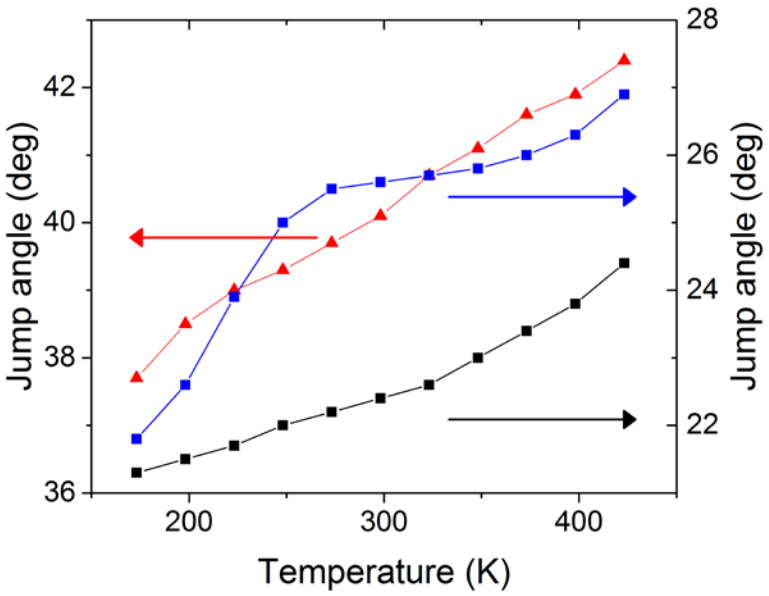

Figure 3.14 Ligand jump angles of ZIF-11 (blue), ZIF-7 (black), and ZIF-8 (red). Data reproduced with permission, Copyright Er-Kang Zhou 2017.[45]

ZIF-7, with a window size of 2.4 Å, generally has no gas uptake until a species-dependent threshold pressure that induces a gate-opening event, slightly changing the topology of the system and allowing molecules to diffuse into the structure. However, ZIF-11 exhibits diffusion of molecules much larger than its 3.2 Å window without any observable structural transition. We hypothesize that this difference in relative accessibility instead comes from the topology of the system, where ZIF-11 (RHO) possesses 8-MR

apertures, and ZIF-7 (SOD) only has 6-MR. By having more "moving parts" with approximately the same degree of flexibility, the overall aperture itself becomes more accessible and permeable, both in the sense of being able to achieve larger pore apertures and being more easily deformed when a molecule passes through it.

The analysis of ZIF-8 linker motions provides an interesting comparison, as the jump angles are calculated to be almost double that of the benzimidazole topologies. This supports our hypothesis that jump angles are largely determined by the moment of inertia of the rotating species, as the 2-methylimidazole of ZIF-8 is a much smaller molecule. Steric effects of the topology must still play a relatively smaller role, as the angle of ZIF-7 and -11 only differ by a few degrees. The extended rotational motion of ZIF-8 is what allows it to adsorb such large molecules into its structure (unlike ZIF-7 which excludes molecules of its crystallographic pore size) but we recall that ZIF-11 still demonstrated faster diffusion behavior for hydrocarbon species. Furthermore, we note that the diffusive selectivity of next carbon number species in ZIF-8 is greater than that seen in ZIF-11. This should only be the case if the overall aperture of ZIF-11 is a more flexible one, as it weakens the molecular sieving effect of the restrictive pore windows. We therefore hypothesize that the additional flexibility offered by the larger ring number of ZIF-11 is more important than the greater individual linker flexibility and larger average pore size of ZIF-8.

Looking at **Figure 3.15**, where the activation energies of diffusion for propane and butane are plotted for both ZIF-8 and ZIF-11, we see that ZIF-11 exhibits a significantly lower activation energy of diffusion than ZIF-8. Combined with other pieces of information presented in this chapter such as faster diffusion and overall poorer sieving qualities, it

seems extremely likely that the ZIF-11 8-MR aperture is indeed a less restrictive diffusive jump than that of the 6-MR in ZIF-8.

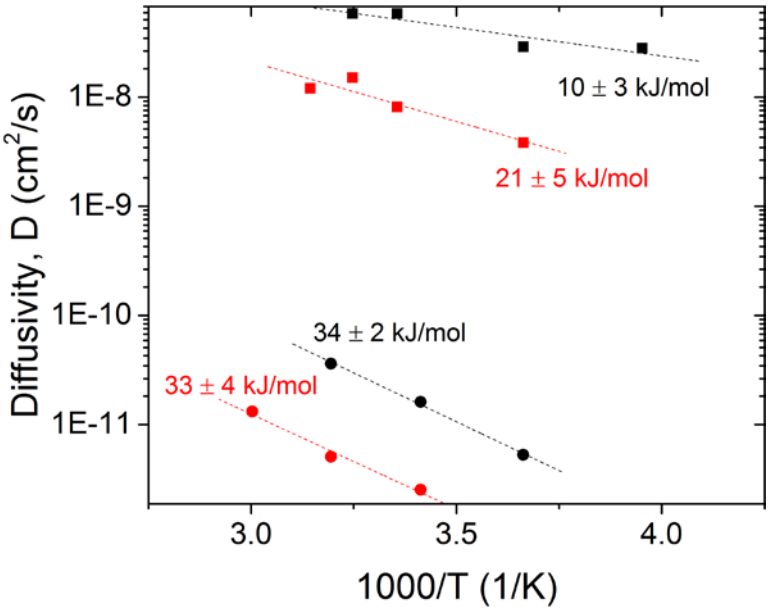

Figure 3.15 Arrhenius plot comparing the activation energies of diffusion of propane (black) and butane (red) in ZIF-8 (●) and -11 (■)

This question can be further elucidated by flexible MD simulations of the structure window sizes. **Figure 3.16** shows the estimated window size distribution without guest molecules for both ZIF-8 and ZIF-11, demonstrating that although ZIF-8 does have a larger average window size, ZIF-11 shows a greater width in the window distribution, indicating, as we hypothesized, that an 8-MR leads to increased aperture flexibility, despite lower individual linker rotation amplitudes.

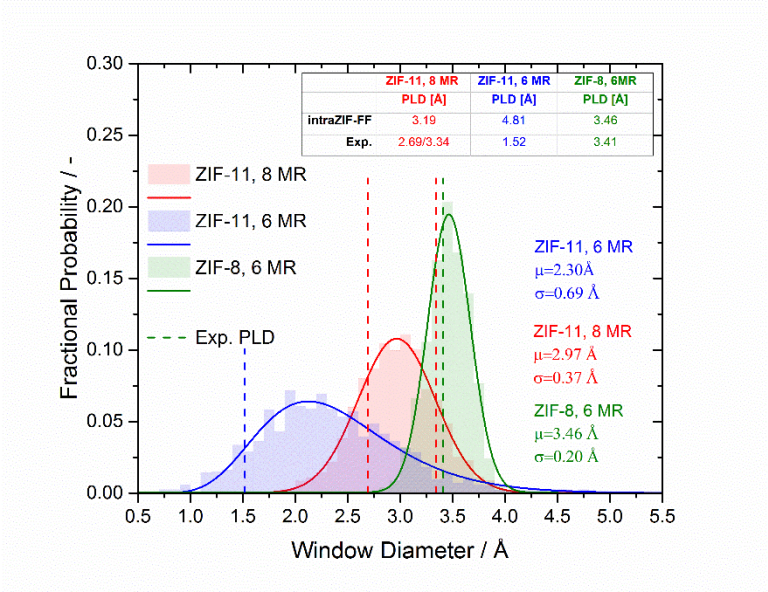

Figure 3.16 Window size distributions of the empty ZIF-8 and ZIF-11 frameworks as predicted by MD simulations

3.2.3.2 Flexibility as a Function of Temperature

We hypothesize that the diffusive limitations of N_2 in ZIF-11 at 77 K stems from a temperature-dependent flexibility of the ligands at the pore opening. We hypothesize that as the rotation of the linkers is limited at lower thermal energies, the pores of the ZIF subsequently "rigidify", and are brought closer to their estimated 3.2 Å dimension. If this hypothesis were true, the decreased flexibility of the pore aperture with decreasing temperature would likely present itself as an increasing activation energy as the sorbate becomes more rigidly constrained within the pore aperture.

We explored this hypothesis by measuring the diffusion of CH_4 in ZIF-11 at various temperatures above 77 K and calculated the activation energy of diffusion. Methane is easily observed to enter the structure only a few tens of degrees above 77 K. **Figure 3.17** plots the fitted thermodynamically corrected diffusivity values at low temperatures along with self-diffusivity at 296 K by PFG NMR from published literature.[47] These forms of

diffusion are not exactly equivalent and direct comparison must be done cautiously. The fit over the measured range yields activation energies of 21 kJ/mol of CH_4, and a slight curvature may suggest a non-constant activation energy, although our data could be reasonably fit by an Arrhenius-type equation. However, it is clear that typical extrapolation of the low temperature data to ambient conditions measured by PFG NMR results in diffusivities almost two orders of magnitude too fast (5.1×10^{-5} cm^2/s).[47] Were the diffusion limitation simply a case of activation energies, we would expect the extrapolation to fall relatively close to measured room temperature values. It is experimentally difficult to measure diffusion of these molecules in the intermediate temperatures, as diffusion becomes too fast to measure by pressure decay methods, and such temperature control in PFG NMR experiments is quite challenging. It could be possible then, that the activation energy of diffusion changes gradually with temperature, or at some specific temperature, rather than exhibit a constant value, and this only is clearly observed over large temperature ranges.

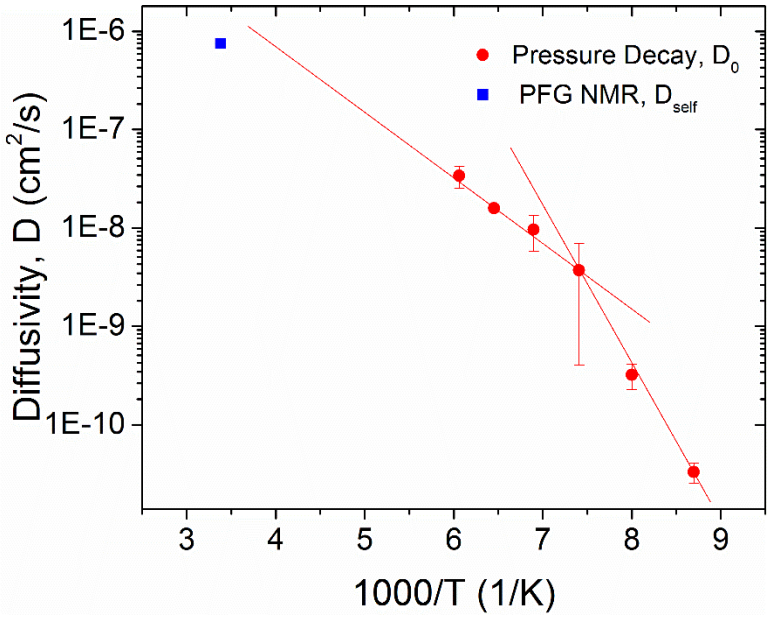

Figure 3.17 Diffusivity of CH_4 in 22 μm ZIF-11 crystals as a function of temperature demonstrating a non-constant activation energy over the temperature range; lines are meant to guide the eye and not indicative of any regression fit. Error bars are the standard error of triplicate runs. PFG NMR data reproduced from published work.[47]

Systems demonstrating a sharp transition in activation energy of diffusion with temperature are not typical in microporous solids but are well known in the polymer literature. Studies of light gases diffusing through polyvinyl acetate near its glass transition temperature demonstrate three different slopes as a function of temperature for all gases.[48] The temperature at which these slope change correlate to the glass transition temperature and another point a few degrees below, presumed to be a related bulk transition. The behavior seemed unaffected by the size of the gas penetrant. Diffusion through ZIFs and other flexible MOFs may then more closely resemble transport through glassy polymers under certain circumstances. The similarities in the diffusion mechanisms of the two materials, the need for the gas penetrant to distort the polymer chains or the aperture ligands, may be the root of this potential similarity.

3.3 Conclusions

This chapter explores the adsorptive behavior of alcohols and hydrocarbon vapors in ZIF-11, and compares their diffusive behavior to that of the more commonly studied ZIF-8 structure. Like ZIF-8, ZIF-11 admits molecules with kinetic diameters well beyond its crystallographic aperture of 3.2 Å, exhibiting diffusionally selective behavior with increasing sorbent size. However, this size-dependent selectivity is less pronounced than that in ZIF-8, suggesting that the pore windows are more flexible, despite their smaller size. Alcohols in ZIF-11 demonstrate inherently slower diffusion due to sorbate clustering not observed in hydrocarbon vapors, and differences in relative alcohol diffusion between the two ZIF structures likely stems from the differences in structural hydrophobicity as well.

The degree of linker flexibility is shown to be temperature dependent using ^{2}H solid echo NMR. This demonstrates how the linkers flex over wider jump angles at higher temperatures, how that angle is dependent on the mass of the linker, and how the topology in which that linker is found may play a pivotal role in the diffusive properties of the structure (i.e., greater ring member number makes more porous apertures). Furthermore, kinetic uptake of methane over wide temperature ranges suggest a non-Arrhenius temperature dependence, further emphasising the role of linker flexibility in diffusion through flexible materials.

In this way, we not only reiterate that material flexibility is a critical component of diffusive selectivity in MOFs, but that this flexibility can be highly dependent on temperature, topology, and linker identity.

3.4 References

1. Zhang, C.; Lively, R. P.; Zhang, K.; Johnson, J. R.; Karvan, O.; Koros, W. J., Unexpected Molecular Sieving Properties of Zeolitic Imidazolate Framework-8. *J. Phys. Chem. Lett.* **2012,** *3* (16), 2130-2134.

2. Zhang, C.; Gee, J. A.; Sholl, D. S.; Lively, R. P., Crystal-Size-Dependent Structural Transitions in Nanoporous Crystals: Adsorption-Induced Transitions in ZIF-8. *J. Phys. Chem. C* **2014,** *118* (35), 20727-20733.

3. Walton, K. S.; Snurr, R. Q., Applicability of the BET method for determining surface areas of microporous metal-organic frameworks. *J. Am. Chem. Soc.* **2007,** *129*, 8552-6.

4. Hu, H.; Liu, S.; Chen, C.; Wang, J.; Zou, Y.; Lin, L.; Yao, S., Two novel zeolitic imidazolate frameworks (ZIFs) as sorbents for solid-phase extraction (SPE) of polycyclic aromatic hydrocarbons (PAHs) in environmental water samples. *Analyst* **2014,** *139* (22), 5818-5826.

5. Morris, W.; He, N.; Ray, K. G.; Klonowski, P.; Furukawa, H.; Daniels, I. N.; Houndonougbo, Y. A.; Asta, M.; Yaghi, O. M.; Laird, B. B., A Combined Experimental-Computational Study on the Effect of Topology on Carbon Dioxide Adsorption in Zeolitic Imidazolate Frameworks. *J. Phys. Chem. C* **2012,** *116* (45), 24084-24090.

6. Reif, B.; Fabisch, F.; Hovestadt, M.; Hartmann, M.; Schwieger, W., Synthesis of ZIF-11 - Effect of water residues in the solvent onto the phase transition from ZIF-11 to ZIF-7-III. *Microporous Mesoporous Mater.* **2017,** *243*, 65-68.

7. He, M.; Yao, J.; Liu, Q.; Zhong, Z.; Wang, H., Toluene-assisted synthesis of RHO-type zeolitic imidazolate frameworks: synthesis and formation mechanism of ZIF-11 and ZIF-12. *Dalton Transactions* **2013,** *42* (47), 16608-16613.

8. Sanchez-Lainez, J.; Zornoza, B.; Mayoral, A.; Berenguer-Murcia, A.; Cazorla-Amoros, D.; Tellez, C.; Coronas, J., Beyond the H2/CO2 upper bound: one-step crystallization and separation of nano-sized ZIF-11 by centrifugation and its application in mixed matrix membranes. *Journal of Materials Chemistry A* **2015,** *3* (12), 6549-6556.

9. Ruthven, D. M.; Lee, L.-K., Kinetics of nonisothermal sorption: Systems with bed diffusion control. *AlChE J.* **1981,** *27* (4), 654-663.

10. Kärger, J. R., Douglas M; Theodorou, Doros N, *Diffusion in Nanoporous Materials*. Wiley-VCH: Weinheim, Germany, 2012; Vol. 1, p 513.

11. Crank, J., *The Mathematics of Diffusion*. 2nd ed.; Oxford University Press: Oxford, 1975.

12. Brandani, S., Analysis of the piezometric method for the study of diffusion in microporous solids: Isothermal case. *Adsorption* **1998,** *4* (1), 17-24.

13. Park, K. S.; Ni, Z.; Côté, A. P.; Choi, J. Y.; Huang, R.; Uribe-Romo, F. J.; Chae, H. K.; O'Keeffe, M.; Yaghi, O. M., Exceptional chemical and thermal stability of zeolitic imidazolate frameworks. *Proc Natl Acad Sci U S A* **2006,** *103* (27), 10186-10191.

14. Groom, C. R.; Bruno, I. J.; Lightfoot, M. P.; Ward, S. C., The Cambridge structural database. *Acta Crystallogr., Sect. B: Struct. Crystallogr. Cryst. Chem.* **2016,** *72* (2), 171-179.

15. Verploegh, R. J.; Kulkarni, A.; Boulfelfel, S. E.; Haydak, J. C.; Tang, D.; Sholl, D. S., Screening Diffusion of Small Molecules in Flexible Zeolitic Imidazolate Frameworks using a DFT Parameterized Force Field. *Submitted.* **2018**.

16. Plimpton, S., FAST PARALLEL ALGORITHMS FOR SHORT-RANGE MOLECULAR-DYNAMICS. *J. Comput. Phys.* **1995,** *117* (1), 1-19.

17. Haldoupis, E.; Watanabe, T.; Nair, S.; Sholl, D. S., Quantifying Large Effects of Framework Flexibility on Diffusion in MOFs: CH4 and CO2 in ZIF-8. *Chemphyschem* **2012,** *13* (15), 3449-3452.

18. Verploegh, R. J.; Nair, S.; Sholl, D. S., Temperature and Loading-Dependent Diffusion of Light Hydrocarbons in ZIF-8 as Predicted Through Fully Flexible Molecular Simulations. *J. Am. Chem. Soc.* **2015,** *137* (50), 15760-15771.

19. Liu, X.; Jin, H.; Li, Y.; Bux, H.; Hu, Z.; Ban, Y.; Yang, W., Metal-organic framework ZIF-8 nanocomposite membrane for efficient recovery of furfural via pervaporation and vapor permeation. *J. Membr. Sci.* **2012,** *428*, 498-506.

20. Bai, Y.; Dong, L.; Zhang, C.; Gu, J.; Sun, Y.; Zhang, L.; Chen, H., ZIF-8 Filled Polydimethylsiloxane Membranes for Pervaporative Separation of n-Butanol from Aqueous Solution. *Sep. Sci. Technol.* **2013,** *48* (17), 2531-2539.

21. Fan, H.; Shi, Q.; Yan, H.; Ji, S.; Dong, J.; Zhang, G., Simultaneous Spray Self-Assembly of Highly Loaded ZIF-8-PDMS Nanohybrid Membranes Exhibiting Exceptionally High Biobutanol-Permselective Pervaporation. *Angewandte Chemie (International ed. in English)* **2014,** *53* (22), 5578-82.

22. Hua, D.; Ong, Y. K.; Wang, Y.; Yang, T.; Chung, T.-S., ZIF-90/1384 mixed matrix membranes for pervaporation dehydration of isopropanol. *J. Membr. Sci.* **2014,** *453*, 155-167.

23. Hua, D.; Ong, Y. K.; Wang, Y.; Yang, T.; Chung, T.-S., ZIF-90/P84 mixed matrix membranes for pervaporation dehydration of isopropanol. *J. Membr. Sci.* **2014,** *453*, 155-167.

24. Liu, S.; Liu, G.; Zhao, X.; Jin, W., Hydrophobic-ZIF-71 filled PEBA mixed matrix membranes for recovery of biobutanol via pervaporation. *J. Membr. Sci.* **2013,** *446*, 181-188.

25. Liu, X.-L.; Li, Y.-S.; Zhu, G.-Q.; Ban, Y.-J.; Xu, L.-Y.; Yang, W.-S., An Organophilic Pervaporation Membrane Derived from Metal-Organic Framework Nanoparticles for Efficient Recovery of Bio-Alcohols. *Angewandte Chemie-International Edition* **2011,** *50* (45), 10636-10639.

26. Shi, G. M.; Chen, H.; Jean, Y. C.; Chung, T. S., Sorption, swelling, and free volume of polybenzimidazole (PBI) and PBI/zeolitic imidazolate framework (ZIF-8) nano-composite membranes for pervaporation. *Polymer* **2013,** *54* (2), 774-783.

27. Shi, G. M.; Yang, T.; Chung, T. S., Polybenzimidazole (PBI)/zeolitic imidazolate frameworks (ZIF-8) mixed matrix membranes for pervaporation dehydration of alcohols. *J. Membr. Sci.* **2012,** *415*, 577-586.

28. Kim, S.; Thiessen, P.; Bolton, E.; Chen, J.; Fu, G.; Gindulyte, A.; Han, L.; He, J.; He, S.; Shoemaker, B.; Wang, J.; Yu, B.; Zhang, J.; Bryant, S., PubChem Substance and Compound databases. Nucleic Acids Res. 2016.

29. Thommes, M.; Kaneko, K.; Neimark, A. V.; Olivier, J. P.; Rodriguez-Reinoso, F.; Rouquerol, J.; Sing, K. S. W., Physisorption of gases, with special reference to the evaluation of surface area and pore size distribution (IUPAC Technical Report). *Pure Appl. Chem.* **2015,** *87* (9-10), 1051-1069.

30. Zhang, K.; Lively, R. P.; Dose, M. E.; Brown, A. J.; Zhang, C.; Chung, J.; Nair, S.; Koros, W. J.; Chance, R. R., Alcohol and water adsorption in zeolitic imidazolate frameworks. *Chem. Commun.* **2013,** *49* (31), 3245-3247.

31. Zhang, K.; Lively, R. P.; Zhang, C.; Chance, R. R.; Koros, W. J.; Sholl, D. S.; Nair, S., Exploring the Framework Hydrophobicity and Flexibility of ZIF-8: From Biofuel Recovery to Hydrocarbon Separations. *J. Phys. Chem. Lett.* **2013,** *4* (21), 3618-3622.

32. Myers, A. L.; Prausnitz, J. M., Thermodynamics of mixed-gas adsorption. *AlChE J.* **1965,** *11* (1), 121-127.

33. Do, D. D., *Adsorption Analysis : Equilibria and Kinetics*. Imperial College Press: London, 1998; p xxi, 892 p.

34. Zhang, K.; Lively, R. P.; Dose, M. E.; Li, L.; Koros, W. J.; Ruthven, D. M.; McCool, B. A.; Chance, R. R., Diffusion of water and ethanol in silicalite crystals synthesized in fluoride media. *Microporous Mesoporous Mater.* **2013,** *170*, 259-265.

35. Zhang, K.; Lively, R. P.; Zhang, C.; Koros, W. J.; Chance, R. R., Investigating the Intrinsic Ethanol/Water Separation Capability of ZIF-8: An Adsorption and Diffusion Study. *J. Phys. Chem. C* **2013,** *117* (14), 7214-7225.

36. Peralta, D.; Chaplais, G.; Paillaud, J.-L.; Simon-Masseron, A.; Barthelet, K.; Pirngruberb, G. D., The separation of xylene isomers by ZIF-8: A demonstration of the extraordinary flexibility of the ZIF-8 framework. *Microporous Mesoporous Mater.* **2013,** *173*, 1-5.

37. Peralta, D.; Chaplais, G.; Simon-Masseron, A.; Barthelet, K.; Pirngruber, G. D., Separation of C-6 Paraffins Using Zeolitic Imidazolate Frameworks: Comparison with Zeolite 5A. *Ind. Eng. Chem. Res.* **2012,** *51* (12), 4692-4702.

38. Ferreira, A. F. P.; Mittelmeijer-Hazeleger, M. C.; Granato, M. A.; Martins, V. F. D.; Rodrigues, A. E.; Rothenberg, G., Sieving di-branched from mono-branched and linear alkanes using ZIF-8: experimental proof and theoretical explanation. *PCCP* **2013,** *15* (22), 8795-8804.

39. First, E. L.; Floudas, C. A., MOFomics: Computational pore characterization of metal–organic frameworks. *Microporous Mesoporous Mater.* **2013,** *165*, 32-39.

40. Chmelik, C., Characteristic features of molecular transport in MOF ZIF-8 as revealed by IR microimaging. *Microporous Mesoporous Mater.* **2015,** *216*, 138-145.

41. Ruthven, D. M.; Loughlin, K. F., Sorption of light paraffins in type-A zeolites. Analysis and interpretation of equilibrium isotherms. *J. Chem. Soc. Farad. T. 1* **1972,** *68* (0), 696-708.

42. Pimentel, B. R.; Lively, R. P., Enabling kinetic light hydrocarbon separation via crystal size engineering of ZIF-8. *Ind. Eng. Chem. Res.* **2016,** *55* (48), 12467-12476.

43. Krishna, R.; van Baten, J. M., Hydrogen Bonding Effects in Adsorption of Water−Alcohol Mixtures in Zeolites and the Consequences for the Characteristics of the Maxwell−Stefan Diffusivities. *Langmuir* **2010,** *26* (13), 10854-10867.

44. Zhao, P.; Lampronti, G. I.; Lloyd, G. O.; Suard, E.; Redfern, S. A. T., Direct visualisation of carbon dioxide adsorption in gate-opening zeolitic imidazolate framework ZIF-7. *Journal of Materials Chemistry A* **2014,** *2* (3), 620-623.

45. Zhou, E.-K. Mobility of the Imidazolate Linkers in Neat and Confined ZIFSs Probed by 2H NMR. Georgia Institute of Technology, Atlanta, 2017.

46. Schmidt-Rohr, K.; Spiess, H. W., *Multidimensional solid-state NMR and polymers*. Academic Press: 1994.

47. Forman, E. M.; Pimentel, B. R.; Ziegler, K. J.; Lively, R. P.; Vasenkov, S., Microscopic diffusion of pure and mixed methane and carbon dioxide in ZIF-11 by high field diffusion NMR. *Microporous Mesoporous Mater.* **2017,** *248*, 158-163.

48. Meares, P., The Diffusion of Gases Through Polyvinyl Acetate1. *J. Am. Chem. Soc.* **1954,** *76* (13), 3415-3422.

CHAPTER 4. DIFFUSIVE TIME SCALE AS A DESIGN PARAMETER IN KINETIC SEPARATIONS

This chapter describes the first steps toward a lower-energy, kinetic pressure-swing-adsorption cycle for the separation of ethane, propane, propylene, and butane using ZIF-8 as a diffusionally-selective adsorbent. Crystal engineering techniques were employed to control the diffusive time scale of the separation, allowing for multiple separations using the same adsorbent within reasonable process times. Equimolar separation of ethane/propane mixtures at 293 K exhibited separation factors of 2.7 in the gas phase under non-optimized conditions, which enhances the concentration of the feed mixture to 75 mol % propane. The separation performance was shown to improve to 3.8 at lower temperatures (81 mol % propane), which is attributed to differences in the activation energy of permeation of the two components. Propane/butane mixtures demonstrated a lower diffusive selectivity and almost negligible enhancement, while propylene/propane showed enhancement beyond ethane/propane due to a strong diffusive selectivity combined with sorption selectivities closer to unity. Single-component adsorption and diffusion results were incorporated into a computational model of the system and shown to be in relatively good agreement with the experimental values. The model was used to predict the separation system performance and recovery at various temperatures. This concept was further extended to dynamic breakthrough experiments, where changing the crystal dimension demonstrated the transition from kinetic to equilibrium breakthrough control. Portions of this chapter have been reprinted with permission from Pimentel, B. R.; Lively, R. P., Enabling kinetic light hydrocarbon separation via crystal size engineering of

ZIF-8. *Ind. Eng. Chem. Res.* **2016,** *55* (48), 12467-12476. Copyright American Chemical Society 2016.[1]

4.1 Materials and Methods

4.1.1 Batch Adsorption of Multicomponent Mixtures

Kinetic adsorption separation experiments of ethane/propane, propane/butane, and propane/propylene mixtures were carried out in a homemade batch adsorption apparatus. In the unit, the evacuated sample (containing ZIF-8, see Chapter 3) was pressurized from the feed ballast for one second via a manual three-way valve and then isolated for a set equilibration time **(Scheme 4.1**, top). A plot of the theoretical time-dependent adsorption behavior occurring during this initial exposure is shown in **Scheme 4.1** (bottom). At predetermined time points, the sample volume was blown down into a gas chromatograph (GC) at atmospheric pressure and analyzed via a flame ionization detector. Blowdown to the GC was performed via a one second opening of the manual three-way valve toward the GC and then closed, in a fashion similar to the dosing procedure. A real possibility of changes to the headspace composition exists via blowdown due to desorption, but for almost all time points investigated, the time of the desorption is much less (i.e., <10 times) than the allowed equilibration time, so we believe this assumption introduces negligible error. The gas sampling line was flushed with inert prior to each time point to remove traces of old sample gases. All experiments were done in triplicate on new powder samples.

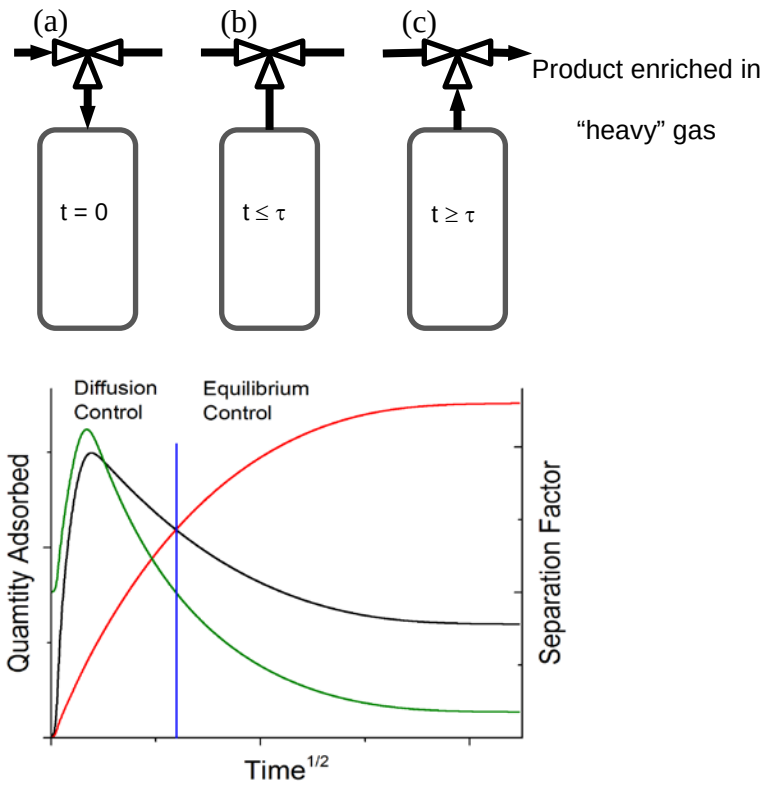

Scheme 4.1 (Top) Three-Step Process Schematic of an Experimental Batch Adsorption Unit with (A) Pressurization, (B) Partial Equilibration, and (C) Headspace Blowdown Steps and (Bottom) Plot of Adsorbed Quantities versus Square Root Time in a Binary Adsorption–Diffusion Process with a Fast/Light Component (Black Line) and a Slow/Heavy Component (Red Line), Where the Blue Line Denotes the Transition from Kinetic to Equilibrium Control and the Separation Factor Plotted on the Right Axis (Green Line)

Samples were evacuated overnight at room temperature before each initial time point after initial postsynthesis activation and for 10 times the previous exposure time before each new time point. Although the same feed ballast was used for all doses in a single run, the ballast pressure averaged 5 ± 0.5 bar over all time points for a given ballast composition. The feed composition was measured at the beginning and end of the sample runs and was found to have no significant variation from the dosing composition.

To illustrate the necessity of crystal size engineering, we began our experimental campaign with the use of 1.5 μm crystals and later demonstrated the need for manipulation

of the crystal dimension by duplicating one of the experiments with 145 μm samples and continuing to utilize these for further studies. It is important to point out that we directly utilized crystal size engineering to create diffusive length scales that permitted experimentation within reasonable time scales. Indeed, this same approach can be easily used to match larger process time scales.

4.1.2 Multicomponent Adsorption Modeling Framework

The multicomponent adsorption and diffusion of gases in ZIF-8 were modeled using *gPROMS Model Builder 4.0.0* to solve the transient partial differential equations associated with the system. The mathematical framework was adapted from that put forth in previously published work[2] from a constant bulk concentration step change to that of a depleting volume system via coupled mass balances between the adsorbed and gas phases. This more accurately captures the time-dependent behavior of our system, especially in the cases of high component depletion, where the driving force in the bulk begins to change dramatically.[3] **Equation (4.1)** describes multicomponent intracrystalline diffusion, **Equation (4.2)** describes a competitive external surface concentration boundary condition, and **Equation (4.3)** provides the mass balance between the gas and adsorbed phases via integration of the crystal concentration profile. **Equation (4.2)** uses a rapid exponential approach ($1 - e^{-10t}$) to minimize temporal discontinuities in the mass balance that could result from a step change in the concentration.

Table 4.1. Set of equations describing the batch adsorption model in this chapter

$$\left.\frac{\partial C_{\mu,i}}{\partial r}\right|_{r=0} = 0 \quad \textbf{(4.1)}$$

$$C_{\mu,i}\big|_{r=R} = \frac{C_{(s,i)} b_i P_i}{1+\Sigma_{j=1}^{n}(b_j P_j)}\left(1 - e^{-10t}\right) \quad \textbf{(4.2)}$$

$$C_{\mu,i}\big|_{0^+}^{R^-} = \frac{C_{s,i} b_i P_i^0}{1+\Sigma_{j=1}^{n}\left(b_j P_j^0\right)} \quad \textbf{(4.3)}$$

$$P_i|_{t=0} = P_{i,d} \quad \textbf{(4.4)}$$

$$\left.\frac{\partial C_{\mu,i}}{\partial t}\right|_{0^+}^{R^-} = \frac{1}{r^2}\frac{\partial}{\partial r}\left[r^2 \sum_{j=1}^{n} D_{\mu,ij}\left(C_\mu\right)\frac{\partial C_{\mu,j}}{\partial r}\right] \quad \textbf{(4.5)}$$

$$D_{\mu,ij} = D_{\mu,i}^0 \frac{C_{\mu,i}}{C_{\mu s,j}\left[1-\Sigma_{k=1}^{n}\left(\frac{C_{\mu,k}}{C_{s,k}}\right)\right]} \quad \textbf{(4.6)}$$

$$D_{\mu,ij} = D_{\mu,i}^0 \left[1 + \frac{C_{\mu,i}}{C_{\mu s,i}\left(1-\Sigma_{k=1}^{n}\frac{C_{\mu,k}}{C_{s,k}}\right)}\right] \quad \textbf{(4.7)}$$

$$n_i = \frac{P_{i,d}\,V}{R_g\,T} - \frac{M}{\frac{4}{3}\pi R^3 \rho}\int_{r=0}^{R} C_{\mu,i} 4\pi \mathrm{r}^2 dr \quad \textbf{(4.8)}$$

$$P_i = \frac{N_i \cdot R_g \cdot T}{V} \quad \textbf{(4.9)}$$

$$Selectivity = \left(\frac{P_1}{P_2}\right) / \left(\frac{P_{2,d}}{P_{1,d}}\right) \quad \textbf{(4.10)}$$

$$Recovery_i = P_i / P_{i,d} \quad \textbf{(4.11)}$$

Langmuir parameters, heats of adsorption, thermodynamically corrected diffusivities, and activation energies of diffusion were extracted from single-component adsorption and diffusion measurements and used to predict mixture diffusion behavior, while values we were unable to measure were taken from previously published work. Model predictions include the gas-phase separation factor and component recovery, as defined by the fraction of dosed moles of component *i* remaining in the sample headspace. The modeling results were compared to experimental data and used to predict behavior under varying temperature and operating conditions.

4.1.3 Packed Bed Breakthrough Experiments

Breakthrough experiments were carried out in a temperature controlled cabinet system built by L&C Science and Technology, connected to a Pfeiffer Omnistar mass spectrometer. Two beds of differing particle size were prepared. The first bed consisted of Basolite nanoparticles pressed into pellets and then ground and sieved to approximately 500 μm size. Approximately 1.7 g of material was packed into the ¼" Swagelok module and held with a glass wool plug on either side. The second bed consisted of 2.1 g of the 145 μm ZIF-8 crystals, without any further modification and again plugged by glass wool on either side. The samples were activated at 110 °C for 8 h prior to initial experiments and for 2 h in between sample runs. The bed was pre-pressurized with nitrogen while feed mixtures consisted of an equimolar ethane/propane stream diluted in helium at 298 K. The system was operated at 5 bar with a total hydrocarbon partial pressure of 0.9 bar. Total flowrate was set to 100 cc STP N_2/min.

4.2 Mixed-Gas Batch Adsorption

Batch adsorption of mixed-gas feeds was employed as the simplest way to demonstrate the applicability of ZIF-8 to kinetic adsorption schemes. The separation factor (not selectivity) was chosen to report the compositional changes, defined for the gas phase as[4]

$$S_F = \left(\frac{y_{1,e}}{y_{2,e}}\right)\left(\frac{y_{2,f}}{y_{1,f}}\right) \tag{4.12}$$

This relates the compositional ratios of the effluent ($y_{i,e}$) and feed ($y_{i,f}$), in which the slower-diffusing component is referred to as y_1, and reduces to traditional selectivity under equimolar feed compositions. The separation factor in a kinetic system should initially increase above unity as the faster component (2) is adsorbed into the crystal, demonstrating diffusive control of the system, which will reach a maximum value at a time (τ_{fast}) that depends on the diffusivity of the faster-diffusing component (2). The separation factor then decreases as the slower component (1) continues to adsorb and displace the faster component (2) that had previously saturated the crystal and is desorbed into the gas phase. An equilibrium value below unity, due to a typically higher affinity toward the slower species (1), is reached at a time scale (τ_{slow}) commensurate with the slower-diffusing component (1). This indicates equilibrium control of the separation, which is typical for most adsorption processes.

4.2.1 Propane/Butane Separation

Kinetic separation of 90/10 propane/butane mixtures was carried out using 1.5 μm crystals. **Figure 4.1** shows the separation factor as a function of the adsorption time in the sample headspace, where a very slight kinetic enhancement of the mixture can be observed. This is likely due to the low diffusive selectivity of propane over butane in ZIF-8, $D_{C3}/D_{C4} \approx 6$ (**Table 3.4**), combined with competitive sorption effects of stronger-adsorbing butane, resulting in an insufficient kinetic selectivity.

From such a low enhancement of the mixture, it is clear that ZIF-8 possesses insufficient diffusive selectivity in propane/butane separations to employ a kinetic separation scheme. Although the ZIF's pore aperture flexibility hinders true molecular sieving, a slightly larger pore may effectively increase the propane diffusivity while maintaining high resistance to butane transport.

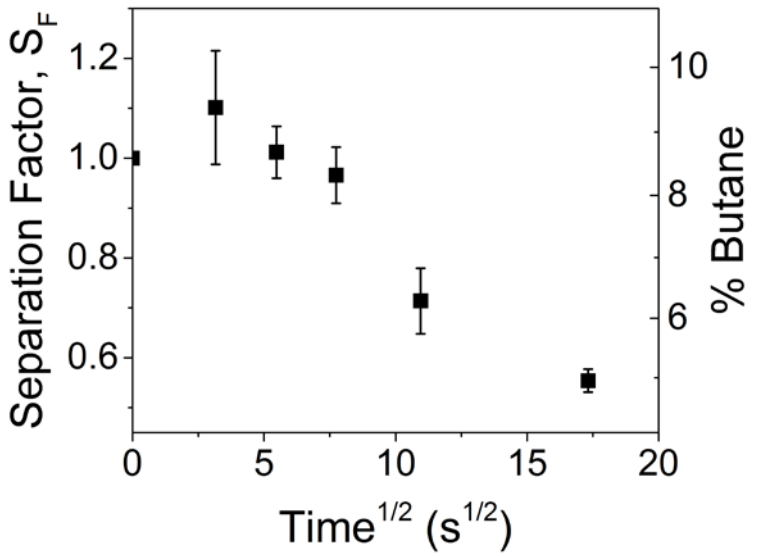

Figure 4.1 Kinetic separation results of 90/10 propane/butane mixtures using 125 mg of 1.5 μm crystals showing almost no kinetic enhancement of butane in the headspace. Error bars represent the standard error of triplicate runs.

4.2.2 Ethane/Propane Separation

Given the inability to separate components with low diffusive selectivities, we elected to investigate a system with poorer competitive sorption behavior but significantly improved selective diffusive behavior. Equimolar separation of ethane and propane was performed using 1.5 μm ZIF-8 crystals (**Figure 4.2**). Despite diffusive selectivity $D_2/D_3 \approx 1000$, the data clearly show a rapid descent toward equilibrium control and no opportunity to capitalize on the expected kinetic enhancement. We believe the failure to demonstrate any kinetic separation in this case came from an inappropriate choice of diffusive time scales rather than the lack of necessary material selectivity. Because kinetic separations are dominated by the rate of sorbate uptake in the system, the time scale of the separation will be controlled by $\tau = R^2/D$. We hypothesize that the equilibration of ethane and propane occurs too rapidly in the 1.5 μm crystals, and therefore the kinetically controlled region of the separation lies below accessible time scales. Crystal size engineering allows for manipulation of this time scale via control over the diffusion length and is a critical parameter in facilitating kinetic separation schemes.

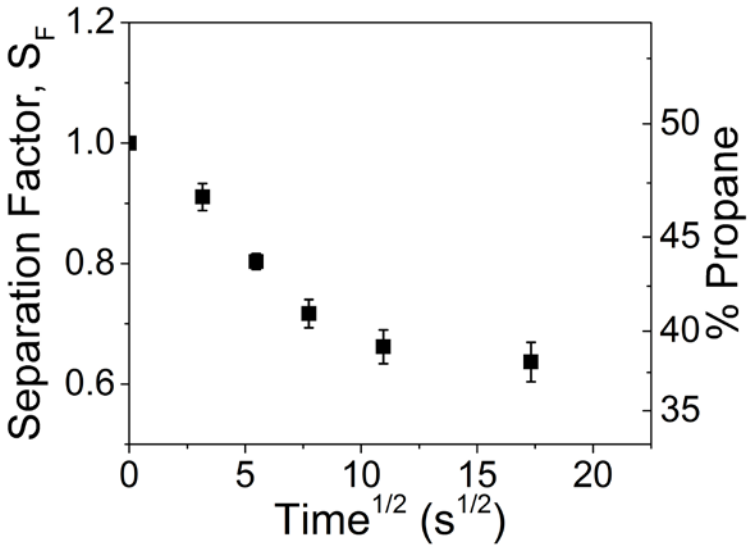

Figure 4.2 Separation of an ethane/propane equimolar mixture using 1.5 μm crystals, showing no opportunity to capitalize on kinetic enhancement of the mixture. Error bars represent the standard error of triplicate runs.

To allow for a slower overall diffusion process and therefore a greater window of time under kinetic control (see **Scheme 4.1**), equimolar separation was repeated using 145 μm ZIF-8 samples. It is expected that the irregular geometry and cracks on these crystals will not impede the kinetic separation process because the material continues to be crystalline ZIF-8 and likely contains domains large enough to demonstrate kinetic enhancement. **Figure 4.3A** plots the experimental behavior of the separation factor of ethane/propane mixtures when a minimal sample mass (125 mg) is used, i.e., under conditions of little change in the bulk driving force due to low overall uptake. Our results demonstrate the expected maximum in the separation factor and a decline in headspace propane enhancement toward equilibrium sorption. This maximum was previously absent in transient adsorption experiments using smaller crystals. The overall separation factor for these experiments is modest because the adsorption capacity-to-dosing volume ratio is too low to significantly alter the headspace composition. Increasing the adsorbent mass in the

system improves the separation factor and is a key design parameter in kinetic PSA processes, as described later.

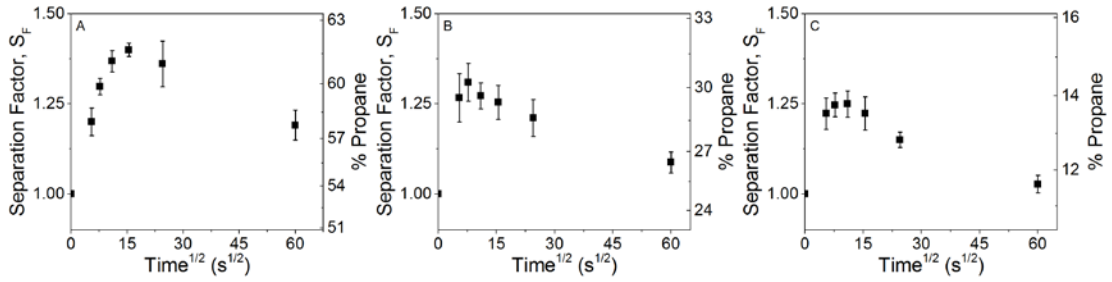

Figure 4.3 Results of various sorption times on the separation of ethane/propane using 125 mg of 145 μm ZIF-8 crystals at 293 K. Nominal feed compositions of (A) 50/50, (B) 75/25, and (C) 90/10. Error bars represent the standard error of triplicate runs.

The use of more ethane-rich feeds (**Figure 4.3B, C**) leads to a more difficult separation as measured by a decrease in the maximum separation factor. A shift of the maximum enhancement to shorter times is also seen to occur. Here, the overall selectivity required to enrich the gas phase of a product-dilute feed is greater than that necessary for an equimolar mixture. Some of this challenge is offset by increased ethane surface occupancy due to higher ethane partial pressures. However, the selectivity of the flux into the crystal monotonically decreases with time due to the initial approach to saturation and subsequent displacement of the faster component, resulting in a more rapid approach to the maximum purity enhancement.

The effect of varying the adsorption capacity-to-dosing volume ratio is demonstrated in **Figure 4.4**, where equimolar ethane/propane experiments were repeated with increasing sample masses in the same sample volume and dosing pressure. Separation factors increase with greater sample mass with a maximum enhancement of propane of 2.7 (75% purity) when using 500 mg of sample, which does not represent the maximum sample

capacity of the cell. A greater sample mass (capacity) adsorbs more ethane from the headspace, which is of a fixed initial dosage and can therefore more drastically change the effluent composition. Continuing to increase the sample mass relative to the headspace volume would be expected to further improve the separation factor while accelerating the equilibrium time of the faster component because of depletion of the bulk driving force, shifting the maxima in the transient response to earlier times.[3] However, because both species are being adsorbed during the kinetic process, recovery of the slower diffusing component necessarily decreases with increasing sample mass. The highest purity achieved by this system would theoretically come from a close-packed bed configuration, where the capacity-to-dosing ratio is highest and approaches ideal selectivities.

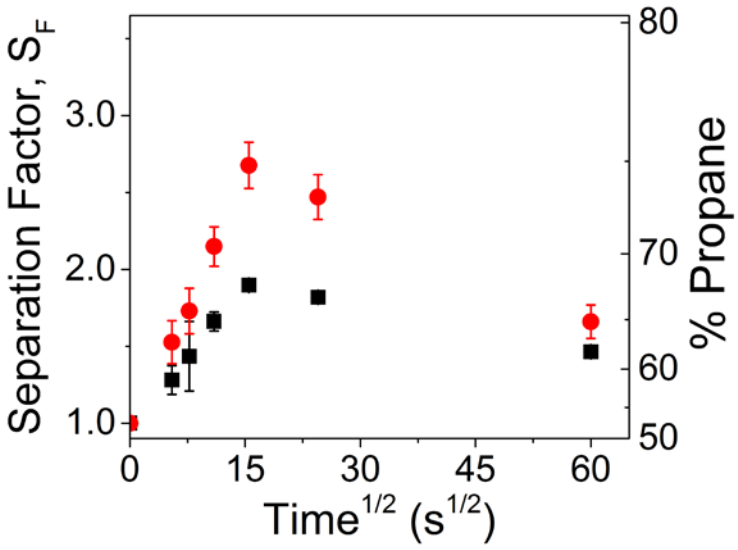

Figure 4.4 Equimolar separation of ethane/propane mixtures at 293 K, demonstrating enhanced separation factors at higher sorbent capacity to-dosing ratios: (black ■) 250 mg; (red ●) 500 mg. Error bars represent the standard error of triplicate runs.

Equimolar separations were replicated using 125 and 500 mg sample sizes at 273 K to investigate the hypothesis that lowering the operation temperature should improve the kinetic selectivity because of the differences in the activation energies of permeation and

heats of sorption (Chapter 3). It can be clearly seen in **Figure 4.5** that the separation factor at 273 K is significantly enhanced compared to the operation at 293 K. This phenomenon is especially useful in the case of light hydrocarbon distillations, where cryogenic distillations are industrially common and streams are already present at subambient temperatures. Indeed, these kinetic adsorption processes can be used to augment (or debottleneck) existing cryogenic distillation systems and are advantageous from a system perspective to operate the adsorption unit at conditions close to that of the distillation column.

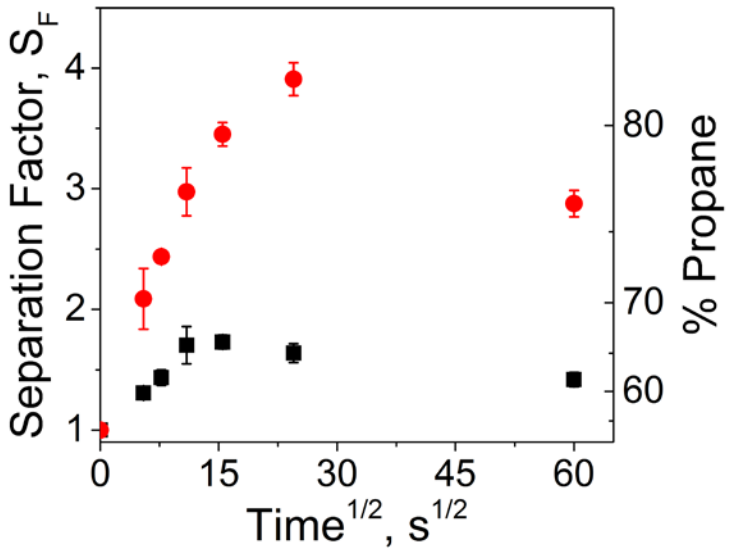

Figure 4.5 Equimolar separation of ethane/propane using 145 μm ZIF-8 crystals at 273 K, demonstrating improved enrichment of propane in the headspace: (black ■) 125 mg; (red ●) 500 mg. Error bars represent the standard error of triplicate runs.

4.2.3 Propane/Propylene Separation

Recognizing the need for high diffusive selectivities but also the effect that a deleterious sorption selectivity can have on a kinetic separation, we looked to propane/propylene kinetic adsorption separations. This olefin/paraffin pair exhibits significant diffusive selectivity ($D_{C3,O}/D_{C3,P} \approx 100$) while benefiting from a sorption

coefficient of essentially 1. Batch adsorption of propane and propylene was conducted using 145 μm crystals to investigate the potential of this separation in a kinetic scheme (**Figure 4.6**). Despite a lowered diffusive selectivity relative to ethane/propane, the maximum system separation factor exceeds that of ethane/propane at identical conditions, demonstrating the key role of sorption in this process.

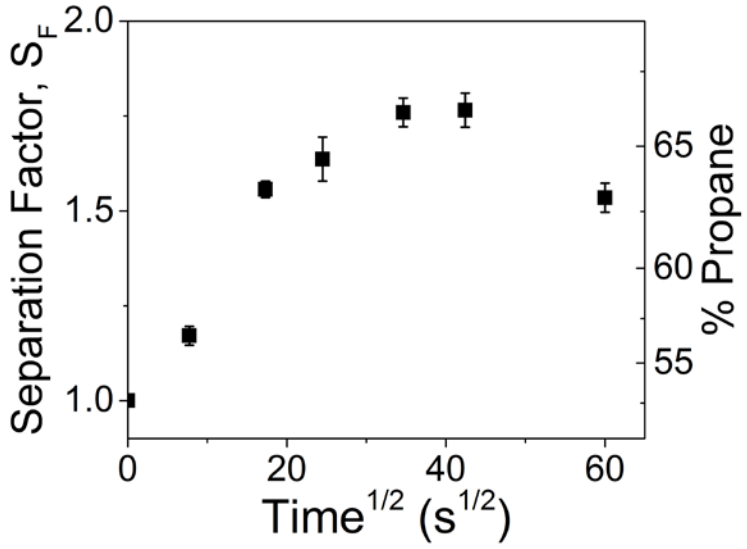

Figure 4.6 Equimolar separation of propylene/propane using 125 mg of 145 μm ZIF-8 crystals, demonstrating an improved separation factor over ethane/propane separation due to a more favorable sorption coefficient ratio. Error bars represent the standard error of triplicate runs.

This also indicates that kinetic adsorption techniques could be uniquely suited for the separation of olefin/paraffin pairs or linear/branched isomers. In these systems, oftentimes the sorption selectivity is near unity, while the diffusive selectivity could remain significant. Furthermore, sorption could be further manipulated in favor of the faster-diffusing olefin by the use of charged species and other traditional techniques to enhance the adsorptive selectivity.[5]

4.3 Kinetic Separation System Modeling

Mathematical modeling of the system was conducted to evaluate the component recovery through the kinetic adsorption process and evaluate the assumptions of intracrystalline resistance control. Because of the irregular shape of the large crystals used in many of the experiments (145 μm synthesis), data from **Figure 4.3** were used to "fit" the dominating crystal dimension in this sample. This yielded an effective diffusion length of 40 μm, which could be reasonably supported from the additional SEM imaging of this crystal population (**Table 3.1**). **Figure 4.7** shows the behavior of our fit against experimental results, demonstrating the characteristic rise and fall of the separation factor in the system. This supports our previous assumptions that our experiments using large crystals were free from confounding external mass-transfer resistances because none are incorporated into our model. The correct prediction of SF maxima indicates the accurate incorporation of Langmuir parameters used to calculate the total sorption from the dosing sample.

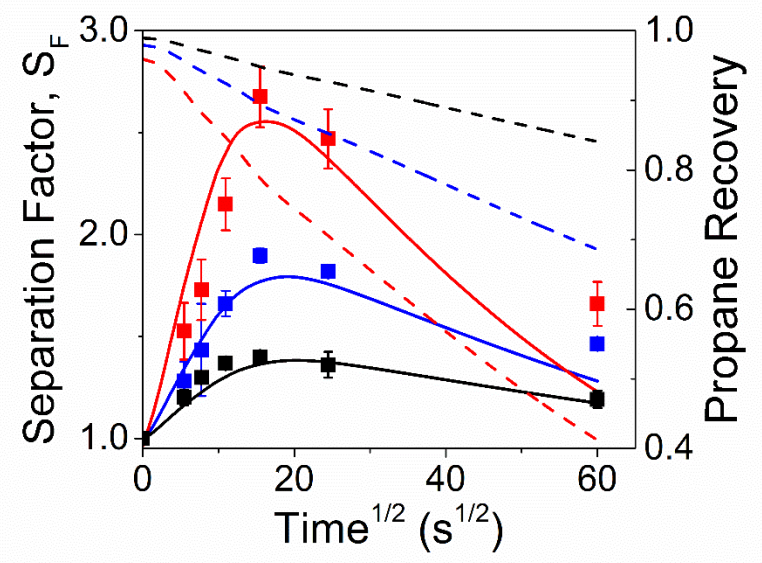

Figure 4.7 Modeling outputs compared to experimental results, showing good agreement in behavioral trends. Crystal diameter was "fit" to 80 μm (i.e., a diffusion length of 40 μm) due to irregularities in the crystal geometries. SF (—) on the left axis and recovery (− −) on the right axis; 125 mg (black); 250 mg (blue); 500 mg (red). Error bars represent the standard error of triplicate runs.

It is important to point out that a maximum in the separation factor of the system is consistent with, but not necessarily experimental evidence for, a transient overshoot in the sorbed ethane concentration. However, our system model does demonstrate a distinct overshoot in the sorbed concentration of ethane as well as non-Fickian concentration profiles indicative of so-called "uphill diffusion" (Section 2.3), as was recently explained by Krishna.[6-7] Modeling outputs of predicted internal concentration profiles are plotted in **Figure 4.8**. In our system, diffusion still occurs "downhill" of the chemical potential gradient, which is the most unambiguous way to describe the driving force. Although the sorbed concentration in this work was not measured directly, experimental evidence of this uphill diffusion behavior exists in the literature for many similar systems and is likely the case here as well.

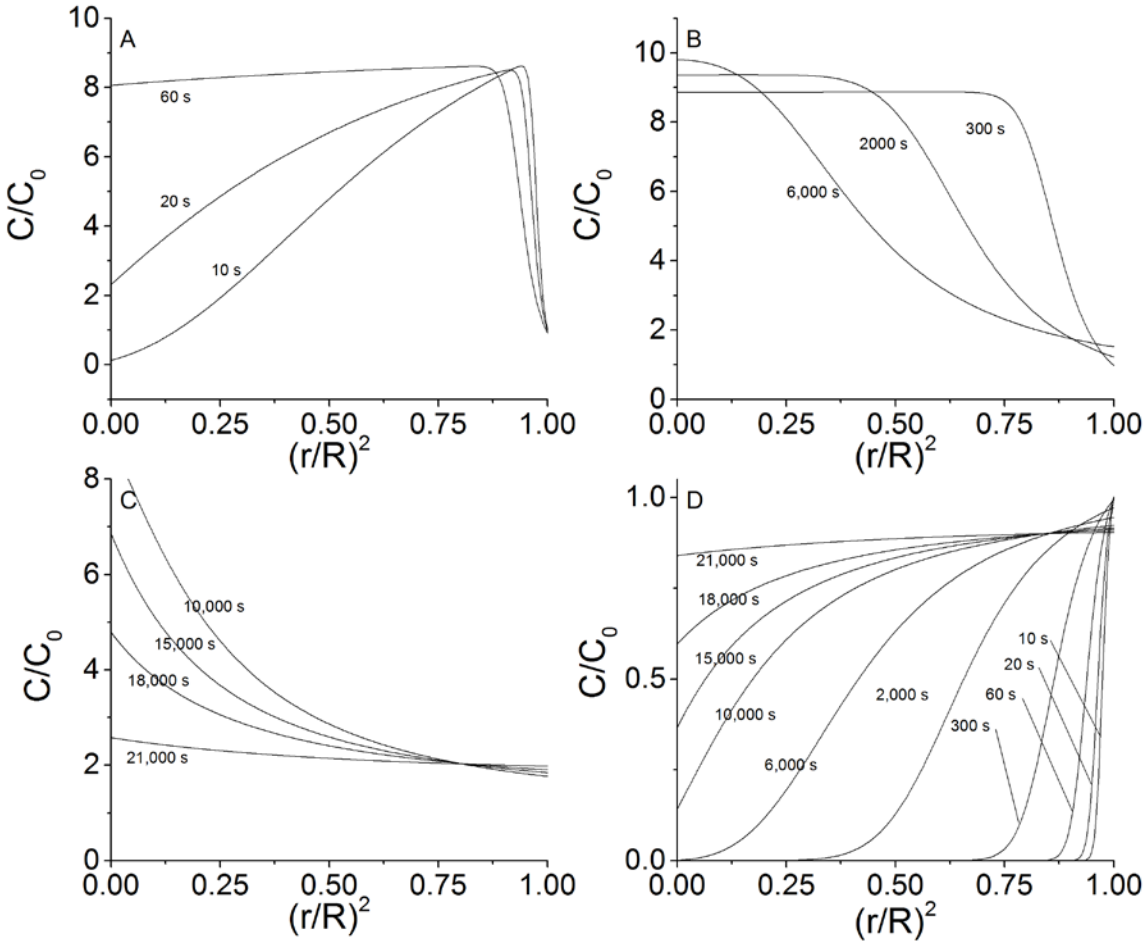

Figure 4.8 Crystal concentration profiles of ethane (A-C) and propane (D) demonstrating the uphill diffusion profile of the light component. Concentrations were normalized to surface concentration at t=0. x-axis is displayed as the square of the normalized radius to better illustrate the concentration profiles near the crystal surface. The drift of the component surface concentration with time is due to depleting concentrations in the head space. T=298 K, R=20 μm.

What is immediately obvious through this model is that a trade-off exists between selectivity and recovery as a function of the sample mass. Slow species recovery is constantly decreasing, and that decrease is made more severe by larger adsorption/ dosing ratios. Therefore, only an increase in the kinetic selectivity is able to yield an increase in both the selectivity and recovery.

Evaluating the activation energy of permeation of ethane and propane, we see that propane yields an Ep ≈ 15 kJ/mol, indicating an increase in the permeation rates at higher temperatures. Ethane, however, yields Ep ≈ 0 kJ/mol, showing little temperature dependence of permeation. This would indicate that the kinetic separation of ethane and propane would be more favorable at lower temperatures, i.e., the kinetic separation unit will more favorably adsorb ethane in short times, thereby generating a purified propane product closer to its original partial pressure in the feed.

We model the change in the system selectivity in an ethane/propane system as a function of the temperature (**Figure 4.9, left**), changing the kinetic selectivity and therefore the recovery of the system. An increase in the kinetic selectivity increases both the separation factor and propane recovery, while increases in the sample mass were shown to increase the separation factor but decrease the recovery. **Figure 4.9 (right)** shows similar modeling outputs for propane/butane separations, which demonstrate little sensitivity to temperature, as previously predicted. The only notable effect of the temperature on the propane/butane results is a more rapid approach toward equilibration at higher temperatures due to increasing diffusivities.

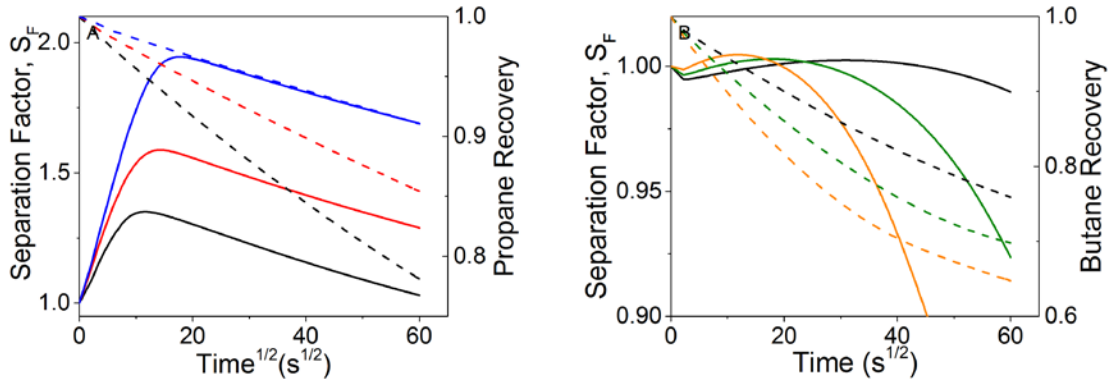

Figure 4.9 Separation factor and heavy-component recovery modeling results of (A) 50/50 ethane/propane, 30 μm radius, and (B) propane/butane, 10 μm radius, mixtures. SF (—) on the left axis and recovery (− −) on the right axis; 253 K (blue); 273 K (red); 293 K (black); 313 K (olive); 333 K (orange).

It is important to note that this model describes this particular system, which resembles more a continuous stirred tank reactor than a PSA, and obvious care must be taken to translate these results into PSA predictions. Nevertheless, these proof-of-concept kinetic adsorption results are encouraging and highlight the potential for kinetically selective materials to impact NGL separations. However, in practice, packed-bed and fiber sorbent operations[8-9] must carefully consider the role of non-constant axial concentration profiles to optimize the performance for flow-through systems as opposed to the relatively simpler batch systems investigated here. The purity/ recovery metrics achieved in this work can also be benchmarked against other adsorption systems. The diffusive selectivity of ethane/propane in ZIF-8 at room temperature is approximately 1000 by our estimates, more modestly 440 by other works, which gives propane purities in excess of 80% and recoveries in excess of 75%, depending on the operating conditions.[10] For this same separation, Zeolite 4A could demonstrate D_{C2H6}/D_{C3H8} = 2200,[11-12] but diffusivities are significantly slower and manipulating the crystal length scale is not straightforward. For comparison to

other kinetic separations, published work on CMS for CO_2/CH_4 have reported 90% purity and 90%+ recovery (D_{CO2} /D_{CH4} = 180; CO_2 is also assisted by stronger sorption than methane),[13] while Ar/O_2 cycles have reported an argon purity in excess of 80% and a recovery above 40% from 5/95 Ar/O_2 feeds (D_{O2} /D_{Ar} = 30).[14] Zeolite 4A has demonstrated potential in kinetic propane/propylene separation with 85%+ recovery of propylene at 99% purity (D_{C3H6} /D_{C3H8} = 190), while 13X achieves 19% recovery at 98% purity with a purely equilibrium vacuum swing adsorption (VSA).[15-16] Based on our data and comparison to other kinetic separation applications, we believe that kinetic separations using ZIF-8 for ethane/ propane mixtures are feasible and can likely achieve reasonable purities and recoveries in practice.

4.4 Fixed Bed Breakthrough Experiments

The next step in process development was the demonstration of the kinetically selective phenomenon in a packed bed configuration. **Figure 4.10** shows the breakthrough results of an adsorption bed packed with 500 μm Basolite pellets, with the individual crystals themselves being in the sub-micron range. The breakthrough represents the expected equilibrium-dominated adsorption behavior, where the lighter hydrocarbon

breakthrough first with characteristic roll-up behavior, followed by the heavier propane species.

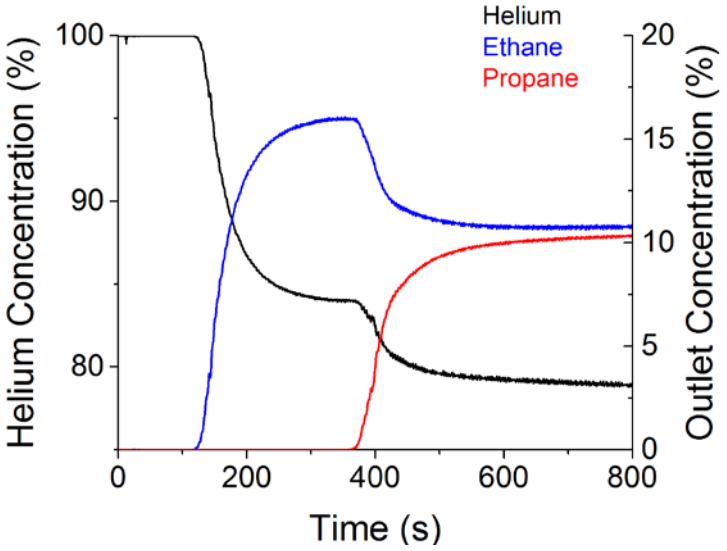

Figure 4.10 Packed bed breakthrough of equimolar ethane/propane mixture at 298 K and 0.9 bar using sub-micron ZIF-8 (Basolite) crystals packed into pellets. t=0 indicates initial helium breakthrough.

The outlet concentration curve in **Figure 4.11** represents a fundamentally different behavior from that of the Basolite pellets. Composed of large ZIF-8 crystals, the adsorption occurring in the bed is far from being able reach equilibrium, and instead we observe a breakthrough dominated by mass transfer resistance. Here, the propane, unable to adsorb into the ZIF-8 crystals quickly enough, is seen to breakthrough first. This happens largely simultaneously with a small bleed of ethane; it is unclear whether this is true ethane breakthrough or simply a confusion of common ion peaks within the mass spectrometer. The ethane, which is able to more fully utilize the kinetically-limited sorbent and is therefore selectively sorbed at shorter time scales, breaks through conclusively a few minutes later and slightly surpasses the propane concentration. This slight crossover in outlet concentration relative to the previous experiment may be an error in calibration or,

more likely, an indication that propane continues to be slowly adsorbed within the column while simultaneously displacing ethane from the sorbent.

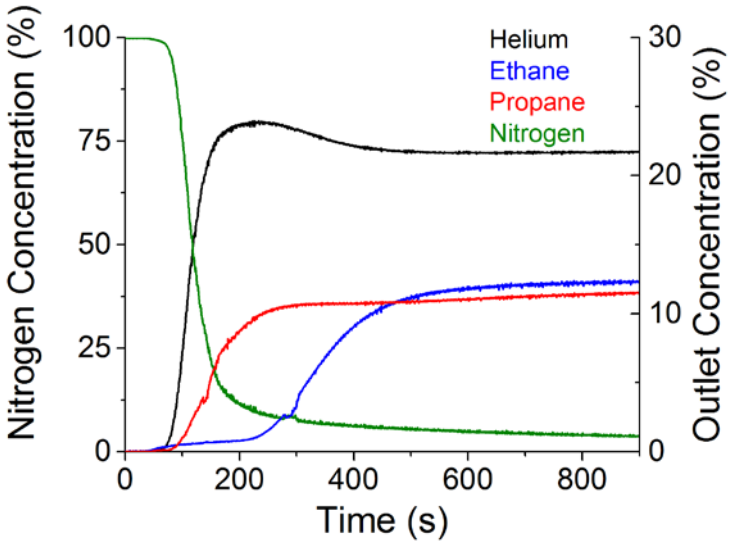

Figure 4.11 Packed bed breakthrough of equimolar ethane/propane mixture at 298 K and 0.9 bar using 145 μm ZIF-8 crystals. t=0 indicates initial feed flow.

It is important to highlight the major conclusion of these experiments: by controlling the time scale of diffusion within a sorbent-sorbate system, the same material can be realistically employed in a kinetic or equilibrium regime and therefore exhibit a reversible selectivity in breakthrough experiments.

4.5 Conclusions

We report kinetic adsorption separation experiments using ZIF-8 that vary the equilibration time scale to enable the relatively effective separation of light hydrocarbons, particularly ethane/propane. The separation factor in ethane/propane mixtures first increased and then declined as a function of the equilibration time, reaching a maximum in purity and separation factor at a time that scales with the diffusivity of the faster component. Increases in the adsorption capacity-to-dosing volume ratios improved the

separation factor while reducing the recovery. Eventual reversal of the selectivity occurred when the separation was allowed to proceed to equilibrium, demonstrating the change in selectivity control from diffusion to adsorption. Lower temperatures were shown to improve the ethane/propane performance and were matched to the differences in the activation energies of permeation of the two components through ZIF-8. The role of diffusive time scales, and by extension the crystal dimensions, is emphasized in ethane/propane experiments, where smaller crystals led to experimentally inaccessible time scales of diffusion while larger crystals led to a measurable kinetic selectivity on the order of minutes.

This separation scheme was extended to propane/propylene because of their promising diffusive selectivity and near-unity sorption selectivity. This saw the peak performance shift to a later time compared to ethane/propane, in line with propylene's lower diffusion coefficient. However, the performance at 293 K exceeded that of ethane/propane due to the more favorable sorption selectivity despite a lower diffusive selectivity. These propane/propylene results point favorably toward the application of kinetic adsorption schemes for other olefin/paraffin pairs. Diffusive selectivity for the propane/butane pair was shown to be insufficient for kinetic separations.

A sorption−diffusion model was employed to demonstrate the effect of selectivity on the system recovery, showing that the recovery monotonically decreases for the slower-diffusing component and is further reduced by an increase in the sample mass relative to the headspace volume. It was demonstrated that only an improvement in the kinetic selectivity may enhance the separation factor without a loss of recovery, and the temperature may serve as an easy variable to manipulate that selectivity in some

separations. Indeed, this temperature sensitivity, when combined with the ability to easily control the crystal size, could reduce the current need to find a new material for each gas pair to be separated in PSA applications.

Kinetic separations enable the fractionation of NGLs via differences in diffusive behavior, which many small-pore MOFs could be ideally suited for. The wide array of material topologies and linker functionalities available make for an almost limitless library of materials from which to select tunable diffusive behaviors. We believe the demonstrated crystal size engineering approach to kinetic PSA is a generalizable strategy to other potentially more selective MOFs. Indeed, the ease of crystal size control in MOFs (relative to zeolites and CMS) strongly differentiates these materials from traditional kinetic adsorbents.

4.6 References

1. Pimentel, B. R.; Lively, R. P., Enabling kinetic light hydrocarbon separation via crystal size engineering of ZIF-8. *Ind. Eng. Chem. Res.* **2016,** *55* (48), 12467-12476.

2. Do, D. D., *Adsorption Analysis : Equilibria and Kinetics*. Imperial College Press: London, 1998; p xxi, 892 p.

3. Crank, J., *The Mathematics of Diffusion*. 2nd ed.; Oxford University Press: Oxford, 1975.

4. Koros, W.; Ma, Y.; Shimidzu, T., Terminology for membranes and membrane processes. *J. Membr. Sci* **1996,** *120* (2), 149-159.

5. Padin, J.; Yang, R. T., New sorbents for olefin/paraffin separations by adsorption via π-complexation: synthesis and effects of substrates. *Chem. Eng. Sci.* **2000,** *55* (14), 2607-2616.

6. Krishna, R., Tracing the origins of transient overshoots for binary mixture diffusion in microporous crystalline materials. *PCCP* **2016,** *18* (23), 15482-15495.

7. Krishna, R., Uphill diffusion in multicomponent mixtures. *Chem. Soc. Rev.* **2015,** *44* (10), 2812-2836.

8. Lively, R. P.; Leta, D. P.; DeRites, B. A.; Chance, R. R.; Koros, W. J., Hollow fiber adsorbents for CO2 capture: Kinetic sorption performance. *Chem. Eng. J.* **2011,** *171* (3), 801-810.

9. Lively, R. P.; Chance, R. R.; Kelley, B. T.; Deckman, H. W.; Drese, J. H.; Jones, C. W.; Koros, W. J., Hollow Fiber Adsorbents for CO2 Removal from Flue Gas. *Ind. Eng. Chem. Res.* **2009,** *48* (15), 7314-7324.

10. Zhang, C.; Lively, R. P.; Zhang, K.; Johnson, J. R.; Karvan, O.; Koros, W. J., Unexpected Molecular Sieving Properties of Zeolitic Imidazolate Framework-8. *J. Phys. Chem. Lett.* **2012,** *3* (16), 2130-2134.

11. Grande, C.; Rodrigues, A., Adsorption kinetics of propane and propylene in zeolite 4A. *Chem. Eng. Res. Des.* **2004,** *82* (12), 1604-1612.

12. Kondis, E. F.; Dranoff, J. S., Kinetics of isothermal sorption of ethane on 4A molecular sieve pellets. *Ind. Eng. Chem. Proc. DD.* **1971,** *10* (1), 108-114.

13. Kapoor, A.; Yang, R. T., Kinetic separation of methane—carbon dioxide mixture by adsorption on molecular sieve carbon. *Chem. Eng. Sci.* **1989,** *44* (8), 1723-1733.

14. Rege, S.; Yang, R., Kinetic Separation of Oxygen and Argon Using Molecular Sieve Carbon. *Adsorption* **2000,** *6* (1), 15-22.

15. Grande, C. A.; Rodrigues, A. E., Propane/propylene separation by pressure swing adsorption using zeolite 4A. *Ind. Eng. Chem. Res.* **2005,** *44* (23), 8815-8829.

16. Lozano-Castelló, D.; Cazorla-Amorós, D.; Linares-Solano, A.; Quinn, D. F., Micropore Size Distributions of Activated Carbons and Carbon Molecular Sieves Assessed by High-Pressure Methane and Carbon Dioxide Adsorption Isotherms. *J. Phys. Chem. B* **2002,** *106* (36), 9372-9379.

CHAPTER 5. SYNTHESIS OF MOF FIBER SORBENTS

We report a synthetic route for the production of water-sensitive metal−organic frameworks (MOFs) in polymer fiber sorbents by use of metal oxides as seeding intermediates. Cellulose acetate/ZnO (48 wt %) fibers were spun via a dry-jet, wet-quench solution processing method and converted via hydroxy double salt (HDS) intermediates into HKUST-1 and ZIF-8. MOF loadings within the fiber sorbent reached 85 and 66 wt %, respectively. We demonstrate this process on module-packaged fibers, in which ready-to-use fiber sorbents are synthesized in a moisture-free environment. Modules are then employed in proof-of-concept CO_2/N_2 breakthrough experiments. This work has been reprinted with permission from Pimentel et al., Synthesis of Water-Sensitive Metal–Organic Frameworks within Fiber Sorbent Modules. *Ind. Eng. Chem. Res.* **2017,** *56* (17), 5070-5077. Copyright American Chemical Society 2017.[1]

5.1 Introduction to Fiber Sorbents

5.1.1 Traditional synthesis of fiber sorbents

Fiber sorbents are a porous and interconnected polymer matrix in which microporous sorbents are highly dispersed, cylindrical in shape and deployed as tube bundles, developed by Lively and Koros.[2] Synthesized via a dry-jet wet-quench spinning method, they resemble the more common hollow fiber membrane materials, but lack the dense, selective skin layer through which membranes separate gas feeds. This enables rapid radial mass transfer within the fiber from the external fluid phases and into the microporous sorbents contained within the porous matrix. Unlike fiber membranes, fiber sorbents may

also be monolithic (i.e., without a bore) rather than hollow, although the bore side of fibers has been shown to be useful as a cooling water channel with the use of appropriate lumen-side barrier layers. Sorbent packing densities upwards of 75 wt% are possible depending on the density of the material being used.

Most work in fiber sorbents has made use of extremely stable microporous materials such as zeolite 13X, due to the harsh nature of the spin dope preparation process. Briefly, the solid is dispersed in a liquid solution of polymer solvent and non-solvent, typically NMP and water. This is sonicated at relatively high power levels and mixed until well dispersed, where a small portion of dissolved polymer is added to stabilize the dispersion. The sonication and mixing process are repeated, after which the remaining dry polymer is added and mixed for several hours at temperatures that allow for complete polymer dissolution and workable mixture viscosities. Specific details can be found in later sections or in previous works.

5.1.2 Pressure drop in structured sorbents

The biggest cost associated with pressure swing adsorption is often feed compression, and therefore pressure drop across the bed represents a significant irrecoverable energy cost. Fiber sorbents are a class of structured mass-transfer contactors, similar to sorbent-loaded ceramic monoliths. They can be arranged in a parallel tube bundle rather than the random pellet packing that most beds use, and therefore provide significant improvements to pressure drop across the bed at equivalent or better mass transfer coefficients.

Packed bed configurations generally have a pressure drop well-described by the Ergun Equation (**5.1**), which contain both a laminar and turbulent component to flow within a bed and is highly dependent on pellet size.

$$\frac{\Delta P}{L} = \frac{150\mu(1-\epsilon)^2 u_0}{\epsilon^3 d_p^2} + \frac{1.75(1-\epsilon)\rho u_0^2}{\epsilon^3 d_p} \tag{5.1}$$

Randomly packed tube bundles parallel to flow exhibit a linear scaling with gas velocity, described in (5.2**)**

$$\frac{\Delta P}{L} = \frac{32}{\epsilon} \cdot \left[\frac{d_f}{d_m} + (1-\epsilon)\right]^2 \frac{\mu \cdot u_0}{d_f^2} \tag{5.2}$$

This translates to greater energy savings and wider operational windows, as higher gas velocities are now realistically accessible, which could result in shorter cycle times and higher sorbent productivities.

5.1.3 Mass transfer resistances in structured sorbents

Much like the use of a pellet or a binder, the incorporation of microporous adsorbents within a fiber sorbent introduces additional mass transfer resistances that slow down transport of gas to the adsorptive sites within a sorbent. These resistances are largely analogous to those encountered within pelletized samples, but tend to be smaller due to the small length scales of the fiber wall. The corresponding trade-off however, is that the volumetric sorbent density is lower than that of a pelletized bed. Three types of mass transport resistance exist in adsorbent systems.

On the outside of a pellet or tube, viscous drag forces on a gas flow near a surface result in the development of a laminar boundary layer. This interrupts the existing well-mixed turbulent flow of the gas stream and imposes what is known as a film resistance, where mass and momentum transfer in the direction normal of flow only occurs via diffusion mechanism. This hinders the radial mass transfer rate into sorbent, reduces the effectiveness of the material and leads to detrimental effects such as axial spreading during operation. The thickness of this film reduces with increasing gas velocity, and the magnitude of the mass transfer resistance is inversely proportional to the film thickness. Hence, the ability of fiber sorbents to operate at higher gas flows with equal pressure drop is a significant advantage in pressure swing operation.

The second sizeable mass transfer resistance in sorbent systems is that of the binder and the interstitial space between sorbent particles, referred to as the meso/macropore regime. Typically, this can be modelled by Knudsen diffusion, but can also take the form of surface diffusion or porous flow (Darcy's law). The smaller these pores are, the more significant the resistance to transport in the particle. In pellets, this is defined by the mesoporosity of the pellet or binder and can dominate the adsorption process in certain cases. In fibers, this is determined by the porosity of the polymer matrix, which is generally quite large and well connected. Furthermore, the well-dispersed nature of the sorbent within the fiber precludes the existence of any further restrictive interstitial spaces. Modeling work by Fan et al. highlights one particular fiber system where these resistances accounted for less than 1% of the mass transfer limitations, demonstrating the positive transport characteristics of these materials.[3] It is important to note that these resistances are

not molecularly selective to any appreciable degree; therefore, systems that rely on kinetic selectivity are hindered by the presence of these non-selective transport mechanisms.

The final mass transfer resistance in sorbent systems is of the sorbent itself, which is generally that of microporous diffusion. The magnitude of this resistance only depends on the particle size of the sorbent and the inherent diffusivity of the sorbent-sorbate pair. In kinetic systems, it is important to isolate and magnify this resistance as it represents the selective mechanism by which molecules are discriminated in this configuration.

5.1.4 Synthesis of MOFs from metal oxides

The highest performing MOFs to date, demonstrating excellent CO_2 capacity and selectivities, tend to be materials that are unstable or somewhat unstable in humid or aqueous conditions.[4] In fact, most MOFs can be classified as at least partially water-unstable, greatly reducing the number of industrially applicable materials that could be incorporated into these scalable and modular fiber contactors.[5-6] Furthermore, it has been demonstrated that sonication may have undesirable effects on the MOF sorbent, such as amorphization and Ostwald ripening of crystals.[7-8] Developing techniques that enable use of the myriad MOF materials as adsorbents in fiber contactors would be a tremendous improvement upon current structured-sorbent capabilities

Given that MOF syntheses often use a large amount of environmentally unfriendly solvents, such as DMF, and may at times take days to synthesize, some recent work has focused on the greener and more rapid synthesis of these important microporous materials.[9-16] Notably, some of these MOFs can be grown from metal oxides and other solid-to-MOF routes.[14, 17-23] The combination of fiber spinning techniques with oxide-to-

MOF strategies provides an avenue for the incorporation of water-sensitive MOFs via post-spinning modification of oxide precursors. The posts-pinning transformation of ZnO into hydroxy double salt (HDS) intermediates allows for the rapid and easy synthesis of MOF crystals within the porous structure while circumventing the harsh conditions associated with fiber spinning (**Figure 5.1**).

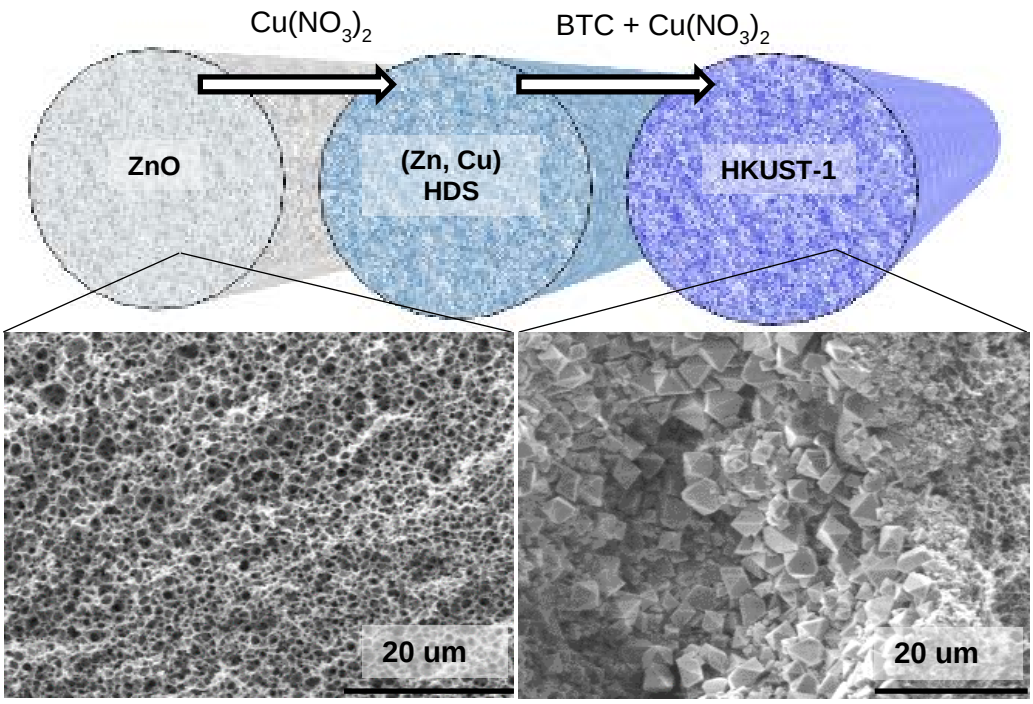

Figure 5.1 (Top) Synthesis of MOF materials within ZnO-loaded fiber sorbent materials. (Bottom) SEM images of the green ZnO-loaded fiber sorbents (left) and the postsynthesis MOF-loaded fiber sorbent (right).

5.2 Materials and Methods

5.2.1 Materials

The following were used as received without any further purification unless otherwise stated. Gases: N2 (UHP grade, Airgas), N_2/CO_2/He (75%/12.5%/12.5%, Airgas). Chemicals: Cellulose acetate (50,000 MW, Sigma Aldrich), polyvinylpyrrolidone (K30

Mw 40,000, TCI), ZnO (<5 µm, 99.9%, Sigma Aldrich), N-methyl-2-pyrrolidone (ACS grade, VWR), ethanol (200 proof, KOPTEC), methanol (ACS grade, VWR), hexanes (ACS grade, VWR), Cu(NO3)2·3H_2O (99−104%, Sigma-Aldrich), $Zn(Ac)_2 \cdot 2H_2O$ (97+%, Alfa Aesar), $Zn(NO_3)_2 \cdot 6H_2O$ (99+%, Alfa Aesar).

5.2.2 Fiber Spinning

Fiber sorbents were spun using a dry-jet, wet-quench spinning technique using water as a quench bath coagulant. After spinning, fibers undergo a solvent exchange process in water for 3 days, followed by methanol (3 × 30 min) and then hexanes (3 × 30 min). Finally, fibers are dried under vacuum overnight at 80 °C. Dope formulation and spinning conditions are detailed in **Table 5.1** and **Table 5.2**.

Table 5.1 Compositions of CA and ZnO/CA spinning dopes

	CA (wt %)	CA/ZnO (wt %)
NMP	70.4	66.4
Water	9.6	8.6
Cellulose Acetate (Mw 50,000)	14.3	10.4
PVP (Mw 40,000)	5.7	4.2
ZnO <5 µm		10.4

Table 5.2 Spinning parameters of CA and ZnO/CA sorbents

	CA	CA/ZnO
Spinneret Temperature (°C)	50	50
Bath Temperature (°C)	50	45
Dope Flow Rate (ml/h)	300	300
Drum Uptake Rate (m/min)	25	25
Air Gap (cm)	5	5
Draw Ratio	22	22

5.2.2.1 Cellulose Acetate Fibers

CA and PVP powders were dried under vacuum at 80 °C overnight to remove sorbed water. Polymers were added to the solvent/nonsolvent solution in a sealed glass jar and set on a mixing roller for 24 h to allow for full dissolution and degassing of the spinning dope. The dope was loaded into a syringe pump and again degassed overnight at 50 °C prior to spinning.

5.2.2.2 ZnO/Cellulose Acetate Dope

CA, PVP, and ZnO were dried under vacuum at 80 °C overnight to remove sorbed water. ZnO was ground using a fine mortar and pestle prior to drying.

Initially, a prime dope consisting of 20% of the total solvent, nonsolvent, and polymer was mixed in a sealed glass jar on a roller 24 h prior to synthesis of the full dope. To a solution of 80% of the total solvent/nonsolvent mixture, all of the ZnO sorbent was added and mixed via rotating impeller until homogeneous. This dispersion dope was further dispersed 3 times using a sonication horn for 60 s and the impeller alternatively. To this dispersion dope, the prime dope was added and similarly mixed and dispersed. Lastly, the rest of the dry polymer was added to the dope and mixed using the impeller for several hours until homogeneous. The dope was then loaded into a syringe pump and degassed overnight at 50 °C prior to spinning

5.2.3 Synthesis of MOF fibers from ZnO precursors

The syntheses of most MOF-loaded fibers for characterization were conducted using a small quantity of ZnO-loaded fiber sorbent (<0.1 g) inside a ~10 cm stainless steel

1/4″ Swagelok tube with elbow connections on both ends. The Swagelok tubing was connected by PTFE tubing to a MasterFlex peristalsic pump and liquid reservoir in a closed loop. This setup is depicted in **Scheme 5.1** and synthesis conditions are summarized in **Table** 5.3 and **Table 5.4** for additional clarity. This method was adapted from reported MOF syntheses using ZnO.[21]

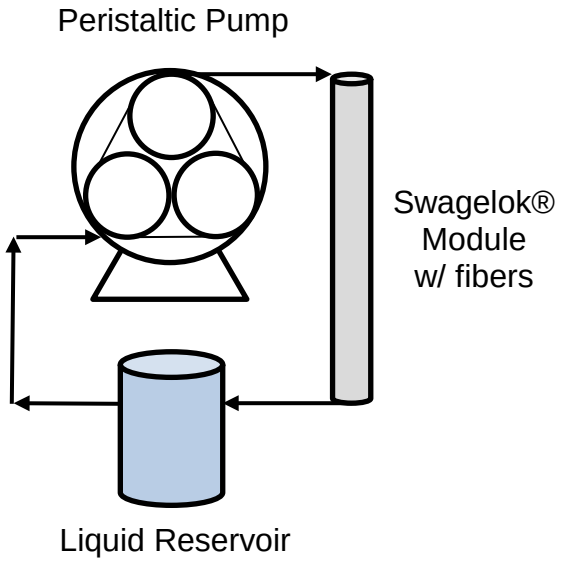

Scheme 5.1 Experimental Set-up of the Fiber Sorbent Synthesis Equipment, Where a Swagelok Fiber Sorbent Module Is Set in a Closed Loop with a Liquid Reservoir by Use of a Peristaltic Pump

5.2.3.1 HKUST-1 Fiber Sorbents (HFS-#)

The liquid reservoir was filled with a solution of $Cu(NO_3)2{\cdot}3H_2O$ (12 g) in DI H_2O (120 mL) and the pump set to 25 mL/min overnight. The lines were drained, and a 50/50 H_2O/ethanol solution was then introduced into the reservoir to wash the fibers and flush the lines. Several fibers were removed, dried under vacuum at 80 °C, and analyzed via XRD. These were labeled as (Zn, Cu) HDS fibers.

The rest of the fibers were kept in the module, and the liquid reservoir was then filled with a solution of H_3BTC (0.583g) in ethanol (90 mL) and H_2O (27 mL) and flowed through the module. After approximately 10 min, a small quantity of $Cu(NO_3)2{\cdot}3H_2O$ (0.068g) was dissolved into the liquid reservoir, and the flow was resumed, continuing overnight. The next day, pure ethanol was introduced into the liquid reservoir to wash the fibers and clean out the pump. The fibers were removed from the module and dried under vacuum at 80 °C, and were then characterized via XRD and N_2 physisorption. These materials were labeled as HFS-1.

Beginning with (Zn, Cu) HDS fibers, the above steps were repeated, increasing the concentration of H_3BTC and of $Cu(NO_3)_2{\cdot}3H_2O$ by factors of 2 (HFS-2) and 4 (HFS-4).

Beginning with wet ZnO-loaded fibers (which had undergone solvent exchange in water but not methanol or hexanes), the fibers were submerged overnight in a beaker containing 16 mL of H_2O and 1.6 g of $Cu(NO_3)_2$. The fibers were washed with H_2O and transferred to a solution of 0.022 g of $Cu(NO_3)_2$ and 0.195 g of H_3BTC in 10 mL of EtOH and 3 mL of H_2O overnight. The fibers were then washed with EtOH, and the solvent exchange was completed by submerging the fibers in MeOH followed by hexanes for 15 min each. These fibers were then dried under vacuum at 80 °C, characterized via XRD and N_2 physisorption, and referred to as “no-exchange” fibers (HFS-N).

5.2.3.2 ZIF-8 Fiber Sorbents (ZFS-#)

The liquid reservoir was filled with a solution of $Zn(Ac)_2{\cdot}2H_2O$ (5.5 g) in H_2O (100 mL) and the pump set to 25 mL/min overnight. MeOH was then introduced into the liquid reservoir to wash the fibers and clean out the pump. Several fibers were removed, dried

under vacuum at 80 °C, and analyzed via XRD. These were labeled as (Zn, Zn) HDS fibers. Attempts at using $Zn(NO_3)_2 \cdot 6H_2O$ were unsuccessful.

Fibers not taken for analysis were kept in the module, and the liquid reservoir was then filled with a solution of 2-methylimidazole (0.685g) in methanol (120 mL) and flowed through the module. After approximately 10 min, a small quantity of $Zn(Ac)_2 \cdot 2H_2O$ (0.343g) was dissolved into the liquid reservoir, and the flow was resumed, continuing overnight. The next day, pure methanol was introduced into the liquid reservoir to wash the fibers and clean out the pump. The fibers were removed from the module and dried under vacuum at 80 °C, and were then characterized via XRD and N_2 physisorption. These materials were labeled as ZFS-1.

Beginning with (Zn, Zn) HDS fibers, the above steps were repeated, increasing the concentrations of 2-methylimidazole and of $Zn(Ac)_2 \cdot 2H_2O$ by factors of 2 (ZFS-2) and 4 (ZFS-4).

Beginning with wet ZnO-loaded fibers (which had undergone solvent exchange in water but not methanol or hexanes), the fibers were submerged overnight in a beaker containing 16 mL of H_2O and 0.88 g of $Zn(Ac)_2$. The fibers were washed with H_2O and transferred to a solution of 0.112 g of $Zn(Ac)_2$ and 0.222 g of 2-methylimidazole in 13 mL of MeOH overnight. The fibers were then washed with MeOH, and the solvent exchange was completed by submerging the fibers in MeOH followed by hexanes for 15 min each. These fibers were then dried under vacuum at 80 °C, characterized via XRD and N_2 physisorption, and referred to as “no-exchange” fibers (ZFS-N).

Table 5.3 Synthesis conditions of HFS samples

Starting Material	Sample	Step 1 (120 mL of H_2O)	Step 2 (90 mL EtOH + 27 mL H_2O)	Step 3 (added to Step 2)
Dry ZnO-Loaded Fiber*	HFS-1	12 g Copper Nitrate	0.58 g BTC	0.07 g Copper Nitrate
	HFS-2		1.16 g BTC	0.14 g Copper Nitrate
	HFS-4		2.32 g BTC	0.28 g Copper Nitrate
		(16 mL of H_2O)	(10 mL EtOH + 3 mL H_2O)	
Water-Exchanged ZnO-Loaded Fiber**	HFS-N	1.6 g Copper Nitrate	0.20 g BTC	0.022 g Copper Nitrate

*Fully exchanged in water, methanol and hexanes. **Initial fiber wet and only exchanged in water; exchanged in methanol and hexanes after Step 3.

Table 5.4 Synthesis conditions of ZFS samples

Starting Material	Sample	Step 1 (100 mL of H_2O)	Step 2 (120 mL of MeOH)	Step 3 (added to Step 2)
Dry ZnO-Loaded Fiber*	ZFS-1	5.5 g Zinc Acetate	0.69 g 2-meIm	0.343 g Zinc Acetate
	ZFS-2		1.37 g 2-meIm	0.69 g Zinc Acetate
	ZFS-4		2.74 g 2-meIm	1.37 g Zinc Acetate
		(16 ml of H_2O)	(13 mL of MeOH)	
Water-exchanged ZnO-Loaded Fiber**	ZFS-N	0.88 g Zinc Acetate	0.22 g 2-meIm	0.11 g Zinc Acetate

*Fully exchanged in water, methanol and hexanes. **Initial fiber wet and only exchanged in water; exchanged in methanol and hexanes after Step 3.

5.2.4 Batch Synthesis of MOF Fiber Controls

Several fiber synthesis experiments were performed in batch to determine the most effective order of addition and provide control experiments to diverse growth scenarios. These were conducted in batch experiments rather than flow to simplify the experimental set-up and consume less reagent. HKUST-1 was chosen to demonstrate these controls rather than ZIF-8 due to its blue color as a visual indicator of material growth.

5.2.4.1 Growth from "Blank" CA fiber

Approximately 0.2g "blank" CA fiber (i.e., no ZnO particles in the fiber) was submerged in a solution of H_3BTC (0.197g) in ethanol (30 mL) and water (9 mL). Under slow stirring, $Cu(NO_3)_2 \cdot 3H_2O$ (0.114g) was added. The mixture was allowed to stir overnight. The fibers were washed with pure ethanol and dried under vacuum at 80°C. The fibers were characterized by XRD and N_2 physisorption.

5.2.4.2 1-Step Growth fibers from ZnO

Approximately 0.1g ZnO-loaded CA fiber was submerged in a solution of H_3BTC (0.197g) in ethanol (30 mL) and water (9 mL). Under slow stirring, $Cu(NO_3)_2 \cdot 3H_2O$ (0.114g) was added. The mixture was allowed to stir overnight. The fibers were washed with pure ethanol and dried under vacuum at 80°C. The fibers were characterized N_2 physisorption.

5.2.4.3 Growth from HDS fibers without additional Copper Nitrate

Approximately 0.12g ZnO-loaded CA fiber was submerged in a solution of $Cu(NO_3)_2 \cdot 3H_2O$ (3.0g) in H_2O (30 mL) overnight. The fibers were washed with H_2O. Approximately 0.1g of the (Zn, Cu) HDS fiber was submerged in a solution of H_3BTC (0.197g) in ethanol (30 mL) and water (9 mL) overnight. The fibers were washed with pure ethanol and dried under vacuum at 80°C. The fibers were characterized by N_2 physisorption.

5.2.4.4 HFS-Batch

Approximately 0.12g ZnO-loaded fiber was submerged in a solution of $Cu(NO_3)_2 \cdot 3H_2O$ (3.0g) in H_2O (30 mL) overnight. The fibers were washed with H_2O. Approximately 0.1g of the (Zn, Cu) HDS fiber was submerged in a solution of H_3BTC (0.197g) in ethanol (30 mL) and water (9 mL). After several minutes, a small quantity of $Cu(NO_3)_2 \cdot 3H_2O$ (0.023g) was added under slow stirring, and the mixture was allowed to stir overnight. The fibers were washed with pure ethanol and dried under vacuum at 80°C. The fibers were characterized by N_2 physisorption.

5.2.5 Synthesis of MOF Powders

5.2.5.1 HKUST-1 Synthesis

HKUST-1 powder samples were synthesized based on published solvothermal methods.[24] In a glass beaker, 0.6 g of $Cu(NO_3)_2 \cdot 2.5\ H_2O$ was dissolved in 25 mL of H_2O while in a separate beaker 0.4 g of H_3BTC was dissolved in 25 mL of a 50/50 H_2O/EtOH mixture. These mixtures were poured into a Teflon autoclave and heated to 110 °C for 19

h under autogenous conditions. After allowing the sample to cool to room temperature, it was washed with a 50/50 H_2O/EtOH solution and then dried under vacuum at 80 °C overnight. The sample was characterized by N_2 physisorption.

5.2.5.2 ZIF-8 Synthesis

ZIF-8 powder samples were originally synthesized and characterized in a previous work (1.5 μm ZIF-8 samples).[25-26] In a glass vial, 0.734 g of zinc nitrate hexahydrate was dissolved in 50 mL of methanol. In a separate 50 mL methanol solution, 0.810 g of 2-methylimidazole and 0.810 g of 1-methylimidazole were dissolved and poured into the first solution. Stirring was stopped after mixing and kept capped at room temperature for 24 h. The sample was washed and filtered in methanol and dried at 80 °C under vacuum overnight.

5.2.6 Material Characterization

X-ray diffraction (XRD) patterns were collected on a Panalytical X'Pert PRO Alpha-1 Xray diffractometer using a rotating sample stage. Fiber samples were taped on a zero-background sample holder and cut into small segments. All samples were background-corrected using the Panalytical HighScore software. N_2 physisorption experiments were performed on a Microtrac Belsorp-MAX and degassed prior to analysis at 110 °C for 12 h under vacuum. Nitrogen uptake was calculated at 0.85 P/P_o to prevent taking into account adsorption attributable to interparticle condensation. Mercury porosimetry experiments were carried out in a Micromeritics Autopore IV Mercury Porosimiter up to 32,500 psi, corresponding to an intrusion pore diameter of 56 Å. Thermogravometric analysis (TGA) experiments were carried out in a TA Instruments

Q500 Series TGA. Details of the ramp protocol can be found in **Table 5.5**. Scanning electron microscopy (SEM) and energy dispersive X-ray (EDX) spectroscopy images were taken on a Hitachi SU8230 FE-SEM. Samples were sputtered using a Hummer 6 Au/Pd Sputter Coater prior to imaging.

Table 5.5 TGA ramp protocol used in the determination of residual mass in MOF fibers

Gas Flow	Temperature Protocol
90 ml/min of N_2	10 °C/min from 25 °C to 110 °C
	60 min hold at 110 °C to remove adsorbed water
90 ml/min of air	10 °C/min to 700 °C
	-20 °C/min to 25 °C

Initial dry masses were taken at the end of the isothermal period, and residual sample mass at 110 °C on the cooling section of the protocol

5.2.7 CO_2/N_2 Breakthrough Analysis

Given the need to process tremendous volumes of gas at minimum cost, fiber sorbents have seen implementation in post-combustion CO_2 capture. Indeed, CO_2 capture from flue gas or ambient air is one of the most common research focuses for new MOFs. To therefore compare this work with existing bodies of work, CO_2/N_2 breakthrough experiments are conducted on these MOFs within fiber sorbents.

5.2.7.1 Sorbent Module Preparation

Sorbent modules were synthesized in a similar fashion to previously described HFS-4 samples, with some minor differences. Briefly, 22 ZnO fibers were placed in a parallel arrangement bundle within a 1/4″ Swagelok stainless steel tubing with elbow connections on both ends. These fibers were converted to (Zn, Cu) HDS samples by a closed-loop flow of aqueous $Cu(NO_3)_2$ solution for 24 h (using the apparatus in **Scheme 5.1**) and then washed with H_2O/EtOH solution. The fibers were then converted to HKUST-

1 by exposure to HFS-4 precursor solution, where the MOF linker is allowed to come into contact with the fibers first and the additional $Cu(NO_3)_2$ is added to the reservoir after 10 min. The fiber module was washed with EtOH, drained of liquid, and immediately placed in a vacuum oven at 80 °C for activation overnight. At no point was the MOF fiber sorbent module exposed to ambient air.

The sample was backfilled with N_2 upon completion of activation, and capped using Swagelok tube plugs. At this point, the module contains a ready-to-use activated MOF sorbent sample which can be easily transported or stored without risking exposure to humid air. The module was installed in the breakthrough unit under a constant N_2 sweep, and degassed for at least 6 h at 60 °C prior to breakthrough experiments.

5.2.7.2 Breakthrough Curve Analysis

Breakthrough experiments were carried out in a temperature controlled cabinet system built by L&C Science and Technology, connected to a Pfeiffer Omnistar mass spectrometer. Feeds to the fiber beds were controlled by mass flow controllers, and bed pressure was set by a back pressure regulator at the end of the unit. The sample was activated under vacuum at 60 °C for 6 h prior to breakthrough experiments, and pressurized with N_2 before introducing the flow of feed gas. The feed flow rate was set to 30 mL/min with a molar composition of 12.5/12.5/75 CO_2/He/N_2; breakthrough curves were measured at 0 and 35 °C and at 1 and 3.5 bar.

Breakthrough experiments were only carried out on HKUST- 1 fibers rather than ZIF-8 due to their appreciable CO_2 affinity. ZIF-8 has a much lower CO_2 capacity than

HKUST-1, and limitations of our mass flow controllers did not allow for low enough feed rates to demonstrate clear breakthrough in ZIF-8 fiber beds for this separation.

The uptake of the bed was calculated using the following equation

$$q_{CO_2} = \dot{n} * \frac{y_{0,CO_2}}{Mass} \int_{t_0}^{t_f} (y_{He} - y_{CO_2}) dt \quad (5.3)$$

where y_i indicates the molar fraction of a given species, $\dot{n}$ indicates the feed flow rate, and Mass refers to the total mass of fiber within the bed, measured by weighing the fibers taken out of the module after all experiments were completed. The boundaries of integration t_0 and t_f represent the beginning of feed flow and the end of the reported data, respectively; generally, until the outlet concentration of CO_2 and He remain constant over 60 s.

5.3 Results and Discussion

5.3.1 CA/ZnO Fiber Characterization

CA/ZnO and pure CA fibers were spun as the precursors to the final MOF-loaded fibers. **Figure 5.2** shows an SEM cross-section image of the initial ZnO fibers used in this work exhibiting a continuous porous substructure and no visible skin layer formation. Significant macrovoids are present within the fiber, which generally lead to lower burst pressures in membrane operations, but are acceptable in sorbent monoliths.

Characterization of the fibers via X-ray diffraction (XRD) revealed only amorphous polymer patterns in the pure CA fibers and clearly observable ZnO patterns in the CA/ZnO fibers (**Figure 5.3A**). Thermogravimetric analysis (TGA) in air indicated a 48% ZnO

weight loading in the CA/ZnO fibers, in agreement with the original polymer dope formulation.

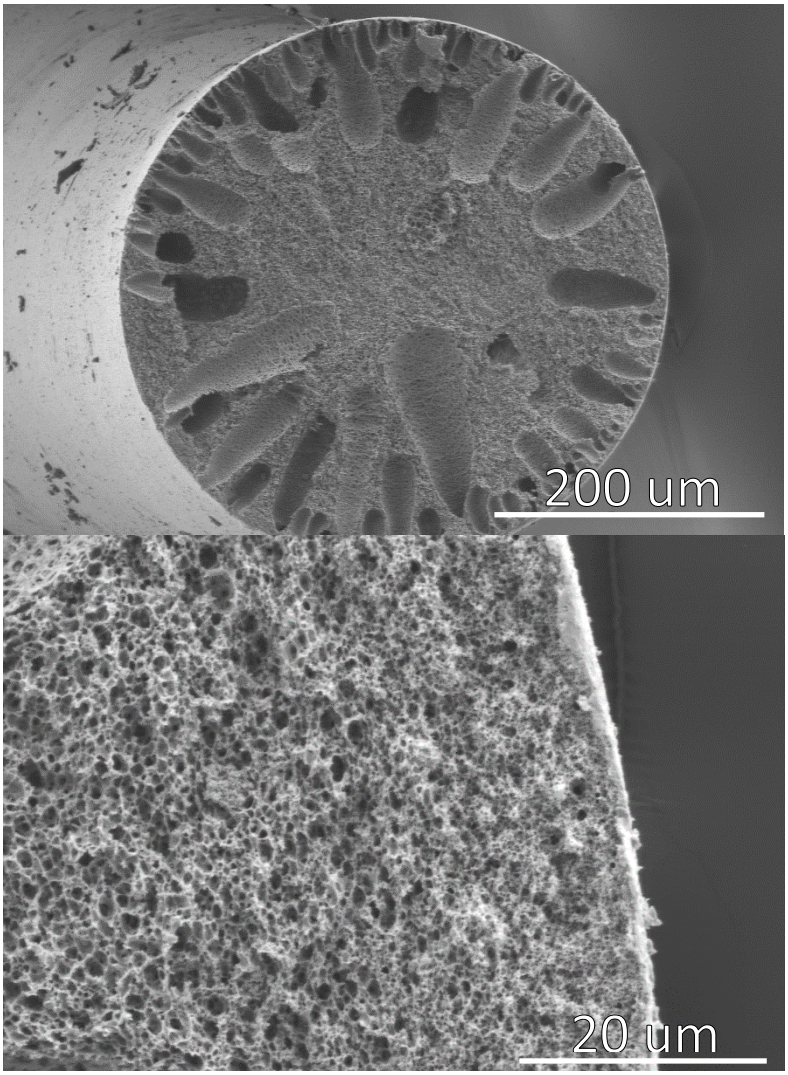

Figure 5.2 SEM cross-sections of ZnO-loaded cellulose acetate fibers

5.3.2 Conversion of ZnO/CA fibers to MOF via HDS precursors

Previous work has shown the rapid promoted growth of various MOFs from ZnO precursors through HDS intermediates.[21] The synthesis of HDS materials has been achieved in the literature using various approaches, and although structural characteristics are known, the mechanism by which these materials are formed from ZnO

is less clear.[27-31] We hypothesized that the use of ZnO particles as water stable "seeds" capable of withstanding the spinning process would enable postspinning MOF growth within the fiber pores. Indeed, any other metal oxide or material that has been shown to be convertible to MOFs and can withstand spinning conditions would likely be an acceptable candidate for this process. CA/ZnO fibers were converted to HDS under flow of aqueous $Zn(Ac)_2 \cdot 2H_2O$ or $Cu(NO_3)2 \cdot 3H_2O$ for 24 h at room temperature and subsequently analyzed by XRD. The copper treated fibers, referred to as (Zn, Cu), exhibited an almost complete loss of X-ray reflections associated with ZnO peaks and developed new reflections attributable to (Zn, Cu) nitrate HDS. Despite the successful synthesis of the (Zn, Zn) HDS material from the neat ZnO powder, the analogous synthesis using ZnO fibers showed almost no conversion by XRD (**Figure 5.3A**).

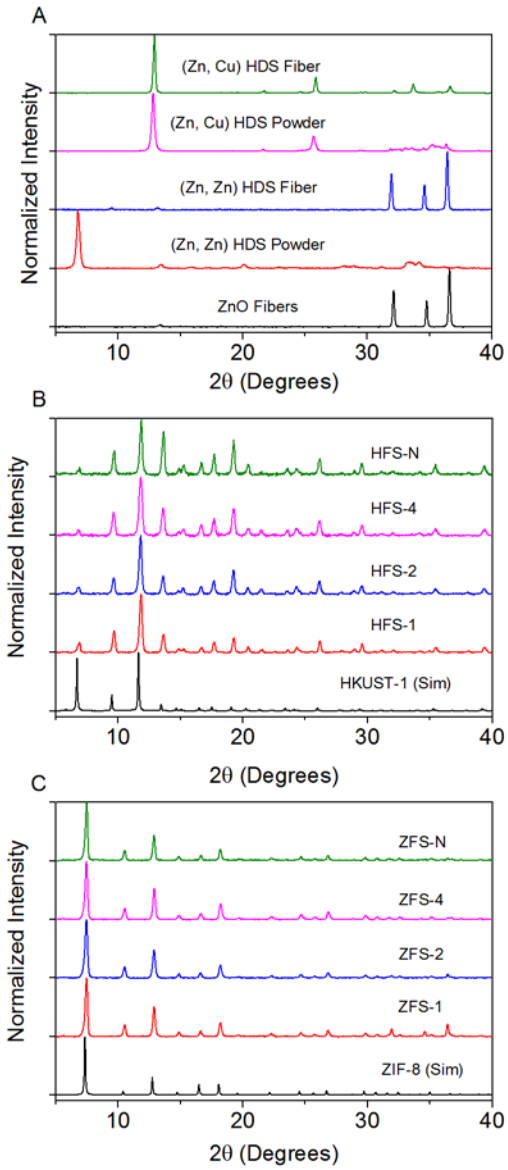

Figure 5.3 (A) XRD patterns of ZnO conversion to HDS precursors; (B) XRD patterns of synthesized HFS samples; (C) XRD patterns of synthesized ZFS samples.

In a second step (Zn, Cu) and (Zn, Zn) fibers were converted under a flow of HKUST-1 and ZIF-8 precursor solutions, respectively, with different concentrations of the metal and ligand at room temperature. The fibers were first exposed to a ligand solution, and the metal solution was added after 10 min. This strategy resulted in complete growth of the MOF throughout the fiber (**Figure 5.4**). In the HKUST-1 fiber sorbent samples, XRD revealed a complete loss of HDS, and the development of

HKUST-1 structure with no discernible differences between the various synthesis solution concentrations (HFS-1,2,4) (**Figure 5.3B**). ZIF-8 fiber sorbents derived from the (Zn, Zn) fibers displayed traces of ZnO reflections, which were observed to decrease in intensity with increasing synthesis concentration (ZFS-1,2,4) (**Figure 5.3C**).

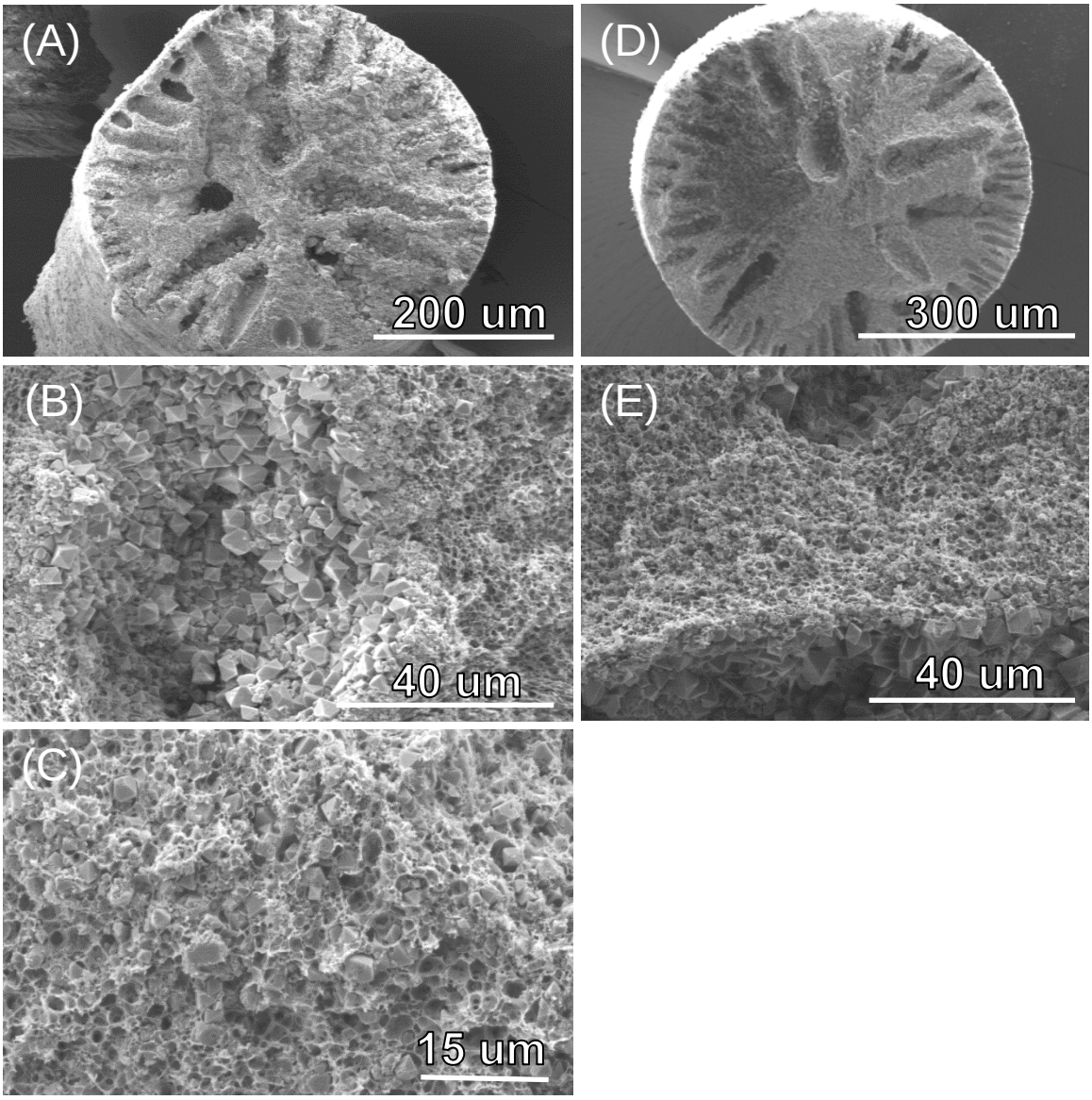

Figure 5.4 SEM cross-section of HFS-4 fibers (A, B, C) and HFS-N fibers (D, E)

5.3.3 Comparison of Synthesis Methods: Sorbent Loading Determination and Substructure Characterization

5.3.3.1 Two-Step Synthesis in Closed Loop Configurations

The results of N_2 physisorption experiments performed on the various HKUST-1 fibers as synthesized in Section 5.2.3 are plotted in **Figure 5.5**. All samples exhibited similar overall capacities, which is in qualitative agreement with XRD results. Discrepancies between samples exist in the low-pressure regions, as is most obvious when the data is plotted on a log scale (**Figure 5.5, left**). Notably, samples synthesized pre and post solvent exchange demonstrate different behavior in the low-pressure region; post solvent-exchange samples exhibit adsorption isotherms indicative of a greater population of small-pore sites. The shapes of the isotherms are repeatable, but the cause of the difference between samples is unclear.

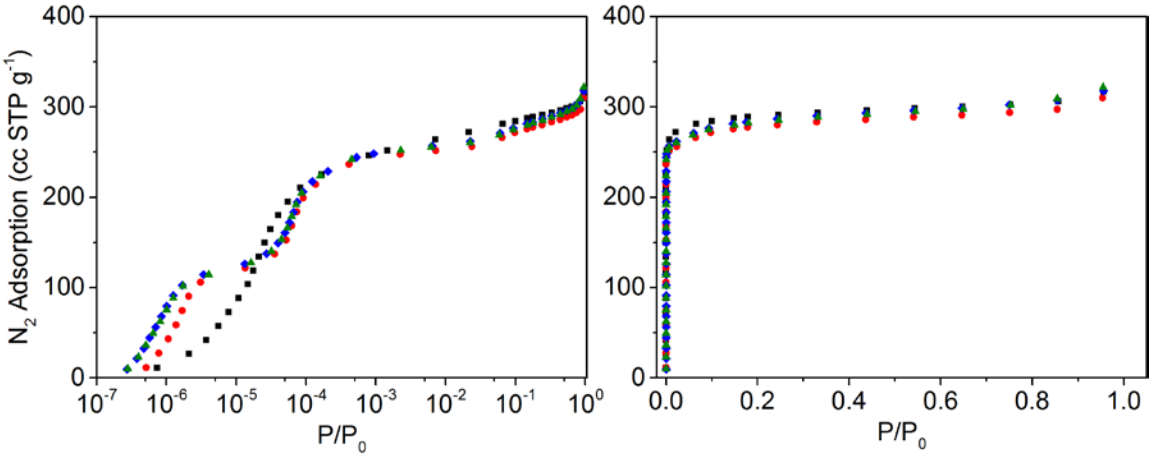

Figure 5.5 HKUST-1 fibers N_2 physisorption in log (Left) and linear (Right) scales. HFS-1 (Green); HFS-2 (Blue); HFS-4 (Red); HFS-N (Black).

HKUST-1 (HFS-4) growth within the polymer fibers is shown in **Figure 5.4 A-C**. Crystals within the macrovoids seem to be able to grow to a size of several microns while smaller crystals are present in

the typical porous substructure of the polymer. No apparent visual differences exist between this sample and the HFS-N fiber (**Figure 5.4 D, E**) despite slight variation in the low-pressure physisorption behavior. Interestingly, despite the lack of ZnO reflections in XRD patterns of any HKUST-1 fibers, EDX elemental mapping shows the presence of residual Zn ions within the fibers, as shown in **Figure 5.6**. The fate of unincorporated metal ions (i.e. zinc ions in HKUST-1 syntheses) remains unclear.

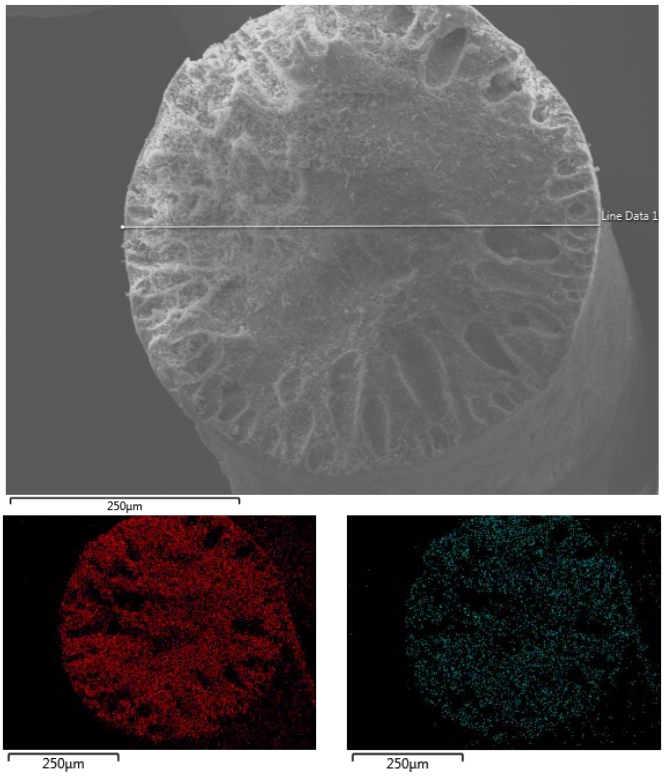

Figure 5.6 SEM-EDX mapping of a cross-section HFS-4 fibers. Copper (Red); Zinc (Teal)

The results of N_2 physisorption experiments performed on the various ZIF-8 fibers are shown in **Figure 5.7**. The observed increase in nitrogen capacity with synthesis concentration is in agreement with XRD experiments that indicated decreasing quantities of ZnO in the post-synthesis fiber. The characteristic "gate-opening" step in the isotherm is present near 1 x 10^{-2} P/P_0 in all samples. It is important to note that

despite having a slightly lower synthesis concentration than the ZFS-4 sample, the ZFS-N synthesized prior to completing the fiber solvent-exchange process demonstrated the highest N_2 capacity. This indicates that the exchange procedure may still be leading to some level of pore structure collapse or shrinking that hinders either monomer transport or overall MOF growth, and that the reaction is not thermodynamically limited.

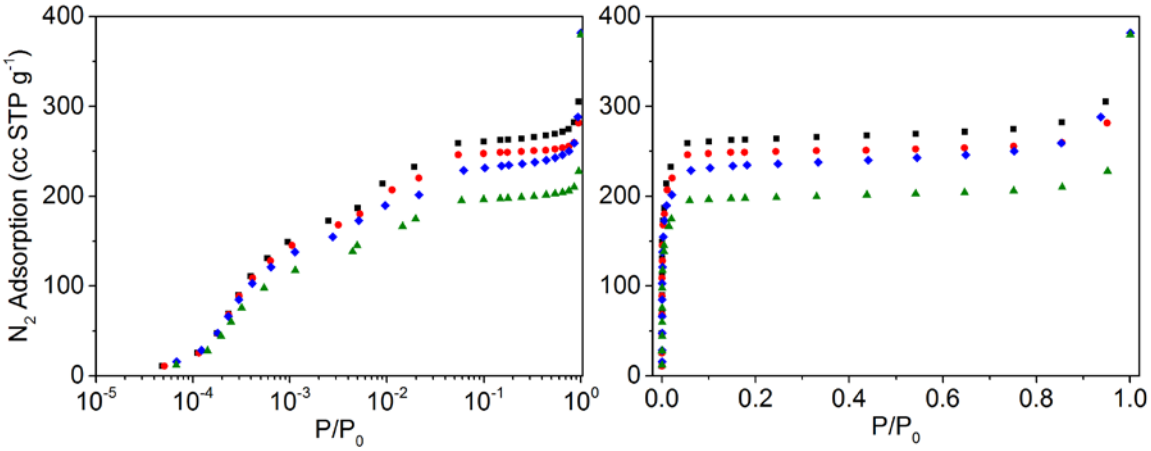

Figure 5.7 ZIF-8 fibers N_2 physisorption in log (Left) and linear (Right) scales. ZFS-1 (Green); ZFS-2 (Blue); ZFS-4 (Red); ZFS-N (Black).

Images of ZFS-4 fibers (**Figure 5.8**) show the growth of large quantities of ~1 μm sized particles, distinctly different from the large and sharply faceted crystals displayed in HKUST-1 macrovoid samples. Crystal morphology is highly variable from MOF to MOF and can change drastically with synthesis conditions.

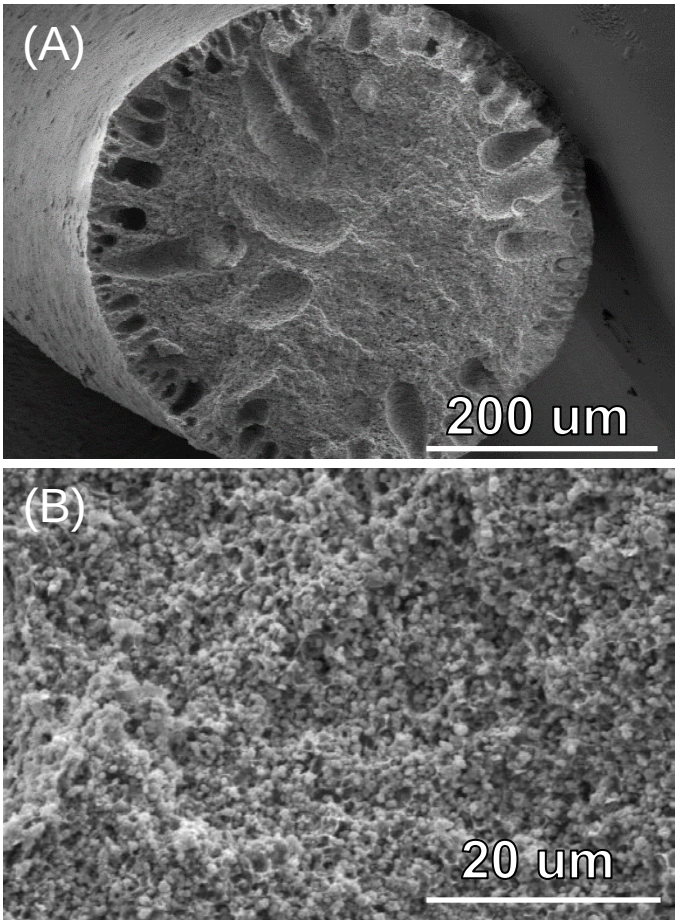

Figure 5.8 SEM cross-section of ZFS-4 fibers

To asses the integrity of the sorbent porosity after the synthesis procedure and ensure no significant substructure collapse, given the ambiguity in physisorption results, mercury porosimetry was conducted to probe the porosity of the polymer network. Results show no significant changes in the porosity of the fibers after growth of the MOF (**Figure 5.9**). A small diameter pore population develops in the HFS-4 samples is likely attributable to inter-crystalline space.

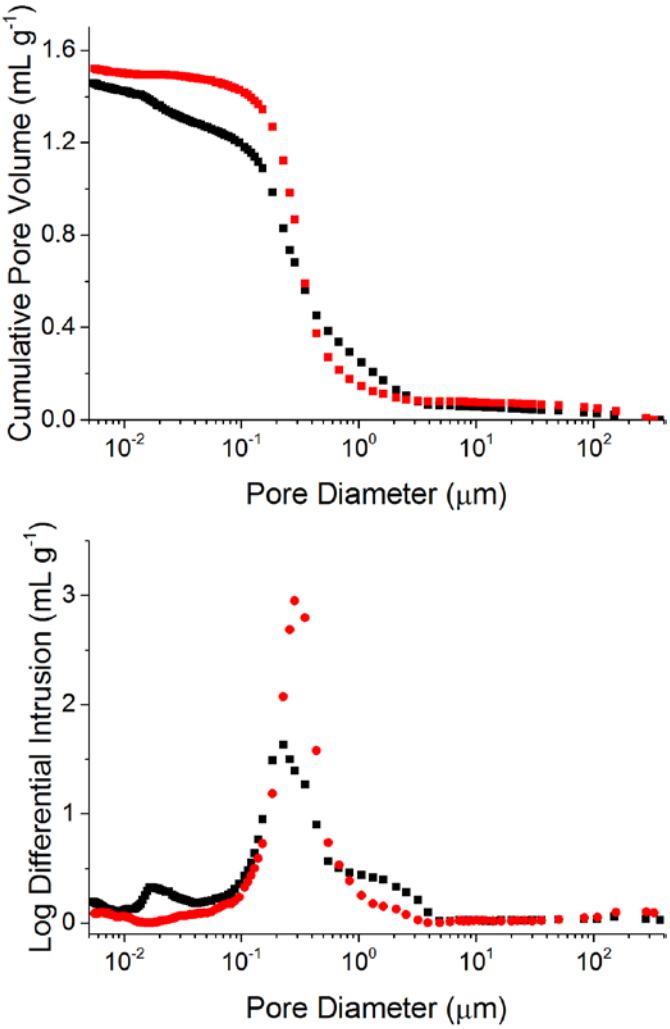

Figure 5.9 *(top)* Cumulative pore volume plots and *(bottom)* log differential intrusion as determined by mercury porosimetry. ZnO Fibers (Red); HFS-4 (Black).

5.3.3.2 Loading Determination via TGA

Figure 5.10 shows the TGA traces of both MOF fiber samples in air. HKUST-1 (top) decomposes sharply below 300 °C to similar residual masses for all samples shown. The variability in residual masses are on the order of ± 2% and indicate no trend with synthesis concentration nor with physisorption loading, as those were essentially identical for all samples.

ZIF-8 TGA traces **Figure 5.10 (bottom)** exhibit a broad 2-step decomposition from 300 to 500 °C; initial mass loss is attributable to the cellulose acetate decomposition while the later mass loss is the thermal decomposition of the organic portions of the ZIF-8 material, which is known for its good thermal stability. Residual masses for the ZFS-N and ZFS-1 samples are both high, but likely for different reasons. The ZFS-N contained a large amount of ZIF-8 as evidenced by physisorption, which decomposed into ZnO, while ZFS-1 likely still possessed some amount of the unreacted ZnO, which was also visible in XRD patterns. Both the ZFS-2 and the ZFS-4 samples left similar residues slightly below ZFS-N sample.

Residual masses were assumed to be entirely ZnO or CuO, depending on the MOF, and it was assumed that all of the metal in the oxide was once part of the MOF structure. Things such as partially amorphous MOF, the presence of unreacted oxides, or excess uncoordinated metal would lead to erroneous values. The results of these calculations are tabulated in Table 5.6 and compared to sorbent loading estimated via isotherm calculations.

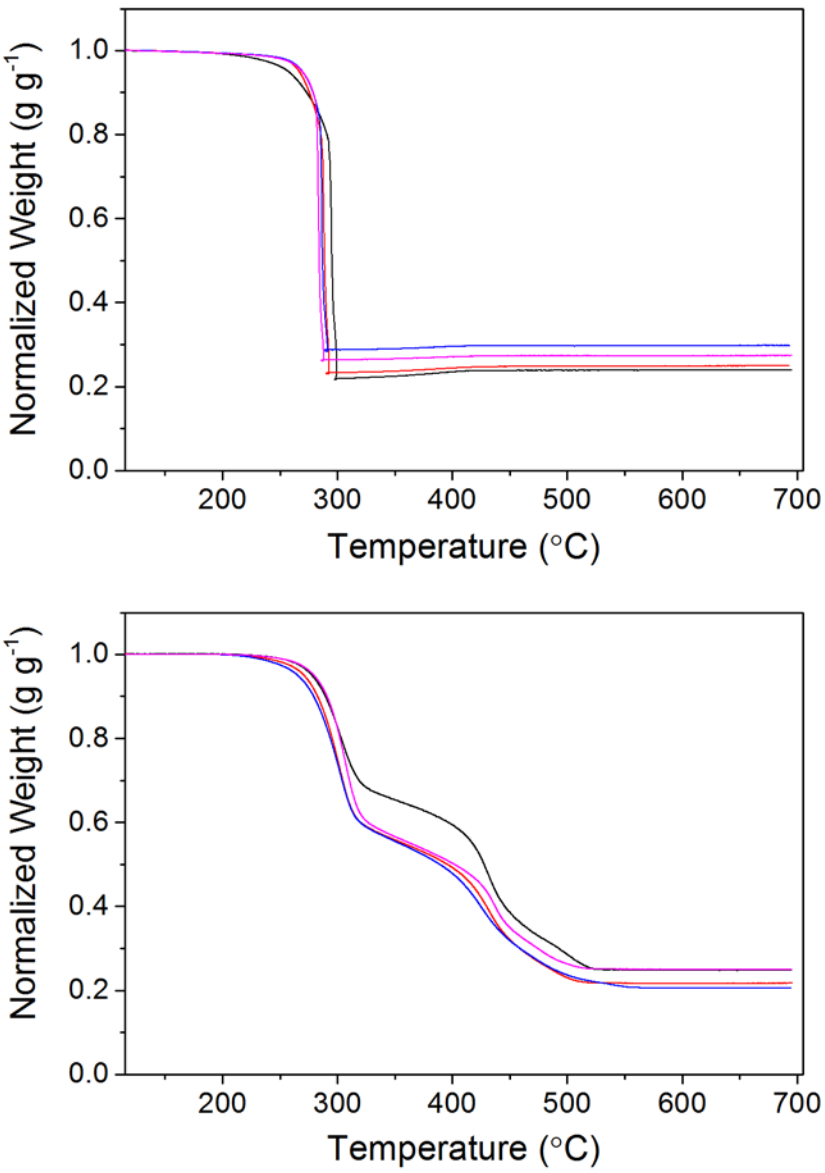

Figure 5.10 Normalized TGA traces of HKUST-1 fibers (top) and ZIF-8 fibers (bottom). Both graphs share the same legend coloring: XFS-1 (magenta); XFS-2 (Blue); XFS-4 (Red); XFS-N (Black).

Table 5.6 Comparison of sorbent loading determination by TGA residual analysis and N_2 physisorption loading

	Residual Mass by TGA [wt %]	MOF Loading by TGA [wt %]	MOF Loading by Physisorption [wt %]
ZIF-8 Samples			
ZFS-N	24.7	69	66
ZFS-4	21.5	60	61
ZFS-2	20.4	57	61
ZFS-1	25.0	70	49
HKUST-1 Samples			
HFS-N	23.8	60	85
HFS-4	24.8	63	83
HFS-2	29.7	75	86
HFS-1	27.2	69	85

5.3.3.3 Alternative Synthetic Protocols

As a control experiment to MOF growth from HDS growth, pure CA fibers were exposed to a water/ethanol solution of $Cu(NO_3)\cdot 3H_2O$ and trimesic acid to promote the growth of HKUST-1 within the material. This resulted in partially blue tinged fibers with negligible nitrogen adsorption at 77 K almost identical to the initial ZnO-loaded fiber material (**Figure 5.11**), indicating essentially no MOF growth. We conclude that bare CA is not a favorable substrate for the growth of MOF crystals.

Attempts to synthesize the HKUST-1 fibers directly from ZnO without first converting to (Zn, Cu) HDS yielded MOF loadings approximately half that of the HFS synthesis route based on physisorption capacity. Upon visual inspection, it was noted that this procedure results in poor penetration of the polymer fiber. This is made evident by a blue ring of HKUST-1 within the fiber surrounding a still white polymer core, indicating an inability to fully penetrate the porous structure of the fiber (**Figure 5.12)**. This is likely

a transport limitation, in that the newly formed MOF layer inhibits diffusion of further building block material into the core of the fiber.

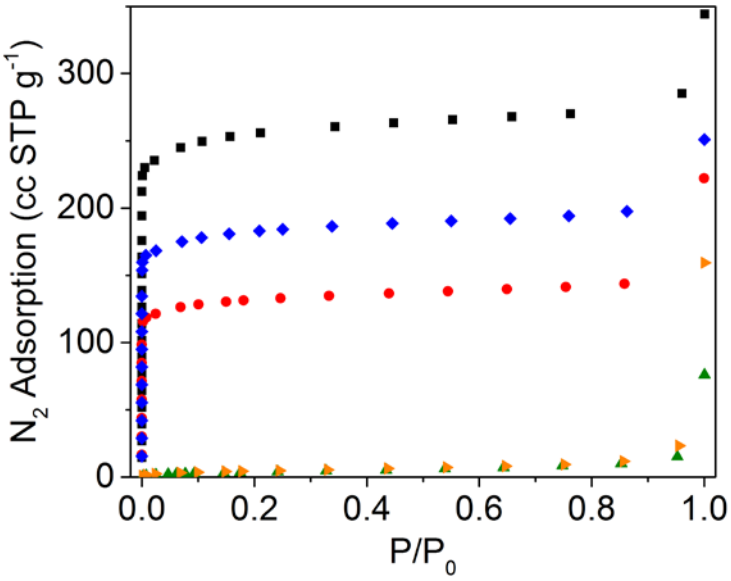

Figure 5.11 N_2 physisorption of HKUST-1 fibers using batch synthesis. From the bottom up: ZnO fibers (Orange); HKUST-1 in blank CA (Green); Direct "1-step" conversion from ZnO fibers (Red); Conversion of HDS fibers without additional copper nitrate in the second step (Blue); HFS-Batch (Black).

Lastly, an HKUST-1 fiber synthesis was attempted in which addition of the organic ligand (BTC) followed the previously demonstrated conversion to (Zn, Cu) HDS, but without the addition of any further $Cu(NO_3)_2$. This was designed to only consume the copper that had been intercalated within the HDS structure to isolate the growth originating from HDS conversion versus that coming from nucleation in solution. This route yielded about 2/3 of the full fiber capacity, indicating that excess copper in the second step is necessary to supplement the initial metal reservoir found within the HDS material. The slightly lower capacity between the batch control and the flow synthesis likely indicates a depletion of the metal and ligand concentration within the batch process that is not present in the flow configuration due to much larger reservoir volumes.

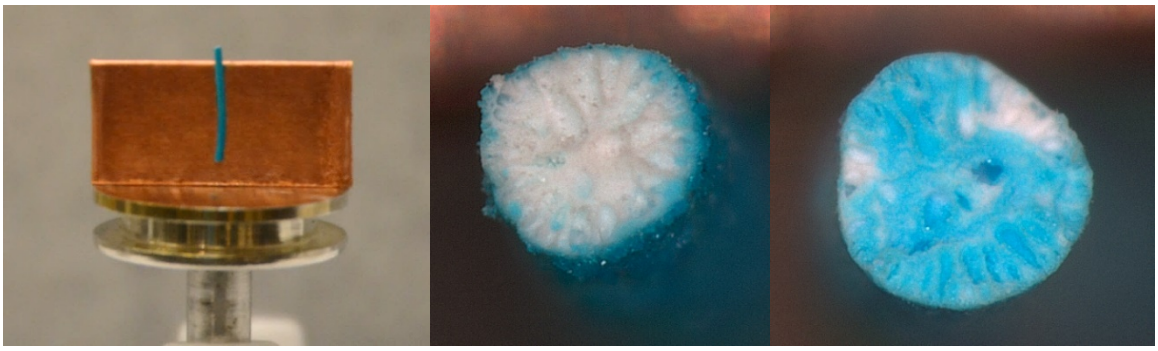

Figure 5.12 (Left and Center) Image of the "1-step" conversion of ZnO fibers into HKUST-1. The core of the fiber remains white, indicating no growth of the MOF material occurred at longer diffusion lengths. (Right) Growth into the center of the fiber in HFS-4 samples shows reduced transport limitations.

Initially, CA/ZnO fibers were easy to handle and relatively flexible, though less so than pure polymer fibers (**Figure 5.13**). When converted to MOF fibers, the increase in volumetric solid loading severely affected the mechanical properties and resulted in brittle fibers that were difficult to incorporate into close-packed modules without breaking; however, assembling the CA/ZnO fibers into modules is straightforward.

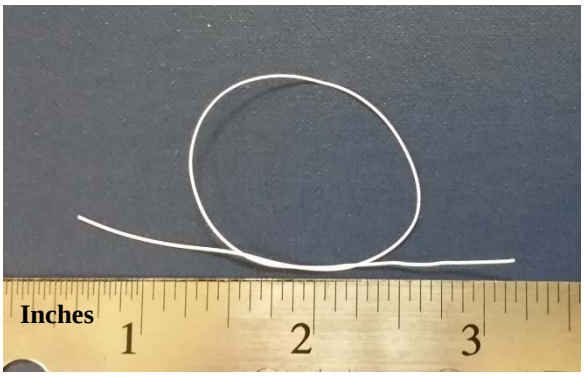

Figure 5.13 Image of a CA/ZnO fiber looped on itself to demonstrate the fiber flexibility. Converted MOF fibers lose this property and can only bend a few degrees before breaking.

To reduce the number of processing steps in the manufacturing of the MOF fiber sorbents, we investigated the possibility of combining the necessary fiber sorbent solvent exchange procedure with the HDS MOF synthesis technique (HFS-N, ZFS-N). These fiber sorbent samples exhibited micropore volumes in excess of those synthesized without

combining solvent exchange and MOF synthesis. This indicates that co-opting the traditional solvent exchange procedure in fiber manufacturing for synthesis is a viable way to reduce both processing time and solvent waste (**Figure 5.14**). Indeed, this seems to indicate that the most effective synthesis route for MOF fiber sorbent production is the conversion of the oxide precursor during the solvent exchange step. However, it would likely necessitate the immediate use of all spun fibers or their storage in water rather than as dried polymer, which would pose supply chain challenges when compared to the conversion from dried fibers.

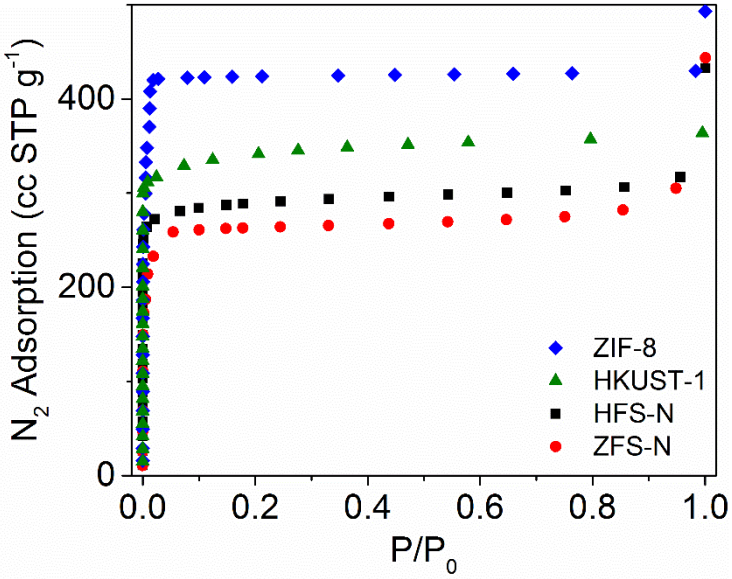

Figure 5.14 N_2 physisorption of ZFS-N (red) and HFS-N (black) compared to neat ZIF-8 (blue) and HKUST-1 (green) powders. BET surface areas (calculated using the method detailed by Walton and Snurr[45]) of powder samples: 1400 m^2 g^{-1} (ZIF-8) and 1350 m^2 g^{-1} (HKUST-1)

Through these experiments, the role of ZnO becomes clear: it is a precursor to both HDS materials when combined with the appropriate salt, which in turn serves as a readily convertible metal source for the MOF structure when the organic ligands are added. In short, it is both a vehicle for rapid synthesis and a repository of metal ions within the fiber.

5.3.4 Fiber Module CO_2/N_2 Breakthrough Experiments

The final goal of this work was to demonstrate the synthesis of fiber sorbents where stability in liquid water or humidity could be a concern, by delivering a ready-to-use mass transfer contactor that could be prepared in dry conditions with minimal handling steps, similar to the use of water-sensitive zeolites (such as Li-ion-exchanged Type X) in air separation applications. To demonstrate this, a fiber sorbent module containing 22 fibers was constructed from the previously described CA/ZnO fibers and 1/4″ Swagelok stainless steel tubing and fittings. All synthesis steps were conducted within the module, which served as the reaction vessel (**Figure 5.15**). During the synthesis, the fibers were fully submerged in solvent and later washed. Modules were then dried under vacuum at 80 °C and packaged under nitrogen for transportation. The prepackaging of the CA/ZnO fibers into Swagelok modules and their subsequent storage under inert gas allows for the elimination of intermediate handling steps that could expose the sorbent to humid conditions, and avoids breakage associated with handling fibers of high sorbent loadings. Given that the sensitivity of HKUST-1 to water is well-known (but not necessarily catastrophic),[6, 32-34] degradation of these fibers would likely not be immediately obvious under ambient conditions. However, protection under an inert atmosphere would certainly be crucial to a more sensitive structure like MOF-5.

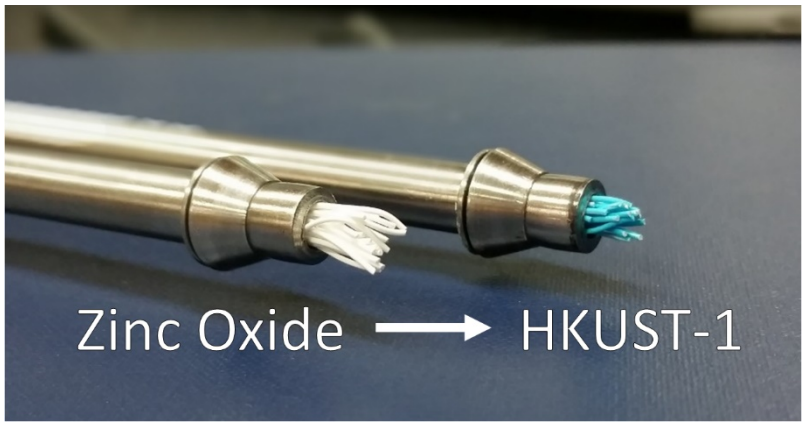

Figure 5.15 Image of HKUST-1 fiber transformation from ZnO within the Swagelok housing module

Breakthrough experiments using HKUST-1 modules were conducted at temperatures of 273 and 308 K, pressures of 1 and 3.5 bar, and feed gas compositions of 12.5 mol %/75% CO_2/N_2 with He as a tracer (**Figure 5.16**). The bed was saturated with N_2 prior to switching to the mixed feed. The sample demonstrates increasing dynamic capacity at lower temperatures and higher pressures, as expected, up to 2.44 mmol/g of fiber, whereas neat HKUST-1 has a pure CO_2 equilibrium uptake of 4.6 mmol/g at 273 K.[35] Dynamic capacities are lower than equilibrium capacities due to nonisothermal operation, nonideal fluid profiles in the fiber sorbent module, or mass transfer limitations (e.g., film transport resistances). Nevertheless, these proof-of-concept experiments highlight that MOF-loaded fiber sorbent modules can be placed into operation without catastrophic loss of the adsorption capacity of the MOFs. Further breakthrough capacities are tabulated in **Table 5.7**.

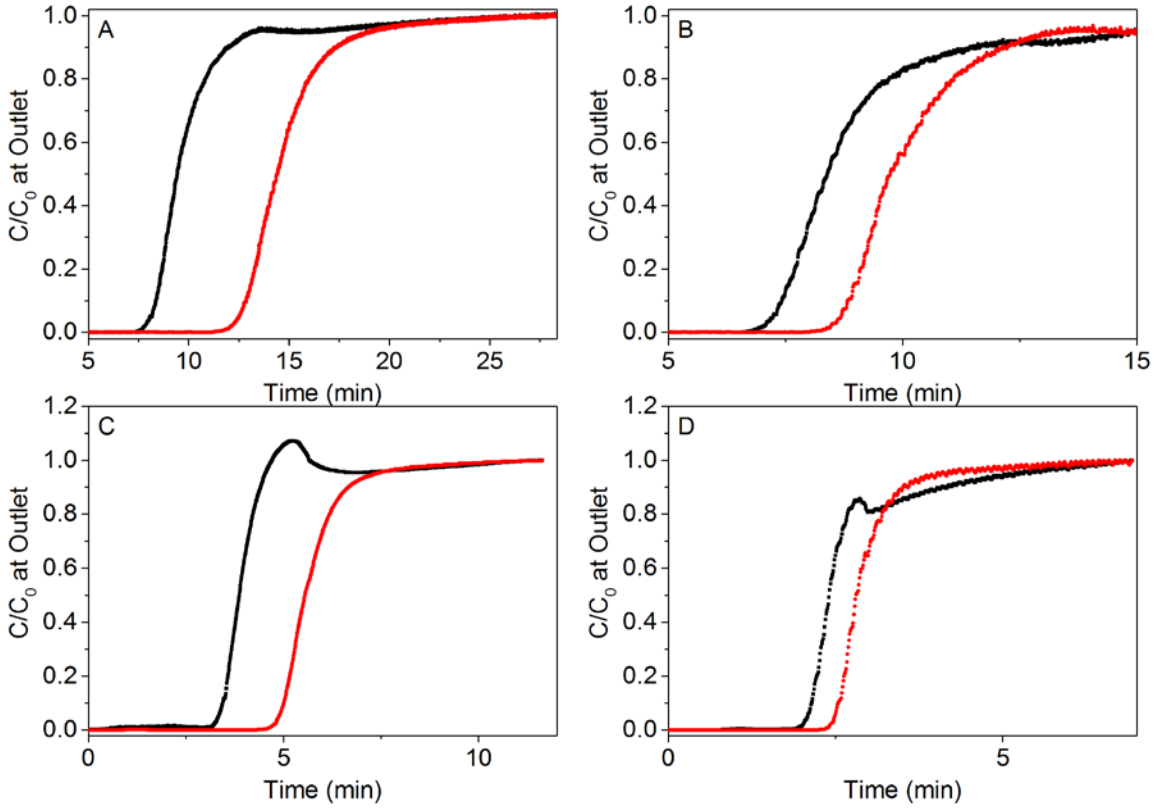

Figure 5.16 CO_2 breakthrough in N_2 at various conditions using an HFS-4 fiber bed. Inlet feed composed of 12.5%/12.5%/75% CO_2/He/N_2 at 30 ccSTP min^{-1}. Helium trace (black); CO_2 (red). (A) 0°C, 3.5 bar (B) 0°C, 1.0 bar (C) 35°C, 3.5 bar (D) 35°C, 1.0 bar

Table 5.7 Bed breakthrough capacities of HKUST-1 fiber sorbent modules

Temperature (°C)	Pressure (bar)	Capacity (mmol CO_2/g fiber)
0	1.0	0.91
0	3.5	2.43
35	1.0	0.15
35	3.5	0.64

5.4 Conclusions

In this work, we have demonstrated the feasibility of a synthesis procedure for the development of fiber sorbent modules that allows for the exclusion of water during and after MOF fiber sorbent synthesis. The use of ZnO as a precursor stable in fiber spinning conditions and its conversion to HDS intermediates allows for the easy and rapid growth

of two MOF structures within a porous polymer. The incorporation of these fibers into stainless steel Swagelok® modules eliminates intermediate handling steps and facilitates their plug-and-play use in an adsorption system without exposure to a humid atmosphere. This opens the door for the use of many more “un-spinnable” MOF materials that exhibit tremendous adsorption capacities but have not moved beyond powder-scale experiments.

5.5 References

1. Pimentel, B. R.; Fultz, A. W.; Presnell, K. V.; Lively, R. P., Synthesis of Water-Sensitive Metal–Organic Frameworks within Fiber Sorbent Modules. *Ind. Eng. Chem. Res.* **2017,** *56* (17), 5070-5077.

2. Lively, R. P.; Chance, R. R.; Kelley, B. T.; Deckman, H. W.; Drese, J. H.; Jones, C. W.; Koros, W. J., Hollow Fiber Adsorbents for CO2 Removal from Flue Gas. *Ind. Eng. Chem. Res.* **2009,** *48* (15), 7314-7324.

3. Fan, Y.; Kalyanaraman, J.; Labreche, Y.; Rezaei, F.; Lively, R. P.; Realff, M. J.; Koros, W. J.; Jones, C. W.; Kawajiri, Y., CO2 Sorption Performance of Composite Polymer/Aminosilica Hollow Fiber Sorbents: An Experimental and Modeling Study. *Ind. Eng. Chem. Res.* **2015,** *54* (6), 1783-1795.

4. Liu, J.; Thallapally, P. K.; McGrail, B. P.; Brown, D. R.; Liu, J., Progress in adsorption-based CO 2 capture by metal–organic frameworks. *Chem. Soc. Rev.* **2012,** *41* (6), 2308-2322.

5. Schoenecker, P. M.; Carson, C. G.; Jasuja, H.; Flemming, C. J.; Walton, K. S., Effect of water adsorption on retention of structure and surface area of metal–organic frameworks. *Ind. Eng. Chem. Res.* **2012,** *51* (18), 6513-6519.

6. Burtch, N. C.; Jasuja, H.; Walton, K. S., Water stability and adsorption in metal-organic frameworks. *Chem. Rev.* **2014,** *114* (20), 10575-612.

7. Thompson, J. A.; Chapman, K. W.; Koros, W. J.; Jones, C. W.; Nair, S., Sonication-induced Ostwald ripening of ZIF-8 nanoparticles and formation of ZIF-8/polymer composite membranes. *Microporous Mesoporous Mater.* **2012,** *158* (0), 292-299.

8. Ortiz, A. U.; Boutin, A.; Fuchs, A. H.; Coudert, F.-X., Investigating the Pressure-Induced Amorphization of Zeolitic Imidazolate Framework ZIF-8: Mechanical Instability Due to Shear Mode Softening. *J. Phys. Chem. Lett.* **2013,** *4* (11), 1861-1865.

9. McKinstry, C.; Cathcart, R. J.; Cussen, E. J.; Fletcher, A. J.; Patwardhan, S. V.; Sefcik, J., Scalable continuous solvothermal synthesis of metal organic framework (MOF-5) crystals. *Chem. Eng. J.* **2016,** *285*, 718-725.

10. Bayliss, P. A.; Ibarra, I. A.; Pérez, E.; Yang, S.; Tang, C. C.; Poliakoff, M.; Schröder, M., Synthesis of metal–organic frameworks by continuous flow. *Green Chem.* **2014,** *16* (8), 3796-3802.

11. Leng, K.; Sun, Y.; Li, X.; Sun, S.; Xu, W., Rapid Synthesis of Metal–Organic Frameworks MIL-101 (Cr) Without the Addition of Solvent and Hydrofluoric Acid. *Cryst. Growth Des.* **2016,** *16* (3), 1168-1171.

12. Sargazi, G.; Afzali, D.; Ghafainazari, A.; Saravani, H., Rapid Synthesis of Cobalt Metal Organic Framework. *J. Inorg. Organomet. P.* **2014,** *24* (4), 786-790.

13. Shah, M. N.; Gonzalez, M. A.; McCarthy, M. C.; Jeong, H.-K., An unconventional rapid synthesis of high performance metal–organic framework membranes. *Langmuir* **2013,** *29* (25), 7896-7902.

14. Feng, X.; Jia, C.; Wang, J.; Cao, X.; Tang, P.; Yuan, W., Efficient vapor-assisted aging synthesis of functional and highly crystalline MOFs from CuO and rare earth sesquioxides/carbonates. *Green Chem.* **2015,** *17* (7), 3740-3745.

15. Guo, Y.; Mao, Y.; Hu, P.; Ying, Y.; Peng, X., Self–confined synthesis of HKUST-1 membranes from CuO nanosheets at room temperature. *ChemistrySelect* **2016,** *1* (1), 108-113.

16. Sachse, A.; Ameloot, R.; Coq, B.; Fajula, F.; Coasne, B.; De Vos, D.; Galarneau, A., In situ synthesis of Cu–BTC (HKUST-1) in macro-/mesoporous silica monoliths for continuous flow catalysis. *Chem. Commun.* **2012,** *48* (39), 4749-4751.

17. Li, S.; Zhang, W.; Zhu, Y.; Zhao, Q.; Huo, F., Synthesis of MOFs and Their Composite Structures through Sacrificial-Template Strategy. *Cryst. Growth Des.* **2015,** *15* (3), 1017-1021.

18. Stassen, I.; Campagnol, N.; Fransaer, J.; Vereecken, P.; De Vos, D.; Ameloot, R., Solvent-free synthesis of supported ZIF-8 films and patterns through transformation of deposited zinc oxide precursors. *CrystEngComm* **2013,** *15* (45), 9308-9311.

19. Reboul, J.; Furukawa, S.; Horike, N.; Tsotsalas, M.; Hirai, K.; Uehara, H.; Kondo, M.; Louvain, N.; Sakata, O.; Kitagawa, S., Mesoscopic architectures of porous coordination polymers fabricated by pseudomorphic replication. *Nat. Mat.* **2012,** *11* (8), 717-723.

20. Darder, M. D.; Salehinia, S.; Parra, J. B.; Herrero-Martinez, J. M.; Svec, F.; Cerda, V.; Turnes Palomino, G.; Maya, F., Nanoparticle-Directed Metal-Organic Framework/Porous Organic Polymer Monolithic Supports for Flow-Based Applications. *ACS Appl Mater Interfaces* **2017,** *9* (2), 1728-1736.

21. Zhao, J.; Nunn, W. T.; Lemaire, P. C.; Lin, Y.; Dickey, M. D.; Oldham, C. J.; Walls, H. J.; Peterson, G. W.; Losego, M. D.; Parsons, G. N., Facile Conversion of Hydroxy Double Salts to Metal–Organic Frameworks Using Metal Oxide Particles and Atomic Layer Deposition Thin-Film Templates. *J. Am. Chem. Soc.* **2015,** *137* (43), 13756-13759.

22. Majano, G.; Pérez-Ramírez, J., Scalable Room-Temperature Conversion of Copper (II) Hydroxide into HKUST-1 (Cu3 (btc) 2). *Adv. Mater.* **2013,** *25* (7), 1052-1057.

23. Zhan, G.; Zeng, H. C., Alternative synthetic approaches for metal–organic frameworks: transformation from solid matters. *Chem. Commun.* **2017,** *53* (1), 72-81.

24. Lin, K.-S.; Adhikari, A. K.; Ku, C.-N.; Chiang, C.-L.; Kuo, H., Synthesis and characterization of porous HKUST-1 metal organic frameworks for hydrogen storage. *Int. J. Hydrogen Energy* **2012,** *37* (18), 13865-13871.

25. Pimentel, B. R.; Lively, R. P., Enabling kinetic light hydrocarbon separation via crystal size engineering of ZIF-8. *Ind. Eng. Chem. Res.* **2016,** *55* (48), 12467-12476.

26. Zhang, C.; Lively, R. P.; Zhang, K.; Johnson, J. R.; Karvan, O.; Koros, W. J., Unexpected Molecular Sieving Properties of Zeolitic Imidazolate Framework-8. *J. Phys. Chem. Lett.* **2012,** *3* (16), 2130-2134.

27. Morioka, H.; Tagaya, H.; Karasu, M.; Kadokawa, J.-i.; Chiba, K., Preparation of hydroxy double salts exchanged by organic compounds. *J. Mater. Res.* **1998,** *13* (04), 848-851.

28. Kandare, E.; Hossenlopp, J. M., Hydroxy double salt anion exchange kinetics: effects of precursor structure and anion size. *The Journal of Physical Chemistry B* **2005,** *109* (17), 8469-8475.

29. Morioka, H.; Tagaya, H.; Karasu, M.; Kadokawa, J.-i.; Chiba, K., Effects of zinc on the new preparation method of hydroxy double salts. *Inorg. Chem.* **1999,** *38* (19), 4211-4216.

30. Rajamathi, J. T.; Britto, S.; Rajamathi, M., Synthesis and anion exchange reactions of a layered copper-zinc hydroxy double salt, Cu1. 6Zn0. 4 (OH) 3 (OAc)· H2O. *Journal of Chemical Sciences* **2005,** *117* (6), 629-633.

31. Tagaya, H.; Sasaki, N.; Morioka, H.; Kadokawa, J., Preparation of new inorganic—organic layered compounds, hydroxy double salts, and preferential intercalation of organic carboxylic acids into them. *Molecular Crystals and Liquid Crystals* **2000,** *341* (2), 413-418.

32. Henninger, S. K.; Jeremias, F.; Kummer, H.; Janiak, C., MOFs for use in adsorption heat pump processes. *Eur. J. Inorg. Chem.* **2012,** *2012* (16), 2625-2634.

33. Henninger, S. K.; Schmidt, F. P.; Henning, H.-M., Characterisation and improvement of sorption materials with molecular modeling for the use in heat transformation applications. *Adsorption* **2011,** *17* (5), 833-843.

34. Liang, Z.; Marshall, M.; Chaffee, A. L., CO2 Adsorption-Based Separation by Metal Organic Framework (Cu-BTC) versus Zeolite (13X). *Energ. Fuel.* **2009,** *23* (5), 2785-2789.

35. Chakraborty, A.; Achari, A.; Eswaramoorthy, M.; Maji, T. K., MOF–aminoclay composites for superior CO 2 capture, separation and enhanced catalytic activity in chemical fixation of CO 2. *Chem. Commun.* **2016,** *52* (76), 11378-11381.

CHAPTER 6. PROPYLENE ENRICHMENT VIA KINETIC PRESSURE SWING ADSORPTION USING ZIF-8 FIBER SORBENTS

This chapter presents the synthesis, testing, and implementation of ZIF-8/Cellulose Acetate fiber sorbents in a kinetic pressure swing adsorption. This is the first time that the successful use of a MOF in a kinetic cycle has been reported. Overall, the process could achieve 81% propane purity in the high-pressure product at 31% recovery without the use of process optimization. The effect of adsorption step time, temperature, and feed rate was investigated and shown to decrease propane product purity while increasing product recovery.

Furthermore, the benefits of structured mass transfer contactors are highlighted by measuring the pressure drop across the utilized fiber bed. This was shown to be significantly smaller than that of packed beds as predicted by the Ergun equation.

This work represents a significant step towards the industrial implementation of MOF-based gas separations and an overall reduction in separation energy consumption.

6.1 Introduction

The separation of propane/propylene is one of the most difficult industrial separations. Due to the close boiling points of both of the components, the relative volatility of the mixture remains low and commercial towers require an excess of 120 stages to achieve polymer-grade (99.5%) propylene.[1] The high reflux conditions necessary to

achieve these purities combine with the cost of refrigeration cycles at below-ambient temperatures to result in an extremely energy intensive separation. Furthermore, the demand for growing plastic and the increased use of natural gas feedstock make this separation more important than ever.[2]

The production of propylene via adsorption is not a novel idea, and most schemes generally involve π-complexation using silver ions or a kinetically-selective adsorbent, typically 4A zeolite.[3-4] However, due to propylene generally being the more strongly adsorbed species in both cases, a highly selective material is required to achieve the target propylene purities.[5] Several reports of metal-organic frameworks with selectivity for the olefin/paraffin pair exist,[6-7] including several demonstrating kinetic selectivity due to restrictive pore apertures.[8] However, previous reports are typically single component investigations or idealized batch adsorptions, and therefore there has never been a report of a successfully implemented kinetic cyclic separation of propane/propylene using metal organic frameworks.

This chapter demonstrates the implementation of ZIF-8 as the molecular sieve supported in fiber contactors, which are utilized in the kinetic separation of propane/propylene.

6.2 Materials and Methods

6.2.1 Materials

The following were used as received without any further purification: Cellulose acetate (50,000 MW, Sigma Aldrich), polyvinylpyrrolidone (K30 Mw 40,000, TCI), N-

methyl-2-pyrrolidone (ACS grade, VWR), methanol (ACS grade, VWR), hexanes (ACS grade, VWR), $Zn(NO_3)_2 \cdot 6H_2O$ (99+%, Alfa Aesar), 2-methylimidazole (97%, Alfa Aesar),), helium (UHP, Airgas), : nitrogen (UHP, Airgas), 50%propylene in propane (certified blend, Airgas).

6.2.2 Spinning of ZIF-8 Fiber Sorbents

Fibers were spun in a dry-jet wet-quench spinning method as described in Chapter 5. In brief, the solids were dispersed using 80% of the total dope solvent by stirring and sonication (3x60s). To this, a polymer solution consisting of 20% of the total dope solvent and polymer was added to maintain solid suspension and dispersion, and again sonicated (3x60s) and stirred via impeller. To the mixed dope, the rest of the dry polymer was added and mixed via impeller for 4 h at 50 °C until homogenous. Overall dope composition is listed under **Table 6.1**. The mixture was loaded into syringe pumps and degassed over night at 50 °C. Due to the high solid volume and size of the particles present within the dope, the fibers were extruded through a 1/8" Swagelok adapter rather than a traditional coaxial spinneret. Fibers were quenched in a water bath and taken up by a rolling drum in a secondary water bath. The spinning conditions for these fibers are detailed in Table 6.2.

Table 6.1 ZIF-8/CA fiber sorbent dope composition

	CA/ZnO (wt %)
NMP	60.10
Water	10.16
Cellulose Acetate (Mw 50,000)	10.24
PVP (Mw 40,000)	3.97
ZIF-8	15.36

Table 6.2 Spinning conditions utilized in this work*

	CA/ZnO
Spinneret Temperature (°C)	60
Bath Temperature (°C)	50
Dope Flow Rate (ml/h)	350
Drum Uptake Rate (m/min)	6.5
Air Gap (cm)	3
Draw Ratio	6.7

*Dope was extruded through 1/8" Swagelok tubing and not a traditional co-annular die

After being cut from the drum, fibers were solvent exchanged in a water bath for 3 days to remove left over NMP from the spinning solution. At this point, while still wet and lightly plasticized, the fibers were loaded into 12" long, ¼" Swagelok® tubing by threading the bundle of fibers from one end of the tube and out the other. This has been found to increase the success rate of loading unbroken fibers, though potentially leads to a lower packing fraction as fibers shrink somewhat after drying. Once inside Swagelok® tubing, the fibers were exchanged 3 times for 1 h in methanol, then hexanes, followed by drying at 110 °C under vacuum.

Fibers were characterized by SEM, XRD, and physisorption to determine their physical properties.

6.2.3 Material Characterization

Sorbent loading of the composite fibers was determined by N_2 physisorption at 77 K in a manner like that previously described in Chapter 5. The microporous volume of the sample was ascribed exclusively to the ZIF-8 within the structure, and fractional approach

to the neat powder loading was used to estimate the sorbent weight loading within the fibers. By this method, the fiber composites were determined to be composed of 57 wt% ZIF-8, closely resembling the expected 60 wt% from the dope formulation. The isotherm of the fibers and the powder sample are shown in **Figure 6.1** and exhibit the same microporous behaviour and gate-opening phenomena, suggesting little difference in the sorbent characteristics.

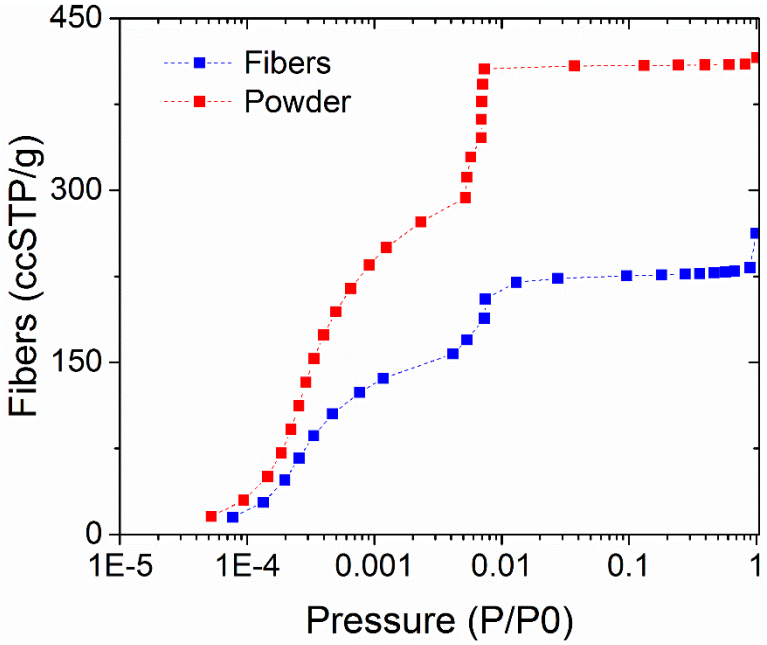

Figure 6.1 N_2 physisorption of the fiber sorbents and the ZIF-8 powder used in the formation of the composite material

XRD was conducted on the fibers after spinning and compared to the powder samples, and revealed that no structural changes had occurred in the ZIF-8 material (**Figure 6.2**). The ability of ZIF-8 to survive the spinning process is not unexpected, as ZIFs are one of the more stable MOF families and are not susceptible to degrading in either water or the spinning solvents employed. The differences in peak intensities are likely a result of statistical distribution of exposed faces, as much fewer crystals are contained in the fiber scan than in a powder scan. A slight systematic shift towards higher 2θ in the fiber peaks

is a result of the fiber dimensions on the sample holder changing distance to sample. The larger dimensions of these fibers exaggerate this artifact relative to other fiber work presented in previous chapters.

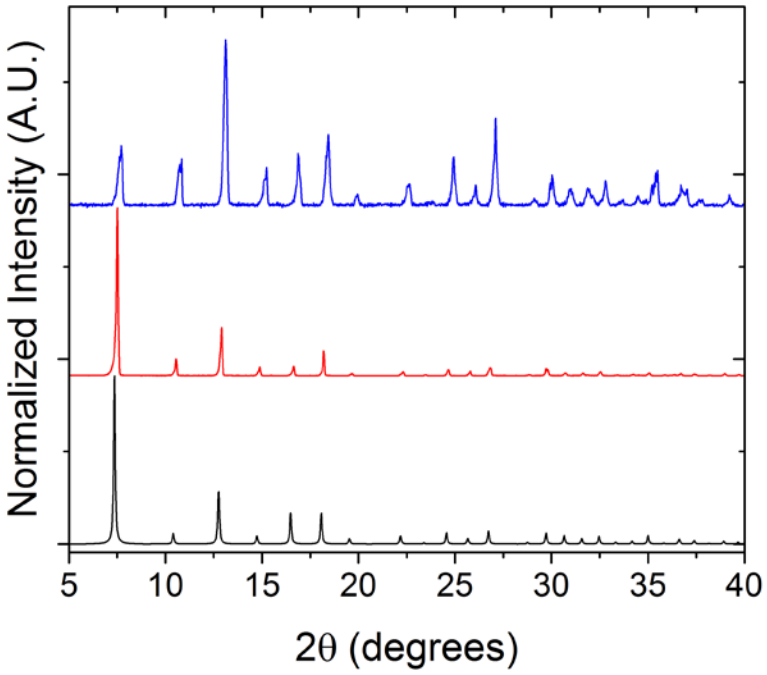

Figure 6.2 XRD patterns of ZIF-8 fiber sorbents (blue), ZIF-8 powder (red), and simulated powder pattern (black)

In SEM, ZIF-8 crystals of varying sizes can be seen within the cross-sectional images, although almost all the crystals are above 20 µm. Most of the sorbent seems to be present in large crystals with diameters greater than 100 µm (**Figure 6.3**). These crystals are well-dispersed throughout the fiber, as are the indentations of other crystals that came away on the other face of the sample fracture. The large size of the crystals with respect to the overall fiber diameter at times gives an impression of maldistribution, but no significant clumping exists and few crystals are seen to be in "face to face" configurations. The average fiber diameter was measured to be 1000 µm, with some variations present due to disturbances of the spinning line by large volumes of solids and some variability in spinning conditions.

Higher magnification cross sections reveal a highly porous polymer substructure largely indicative of spinodal decomposition, although some nucleation and growth domains can be observed (**Figure 6.3** Cross-sectional image of ZIF-8 fiber sorbents demonstrating large crystals dispersed throughout the polymer matrix

Figure 6.4). It may be possible to further enhance the substructure transport by slight modifications to the spinning dope composition. Some portions of the fiber outer diameter show a slight densification of the polymer, potentially creating a less permeable skin layer, despite the absence of any significantly volatile solvent in the dope that typically leads to skin formation (**Figure 6.5**). However, this layer is likely extremely defective and does not pose a serious barrier to transport. Previous work has been able to make ultra-permeable sorbent fibers by employing an acetone sheath layer to dissolve any skin that may form in the air gap,[9] but that technique was not possible here due to the inability to extrude the dope through a traditional co-annular spinneret.

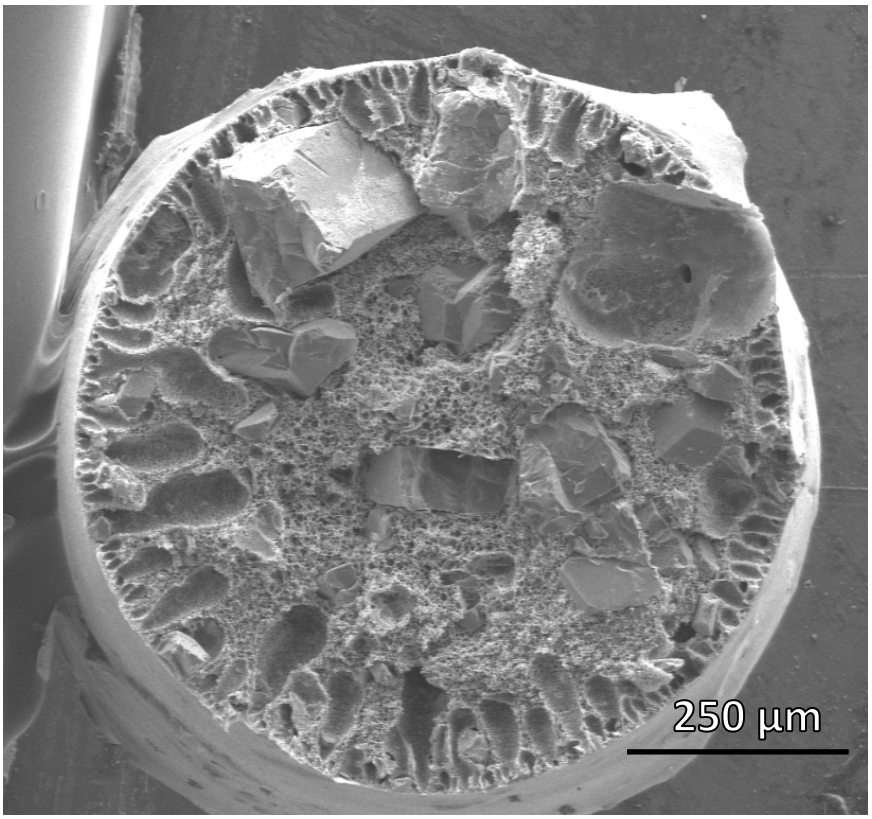

Figure 6.3 Cross-sectional image of ZIF-8 fiber sorbents demonstrating large crystals dispersed throughout the polymer matrix

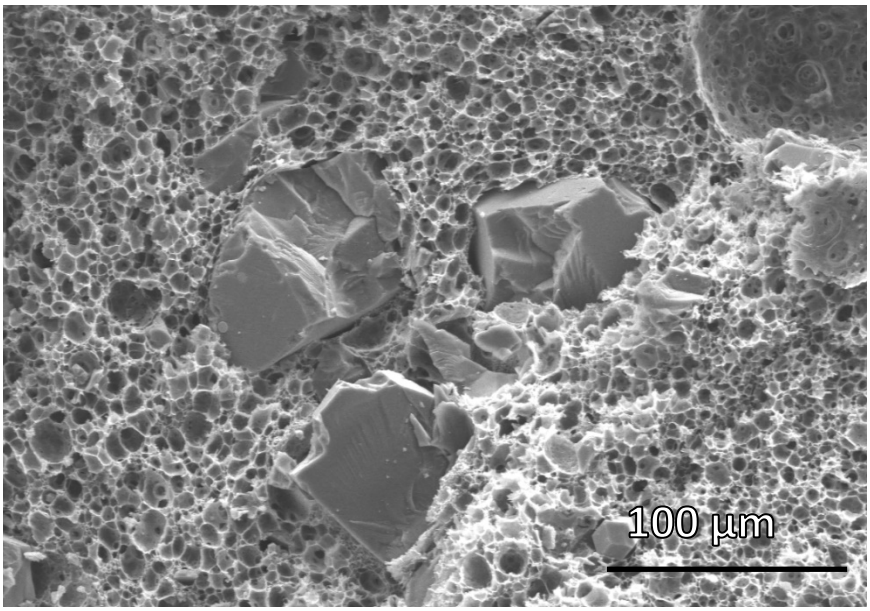

Figure 6.4 Close-up of ZIF-8 dispersed within the polymer matrix, which exhibits a fairly open pore structure indicative of spinodal decomposition

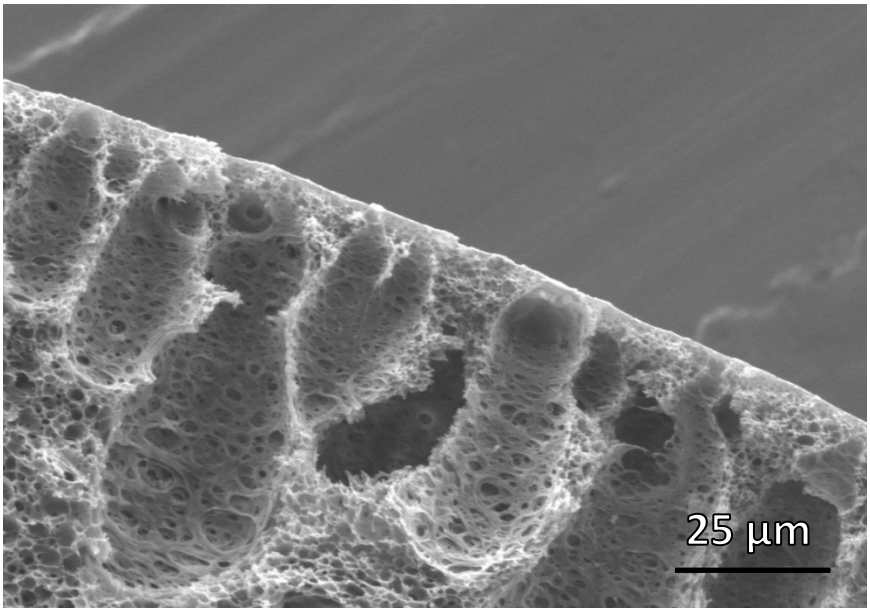

Figure 6.5 Higher magnification view of the ZIF-8 fiber sorbent outer edge

6.2.4 Operation of the Pressure Swing Adsorption Unit

Cyclic studies and breakthrough experiments were carried out in a custom PSA cabinet by L&C Technologies within a climate controlled chamber. The system has been previously described in Chapter 5. Samples were initially degassed at 110 °C for 12 h under vacuum prior to breakthrough experiments, where they were pre-saturated with N_2 before being introduced to an equimolar propane/propylene stream diluted in helium (80%) at 1 bar. Cyclic experiments used undiluted equimolar propane/propylene feed at 2 bar. Cyclic experiments were carried out in a symmetric two-bed configuration. Prior to the first cyclic experiments, beds were equilibrated under approximately 10 ccSTP of the feed mixture at 1 bar and 40 °C to rapidly saturate the slower diffusing species, then brought down to 0 °C under the same flow. This aids in the rapid approach to cyclic steady state of kinetic separations, and similarly beds were subsequently not evacuated in between different cycle

configurations. Each configuration was evaluated over 30 cycles and was generally seen to achieve a cyclic steady state after 15 cycles.

Cycles were simple 4-step VPSA configurations consisting of (1) co-current feed pressurization at 2 bar, (2) co-current adsorption under feed flow at 2 bar, (3) product-end pressure equalization, (4) counter-current bed evacuation under full vacuum. No blowdown was necessary given the bed equilibration occurring at 1 bar. Due to the configurational limitations of the unit, the adsorbed product could not be directly measured and instead the cycle performance has been gauged by the high-pressure propane rich product, rather than the more valuable propylene rich stream. For similar reasons, the typical purge steps associated with kinetic production of high-purity propylene could not be incorporated, and therefore we present this work as a demonstration of the viability of the composite material towards kinetic separations rather than as a direct comparison with other published works.

Table 6.3 Bed characteristics used in this study

Bed Length (cm)	30
Bed Diameter (cm)	0.48
Number of Fibers (-)	11
Fiber Diameter (μm)	1000
Void Fraction (-)	0.5
Total Sorbent Mass (g)	1.2

Cycles were evaluated through the conventional metrics of purity, recovery, and productivity over the last 6 cycles. Purity was determined via mass spectrometry while purity and recovery were calculated as follows:

$$Recovery = \frac{\int n_{2,out} \cdot y_{out}}{\int \left(n_{1,feed} + n_{2,feed}\right) \cdot y_{1,feed}} \tag{6.1}$$

$$Productivity = \frac{\int n_{2,out} \cdot y_{out}}{t_{cycle} \cdot m_{sorbent}} \tag{6.2}$$

Propylene stream compositions were estimated from the mass balance of the system.

6.3 Results and Discussion

6.3.1 Fixed Bed Experiments

Breakthrough analysis of the fiber reveal behavior like that observed in Chapter 5 when using large ZIF-8 crystals, where propane is seen to breakthrough before propylene due to greater mass transfer limitations to the olefin. The initial low level of propane detected in the outlet prior to helium breakthrough is a result of calibration error where the shared 28 m/z peak of nitrogen is partially attributed to propane. The breakthrough of propane suggests that adsorption is still occurring at time scales relevant to the experiment, given that the concentration curve is much broader than that of the helium tracer. However, at these temperatures and crystal dimensions, propylene is still significantly mass transfer limited, although obviously less so than propane, and its breakthrough shows relatively little sharpness and little of the typical light component roll up that comes from adsorptive displacement fronts. This, coupled with the knowledge that equilibrium isotherms are nearly identical in ZIF-8 for these two gases, supports the hypothesis that large ZIF-8

crystals are present within the fiber sorbent and are sufficiently accessible to enable operation under a selective kinetic regime.

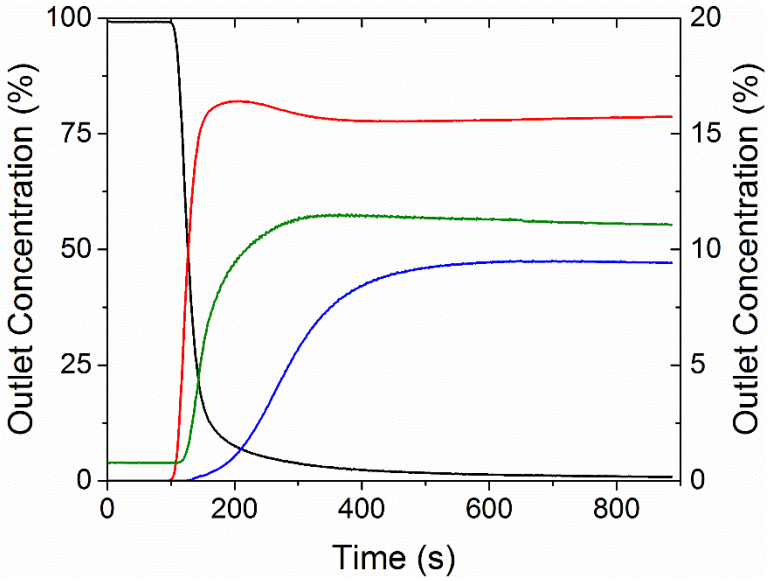

Figure 6.6 Fixed bed breakthrough of a propane/propylene mixture diluted in helium at 1 bar and 0 °C. N_2 (black), He (red), propane (green), propylene (blue).

6.3.2 Fiber Bed Pressure Drop

The pressure drop across the fiber modules were evaluated as a function of superficial velocity using a differential pressure gauge. The results are presented in where four different modules constructed from the spun fibers are compared to predictions of the Ergun equation for particle sizes of similar dimensions and comparable bed porosity. This most fairly compares the diffusive length scales present in both systems, although packed beds typically use extrudates 3 to 8 times larger than our current fiber dimensions to mitigate excessive pressure drop.

As expected of structured contactors versus randomly packed particles, the pressure drop across the fiber modules is significantly smaller than that predicted by the Ergun equation, and increases much more slowly with superficial velocity. The ability to employ

higher fluid velocities results in an increase in overall mass transfer throughout the bed and improved cycle productivity, which can outweigh the lower mass of sorbent compared to extrudate packed beds.

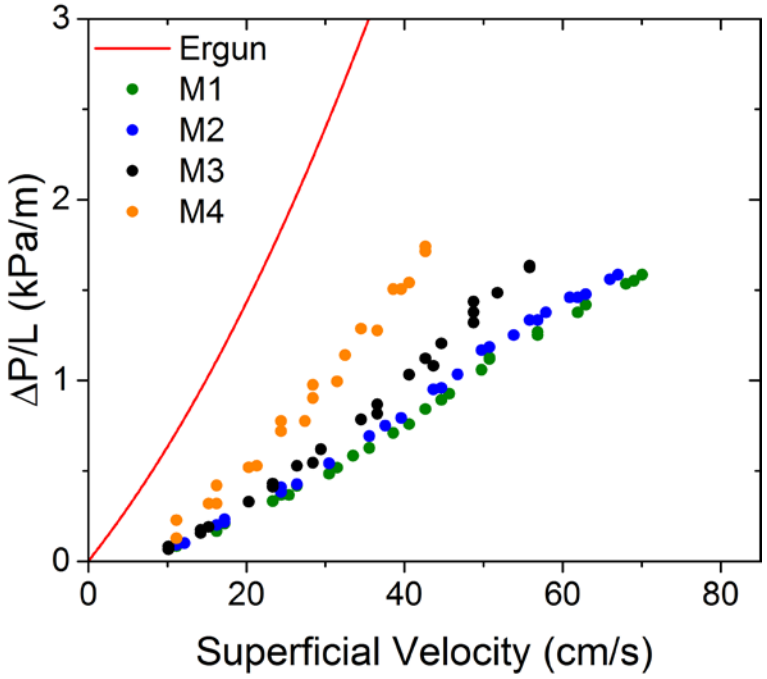

Figure 6.7 Measured pressure drop of fiber modules prepared in this work compared to a traditional Ergun calculation. Packed beds were calculated to have 50% porosity and a particle size of 1 mm to correspond with measured fiber bed characteristics. Modules 1 and 2 were used in the cyclic performance studies.

It is important to note that a fair amount of variance exists in the pressure data across the four modules. This is a result of several factors, some unique to this specific batch of fibers and others a more general trait of packed modules. As previously mentioned, slight variations in the draw ratio during spinning as well as large solid particle dimensions within the dope led to some differences in fiber diameter as a function of length. These likely introduce some degree of non-uniformity amongst the module, and indeed so much so that one module (M4) only contains 10 fibers as opposed to the 11 fibers in other modules. A similar problem arose in M3, where frictional resistance during loading led to

fibers breaking approximately 3/4 of the way into the module, and therefore the last ¼ of the module was packed from the other direction rather than threaded through the tube opening. The discontinuity in the packing at the break interface is certainly a source of variability and contributes to a higher pressure drop relative to the two “perfectly packed” modules, M1 and M2.

A largely unavoidable aspect of the fiber modules is their difficulty in packing, especially in the case of high solid fraction fibers or fibers supporting large particles, both of which tend to be brittle. This makes packing fractions in excess of 50-60% difficult to achieve, and therefore the most structured state of the structured packing is rarely achieved in these experiments. The greater configurations available at lower void fractions and the space allowed for fibers to curl and curve while in the module lead to non-ideal pressure drop and mass transfer behavior. Lower packing fractions also increase the risk of channelling pathways and decrease product purity; the development of a reliable low-void bundling process for brittle sorbent fibers should be a high priority in the development of module technology.

6.3.3 Cyclic Pressure Swing Experiments

The kinetic cyclic performance of the ZIF-8/CA fiber modules were evaluated using two fiber beds packed with 11 unbroken fibers of 1000 μm diameters, M1 and M2. Various conditions were tested to explore the parameter space, including pressurization and feed rate, feed time, and process temperature. Most experiments were conducted at 0 °C, with some at 15 and 35 °C. The pressure cycle of a single bed in the experiment is show in **Figure 6.8** for several cycles, where an omitted second bed exhibits identical but

offset pressure histories to maintain a constantly operating separation unit. An example of the approach to cyclic steady state of the outlet concentration is presented in **Figure 6.9**. The experiment was begun immediately after investigating other parameters, therefore initial concentrations do not match feed conditions. Forgoing the use of a product storage tank allows for faster approach to equilibrium in low productivity situations, but the lack of outlet buffer leads to some degree of noise in the outlet concentration.

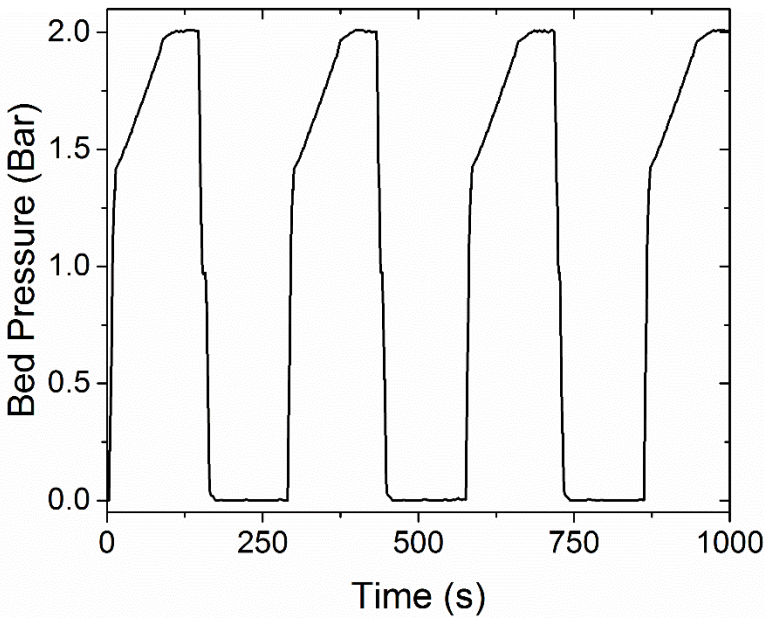

Figure 6.8 Pressure history of a single bed within the PSA cycle for a given two-bed cycle

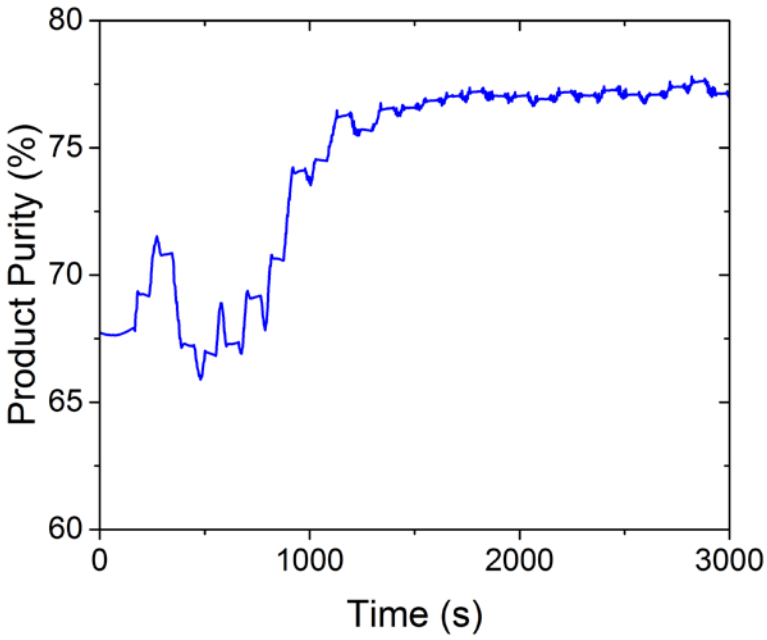

Figure 6.9 Outlet concentration during cycle operation demonstrating the approach to cyclic steady state.

We observe that cycles with longer bed residence times for the feed (i.e. slower pressurization and lower feed rates) generally produced a higher purity product. This is likely due to propylene having longer time to adsorb into the crystal, and suggests that the diffusive time scale of the propylene in the system is still greater than our operating parameters. As we did not observe a maximum in purity with decreasing flow rate, where we would see a return to equilibrium control, we assume that system was still operating within the kinetic regime. Were propane given enough time to adsorb, it would displace propylene and move towards equilibrium control of the separation, while overly fast residence times do not allow for enough adsorption to significantly alter the void composition. These transitions are more clearly demonstrated in the batch adsorption experiments conducted in Chapter 4. A table summarizing the results of all tested cycle configurations is presented in Table 6.4.

Table 6.4 Summary of cyclic PSA results using kinetic ZIF-8 fiber sorbents

Temperature (K)	Pressurization[d] (cc/min)	Feed[d] (cc/min)	Feed Time (s)	Purity[a,b] (%)	Recovery[a] (%)	Productivity[d] (cc/g min)
273	154	77	60	62 [76]	85	33
	77	77	30	67 [65]	64	20
			60	63 [77]	85	27
		39	30	74 [58]	38	9
			60	69 [65]	62	13
			90	64 [68]	72	15
		19	60	77 [58]	35	6
	39	39	60	71 [63]	60	10
		19	60	79 [57]	34	4
		19	90	77 [65]	49	6
		10	120	81 [58]	31	3
288	77	39	60	70 [65]	61	13
		19	60	76 [58]	34	5
	39	39	60	72 [67]	62	10
		19	60	79 [57]	29	3
308	77	39	60	69 [65]	60	13
		19	60	77 [57]	30	5
	39	39	60	71 [65]	60	10
		19	60	78 [56]	26	3

[a]Purity and recovery are based propane. [b]Propylene purity calculated from a mass balance, reported in [brackets]. [d]Volume units of cc are specifically ccSTP as measured by mass flow controller and corrected for thermal conductivity.

A non-optimized parametric study of some of the cycle variables reveals opposing trends in purity and recovery, as is typical of most PSA systems. Increasing the feed flow rate during the adsorption step increased product recovery, as a greater portion of the total inlet gas (feed and pressurization) from the cycle is now creating high-pressure product. However, both the reduced residence time that results from the parameter change and the increased mass needing to be adsorbed decreases product purity, as the sorbent becomes more saturated and less time is permitted for propylene adsorption. Clearly, it is not only a matter of saturating the sorbent, as would be expected in equilibrium separations, since cycles with equivalent feed production (i.e. twice the feed time, half the feed rate) demonstrate higher purity at lower flow rates. The only discrepancy in this comparison is that longer cycle times also mean longer evacuation steps, as the 2-bed cycle used in this work is necessarily symmetric.

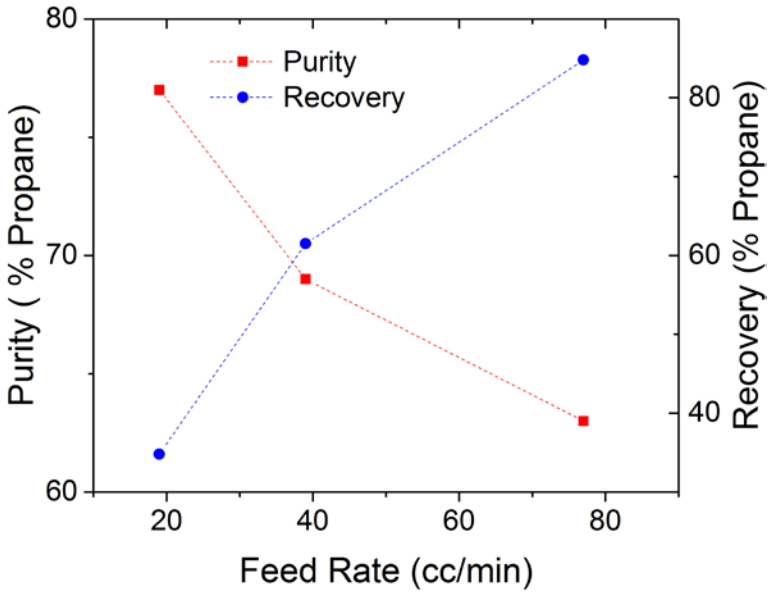

Figure 6.10 Effect of feed rate on purity and recovery of propane at 0 °C. Pressurization (77 cc/min) and cycle time (60 s) held constant.

The effect of feed time on purity and production was similarly typical to that of equilibrium PSA systems. As the sorbents become saturated at higher feed times, lower

purity product is produced. However, product recovery increases since a greater portion of the cycle time is spent producing high pressure product relative to pressurization steps.

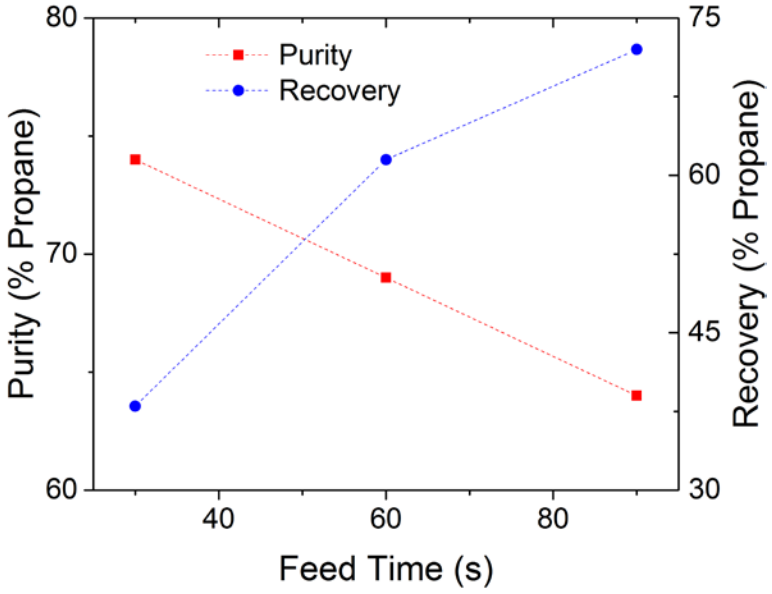

Figure 6.11 Effect of feed time on purity and recovery of propane at 0 °C. Pressurization (77 cc/min) and feed rate (39 cc/min) held constant.

The highest achievable purity in this configuration was 81% propane at 31% recovery, demonstrating the ability of this composite material to partially separate the difficult olefin paraffin mixture. At higher temperatures, we expect the diffusion coefficients of both components to increase, but propane more so than propylene given measured activation energies. This would result in decreased product purity but potentially an increase in productivity, since the mass transfer of the system would be faster overall.[10] Our experiments at higher temperatures only saw mild changes in performance, which indicates that this separation could potentially be performed at room temperature conditions. It is likely that the effect of changing kinetic selectivities in the system would be more pronounced with the use of smaller crystal dimensions (characteristic times more

closely resembling reasonable cycle parameters), or in the measurement of the evacuated propylene product.

The overall trends in purity and recovery can be visualized in a Pareto plot, shown in **Figure 6.12**. These demonstrate the common trade-off between purity and recovery exhibited in all pressure swing adsorption systems where the Pareto front was drawn based on available experimental data. The goal of future work and process optimization should be to push the front towards the upper right corner, indicative of a more effective separation and visualized by the secondary front and arrow within the figure.

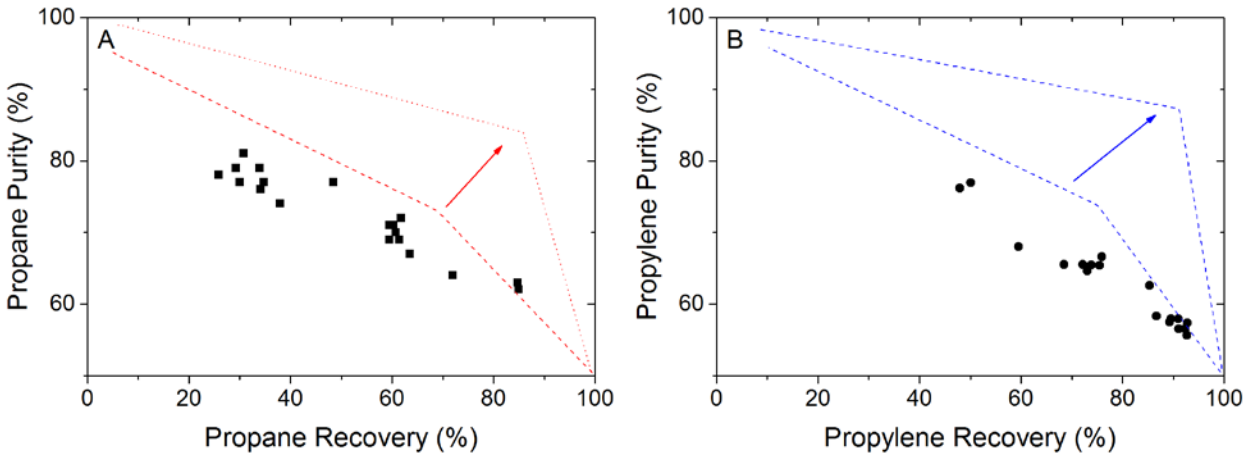

Figure 6.12 Pareto plots of propane (A) and propylene (B) streams from experimental conditions and results reported in Table 6.4. Propane streams were measured directly while propylene values were calculated via a mass balance of the system.

6.4 Conclusions

In this chapter, we present the first reported use of a metal-organic framework (ZIF-8) in a kinetic PSA cycle, along with its incorporation into a structured sorbent fiber contactor. The composite material exhibits high sorbent loadings and fast mass-transfer properties, in addition to demonstrating a lower pressure drop across the bed due to its

ordered packing at 50% void fraction. The sorbent was demonstrated to have survived the spinning process and maintained its large crystal domains which enable its application in diffusionally-selective adsorption of propane over propylene.

Simple 4-step cycles which used these fiber beds were able to produce high pressure product of up to 81% propane from an equimolar mixture. Increasing feed rate or feed time was shown to decrease product purity and increase recovery, a function of both mass transfer limitations and sorbent saturation. Temperature was found to only have a slight effect on product outcome, likely due to the size of the crystals being employed. Future work will emphasize the use of a mathematical model for robust process optimization and the increase of module packing fraction to increase product purity and productivity.

6.5 References

1. Eldridge, R. B., Olefin/paraffin separation technology: a review. *Ind. Eng. Chem. Res.* **1993,** *32* (10), 2208-2212.

2. Waldheim, J., OUTLOOK '18: US propylene production set to expand in 2018. *ICIS News* 3 Jan, 2018, 2018.

3. Padin, J.; Rege, S. U.; Yang, R. T.; Cheng, L. S., Molecular sieve sorbents for kinetic separation of propane/propylene. *Chem. Eng. Sci.* **2000,** *55* (20), 4525-4535.

4. Rege, S. U.; Padin, J.; Yang, R. T., Olefin/paraffin separations by adsorption: π-Complexation vs. kinetic separation. *AlChE J.* **1998,** *44* (4), 799-809.

5. Da Silva, F. A.; Rodrigues, A. E., Propylene/propane separation by vacuum swing adsorption using 13X zeolite. *AlChE J.* **2001,** *47* (2), 341-357.

6. Bloch, E. D.; Queen, W. L.; Krishna, R.; Zadrozny, J. M.; Brown, C. M.; Long, J. R., Hydrocarbon Separations in a Metal-Organic Framework with Open Iron(II) Coordination Sites. *Science* **2012,** *335* (6076), 1606-1610.

7. Xiang, S.; Zhou, W.; Gallegos, J. M.; Liu, Y.; Chen, B., Exceptionally high acetylene uptake in a microporous metal-organic framework with open metal sites. *J. Am. Chem. Soc.* **2009,** *131*, 12415-9.

8. Eddaoudi, M.; Kim, J. Y.; Rosi, N. L.; Vodak, D.; Wachter, J.; O'Keeffe, M.; Yaghi, O. M., Systematic design of pore size and functionality in isoreticular MOFs and their application in methane storage. *Science* **2002,** *295*, 469.

9. Lively, R. P.; Koros, W. J.; Johnson, J., Enhanced cryogenic CO2 capture using dynamically operated low-cost fiber beds. *Chem. Eng. Sci.* **2012,** *71*, 97-103.

10. Grande, C. A.; Rodrigues, A. E., Propane/propylene separation by pressure swing adsorption using zeolite 4A. *Ind. Eng. Chem. Res.* **2005,** *44* (23), 8815-8829.

CHAPTER 7. PROPYLENE SPLITTER ENHANCEMENT BY PRESSURE SWING ADSORPTION

The high-level assessment of a PSA prefractionation retrofit to a propylene splitter system is modeled in ASPEN to determine the potential energy savings associated with a hybrid distillation configuration. The system is first assessed as a stand-alone column at 9 bar and a 70% propylene feed, then the feed is prefractionated at modest PSA performance levels and fed into the column as two distinct streams. The PSA reduces the tower reflux ratios and lowers the overall energy consumption.

Analysis of the system indicates that a PSA system with a 90 mol% propylene product at 50% propylene recovery can reduce the tower energy costs by 41%, and maintain constant energy usage while increasing unit throughput by 77%.

7.1 Introduction

The industrial separation of propane and propylene is an extremely challenging and expensive distillation. The close boiling points of the components typically requires an excess of 120 stages, and the cost of low-temperature refrigeration cycles leads to the use of higher pressure distillation systems that further decrease the relative volatility ratio.[1] Furthermore, propylene is generally required in purities >99.5 mol% for polymer polypropylene production, leading to high reflux ratios and associated energy costs. The separation of this mixture via adsorption techniques could aid or replace distillation columns, although very selective sorbents are required since propylene is often the stronger

adsorbed component in these systems and recovered as the heavy product during the blowdown and evacuation step.

In this chapter, we aim to quantify the potential energy savings that could arise from the implementation of an adsorptive prefractionation in a propylene splitter train. When the separation work done by the PSA occurs at a lower energy cost than that in a distillation column, such as in the case of low relative volatility separations, the inclusion of a hybrid distillation system can result in a reduction of reflux ratio at constant outlet specifications.[2-3] This reduction in reflux ratio can similarly be used to increase overall tower throughput and debottleneck the separation trains.

This work attempts to make an estimation of the potential energy savings associated with the inclusion of a pre-fractionation system in a propylene splitter and subsequently identify the potential for increased feed throughput under nominal PSA performance metrics.

7.2 Modeling Methods

Distillation was modelled using ASPEN Plus V9 software with the use of various column models. The shortcut DSTWU (Distillation Winn-Underwood-Gilliland Method) was initially employed for the determination of minimum reflux ratio, number of stages and feed stage number, which were then used as starting points for more rigorous simulation using the RadFrac column model. Columns used total condensers and partial reboiler stages, from which heating and cooling duties were extracted. The overall energy usage of the column was considered the absolute sum of the condenser and reboiler. Material properties were estimated by use of the Soave-Redlich-Kwong equation of state.

As a base case, RadFrac columns were operated at $R = 1.5\ R_{min}$ with a Murphree efficiency $EM = 85\%$ and a corresponding stage count of $Stages = \frac{Stages_{Shrct}}{EM} \times 100$. A pressure drop of 0.1 bar across the entire tower was assumed. The column feed consisted of 100 kmol/h saturated vapor with a composition of 30 mol% propane and 70mol% propylene.

PSA units were implemented as a single stage separator with outlet compositions dictated by pre-determined purity and recovery values that are likely achievable based on results in chapter X. The energy consumption of these units were calculated separately as compression costs and exit streams were assumed to be saturated vapor. When including PSA systems, the entire feed was pre-fractionated then fed to the distillation column at the stage most closely resembling the stream composition.

Columns were not attempted to be heat integrated as it was determined to fall outside the scope of this chapter. Improvements to the process were quantified by total energy consumption rather than monetary cost.

7.3 Propylene Separation by Cryogenic Distillation

A great number of configurations for propylene splitters exist in practice and literature.[1] These often come down to the availability of cooling fluid at a given temperature and the associated economic analysis, including the source and enthalpy of the feed stream. These configurations mainly differ in their operating pressure: lower pressure units operate at colder temperatures, generally require a refrigeration cycle, but have a higher relative volatility and therefore require fewer stages and lower reflux. Higher

pressure units operate above room temperature and can use lower cost cooling water, but require more column stages and higher reflux ratios to achieve the same purities, given that relative volatilities decrease at higher pressures.

The process requirements were set to a propylene product purity of 99.5% and a recovery of 99.5% with a condenser pressure of 9 bar and a tower pressure drop of 0.1 bar. This results in a condenser temperature of 15 °C and a boiler temperature of 23 °C. Towers operated at a molar reflux ratio of 12.7 with 120 stages. The base case results in a condenser cooling load of 4.6 MW and a boiler heating load of 4.1 MW. The base case is summarized in **Figure 7.1**.

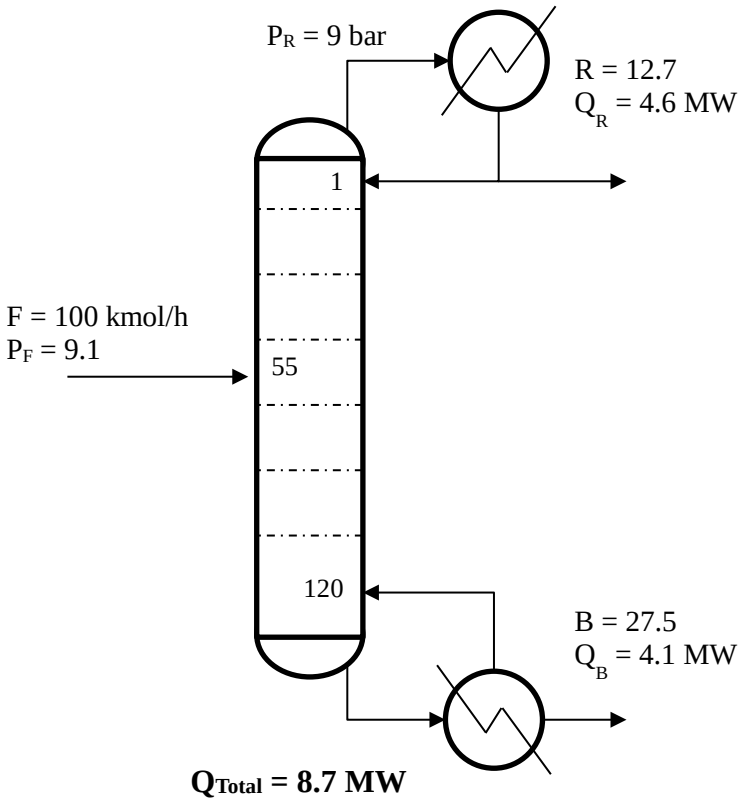

Figure 7.1 Base energy case for propane/propylene distillation. Feed composed of 70 mol% propylene with a 99.5 mol% propylene purity and recovery in the distillate.

7.4 Propylene Separation by Pressure Swing Adsorption

The prefractionation of the tower feed by PSA was modeled as a black box, where only the vacuum and recompression costs were considered. The work done per mole of gas by compressors and vacuums were modeled by **Eq 7.1**[4]

$$W_P = \left[\frac{J}{mol}\right] = \frac{RTln\left(\frac{P_H}{P_L}\right)}{\eta} \tag{7.1}$$

where P_H and P_L represent the high and low pressures respectively, and η the isentropic efficiency of the machine, set to 80%. Vacuum work was taken to be equivalent to compression in reverse, but with a lower efficiency (70%). Based on results from previous chapters, the performance metrics of the PSA system were taken to be that of 90% purity in the propylene product with 64% recovery. This represents a separation factor of 3.85 where our most reasonable comparison yields 3.35 at 49% recovery. This performance is slightly beyond that of what we have so far been able to achieve, but is a reasonable expectation of achievable optimized cycle performance and bed packing.

The PSA cycle is assumed to operate between pressures of 3 bar and 0.1 bar, given that propane and propylene saturate the surface of ZIF-8 near these values at the hypothetical distillation temperature. The incoming feed is present at 9.1 bar, and we assume it can be expanded isothermally to 3 bar, the energy potentially recovered in a heat integration scheme but will not be currently included in the energy balance. The selection of a 64% propylene recovery yields equimolar outlet streams of the PSA, per 100 kmol/h: (S1) 50% propylene, 50 kmol/h, 3 bar. (S2) 90% propylene, 50 kmol/h, 0.1 bar. S1 must

be compressed to 9.1 bar for reintroduction into the tower, while S2 may be produced from a blowdown stream at 1 bar and then recompressed to 9.1 bar. That results in the following pressure work calculations:

$$W = \frac{8.314 \frac{J}{mol \cdot K} \times 292\ K \times \ln\left(\frac{9.1\ bar}{3\ bar}\right) \times 50 \frac{kmol}{h}}{0.8} = 46.8\ kW \tag{7.2}$$

$$W = \frac{8.314 \frac{J}{mol \cdot K} \times 292\ K \times \ln\left(\frac{1\ bar}{0.1\ bar}\right) \times 50 \frac{kmol}{h}}{0.7} = 110.9\ kW \tag{7.3}$$

$$W = \frac{8.314 \frac{J}{mol \cdot K} \times 292\ K \times \ln\left(\frac{9.1\ bar}{0.1\ bar}\right) \times 50 \frac{kmol}{h}}{0.8} = 190.1\ kW \tag{7.4}$$

Total compressive work amounts to 350 kW for a feed of 100 kmol/h.

7.5 Hybrid Distillation/Pressure Swing Systems

Prefractionation of the incoming feed results in an easing of the pinch point created at the feed stage, and instead creates two lesser pinch points and a more favorable operating curve throughout the column. By keeping the number of feed stages and process specifications constant, we are able to assess the effect of feed prefractionation on the propylene splitter. The improvements to the operating line provided by the new feed configuration allows for a reduction in the reflux and boilup ratio within the column, reducing the overall energy expenditure. An interesting design consideration should be noted here: because an increase in relative volatilities requires higher reflux ratios and greater energy expenditure, the same performance metrics achieved by a PSA system (i.e. purities and recoveries) have an increasingly greater energy value at higher temperatures.

However, the PSA system has its own temperature dependence, and the trade-off between process cooling costs and compressive separation efficiency should be evaluated within a larger optimization framework.

Using the previously selected performance metrics of 90 mol% propylene purity and 64% recovery of propylene through the PSA, a prefractionated configuration resulted in an estimated condenser cooling load of 2.6 MW with a new reflux ratio of 6.7. The results of the new configuration are summarized in **Figure 7.2**. The new configuration results in a 41% reduction in energy consumption.

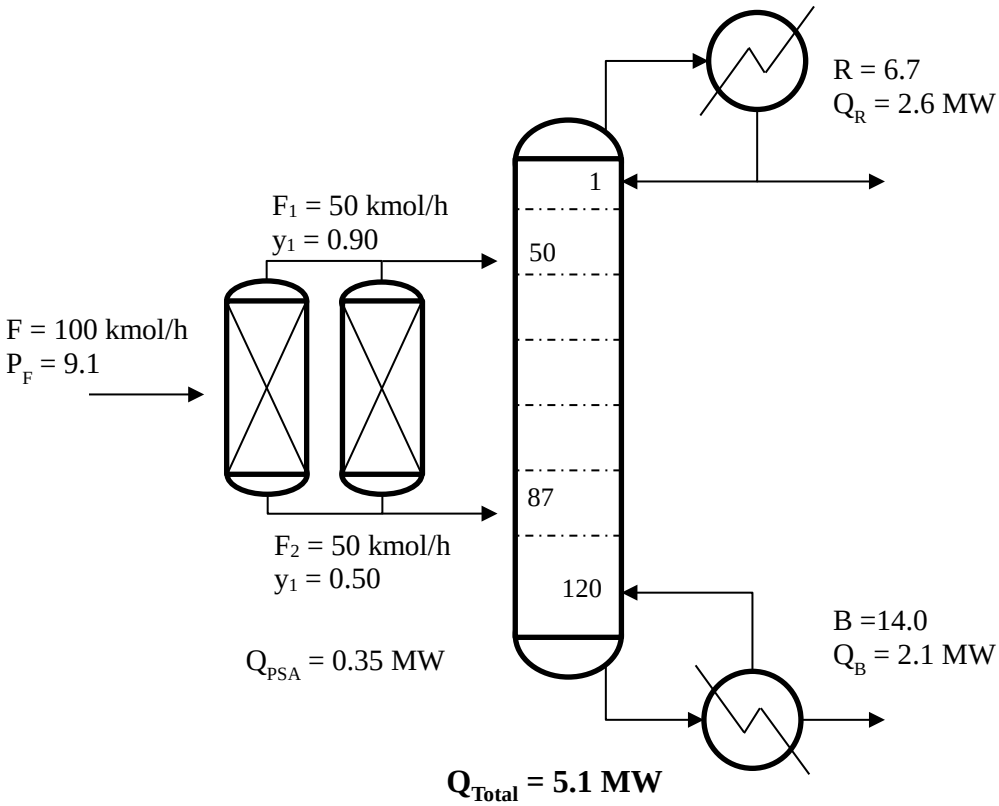

Figure 7.2 Hybrid PSA/Distillation scheme explore in this chapter demonstrating a 41% reduction in energy consumption as a result of adsorptive prefractionation.

Two variations on the PSA performance have also been evaluated, the case of higher propylene purity and of lower propylene recovery. In a two-component PSA, the

independent increase of either recovery or purity yields streams that are increasingly more fractionated relative to the parent stream; higher recovery and purity mean more separation work was done. It is therefore unsurprising that the two variant cases respond accordingly. By not including any new compression and vacuum work except to account for the changes in stream flows, we are modeling the system as having a better or worse sorbent, rather than changing the process itself, the results of which are trivial to infer. However, it is interesting to note that PSA costs may decline in tandem with distillation costs, namely in the cases where the vacuum product (propylene) is more highly purified, as it reduces the size of the more expensive vacuum stream while increasing the separation work done. The results of these scenarios along with the others investigated in this chapter are summarized in **Table 7.1**.

Table 7.1 Summary of various propylene splitter configuration schemes

Pressure Swing Adsorption Unit*			Distillation Unit				
Purity (%)	Recovery (%)	Cost (MW)	Reflux (mol/mol)	Boilup (mol/mol)	Cost (MW)	Intensity† (kmol /MW)	Change (%)
---	---	---	12.7	27.5	8.7	11.5	---
90	64	0.35	6.7	14.0	4.7	19.8	-42
95	64	0.33	6.1	12.5	4.2	22.1	-48
90	30	0.21	7.4	15.5	5.1	18.8	-39
At constant tower liquid & vapor levels							
90	64	0.7	12.7	27.5	8.7	18.8	+8

*Percentages shown on a propylene mole basis. †Intensity calculated on a feed flow basis

The lower reflux and boilup ratios under these new configurations mean that the towers are operating below their designed flow specifications, creating an opportunity for the increased throughput of feed to the tower. Under the new configuration, there exists a higher flow rate that results in equivalent tower energy usage as the base case. This is also

important because towers are often designed to operate at certain liquid and vapor flow rates, and significant deviations from that design point arising from retrofit activities may lead to entrainment or flooding. With the assumption of constant molar overflow, the ratio of flow rates is equal to the inverse ratio of the reflux or boilup ratios, as these are the source of the liquid and vapor flow within the column. For a given composition, an equal amount of vapor and liquid flows results in equal energy consumption under a constant molar overflow assumption. The reduction in reflux leads to an increased feed throughput of 77 %.

7.6 Conclusions

This work examines the potential savings incurred by the introduction of an adsorption based pre-fractionation system within the scope of a propylene splitter. High level estimates of the system predict that energy savings of near 50% are possible over the non-heat integrated distillation base case if a PSA system is able to produce 90% purity product at 64% recovery from 70% propane feed. The beneficial part of this analysis is that both streams from the PSA are returned to the tower, and therefore this analysis is valid for any sort of adsorption system with selectivity between the olefin/paraffin pair, and not restricted to the high-pressure propane feed that results from the work presented in previous chapters.

This modeling effort serves to validate the pursuit of hybrid adsorption/distillation schemes as a method to reduce energy consumption in industrial separations. More thorough work in the future is likely to explore partial feed fractionation and necessary PSA performance metrics for the economically viable implementation of such a unit.

7.7 References

1. Eldridge, R. B., Olefin/paraffin separation technology: a review. *Ind. Eng. Chem. Res.* **1993,** *32* (10), 2208-2212.

2. Baker, R. W., Future directions of membrane gas separation technology. *Ind. Eng. Chem. Res.* **2002,** *41* (6), 1393-1411.

3. Baker, R. W.; Lokhandwala, K., Natural gas processing with membranes: an overview. *Ind. Eng. Chem. Res.* **2008,** *47* (7), 2109-2121.

4. Lively, R. P.; Realff, M. J., On thermodynamic separation efficiency: Adsorption processes. *AlChE J.* **2016,** *62* (10), 3699-3705.

CHAPTER 8. DISSERTATION CONCLUSIONS, SUMMARY, AND FUTURE WORKS

This dissertation explored the fundamental and applied engineering principles in the development of structured metal-organic framework fiber sorbents for the kinetic separation of light hydrocarbons. The research presented in this work can be summarized as follows:

1) Zeolitic imidazolate frameworks are confirmed to be flexible in nature, allowing for the adsorption of molecules substantially larger that their crystallographic pore size and hindering the framework's ability to exhibit sharp molecular sieving behavior. NMR experiments show that larger linkers exhibit a smaller range of motion within the framework, and the reduction of that motion at low temperatures results in non-Arrhenius behavior in guest diffusion. It is demonstrated that structures with smaller pore apertures are not necessarily more restrictive in their transport, and suggests that an increased number of members in a pore ring result in a less rigid aperture despite individually being made up of less flexible components.
2) The kinetic separation of light hydrocarbons is demonstrated to be feasible in multicomponent batch sorption experiments. The temporal nature of multicomponent adsorption is highlighted by demonstrating the transition from equilibrium to diffusive selectivity in the system as a function of sorption time. Furthermore, it is shown for certain mixtures that the same material may demonstrate reversed breakthrough selectivity by a change in the diffusive time scale of the system.

3) The synthesis of water-sensitive metal-organic framework fiber sorbents is shown to be possible by a post-spinning growth route. The use of spinning-stable metal oxides as metal repositories and nucleation sites can result in cellulose acetate composite fibers that are up to 85 wt% MOF, while preventing exposure to air and moisture. However, crystal size control with this technique remains limited.
4) The kinetic separation of a propane/propylene mixture is demonstrated under cyclic conditions in a realistic vacuum pressure swing adsorption unit. Spinning of ZIF-8/Cellulose Acetate fibers with large crystal dimensions enabled the employment of appropriate diffusive time scales to operate within the kinetically controlled regime. Structured contactor beds result in lower pressure drops than packed beds, but the loading process of brittle sorbent fibers remain a drawback to the scalability of these materials.
5) The use of pressure swing adsorption technologies for the prefractionation of difficult distillation feeds can result in significant energy savings during separation. Although adsorption may not be able to replace distillation, especially in cases where high purity and recovery of multiple components is necessary, implementation of hybrid separation configurations can greatly process efficiency.

8.1 Dissertation Overview

This thesis presents the fundamental and applied framework for the use of metal-organic framework fiber sorbents in the separation of light hydrocarbons, specifically the kinetic separation of propane from propylene. ZIF materials demonstrate an exceptional level of pore aperture flexibility, which leads to unintuitive results in guest diffusivities; namely, that smaller windows may be less restrictive if they are composed of a greater

number of moving parts. The fundamental measurements of diffusion allow for the demonstration of idealized kinetic hydrocarbon separations, where the time scale of kinetic selectivities may be manipulated by both crystal size and system temperature. Finally, the incorporation of kinetically-selective materials with sufficiently large crystal dimensions allows for the separation of propane from propylene in a cyclic vacuum pressure swing adsorption process.

A portion of this thesis focuses on the post-spinning synthesis of water-sensitive MOF fiber sorbents. The ability to incorporate MOF structures that may be unstable under spinning conditions opens the door for a wider application of fiber sorbents and MOFs in gas separations.

8.2 Summary

8.2.1 Objective 1

The fundamental measurement of adsorption and diffusion phenomena within zeolitic imidazolate frameworks, and the investigation of how the structural flexibility of these affect guest transport.

Objective 1 in this thesis is largely covered by Chapter 3, where pressure decay experiments, gravimetric uptake measurements, and volumetric sorption data explore the guest-host interactions between two different ZIF structures and a wide variety of guest molecules, including hydrocarbons and alcohols. The work first focused on the equilibrium isotherms of the system, where alcohols displayed an S-shaped uptake indicative of pore-filling, which occurred at lower activities for higher alcohols. Hydrocarbons demonstrated

Langmuir behavior which sharpened with carbon number, although little selectivity was observed between the vapors of species which were liquid at room temperature. Overall, it is concluded that the hydrophobicity of ZIF structured may be harnessed somewhat for bio-alcohol applications, but structures without heterofunctionalizations are likely to not be thermodynamically selective for many gas pairs.

The comparison of guest transport between the two structures indicated that ZIF-11, despite having a smaller pore aperture, was as open, or even more so, than ZIF-8. NMR experiments (which demonstrated that benzimidazole linkers in the ZIF-11 structure had a smaller range of motion that 2-methylimidazole in ZIF-8) led to the conclusion that the 8-MR in the RHO topology result in a less restrictive aperture than the 6-MR in the SOD topology, despite having less flexible individual linkers, by virtue of having more moving parts. This conclusion is supported by GCMC simulations that predict a much broader aperture size in ZIF-11 than ZIF-8. ZIF-8; however, ZIF-8 has previously been demonstrated to have high kinetic selectivity between propane and propylene.

8.2.2 Objective 2

Determining the role of diffusive time scales in the kinetically-selective uptake of a multicomponent mixture and the manipulation of those time scales for the separation of such a mixture.

The role of diffusive time scales in adsorption is addressed in Chapter 4. Because kinetic adsorption separations are transient by nature, it is necessary to understand how the various time scales in the uptake of gas mixtures interact. Using a model batch adsorption system with a feed of ethane and propane, the transient selectivity in adsorption could be

monitored by the change in gas head space. Under conditions where the fast diffusing species has a time scale of order with the sampling time, while the slower component is at least an order of magnitude slower, the kinetic control is readily observable. If both species are exceedingly slow, the sorbent appears to have no component uptake, while fast uptake of both species results in immediate equilibrium. This tuning of the time scales as fast or slow is relative to the sampling time, which mimics cycle time in a PSA, and can be manipulated in various ways. The first modification is a trivial solution, and simply involves the selection of an appropriate gas pair for the sorbent. Despite having large differences in diffusivities, if the selected gases diffuse extremely rapidly, no practical system will be able to take advantage of that difference. The second is by a change in the sorbent dimensions, whereby increasing the size of the crystal increasing the diffusive time scale as a square law. This affects both species and can also affect selectivity in the case of significant uphill diffusion, but may be difficult to achieve depending to the material. Lastly, changes in temperature increase or decrease the diffusion coefficient of each component separately, the magnitude of the change depending of the activation energy of the molecule, and can be used to speed up or slow down the system. This brings with it changes in selectivity, as the overall kinetic adsorption of the system more closely follows activation energies of permeation, where the sorption coefficient must also be taken into account. The final demonstration of the change in sorption control, from equilibrium to kinetic, was achieved by means of an ethane/propane breakthrough experiment, in which the substitution of nanocrystalline pellets with many micron domain crystals showed a reversal in selectivity.

8.2.3 Objective 3

The operation and evaluation of a kinetic pressure swing adsorption system for the separation of light hydrocarbons using structured Metal-Organic Framework fiber sorbent beds.

After the demonstrating the potential for MOF-enabled kinetic separations through proof-of-concept work, the next step in the process development is the incorporation of the sorbents into a scaleable mass-transfer contact vehicle that preserves the kinetic and thermodynamic properties of the material. The fiber spinning of ZIF-8/cellulose acetate was successfully achieved, creating a porous polymer sub-structure in which large, kinetically selective sorbent particles were dispersed at 60 wt%. This work was presented in Chapter 6. These fibers were packaged into a Swagelok® module and operated in a two-bed VPSA cycle for the separation of propane from propylene. Initial breakthrough testing of the fibers demonstrated kinetic selectivity of the pair towards the faster propylene species, as did cyclic operation of the bed. Parameter exploration pointed towards longer adsorption times as increasing the purity of the high-pressure propylene product. Final propane purities reached as high as 81 mol% at a relatively low recovery of 31 %. We expect further process optimization to improve on that metric.

The incorporation of MOFs within fiber sorbents without the need for crystal size control leverages the diverse adsorptive properties of the thousands of MOF structures available with the improved mass-transfer properties of fiber sorbent composites. The conversion of metal oxides to hydroxy double salts allows for the circumvention of spinning solvents and the synthesis of high wt% composites for diverse gas separations.

While only two MOFS have so far been made using this technique, it provides a solid basis for the expansion of the platform into numerous metal and linker combinations.

8.3 Future Directions

This thesis reports the development of a kinetic PSA cycle for propane/propylene based on diffusionally selective MOF sorbents. Although the overall goal of creating the cycle has been successfully demonstrated and preliminary process analysis demonstrates that large energy savings are possible, improvements to the technology are necessary for the eventual large-scale implementation of these materials. Some paths forward are outlined below:

8.3.1 Investigation of Diffusion-Dependent Flexibility in ZIFs

The interesting findings regarding diffusion and flexibility in ZIFs in Chapter 3 should be further explored to more deeply understand more wide-spread structure property relations. Decoupling the effects of topology, pore aperture size, and linker flexibility on diffusion is extremely difficult, namely due to the amount of effort required to synthesize and test the various materials with no guarantee that an appropriate family of materials exists. However, if it can be more solidly established that rings with fewer members are less flexible than larger ones, an extremely useful design principle comes to light. This investigation is best conducted through computational means, to span the large variable space required to draw solid conclusions and avoid the difficulties of crystal size engineering. Furthermore, the continued investigation of temperature-dependent diffusion in these flexible materials and the additional corroboration of the change in activation energy can be performed by building a continuum of overlapping low-temperature

diffusion curves. Using other light gases like xenon or ethylene could map out the temperature regions in which methane has proved to rapid and elucidate the effect of the suspected change in flexibility.

8.3.2 Incorporation of DMF-based MOFs into fiber sorbents

Although Chapter 5 described a scalable route for the incorporation of MOFs within fiber sorbents without the need to spin the materials, the truth is that the use of cellulose acetate severely limits the types of structures that can be included into the polymer. Because a fair number of MOFs are synthesized from CA solvents, like DMF, the technique can so far only be used with aqueous or alcohol-based syntheses. The true extension of this synthesis requires a solvent-resistant substructure. The spinning approach to this problem would likely employ a cross-linkable polyimide as the base, while an alternative approach may explore a different support entirely, such as an aerogel or porous alumina. Being able to synthesize by this route high-affinity sorbents with extremely poor water stability, like MOF-5, would definitively prove the generalizability of this concept.

8.3.3 Process Modeling Optimization of Kinetic Fiber Sorbent Cycles

The operation of the kinetic cycle presented in Chapter 6, although successful in creating some degree of separation from the feed mixture, is in no way optimized within a formal framework. The construction of a Pareto plot through simulated unit operation, modification of cycle time steps, temperature, configuration, and crystal size would allow for the discovery of how effective this material can truly be. Unit operation could be modified to produce high-purity propylene product for polymer-grade applications, or

could be used within a greater superstructure to optimize its implementation as a distillation pre-fractionator.

8.3.4 Direct Comparisons of Packed Beds and Fiber Sorbents

Most work which claims cycle improvements from the utilization of fiber sorbents over packed beds are based on solid theoretical calculations and estimations, as well as more detailed modeling work. However, little, if any work, has demonstrated experimental evidence of these improvements. In fact, this thesis presents the first experimental validation of the claim of lower pressure drop across the bed, although this could have been easily verifiable using existing correlations. The issue behind this lack of data may be two-fold: 1) early fiber sorbents utilized zeolites, which are difficult to activate properly for separations such as O_2/N_2, due to the decomposition temperatures of the cellulose acetate polymer. 2) MOFs, although commonly available in pellet form and being continually tested for gas adsorption properties, were not able to be incorporated into fiber sorbents until recently. Therefore, it is proposed that direct comparison of packed bed versus packed fibers be undertaken, utilizing Matrimid® supports in zeolites to allow for the high-temperature material activation, and the metal-oxide to MOF conversion route presented in this thesis. This will provide experimental evidence of the differences in purity and productivity between the two configurations, as well as bring to light any discrepancies that modeling work has not previously considered.

8.3.5 Improved Packaging Strategies for the Rapid and Efficient Assembly of Fiber Modules

As discussed in Chapter 7, the packaging of fiber sorbents, especially those of high sorbent loadings and particularly those with large particles, can be a very time-consuming process and may often result in broken fibers. The method for packing fiber modules, especially a scalable method beyond that of ¼" and ½" Swagelok ® tubing, should be developed. A technique that protects the mechanical integrity of the fibers during packaging and could be used to load a 1" diameter fiber bed with greater than 55% packing fraction, is necessary. It should be reproducible, cause little to no breakages, and be semi-automatable where the effect of fiber size, uniformity, and mechanical properties can be related to failure rate. Approaches may include a compressive sleeve to pre-package the fibers that can then be inserted into the module, or a redesign of a flexible module housing rather than the standard stainless steel tube, where the module could be closed after fiber loading and lessen the risk of breakage while threading.

APPENDIX A. MATLAB CODES

A.1 The Parsing of Raw Data Arising from Pressure Decay Experiments Using the Micromeritics HPVA-II

DataParse.m

Cuts up the data from time-logged pressure decay experiments from the HPVA-II .csv output.

Assumes that experiments are carried out sequentially from an initial pressure of 0 bar

"Loading" column in the excel file produced by this code should be replaced by some sort of string, may contain numbers as well. Inputting just numbers in that column leads to compatibility issues with later codes.

```
% Command screen and variable clear
clear
clc

%Start Time measurement
tic

% Number of pressure decay points in the file (or to be measured)
IsoSteps=1;

% Expansion factor from manifold to cell, calculated from free volume
% data. Expected 'no adsorption' pressure change
ExpCoef=0.7526;

% Percent of final equilibrium point at which to cut data off; reduced long
% tails which haven't ended the experiment due to noise. >0.99
DataCut=1;

% Windows explorer file call
filename=uigetfile('*.csv');
fileID=fopen(filename);
data=[];
```

```
% Data parsing, specific to the format of the HPVA.csv
for i=1:IsoSteps
    C(i,:)=textscan(fileID,'%s %s',1,'Delimiter',',');
    Temp(i,:)=textscan(fileID,'%f %f','Delimiter',',');

% Deleting data before "no adsorption" pressure
    if i==1
        start=Temp{i,2}(1)*ExpCoef;
        b=[];
        for a=1:length(Temp{i,2})-1
            if (Temp{i,2}(a+1)-start)> 0
                b=[b,a]; %#ok<AGROW>
            end
        end

% Resets "starting pressure" based on final pressure of last uptake
        Temp{i,1}(b)=[];
        Temp{i,2}(b)=[];

% Deleting data before "no adsorption" pressure
    else
        start=(Temp{i,2}(1)-Temp{i-1,2}(end))*ExpCoef+Temp{i-1,2}(end);
        b=[];
        for a=1:length(Temp{i,2})-1
            if (Temp{i,2}(a+1)-start)> 0
                b=[b,a]; %#ok<AGROW>
            end
        end

% Resets "starting pressure" based on final pressure of last uptake
        Temp{i,1}(b)=[];
        Temp{i,2}(b)=[];
    end




% Trimming of the data based on DataCut approach criteria
    criteria=(Temp{i,2}(:)-Temp{i,2}(1))./(Temp{i,2}(end)-Temp{i,2}(1));
    flag=0;
    a=1;
    while flag==1
        if criteria(a) > DataCut
            Temp{i,1}(a:end)=[];
            Temp{i,2}(a:end)=[];
            flag=0;
        end
        a=a+1;
    end

% Saving parsed data in a formatted variable
    if i==1
```

```
        data(1:numel(Temp{i,1}),i)=Temp{i,1};
        data(1:numel(Temp{i,2}),i+1)=Temp{i,2};
        data(1,i+2)=0;
        data(1,i+3)=0;
        headers={'Elapsed' 'P (bar)' 'Loading'};
    else
        data(1:numel(Temp{i,1}),4*(i-1)+1)=Temp{i,1};
        data(1:numel(Temp{i,2}),4*(i-1)+2)=Temp{i,2};
        data(1,4*(i-1)+3)=0;
        data(1,4*(i-1)+4)=0;
    end

end

% Removing excess zeros that arise from needing a full matrix
data(~data)=NaN;

% Saving data into Excel file
save_file_name=strcat(inputdlg('Save File As...',filename),'.xlsx');
xlswrite(save_file_name{1},data,1, 'A2')
xlswrite(save_file_name{1},headers,1, 'A1')

% Open Excel file
winopen(save_file_name{1})
toc
```

Published with MATLAB® R2017a

A.2 The Fitting of Pressure Decay Data to the Model of Uptake from a Stirred Tank of Limited Volume

HPVA_Full_Iso_Call.m

Uses the excel file created by the previous DataParse code and calls the subroutine HPVA_Kinetic to perform a least squares fit on as many decay events as are in the data file.

Excel file must be saved within the Matlab folder to be accessed

```
%% HPVA_Full_Iso_Call
% Command screen and variable clear
clear
clc

% Select the excel file containing the experimental data
filename=uigetfile('*.xlsx')

% Read excel data, save as variable "Num"
[Num, Txt, ~] = xlsread(filename,1);

% Start of time measurement
tic

% Deleting excess zeroes from variable
Num=Num(:,~isnan(Num(1,:)));

% Number of decay steps within the excel file, or to be measured. iso_count
% may not exceed actual number of decay events in the file
iso_count= 1;

% Step count flag
steps=0;

% Feed data from the Num variable to the HPVA_Kinetic subroutine; saves
% diffusion values under variable D
for i=1:2:iso_count*2
    steps=steps+1;
    Data=Num(:,(i:i+1));
    Data=Data(~isnan(Data(:,1)),:);
    save('Data.mat','Data')
    loading=Txt(1,3+(steps-1)*4);
```

```
    D(steps)=HPVA_Kinetic(loading);
end

toc
```

Published with MATLAB® R2017a

HPVA_Kinetic.m

HPVA Kinetic Uptake Data Fitting

To be used in conjunction with HPVA_Full_Iso_Call

Using the mathematical model of a sphere adsorbing from a limited volume to fit the kinetic adsorption data from the HPVA. Including a particle size distribution for accuracy and a non-linear fit routine to extract diffusivity values from the data.

Base equation is given by Crank, pg 94. Eq(6.30)

M_t/M_inf=1-Sum_n(6*alpha*(alpha+1)*exp(-D*q_n^2*t/R^2)
/(9+9*alpha+q_n^2*alpha^2))

Where q_n are the non-zero roots of

tan(q_n)=3*q_n/(3+alpha*q_n^2)

q_n solved using "transcendental.m" and loaded into variable workspace "Alpha_Lookup.mat" for eficiency. "Alpha_Table" (1,:) contains Fractional Uptake, "Qval_Table" (2,:) contains Alpha.

Upload Data.mat file as (P,time), in normalized P/P0 starting at 0 and moving to 1, and time in linear seconds.

Crystal distribution must be loaded into 'Cryst_Dist.mat', which holds sample populations. Each sample must be saved as a variable containing n x 1 crystal diameters.

```
function [D] = HPVA_Kinetic(loading)
```

```
%% Crystal Size Distribution
% Load crystal distribution database
C=load('Cryst_Dist.mat');

%Sample size distribution file being used
% List of samples contained for easy reference
% Sample1
% Sample2
% Sample3
% Sample4

% Sample being used in this fit
file=C.Sample1;

% Histogram analysis of crystal size distribution
[Count, Edg]= histcounts(file);
Edges=zeros(1,length(Count));
for i=1:length(Count)
    Edges(i)=1e-4*(Edg(i)+Edg(i+1))/2;
end

% Weighted fraction of population by volumetric fraction
V=1/6*pi.*Edges.^3;
Weights=V/sum(V);
Weight_avgR= Weights*Edges'/2; %#ok<NASGU>
```

```
%% Data Loading
% Load data from 'Data.mat' file created by HPVA_Full_Iso_Call
Data=load('Data.mat');
P_r= Data.Data(:,2);
t_test= Data.Data(:,1)-Data.Data(1,1); %#<NODEF>

% Downsampling of the data
% Takes every B points in the A1: B : A2 string between point A1 and A2
% Divided into two sections for some degree of granularity
try
    P_test=[P_r(1:2:1000)' P_r(1001:50:end)'];
    t=[t_test(1:2:1000)' t_test(1001:50:end)'];

% Catch error in case of data having fewer than A2 points
catch
    P_test=P_r(1:2:end)';
    t=t_test(1:2:end)';
end

% Normalized pressure data
P=((P_test(1)-P_test)./range(P_test))';
```

```
%% Crank Table 6.1 Loading
% Loading of alpha values from the Alpha_Lookup file as a function of
% fractional uptake
A=load('Alpha_Lookup.mat');
```

```
%Fractional Uptake of Solute relative to total cell
frac_up= range(P_r)/P_r(1);
[frac_up, table_lookup]= min(abs(frac_up-A.Alpha_Table(:,1))); %#ok<ASGLU>

% Alpha and q_n root values for given fractional uptake
alpha= A.Alpha_Table(table_lookup,2)
q_n= A.Qval_Table(table_lookup,:);
```

```
%% Equation Formulation
% Initial diffusivity guess
D_o=1e-9;

% Crystal sizes to be used in fit
R=Edges/2;

% Determination of tolerances and lsqnonlin fit paremeters
options=optimoptions(@lsqnonlin,'TolX',1e-14,'MaxFunEvals',10000,...
    'TolFun', 1e-8);

% Full analytical vs short time flag. Short time flg=1
% Use of short time solution not recommended, not fully verified
flg=0;

% Least square fit function call
D=lsqnonlin(@Adsorption_fit,D_o,1e-16,1,options);

    function [E]= Adsorption_fit(D)
        if flg==0
            steps=zeros(length(t),length(q_n),length(R));
            for k=1:length(R)
                for j=1:length(q_n)
                    steps(:,j,k)= (Weights(k)*6*alpha*(alpha+1)*...
                        exp(-D*q_n(j)^2*t/R(k)^2))/(9+9*alpha+q_n(j)^2*alpha^2);
                end
            end
            step_sum= sum(sum(steps,3),2);
            M_t= 1-step_sum;
            E=(M_t-P);
        else
% Short time solution, data from P/P_inf 0-> 0.2
            gamma1= (1/2)*((1+4/3*alpha)^(1/2)+1);
            gamma2=gamma1-1;

            [~, a]=min(abs(0.3-P));

            P_short=P(2:a);
            t_short=t(2:a);
            M_t=0;
            for l=1:length(R)

                a=3*gamma1/alpha*(D*t_short./R(l)^2).^(1/2);
                b=-3*gamma2/alpha*(D*t_short./R(l)^2).^(1/2);
```

```
                M_o=Weights(l)*(1+alpha).*(1-(gamma1/(gamma1+gamma2)).*...
                    (exp(a.^2).*erfc(a))-(gamma2/(gamma1+gamma2))...
                    .*(exp(b.^2).*erfc(b)));
                M_t=M_t+M_o;
            end
            E=(M_t-P_short);
        end

    end

% Recalculation of the fitted curve for the full time solution. Was unable
% to export fitted curve along with diffusivity value, created need for
% recalculation
if flg==0
    L=2000;
    t_plot=linspace(0,t(end),L);
    step_plot=zeros(L,length(q_n),length(R));
    for k=1:length(R)
        for j=1:length(q_n)
            step_plot(:,j,k)= (Weights(k)*6*alpha*(alpha+1)*exp(-
D*q_n(j)^2*t_plot/R(k)^2))/(9+9*alpha+q_n(j)^2*alpha^2);
        end
    end

    stepplot_sum= sum(sum(step_plot,3),2);
    M_plot= 1-stepplot_sum;

% Plotting of experimental data with fitted curve in exported figure.
% Figure includes text box with the diffusivity value.
    figure
    plot(sqrt(t_plot),M_plot,'b')
    annotation('textbox',[.55 .35 .25 .1],'string',['D= ', num2str(D), 'cm^2/s'])
    title(loading)
    hold on
    scatter(sqrt(t),P)
    xlabel('t^{1/2}')
    ylabel('P/(P_o-P_f)')
    hold off


% Recalculation of the fitted curve for the full time solution. Was unable
% to export fitted curve along with diffusivity value, created need for
% recalculation

else
    L=1000;
    t_plot=linspace(0,t_short(end),L);
    gamma1= (1/2)*((1+4/3*alpha)^(1/2)+1);
    gamma2=gamma1-1;

    M_plot=(1+alpha).*(1-
(gamma1/(gamma1+gamma2))*eerfc(3*gamma1/alpha*(D*t_plot./R^2)^(1/2))-
(gamma2/(gamma1+gamma2))...
```

```
        .*eerfc(-3*gamma2/alpha*(D*t_plot./R^2)^(1/2)));

% Plotting of experimental data with fitted curve in exported figure.
% Figure includes text box with the diffusivity value.
    hold on
    figure
    plot(sqrt(t_plot),M_plot,'b')
    annotation('textbox',[.55 .35 .25 .1],'string',['D= ', num2str(D), 'cm^2/s'])
    title(loading)

    scatter(sqrt(t_short),P_short)
    xlabel('t^{1/2}')
    ylabel('P/(P_o-P_f)')
    hold off

end

% Save results in an exported variable, only works for last run performed
save('Results','M_plot','t_plot','D', 'P', 't' )
```

```
end
```

Published with MATLAB® R2017a

Transcendetal.m

Presolving the roots of q_n for use in the adsorption from a solution of limited volume. Depending on number of points, may take up to 10 minutes to solve.

alpha and qn values must be saved as specified by HPVA_Kinetic

```
%% transcendental
clc
tic

% number of points
n=10000;
a=0;
ep=1e-6;
qn=zeros(100,n);

% Solution for ranges of alpha
for alpha= [linspace(0,1,200),linspace(2,20,18),100,1000]
    a=a+1;
    for i=1:n
        qn(a,i)= fzero(@(q) tan(q)*(3+alpha*q^2)-3*q, [pi/2+pi*(i-1)+ep, pi/2+i*pi-ep]);
    end
end

toc
```

Published with MATLAB® R2017a

A.3 Determination of Valve Limitations in Pressure Decay Experiments

Attempt to fit data to the valve constant model developed by Brendani and simplified by Ruthven in Diff of Nanoporous Materials. Watch for typo in book. Set of equations are quite complex and not well explained, changing scale of x-axis depending on the problem makes this code unwieldy.

Pressure decay data must first be normalized and uploaded as Data.mat (P,t)

```
function [Df, w , gamma, delta] = Brendani_Valve( ~ )
```

```
%% Problem definition

Pou= 0;         % Pressure in dosing cell prior to dosing, 0 if InfDil

Do= 2e-10;      % Initial Diffusion guess, cm^2/s
Rc= 0.002;      % Volume-weighted average crystal radius, cm
Ms= 15/1000;    % Mass of sample, in grams
K=  405;        % Affinity constant, multiply by 1.0876 from cc/g/bar

Vu= 13.14;       % Volume of the uptake cell
Vd= 43.6;       % Volume of dosing manifold
ds= .9;        % Density of sample, g/cc
Vs= Ms/ds;      % Volume of sample, cm^3
R= 83.14;       % Gas constant, cc*mol/bar*K
T= 308;         % Temperature, K, unsure if this should be dosing or sample
Chi= .01;      % Valve constant, mol/bar*s,;(unique to system, get from blank curve)
```

```
%% Data Normalization

% Load data from 'Data.mat' file, must be uploaded prior to running
Data=load('Data.mat');
P_r= Data.Data(:,2);
t_test= Data.Data(:,1)-Data.Data(1,1);

% Downsampling of the data
% Takes every B points in the A1: B : A2 string between point A1 and A2
% Divided into two sections for some degree of granularity
try
    P=[P_r(1:1:1000)' P_r(1001:10:end)'];
    t=[t_test(1:1:1000)' t_test(1001:10:end)']';

% Catch error in case of data having fewer than A2 points
catch
    P=P_r(1:2:end)';
    t=t_test(1:2:end)';
```

```
end

Pn=((P-Pou)/(P(end)-Pou));
Pn=Pn'/Pn(1);
```

```
%% Developing Pu

% Least square fit function call
options=optimoptions(@lsqnonlin,'TolX',1e-15,'MaxFunEvals',10000, 'TolFun', 1e-10);
Df=lsqnonlin(@Brendani_Fit,Do,1e-13,1e-6,options);
Beta=0;
    function [E] = Brendani_Fit(D)
% Normalized time scale of the problem
        tau=t*D/Rc^2;

% Normalized system description terms
        w=R*T*Chi*Rc^2/(Vd*D);
        gamma= Vu/(3*K*Vs);
        delta= Vd/(3*K*Vs);


        n=500;                          % Number of Beta terms

        Beta=zeros(n,1);                % Memory allocation for series terms
        Terms=zeros(length(tau),1);

        count=1;
        er=1e-10;
        while count < n+1                %Solving for Beta
            Beta(count)= fzero(@(B) B*cot(B)-(1+gamma*B^2+w*delta*B^2/(w-
B^2)),[pi*count+er,pi*count+pi-er]);
            count=count+1;
        end
        z= 1+gamma*Beta.^2+w*delta.*Beta.^2./(w-Beta.^2);

        a_top= 2*w^2*delta*Beta.^2;
        a_bot= 2*w^2*delta*Beta.^2+(w-Beta.^2).^2.*(Beta.^2+z.^2-z+2*gamma*Beta.^2);
        a=a_top./a_bot;

        Cst= 3*delta/(1+3*delta+3*gamma);

        for i=1:length(tau)
            q=a.*exp(-Beta.^2*tau(i)); % at one time
            Terms(i)=sum(q);
        end
        Pd=Cst+Terms;

        E= (Pd-Pn);
    end
```

```
%% Plotting
% Recalculation of values outside of minimization routine
tau=t*Df/Rc^2;
w=R*T*Chi*Rc^2/(Vd*Df);
```

```
gamma= Vu/(3*K*Vs);
delta= Vd/(3*K*Vs);


n=500;                          % Number of Beta terms

Beta=zeros(n,1);                % Memory allocation for series terms
Terms=zeros(length(tau),1);

count=1;
er=1e-10;
while count < n+1                 %Solving for Beta
    Beta(count)= fzero(@(B) B*cot(B)-(1+gamma*B^2+w*delta*B^2/(w-
B^2)),[pi*count+er,pi*count+pi-er]);
    count=count+1;
end
z= 1+gamma*Beta.^2+w*delta.*Beta.^2./(w-Beta.^2);

a_top= 2*w^2*delta*Beta.^2;
a_bot= 2*w^2*delta*Beta.^2+(w-Beta.^2).^2.*(Beta.^2+z.^2-z+2*gamma*Beta.^2);
a=a_top./a_bot;

Cst= 3*delta/(1+3*delta+3*gamma);

for i=1:length(tau) %#ok<FXUP>
    q=a.*exp(-Beta.^2*tau(i)); % at one time
    Terms(i)=sum(q);
end
Pd=Cst+Terms;


% Figure plotting
figure

plot(tau(1:end),Pd(1:end),'r')
hold on
plot(tau(1:end),Pn(1:end), 'b')
legend('Model', 'Data')
xlabel('tau= {tD_o}/{R^2}')
ylabel('P_normalized')

end
```

Published with MATLAB® R2017a

A.4 The Fitting of Uptake Data to the Model of Exponential Surface Condition

DiffusionModeling.m

This code is the non-GUI portion of the work, but requires an accompanying DiffusionModelingUI.fig file to operate properly.

Alternatively, minimization routine and fit functions could be extracted and create a new script code. This code could likely be significantly improved by changing the fit variable to R^2/D, rather than D, and solving for τ in seconds. Personal experience leads me to believe this is a more stable routine and can more easily accommodate diffusivities of varying orders of magnitude without the need to change the ranges and tolerances when dealing with exceedingly slow molecules (finding a zero at D= 1e-16 is computationally more difficult than rescaling the problem as a time scale of R^2/D = 400e6).

```
function varargout = DiffusionModelingUI(varargin)
% DIFFUSIONMODELINGUI MATLAB code for DiffusionModelingUI.fig
%      DIFFUSIONMODELINGUI, by itself, creates a new DIFFUSIONMODELINGUI or raises the
existing
%      singleton*.
%
%      H = DIFFUSIONMODELINGUI returns the handle to a new DIFFUSIONMODELINGUI or the
handle to
%      the existing singleton*.
%
%      DIFFUSIONMODELINGUI('CALLBACK',hObject,eventData,handles,...) calls the local
%      function named CALLBACK in DIFFUSIONMODELINGUI.M with the given input arguments.
%
%      DIFFUSIONMODELINGUI('Property','Value',...) creates a new DIFFUSIONMODELINGUI or
raises the
%      existing singleton*.  Starting from the left, property value pairs are
%      applied to the GUI before DiffusionModelingUI_OpeningFcn gets called.  An
%      unrecognized property name or invalid value makes property application
%      stop.  All inputs are passed to DiffusionModelingUI_OpeningFcn via varargin.
%
%      *See GUI Options on GUIDE's Tools menu.  Choose "GUI allows only one
%      instance to run (singleton)".
%
```

```
% See also: GUIDE, GUIDATA, GUIHANDLES

% Edit the above text to modify the response to help DiffusionModelingUI

% Last Modified by GUIDE v2.5 12-Oct-2015 16:58:26

% Begin initialization code - DO NOT EDIT
gui_Singleton = 1;
gui_State = struct('gui_Name',       mfilename, ...
    'gui_Singleton',  gui_Singleton, ...
    'gui_OpeningFcn', @DiffusionModelingUI_OpeningFcn, ...
    'gui_OutputFcn',  @DiffusionModelingUI_OutputFcn, ...
    'gui_LayoutFcn',  [] , ...
    'gui_Callback',   []);
if nargin && ischar(varargin{1})
    gui_State.gui_Callback = str2func(varargin{1});
end

if nargout
    [varargout{1:nargout}] = gui_mainfcn(gui_State, varargin{:});
else
    gui_mainfcn(gui_State, varargin{:});
end
% End initialization code - DO NOT EDIT


% --- Executes just before DiffusionModelingUI is made visible.
function DiffusionModelingUI_OpeningFcn(hObject, eventdata, handles, varargin)
% This function has no output args, see OutputFcn.
% hObject    handle to figure
% eventdata  reserved - to be defined in a future version of MATLAB
% handles    structure with handles and user data (see GUIDATA)
% varargin   command line arguments to DiffusionModelingUI (see VARARGIN)

% Choose default command line output for DiffusionModelingUI
handles.output = hObject;
handles.xdata= 0;
handles.ydata= 0;

% Update handles structure
guidata(hObject, handles);

% UIWAIT makes DiffusionModelingUI wait for user response (see UIRESUME)
% uiwait(handles.figure1);


% --- Outputs from this function are returned to the command line.
function varargout = DiffusionModelingUI_OutputFcn(hObject, eventdata, handles)
% varargout  cell array for returning output args (see VARARGOUT);
% hObject    handle to figure
% eventdata  reserved - to be defined in a future version of MATLAB
% handles    structure with handles and user data (see GUIDATA)
```

```
% Get default command line output from handles structure
varargout{1} = handles.output;


% --- Executes on button press in pushimport.
function pushimport_Callback(hObject, eventdata, handles)
% hObject    handle to pushimport (see GCBO)
% eventdata  reserved - to be defined in a future version of MATLAB
% handles    structure with handles and user data (see GUIDATA)
filename=uigetfile('*');     % Interactive file sarch

data=xlsread(filename); % Read xls data into Matlab variable. x-time; y- M/M_inf
x=data(:,1);            % data decomposition into vectors
y=data(:,2);

handles.xdata= x;
handles.ydata= y;
set(handles.datafile,'String',filename)
cla(handles.plot1)
cla(handles.plot3)
cla(handles.plot3)

% Clear graph, plot raw data, no fit because no system data

scatter(handles.plot1, sqrt(x),y,5,'k', 'filled')
xlabel(handles.plot1,'time, s^{1/2}')
ylabel(handles.plot1,'Normalized Uptake, M/M_{final}')
title(handles.plot1,'Raw Data')
set(handles.plot1,'XMinorTick','on', 'YMinorTick','on');
ylim(handles.plot1,[0 1.1])

guidata(hObject, handles);

% --- Executes on selection change in dropdown1.
function dropdown1_Callback(hObject, eventdata, handles)
% hObject    handle to dropdown1 (see GCBO)
% eventdata  reserved - to be defined in a future version of MATLAB
% handles    structure with handles and user data (see GUIDATA)

% Hints: contents = cellstr(get(hObject,'String')) returns dropdown1 contents as cell
array
%        contents{get(hObject,'Value')} returns selected item from dropdown1

plottype= get(handles.dropdown1,'Value');
if plottype ~= 1
    x= handles.xdata;
    y= handles.ydata;
end

if plottype==2
    cla(handles.plot2)
    plot(handles.plot2,sqrt(x),handles.ybest(:,3),'r','LineWidth',2)
    scatter(handles.plot2, sqrt(x),y,6,'k', 'filled')
```

```
    set(handles.plot2,'XMinorTick','on', 'YMinorTick','on');
    xlabel(handles.plot2,'time, s^{1/2}')
    ylabel(handles.plot2,'Normalized Uptake, M/M_{final}')
    title(handles.plot2,'Fickian- Exponential BC')
    ylim(handles.plot2,[0 1.1])

elseif plottype==3
    cla(handles.plot2)
    plot(handles.plot2,sqrt(x),handles.ybest(:,2),'r','LineWidth',2)
    scatter(handles.plot2, sqrt(x),y,6,'k', 'filled')
    set(handles.plot2,'XMinorTick','on', 'YMinorTick','on');
    xlabel(handles.plot2,'time, s^{1/2}')
    ylabel(handles.plot2,'Normalized Uptake, M/M_{final}')
    title(handles.plot2,'Berens-Hopfenberg- Constant BC')
    ylim(handles.plot2,[0 1.1])

elseif plottype==4
    cla(handles.plot2)
    plot(handles.plot2,sqrt(x),handles.ybest(:,4),'r','LineWidth',2)
    scatter(handles.plot2, sqrt(x),y,6,'k', 'filled')
    set(handles.plot2,'XMinorTick','on', 'YMinorTick','on');
    xlabel(handles.plot2,'time, s^{1/2}')
    ylabel(handles.plot2,'Normalized Uptake, M/M_{final}')
    title(handles.plot2,'Berens-Hopfenberg- Exponential BC')
    ylim(handles.plot2,[0 1.1])
end


% --- Executes during object creation, after setting all properties.
function dropdown1_CreateFcn(hObject, eventdata, handles)
% hObject    handle to dropdown1 (see GCBO)
% eventdata  reserved - to be defined in a future version of MATLAB
% handles    empty - handles not created until after all CreateFcns called

% Hint: popupmenu controls usually have a white background on Windows.
%       See ISPC and COMPUTER.
if ispc && isequal(get(hObject,'BackgroundColor'),
get(0,'defaultUicontrolBackgroundColor'))
    set(hObject,'BackgroundColor','white');
end



function DABGUESS_Callback(hObject, eventdata, handles)
% hObject    handle to DABGUESS (see GCBO)
% eventdata  reserved - to be defined in a future version of MATLAB
% handles    structure with handles and user data (see GUIDATA)

% Hints: get(hObject,'String') returns contents of DABGUESS as text
%        str2double(get(hObject,'String')) returns contents of DABGUESS as a double


% --- Executes during object creation, after setting all properties.
```

```
function DABGUESS_CreateFcn(hObject, eventdata, handles)
% hObject    handle to DABGUESS (see GCBO)
% eventdata  reserved - to be defined in a future version of MATLAB
% handles    empty - handles not created until after all CreateFcns called

% Hint: edit controls usually have a white background on Windows.
%       See ISPC and COMPUTER.
if ispc && isequal(get(hObject,'BackgroundColor'),
get(0,'defaultUicontrolBackgroundColor'))
    set(hObject,'BackgroundColor','white');
end



function phiguess_Callback(hObject, eventdata, handles)
% hObject    handle to phiguess (see GCBO)
% eventdata  reserved - to be defined in a future version of MATLAB
% handles    structure with handles and user data (see GUIDATA)

% Hints: get(hObject,'String') returns contents of phiguess as text
%        str2double(get(hObject,'String')) returns contents of phiguess as a double


% --- Executes during object creation, after setting all properties.
function phiguess_CreateFcn(hObject, eventdata, handles)
% hObject    handle to phiguess (see GCBO)
% eventdata  reserved - to be defined in a future version of MATLAB
% handles    empty - handles not created until after all CreateFcns called

% Hint: edit controls usually have a white background on Windows.
%       See ISPC and COMPUTER.
if ispc && isequal(get(hObject,'BackgroundColor'),
get(0,'defaultUicontrolBackgroundColor'))
    set(hObject,'BackgroundColor','white');
end



function kguess_Callback(hObject, eventdata, handles)
% hObject    handle to kguess (see GCBO)
% eventdata  reserved - to be defined in a future version of MATLAB
% handles    structure with handles and user data (see GUIDATA)

% Hints: get(hObject,'String') returns contents of kguess as text
%        str2double(get(hObject,'String')) returns contents of kguess as a double


% --- Executes during object creation, after setting all properties.
function kguess_CreateFcn(hObject, eventdata, handles)
% hObject    handle to kguess (see GCBO)
% eventdata  reserved - to be defined in a future version of MATLAB
% handles    empty - handles not created until after all CreateFcns called
```

```
% Hint: edit controls usually have a white background on Windows.
%       See ISPC and COMPUTER.
if ispc && isequal(get(hObject,'BackgroundColor'),
get(0,'defaultUicontrolBackgroundColor'))
    set(hObject,'BackgroundColor','white');
end



function tauguess_Callback(hObject, eventdata, handles)
% hObject    handle to tauguess (see GCBO)
% eventdata  reserved - to be defined in a future version of MATLAB
% handles    structure with handles and user data (see GUIDATA)

% Hints: get(hObject,'String') returns contents of tauguess as text
%        str2double(get(hObject,'String')) returns contents of tauguess as a double


% --- Executes during object creation, after setting all properties.
function tauguess_CreateFcn(hObject, eventdata, handles)
% hObject    handle to tauguess (see GCBO)
% eventdata  reserved - to be defined in a future version of MATLAB
% handles    empty - handles not created until after all CreateFcns called

% Hint: edit controls usually have a white background on Windows.
%       See ISPC and COMPUTER.
if ispc && isequal(get(hObject,'BackgroundColor'),
get(0,'defaultUicontrolBackgroundColor'))
    set(hObject,'BackgroundColor','white');
end


% --- Executes on selection change in dropdown2.
function dropdown2_Callback(hObject, eventdata, handles)
% hObject    handle to dropdown2 (see GCBO)
% eventdata  reserved - to be defined in a future version of MATLAB
% handles    structure with handles and user data (see GUIDATA)

% Hints: contents = cellstr(get(hObject,'String')) returns dropdown2 contents as cell
array
%        contents{get(hObject,'Value')} returns selected item from dropdown2

plottype=get(handles.dropdown2,'Value');

if plottype ~= 1
    x= handles.xdata;
    y= handles.ydata;
end

if plottype==2
    cla(handles.plot3)
    plot(handles.plot3,sqrt(x),handles.ybest(:,3),'r','LineWidth',2)
    scatter(handles.plot3, sqrt(x),y,6,'k', 'filled')
```

```
    set(handles.plot3,'XMinorTick','on', 'YMinorTick','on');
    xlabel(handles.plot3,'time, s^{1/2}')
    ylabel(handles.plot3,'Normalized Uptake, M/M_{final}')
    title(handles.plot3,'Fickian- Exponential BC')
    ylim(handles.plot3,[0 1.1])

elseif plottype==3
    cla(handles.plot3)
    plot(handles.plot3,sqrt(x),handles.ybest(:,2),'r','LineWidth',2)
    scatter(handles.plot3, sqrt(x),y,6,'k', 'filled')
    set(handles.plot3,'XMinorTick','on', 'YMinorTick','on');
    xlabel(handles.plot3,'time, s^{1/2}')
    ylabel(handles.plot3,'Normalized Uptake, M/M_{final}')
    title(handles.plot3,'Berens-Hopfenberg- Constant BC')
    ylim(handles.plot3,[0 1.1])

elseif plottype==4
    cla(handles.plot3)
    plot(handles.plot3,sqrt(x),handles.ybest(:,4),'r','LineWidth',2)
    scatter(handles.plot3, sqrt(x),y,6,'k', 'filled')
    set(handles.plot3,'XMinorTick','on', 'YMinorTick','on');
    xlabel(handles.plot3,'time, s^{1/2}')
    ylabel(handles.plot3,'Normalized Uptake, M/M_{final}')
    title(handles.plot3,'Berens-Hopfenberg- Exponential BC')
    ylim(handles.plot3,[0 1.1])
end


% --- Executes during object creation, after setting all properties.
function dropdown2_CreateFcn(hObject, eventdata, handles)
% hObject    handle to dropdown2 (see GCBO)
% eventdata  reserved - to be defined in a future version of MATLAB
% handles    empty - handles not created until after all CreateFcns called

% Hint: popupmenu controls usually have a white background on Windows.
%       See ISPC and COMPUTER.
if ispc && isequal(get(hObject,'BackgroundColor'),
get(0,'defaultUicontrolBackgroundColor'))
    set(hObject,'BackgroundColor','white');
end


% --- Executes on button press in pushrecalculate.
function pushrecalculate_Callback(hObject, eventdata, handles)
% hObject    handle to pushrecalculate (see GCBO)
% eventdata  reserved - to be defined in a future version of MATLAB
% handles    structure with handles and user data (see GUIDATA)

x= handles.xdata;
y= handles.ydata;

handles.shape= get(handles.dropdown3, 'Value');      % Shape factor 2 = film, 3 = sphere
```

```
if get(handles.thickness, 'String')== '-'
    waitfor(msgbox('Input Characteristic Length'))

elseif handles.shape == 1
    waitfor(msgbox('Select Diffusion Geometry'))
else

    L= str2double(get(handles.thickness,'String'));     % get thickness
    handles.summation= str2double(get(handles.terms,'String'));     % Get terms
    IG= [str2double(get(handles.DABGUESS,'String')),...
        str2double(get(handles.phiguess,'String')),...
        str2double(get(handles.kguess,'String')),...
        str2double(get(handles.tauguess,'String'))]; % Get initial guess

    [pbest1,~,residual_1]=lsqnonlin(@(x)Fick(x,L,hObject,handles),IG(1),1e-16,100);   %
solve model

    [pbest2,~,residual_2]=lsqnonlin(@(x)BH(x,L,hObject,handles),IG(1:3));   % solve model

    [pbest3,~,residual_3]=lsqnonlin(@(x)Fick_exp(x,L,hObject,handles),[IG(1),IG(4)],[1e-
16,0],[1e-7,2]); % solve model

    [pbest4,~,residual_4]=lsqnonlin(@(x)BH_exp(x,L,hObject,handles),IG); % solve model

    ybest1=residual_1+y;
    ybest2=residual_2+y;
    ybest3=residual_3+y;
    ybest4=residual_4+y;

    cla(handles.plot1)
    plot(handles.plot1,sqrt(x),ybest1,'r','LineWidth',2)
    scatter(handles.plot1, sqrt(x),y,6,'k', 'filled')
    set(handles.plot1,'XMinorTick','on', 'YMinorTick','on');
    xlabel(handles.plot1,'time, s^{1/2}')
    ylabel(handles.plot1,'Normalized Uptake, M/M_{final}')
    title(handles.plot1,'Fickian, Constant BC')
    ylim(handles.plot1,[0 1.1])

    if get(handles.dropdown1,'Value')== 3

        cla(handles.plot2)
        plot(handles.plot2,sqrt(x),ybest2,'r','LineWidth',2)
        scatter(handles.plot2, sqrt(x),y,6,'k', 'filled')
        set(handles.plot2,'XMinorTick','on', 'YMinorTick','on');
        xlabel(handles.plot2,'time, s^{1/2}')
        ylabel(handles.plot2,'Normalized Uptake, M/M_{final}')
        title(handles.plot2,'Berens-Hopfenberg, Constant BC')
        ylim(handles.plot2,[0 1.1])

    elseif get(handles.dropdown1,'Value')== 4
```

```
        cla(handles.plot2)
        plot(handles.plot2,sqrt(x),ybest4,'r','LineWidth',2)
        scatter(handles.plot2, sqrt(x),y,6,'k', 'filled')
        set(handles.plot2,'XMinorTick','on', 'YMinorTick','on');
        xlabel(handles.plot2,'time, s^{1/2}')
        ylabel(handles.plot2,'Normalized Uptake, M/M_{final}')
        title(handles.plot2,'Berens-Hopfenberg, Exponential BC')
        ylim(handles.plot2,[0 1.1])

    else

        cla(handles.plot2)
        plot(handles.plot2,sqrt(x),ybest3,'r','LineWidth',2)
        scatter(handles.plot2, sqrt(x),y,6,'k', 'filled')
        set(handles.plot2,'XMinorTick','on', 'YMinorTick','on');
        xlabel(handles.plot2,'time, s^{1/2}')
        ylabel(handles.plot2,'Normalized Uptake, M/M_{final}')
        title(handles.plot2,'Fickian, Exponential BC')
        ylim(handles.plot2,[0 1.1])
    end

    if get(handles.dropdown2,'Value')== 3

        cla(handles.plot3)
        plot(handles.plot3,sqrt(x),ybest2,'r','LineWidth',2)
        scatter(handles.plot3, sqrt(x),y,6,'k', 'filled')
        set(handles.plot3,'XMinorTick','on', 'YMinorTick','on');
        xlabel(handles.plot3,'time, s^{1/2}')
        ylabel(handles.plot3,'Normalized Uptake, M/M_{final}')
        title(handles.plot3,'Berens-Hopfenberg, Constant BC')
        ylim(handles.plot3,[0 1.1])

    elseif get(handles.dropdown2,'Value')== 4


        cla(handles.plot3)
        plot(handles.plot3,sqrt(x),ybest4,'r','LineWidth',2)
        scatter(handles.plot3, sqrt(x),y,6,'k', 'filled')
        set(handles.plot3,'XMinorTick','on', 'YMinorTick','on');
        xlabel(handles.plot3,'time, s^{1/2}')
        ylabel(handles.plot3,'Normalized Uptake, M/M_{final}')
        title(handles.plot3,'Berens-Hopfenberg, Exponential BC')
        ylim(handles.plot3,[0 1.1])

    else

        cla(handles.plot3)
        plot(handles.plot3,sqrt(x),ybest3,'r','LineWidth',2)
        scatter(handles.plot3, sqrt(x),y,6,'k', 'filled')
        set(handles.plot3,'XMinorTick','on', 'YMinorTick','on');
        xlabel(handles.plot3,'time, s^{1/2}')
        ylabel(handles.plot3,'Normalized Uptake, M/M_{final}')
        title(handles.plot3,'Fickian, Exponential BC')
```

```
        ylim(handles.plot3,[0 1.1])

    end

    handles.ybest= [ybest1, ybest2, ybest3, ybest4];
    handles.xdata=x;
    handles.ydata=y;

    set(handles.DABFick,'String', pbest1(1))
    set(handles.DABBH,'String', pbest2(1))
    set(handles.DABFICKEXP,'String', pbest3(1))
    set(handles.DABBHEXP,'String', pbest4(1))
    set(handles.PHIBH,'String', pbest2(2))
    set(handles.KBH,'String', pbest2(3))
    set(handles.TAUFICKEXP,'String', pbest3(2))
    set(handles.PHIBHEXP,'String', pbest4(2))
    set(handles.KBHEXP,'String', pbest4(3))
    set(handles.TAUBHEXP,'String', pbest4(4))


end




guidata(hObject, handles);




function terms_Callback(hObject, eventdata, handles)
% hObject    handle to terms (see GCBO)
% eventdata  reserved - to be defined in a future version of MATLAB
% handles    structure with handles and user data (see GUIDATA)

% Hints: get(hObject,'String') returns contents of terms as text
%        str2double(get(hObject,'String')) returns contents of terms as a double


% --- Executes during object creation, after setting all properties.
function terms_CreateFcn(hObject, eventdata, handles)
% hObject    handle to terms (see GCBO)
% eventdata  reserved - to be defined in a future version of MATLAB
% handles    empty - handles not created until after all CreateFcns called

% Hint: edit controls usually have a white background on Windows.
%       See ISPC and COMPUTER.
if ispc && isequal(get(hObject,'BackgroundColor'),
get(0,'defaultUicontrolBackgroundColor'))
    set(hObject,'BackgroundColor','white');
```

```
end



function thickness_Callback(hObject, eventdata, handles)
% hObject    handle to thickness (see GCBO)
% eventdata  reserved - to be defined in a future version of MATLAB
% handles    structure with handles and user data (see GUIDATA)

% Hints: get(hObject,'String') returns contents of thickness as text
%        str2double(get(hObject,'String')) returns contents of thickness as a double


% --- Executes during object creation, after setting all properties.
function thickness_CreateFcn(hObject, eventdata, handles)
% hObject    handle to thickness (see GCBO)
% eventdata  reserved - to be defined in a future version of MATLAB
% handles    empty - handles not created until after all CreateFcns called

% Hint: edit controls usually have a white background on Windows.
%       See ISPC and COMPUTER.
if ispc && isequal(get(hObject,'BackgroundColor'),
get(0,'defaultUicontrolBackgroundColor'))
    set(hObject,'BackgroundColor','white');
end


% --- Executes on selection change in dropdown3.
function dropdown3_Callback(hObject, eventdata, handles)
% hObject    handle to dropdown3 (see GCBO)
% eventdata  reserved - to be defined in a future version of MATLAB
% handles    structure with handles and user data (see GUIDATA)

% Hints: contents = cellstr(get(hObject,'String')) returns dropdown3 contents as cell
array
%        contents{get(hObject,'Value')} returns selected item from dropdown3


% --- Executes during object creation, after setting all properties.
function dropdown3_CreateFcn(hObject, eventdata, handles)
% hObject    handle to dropdown3 (see GCBO)
% eventdata  reserved - to be defined in a future version of MATLAB
% handles    empty - handles not created until after all CreateFcns called

% Hint: popupmenu controls usually have a white background on Windows.
%       See ISPC and COMPUTER.
if ispc && isequal(get(hObject,'BackgroundColor'),
get(0,'defaultUicontrolBackgroundColor'))
    set(hObject,'BackgroundColor','white');
end

function [y] = Fick(D, L, hObject, handles)
% Solves for the infinite series solution of a flat sheet with a step
```

```
% change in concentration using time data and diffusivity
%   U(1)- Diffusivity, x- time data, L- sheet thickness

%global L terms

Sum = 0;

t= handles.xdata;
q= handles.ydata;
terms=handles.summation;

if handles.shape == 2  % Film
    for i=0:terms
        m = 8/((2*i+1)^2*pi^2)*...
            exp(-D*(2*i+1)^2*pi^2*t/(4*L^2));
        Sum = m+Sum;
    end

elseif handles.shape== 3 % Sphere
    for i=1:terms
        m = (6/pi^2)*1/i^2*exp(-D*i^2*pi^2*t/L^2);
        Sum = m+Sum;
    end
end

fit = 1-Sum;
y=fit-q;


function [y] = BH(U, L, hObject, handles)
% Solution to the Berens-Hopfenberg model using initial guesses and time
% data
%   Superposition of linera relaxation of the polymer on the fickian
%   diffusion model. U- [D, phi, k], x- time data, L- film thickness
Sum = 0;

t= handles.xdata;
q= handles.ydata;
terms=handles.summation;

if handles.shape == 2  % Film
    for i=0:terms
        m = 8/((2*i+1)^2*pi^2)*...
            exp(-U(1)*(2*i+1)^2*pi^2*t/(4*L^2));
        Sum = m+Sum;
    end

elseif handles.shape== 3 % Sphere
    for i=1:terms
        m = (6/pi^2)*1/i^2*exp(-U(1)*i^2*pi^2*t/L^2);
        Sum = m+Sum;
    end
end
```

```
fick_fit = 1-Sum;

fit = U(2)*fick_fit+(1-U(2))*(1-exp(-U(3).*t));
y=fit-q;

function [ y ] = Fick_exp(U, L, hObject, handles)
% Fickian fit using an exponential boundary condition for non-step changes
% in concentration during isotherms
%   Uses time data to fit the analytical solution with a diffusivity and a
%   transfer function time constant. U(1)- Diffusivity, U(2)-transfer
%   function time constant.

t= handles.xdata;
q= handles.ydata;
terms=handles.summation;

Sum=0;



if handles.shape == 2  % Film

    for i=0:terms
        m=exp(-U(1)*(2*i+1)^2*pi^2*t./(4*L^2))/((2*i+1)^2*(1-(2*i+1)^2*...
            (U(1)*pi^2/(4*L^2*U(2)))));
        Sum=Sum+m;
    end

    exponential=(8/pi^2)*Sum;

    trans= exp(-t*U(2)).*(U(1)/(U(2)*L^2))^(0.5).*tan((L^2*U(2)/(U(1)))^0.5);

elseif handles.shape== 3 % Sphere



    for i=1:terms
        m=exp(-U(1)*i^2*pi^2*t/L^2)/(i^2*(i^2*pi^2-L^2*U(2)/U(1)));
        Sum=Sum+m;
    end

    trans=-6*L^2*U(2)/(pi^2*U(1))*Sum;

    exponential= 3*U(1)/(U(2)*L^2)*exp(-t*U(2))*(1-(L^2*U(2)/U(1))^0.5*...
        cot((L^2*U(2)/U(1))^0.5));
end

fit=1-trans-exponential;
y=fit-q;

function y = BH_exp(U, L, hObject, handles)
%Solution to the Berens-Hopfenberg model using initial guesses and time
```

```
% data with an exponential boundary condition
%   U(1)- D, U(2) phi, U(3)- k, U(4)- beta

t= handles.xdata;
q= handles.ydata;
terms=handles.summation;

Sum=0;
if handles.shape == 2  % Film

    for i=0:terms
        m=exp(-U(1)*(2*i+1)^2*pi^2*t./(4*L^2))/((2*i+1)^2*(1-(2*i+1)^2*...
            (U(1)*pi^2/(4*L^2*U(4)))));
        Sum=Sum+m;
    end

    exponential=(8/pi^2)*Sum;

    trans= exp(-t*U(4)).*(U(1)/(U(4)*L^2))^(0.5).*tan((L^2*U(4)/(U(1)))^0.5);

elseif handles.shape== 3 % Sphere



    for i=1:terms
        m=exp(-U(1)*i^2*pi^2*t/L^2)/(i^2*(i^2*pi^2-L^2*U(4)/U(1)));
        Sum=Sum+m;
    end

    trans=-6*L^2*U(4)/(pi^2*U(1))*Sum;

    exponential= 3*U(1)/(U(4)*L^2)*exp(-t*U(4))*(1-(L^2*U(4)/U(1))^0.5*...
        cot((L^2*U(4)/U(1))^0.5));
end

fit=1-trans-exponential;

fit = U(2)*fit+(1-U(2))*(1-exp(-U(3).*t));
y=fit-q;
```

Published with MATLAB® R2017a

A.5 The Calculation of Adsorbed Selectivity Using IAST

Iast_Call.m

Use for calculating IAST selectivities given isotherms

Pre-load variables for P and y into the workplace if using vapor phase data IAST_fit

Use IAST_a and set isotherm parameters in the code if using gas isotherms. Set linspace of P, keep y constant.

```
%% IAST Call
% Change IAST_fit to IAST_a as necessary
for i=1:length(P)
    [S(i),Q(i,:)]=IAST_fit(P(i),y(i,:));
end

S=S';

scatter(P,S)
```

Published with MATLAB® R2017a

IAST_fit.m

Will output q1=(y's,P's), q2=(y's,P's)

```
function [S,Q]=IAST_fit(P,y)
```

```
%% Isotherm Specification
tic

%P=P;        % Total Pressure

y=y'; % Gas phase comp

% Isotherms, x=P, y=q

x1=[0 0.0364 0.0455 0.091 0.1365 0.182 0.364 0.546 0.728 0.91 1.092 1.274 1.456];

y1=[0 2.3053 2.37458 2.57831 2.68446 2.76033 2.95492 3.06713 3.15363 3.21031 3.25544...
3.30104 3.33303];

x2=[0 0.27695 0.55952 1.12242 1.68363 2.24259 2.80324 3.3667 3.93805...
4.49194 5.04077 5.36331 5.58622];

y2=[0 0.00357 0.00648 0.01149 0.01504 0.02014 0.02689 0.0349 0.0432 0.05085...
0.16873 0.38617 0.61132];

%Isotherm function

% 'pchipinterp'
% 'linearinterp'

[fit1, ~] = fit( x1', y1', 'linearinterp' );
[fit2, ~] = fit( x2', y2', 'linearinterp' );

% Interpolation fit of isotherms in the abscence of analytical fits
iso={fit1, fit2};

%iso=@(b0,q0,p) b0(1)*q0(1)*p/(1+b0(1)*p)+b0(2)*q0(2)*p/(1+b0(2)*p);
```

```
%% Iterative Initialization
eta= 10^-4; %Tolerance
eta_1=10;   %z convergence
eta_2=[10 10];  %Hypothetical pressure convergence

% Estimate Spreading Pressure
z=y(1)*integral(@(x)fit1(x)/x,0,P*y(1),'ArrayValued',true)+y(2)*integral(@(x)fit2(x)/x,0,
P*y(2),'ArrayValued',true);

%.*(exp(z./[y1(end),y2(end)]')-1); % First estimate at single component pressure
P_0=P.*y;
```

```
Pr_last=P_0;
count=0;

% Zero finding routine
while any(eta_1 > eta)
    while any(eta_2 > eta)
        for i=1:2

            G(i)=integral(@(x)feval(iso{i},x)/x,0,P_0(i),'ArrayValued',true)-z;
%#ok<AGROW>
            G_prime(i)=feval(iso{i},P_0(i))/P_0(i); %#ok<AGROW>
            Pr_last(i)=P_0(i);
            P_0(i)=Pr_last(i)-G(i)./G_prime(i);
            eta_2(i)=abs(P_0(i)-Pr_last(i))./Pr_last(i);
        end
    end

    for i=1:2
        Cu_0(i)=feval(iso{i},P_0(i)); %#ok<AGROW>
    end

    F=sum(P.*y./P_0)-1;
    F_prime=-sum(P*y./(P_0.*Cu_0'));

    z_last=z;
    z=z_last-F/F_prime;
    eta_1=abs(z-z_last)/z_last;
    count=count+1;
    eta_2=[10,10];
end

x=P*y./P_0;
Qtot=sum(x./Cu_0')^-1;

Q=Qtot*x;
S=(Q(1)/(P*y(1)))/(Q(2)/(P*y(2)));


toc
```

Published with MATLAB® R2017a

IAST_a.m

Will output q1=(y's,P's), q2=(y's,P's)

```
function [S,Q]=IAST_a(P,y)
```

```
%% Isotherm Specification

tic
%
%  P=0.1;        % Total Pressure
%
%  y=[0.78, 0.22]; % Gas phase comp

% Dual-Site Langmuir Isotherms

b1=[.01533 .006895];  % comp 1 site 1 / site 2
q1=[27.25 2.122];

b2=[.001170 .02609];  % comp 2 site 1 / site 2
q2=[27.87 1.919 ];

b=[b1' b2']';
q=[q1' q2']';

%Isotherm function
lang=@(b0,q0,p) b0(1)*q0(1)*p/(1+b0(1)*p)+b0(2)*q0(2)*p/(1+b0(2)*p);
```

```
%% Iterative Initialization
eta= 10^-4; %Tolerance
eta_1=10;   %z convergence
eta_2=[10 10];  %Hypothetical pressure convergence

% Estimate Spreading Pressure
z=y(1)*integral(@(x)lang(b(1,:),q(1,:),x)/x,0,P,'ArrayValued',true)+y(2)*integral(@(x)lan
g(b(2,:),q(2,:),x)/x,0,P,'ArrayValued',true);

%.*(exp(z./(sum(q,1)')-1))'; % First estimate at single component pressure
P_0=P.*y;
Pr_last=P_0;
count=0;

% Zero finding routine
while any(eta_1 > eta)
    while any(eta_2 > eta)
        for i=1:2

            G(i)=integral(@(x)lang(b(i,:),q(i,:),x)/x,0,P_0(i),'ArrayValued',true)-z;
%#ok<AGROW>
            G_prime(i)=lang(b(i,:),q(i,:),P_0(i))/P_0(i); %#ok<AGROW>
```

```
            Pr_last(i)=P_0(i);
            P_0(i)=Pr_last(i)-G(i)./G_prime(i);
            eta_2(i)=abs(P_0(i)-Pr_last(i))./Pr_last(i);
        end
    end

    for i=1:2
        Cu_0(i)=lang(b(i,:),q(i,:),P_0(i)); %#ok<AGROW>
    end

    F=sum(P.*y./P_0)-1;
    F_prime=-sum(P*y./(P_0.*Cu_0));

    z_last=z;
    z=z_last-F/F_prime;
    eta_1=abs(z-z_last)/z_last;
    count=count+1;
    eta_2=[10,10];
end

x=P*y./P_0;
Qtot=sum(x./Cu_0)^-1;

Q=Qtot*x;
S=(Q(1)/(P*y(1)))/(Q(2)/(P*y(2)));

toc
```

Published with MATLAB® R2017a

APPENDIX B. GPROMS CODES

B.1 The Modeling of Multicomponent Adsorption in a Tank of Limited Volume

PROCESS OVERALL (KINETIC BATCH)

```
Unit
Batch AS Batch_Decay

SCHEDULE
Continue for 3600
```

MODEL BATCH_DECAY (KINETIC BATCH)

```
Parameter
    Radius          AS      REAL
    Nc              AS      INTEGER
    D0              AS      Array(Nc) OF REAL
    b               AS      ARRAY(Nc) OF REAL
    C_s             AS      ARRAY(Nc) OF REAL
    Po              AS      ARRAY(Nc) OF REAL
    P_i             AS      ARRAY(Nc) OF REAL
    T               AS      REAL
    Mass            AS      REAL
    Rg              AS      Real
    Density         AS      Real
    V               AS      Real
    Pi              AS      Real

Distribution_Domain

    Radial      AS  [0 : Radius]

Variable

    C_u                     AS Distribution(Nc,Radial) OF Concentration
# Ads Conc
    Bulk_Moles              AS ARRAY(Nc) OF Moles
# Moles in the bulk gas
    Adsorbed_Total          AS ARRAY(Nc) OF Moles
# Moles in the adsorbate
    P                       AS ARRAY(Nc) OF Pressure
# Pressures in bulk
    Dc                      AS Distribution(Nc,Nc,Radial) OF Diffusivity
# Diffusivities
    Selectivity             AS Sel
    Recovery                As Perc
    PPropane                As Perc
```

```
    MyTime                          As counter

Set

    Radius:=80e-4 ;   # Particle Size
    Nc:= 2;           # Number of Components
    D0:= [ 1.58e-8 , 1.52e-11];      # Diffusion Coeff @ 0 load b:= [.003, 0.055]; #
    Henry's for langmuir
    C_s:= [8*0.8, 5*0.8]; # Saturation for langmuir Po:= [0, 0];     # Initial
    Pressure
    P_i:= [250, 250];                # Dosing bulk pressure
    T:= 293;                         # Temp
    Mass:= .500;                          # Sample Mass
    Density:= 0.8;                   # Sample Density
    Rg:= 8.314;                      # Gas constant
    V:= 10;                          # Sample volume
    Radial:= [CFDM, 2, 200];         # Discretization of radial element Pi:= 3.14159;     # Pi

Boundary

    partial(C_u(,0),Radial)=0;  # Symmetry condition
    for i:= 1 to Nc do
    C_u(i,Radius)= C_s(i)*(b(i)*P(i))/(1+sigma(b*P))*(1-exp(-10*MyTime));
    #Surface Condition- fast exponential equilibration end

    Equation
    $MyTime=1;

    for i:=1 to Nc do
    Bulk_Moles(i)= P_i(i)*V/(Rg*T)-integral(r:= 0:Radius; C_u(i,r)*4*Pi*r^2)
    *Mass/(4/3*pi*Radius^3*Density); end

    P=Bulk_Moles*Rg*T/V;

    Adsorbed_Total= integral(r:= 0:Radius; C_u(,r)*4*Pi*r^2)*Mass/ (4/3*pi*Radius^3*Density);

    #Diffusion Equation for
    i:= 1 to Nc do
    for r:= 0|+ to Radius|- do
    $C_u(i,r) =(1/r^2)*(2*r*(Dc(i,1,r)*partial(C_u(1,r),Radial)+Dc(i,2,r)
    *partial(C_u(2,r),Radial))
    +r^2*((partial(Dc(i,1,r),Radial)*Partial(C_u(1,r),Radial)+Dc(i,1,r)
    *partial(C_u(1,r),Radial,Radial))
                    +(partial(Dc(i,2,r),Radial)*Partial(C_u(2,r),Radial)+Dc(i,2,r)
    *partial(C_u(2,r),Radial,Radial)))); END
    END

    #Diffusion/Langmuir Isotherms for
    i:=1 to Nc do
    for j:=1 to Nc do
    for r:= 0 to Radius do if i=j then
    Dc(i,j,r)= D0(i)*(1+(C_u(i,r)/C_s(i))/(1-sigma(C_u(,r)
    /C_s)));


end
```

```
 else
 Dc(i,j,r)= D0(i)*(C_u(i,r)/(C_s(j)*(1-sigma(C_u(,r)/C_s)))); end
                    end
            end

            Selectivity= (P(2)/P(1))/(P_i(2)/P_i(1)); Recovery=P(2)/P_i(2);
            PPropane=P(2)/sigma(P);

            Initial

            for i:= 1 to Nc do
            C_u(i,0|+:Radius|-) = C_s(i)*(b(i)*Po(i))/(1+sigma(b*Po)); end

MyTime=0;
```

APPENDIX C. INCOMPLETE WORKS

C.1 Sorption-Induced Gate-Opening of ZIF-8 by N_2

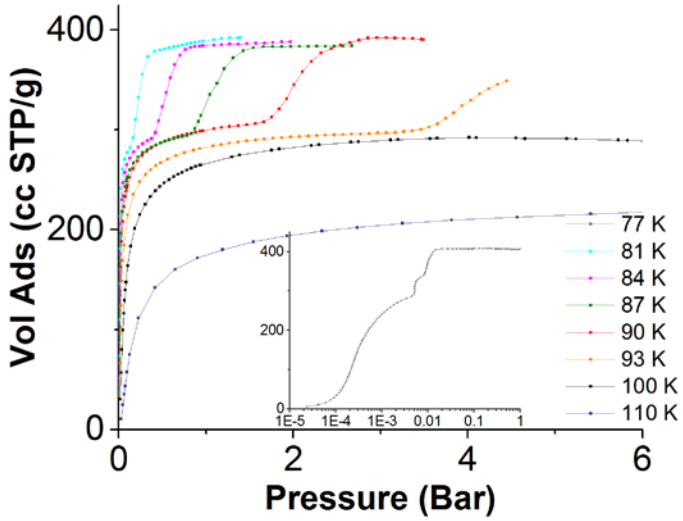

Figure C.1 ZIF-8 N_2 isotherms showing a shift of the gate opening event to higher pressures with increasing temperature. Isotherms measured in the HPVA-II.

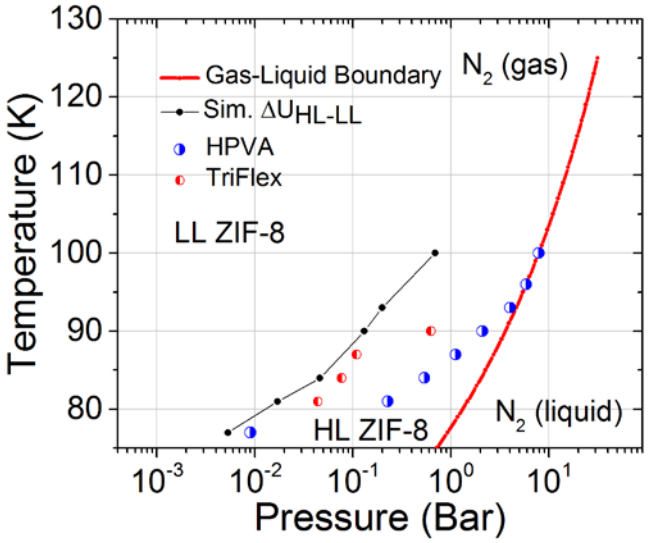

Figure C.2 Plotting of phase boundary measurements by an HPVA-II, TriFlex, and simulated GCMC transitions.

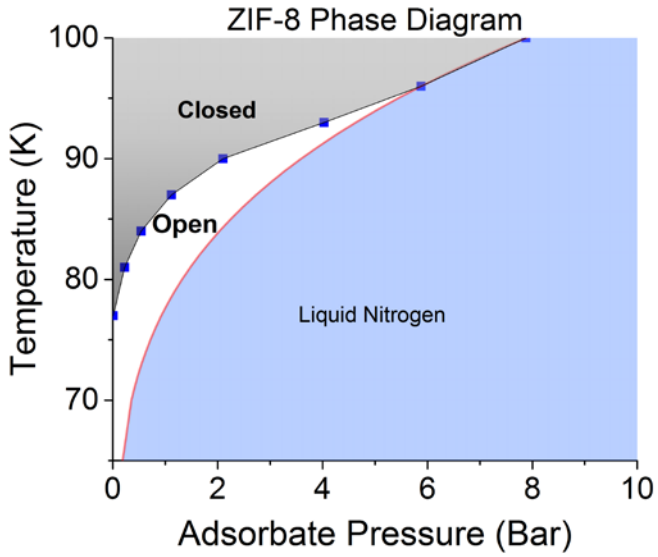

Figure C.3 Summarized phase boundary of the ZIF-8 gate-opening transition. It is unclear and unlikely the phase diagram contains an open structure at 0 bar at lower pressures, rather an increasingly closer approach.

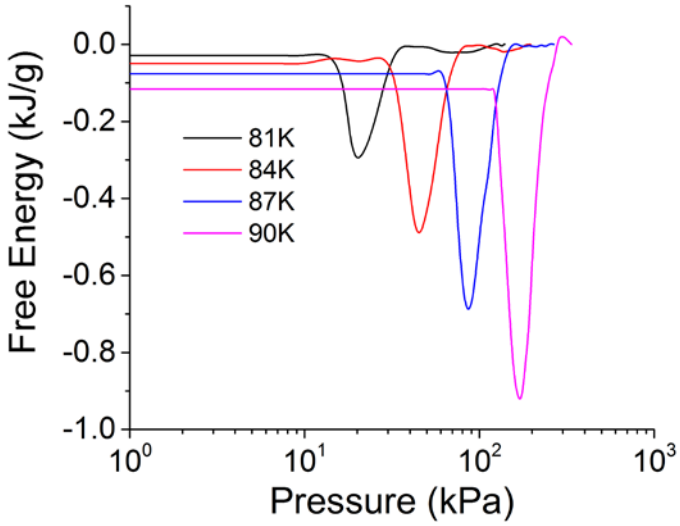

Figure C.4 Free energy differences between the adsorption and desorption branches of the isotherms, as put for by Pera-Titus[1]

C.2 References

1. Pera-Titus, M., Intrinsic Flexibility of the Zeolitic Imidazolate Framework ZIF-7 Unveiled by CO2 Adsorption and Hg Intrusion. *Chemphyschem : a European journal of chemical physics and physical chemistry* **2014,** *15* (8), 1581-6.